C.E.A. / D.S.M.

Service de Physique Théorique

Thèse de doctorat de l'université Paris XI

Spécialité : Physique théorique

présentée par :

Jérôme RECH

pour obtenir le grade de Docteur de l'Université Paris XI

Sujet de la thèse :

Phénomènes quantiques macroscopiques dans les systèmes d'électrons fortement corrélés

soutenance prévue le 19 Juin 2006 devant le jury composé de :

Mme LHUILLIER Claire	Présidente
Melle PEPIN Catherine	Co-Directrice
M. COLEMAN Piers	Co-Directeur
M. JOLICOEUR Thierry	Rapporteur
M. PUJOL Pierre	Rapporteur
M. KOTLIAR Gabriel	Examinateur
M. KIRYUKHIN Valery	Invité
M. SHAPIRO Joel	Invité

MACROSCOPIC QUANTUM PHENOMENA IN STRONGLY INTERACTING FERMIONIC SYSTEMS

BY JÉRÔME RECH

A dissertation submitted to the
Graduate School – New Brunswick
Rutgers, The State University of New Jersey
in partial fulfillment of the requirements
for the degree of
Doctor of Philosophy
Graduate Program in Physics and Astronomy
Written under the direction of
Doctor Catherine Pépin and
Professor Piers Coleman
and approved by

New Brunswick, New Jersey
June, 2006

Contents

Introduction

From the crystalization of water into snowflakes, the alignment of electron spins in a ferromagnet, the emergence of superconductivity in a cooled metal, to the very formation of the large scale structure of the universe, all involve phase transitions.

Understanding this so-called "critical behavior" has been a great challenge and more than a century has gone by from the first discoveries until a consistent picture emerged. The theoretical tools and concepts developed in the meantime now belong to the central paradigms of modern physics.

When the temperature at which a phase transition occurs is suppressed to near absolute zero, quantum effects become important and the new puzzling behavior that develops around this "quantum critical point" is still very far from being completely resolved.

1 From critical opalescence to quantum criticality

A typical material consist of many elementary particles or degrees of freedom. The fundamental microscopic laws that capture the physics of such systems are known: we have to solve a Schrödinger equation for an ensemble of about 10^{23} atoms. This, however, is like trying to understand the layout of a city by examining it one brick at a time.

Instead, new ways of thinking are required, ones that can describe the behavior of complex collections of atoms. Statistical physics, by arguing that although the individual motions are complex the collective properties acquire qualitatively new forms of simplicity, does exactly that. Collective behavior is also important at the unstable interface between two stable states: the critical point.

The notion of a critical phenomenon traces back to 1869, when Andrews [1] discovered a very special point in the phase diagram of carbon dioxide: at 31°C and under 73 atm, the properties of the liquid and the vapar become indistinguishable. Andrews called this point a "critical point", and the associated strong scattering of light displayed by the system close to this point, the critical opalescence.At the critical point, the system undergoes a transition from one state to another – a phase transition – in a quest to minimize its free energy. Close to this critical point, the material is in maximum confusion, fluctuating between the two competing phases.

Seventy years later, pioneering work by Lev Landau [2] proposed that the development of phases in a material can be dexcribed by the emergence of an "order parameter", a quantity which describes the state of order as it develops at each point in the material. In this picture, the critical state of the system, close to the phase transition, corresponds to the development of thermal fluctuations (responsible for the "confusion" of the system at criticality) over successively larger regions: the associated length scale ξ diverges at the critical point. In the meantime, the typical time scale τ that determines the relaxation of the order parameter also diverges at criticality, verifying:

$$\tau \sim \xi^z \tag{1}$$

where z is the dynamical exponent.

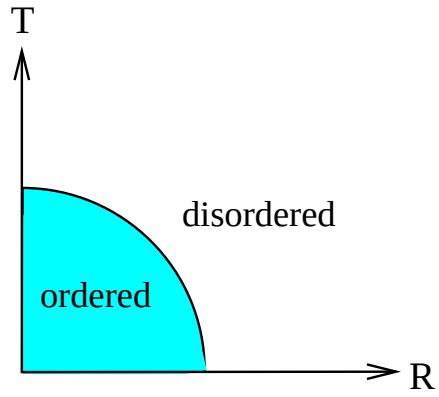

Ordered state	Disordered state	Order parameter
Gas	Liquid	Density difference
Ferromagnet	Paramagnet	Magnetization
Ferroelectric	Paraelectric	Polarization
Nematic liquid crystal	Isotropic liquid	Director

a) b)

Figure 1: a) Typical phase diagram of a classical continuous phase transition. The line separating the ordered and disordered states is a line of critical points. b) A few examples of order parameters and their associated phase transition.

Later on, it was realized that in the vicinity of the critical point, the physical properties of the system could be described by a handful of numbers: the critical exponents. The critical exponent z defined above is one of them.

It tunrs out that the same set of these exponents allows to describe phase transitions with totally different microscopic origins. This feature led to the concept of universality: the details of the microscopic laws governing the behavior of atoms in the material are no longer important in specifying its physical properties.

In the mid-seventies, when the study of phase transitions was undergoing a renaissance triggered by the development of Wilson's renormalization group, John Hertz [3] asked the following question: what happens to a metal undergoing a phase transition whose critical temperature is tuned down to absolute zero?

2 Stirring up a quantum cocktail

What is so special about a zero-temperature phase transition? First of all, if the temperature is fixed at absolute zero, one needs another control parameter to drive the system through the critical point: the change of state now results from modifying pressure, magnetic field, or even chemical composition.

Moreover, at zero temperature, the thermal fluctuations that drive the transition no longer exist. In this situation, the phase transition os triggered by quantum fluctuations: due to the uncertainty principle, a particle cannot be at rest at zero temperature (since then both its position and velocity would be fixed), so that all particles are in the state of quantum agitation. This "zero point motion" plays the same role as the random thermal motion of the classical phase transitions: when it becomes too wild, it can melt the long-range order.

Hertz showed in his original work that the key new feature of the quantum phase transition is an effective increase of the number of dimensions, associated to quantum mechanics. While a statistical description of a classical system is based on an average over all possible spatial configurations of the particles, weighted by the Boltzmann factor[1] $e^{-E/(k_B T)}$, a probabilistic description of a quantum system relies on averaging all the ways in which a particle moves in time weighted by a Schrödinger factor $e^{-iHt/\hbar}$. Due to the close resemblance of these two weighting factors, a single combined description of a quantum statistical system is possible. Therefore a quantum phase transition looks like a classical one, except that the configurations now vary in "imaginary time" in addition to varying in space. The imaginary time now appears as an extra dimension, or more accurately as z extra dimensions, where z is the dynamical critical exponent defined in Eq. (1). The effective dimensionality d_{eff} of the model increases compared to the spatial dimension d according to:

$$d_{\text{eff}} = d + z \tag{2}$$

One might legitimately wonder why the appearance of such new dimensions do not invalidate previous classical thermodynamic results. It turns out that at finite temperature, there always exist a region close to the critical point, where the thermal fluctuations are much more important than the quantum ones. It follows that, in the vicinity of a finite temperature critical point, the phase transition can be described within the framework of classical statistical mechanics. This naturally does not mean that quantum mechanics plays no role in this case as it might determine the very existence of the order parameter. This only points out that the behavior of this order parameter, close to the finite temperature critical point, is controlled by classical thermal flcutuations.

Hertz's idea of a quantum critical point may seem like a rather esoteric theoretical observation. After all, the zero temperature is impossible to access experimentally,

[1] where E is the energy of the configuration

so that quantum critical points look more like mathematical oddities rather than observable physical phenomena.

It took several years after Hertz's work to realize that the quantum critical point governs the physics of a whole region of the phase diagram: the quantum critical regime. Moving away from the quantum critical point by increasing the temperature, one enters a region of the phase diagram where there is no scale to the excitations other than temperature itself: the system "looks" critical, as the quantum fluctuations are still very strong. As a consequence, the properties of the system in this region of the phase diagram are qualitatively transformed in a fashion that is closely related to the physics behind the quantum phase transition.

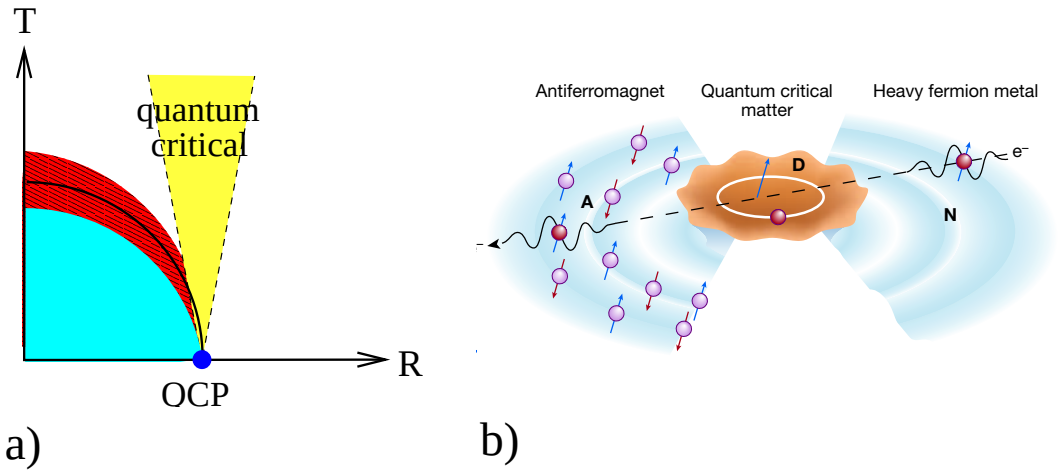

Figure 2: a) Typical phase diagram of a phase transition whose critical temperature has been tuned to zero, leading to a quantum critical point, and the corresponding quantum critical region. b) Picturesque view of droplets of nascent order developing at quantum criticality. Inside the droplet, the intense fluctuations radically modify the motion of the elctrons (from [4]).

3 Quantum criticality observed

Indeed, the quantum critical region, through its unusual properties, has been extensively observed experimentally. The best studied examples involve magnetism in metals.Gold-doped $CeCu_6Si$ was among the first ones [5].

When pressure is applied to this compound, the transition towards an antiferromagnetic ordering (associated to the cerium atoms acting as local magnetic moments) is tuned to occur at zero temperature. In the quantum critical region, experimentalists found an almost linear resistivity (unseen in both phases surrounding the quantum critical region) extending way above the quantun critical point, on almost a decade in temperature. Since then, more than fifty other compounds, built

on the same recipe of localized moments buried inside a non-magnetic bulk, have been discovered. We even have an apparent case of a line of quantum criticality instead of a sinle point.

But the observation of quantum criticality is not limited to these magnetic materials. Quantum critical behavior has been reported, e.g., in organic material where the change of pressure or chemical doping leads to quantum critical fluctuations of the electric charge. Quantum criticality has even been observed in a surprisingly simple metal: chromium.

Hertz's original idea of a zero-temperature phase transition was once regarded as an intellectual curiosity. It has now become a rapidly growing field of condensed-matter physics.

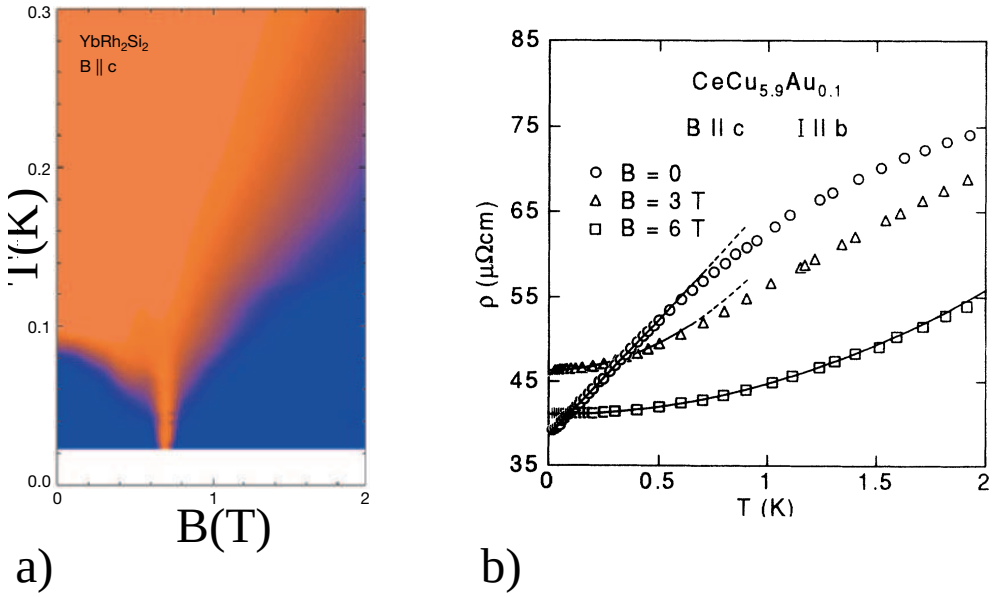

Figure 3: a) Temperature-magnetic field phase diagram of $YbRh_2Si_2$. Blue regions indicate normal metallic behavior. Orange regions correspond to the quantum critical regime (from [6]). b) Resistivity as a function of temperature for the compound $CeCu_5.9Au_0.1$. Solid lines indicate a linear ($B = 0$) and a quadratic fit ($B \neq 0$) (from [5]).

4 Unsolved puzzles

Some of the strange properties reported experimentally in the quantum critical region echo the predictions of Hertz (and subsequent extensions of his original theory). But this conventional wisdom is flouted in several aspects, and Hertz thirty-year-old theory cannot account for present experiments. The discrepancy ranges from an incorrect order of the transition (like itinerant ferromagnetic systems that turn out

to order magnetically through a first-order transition where a continuous one was predicted) to a profound inadequacy in the physical properties of the quantum critical regime (like the antiferromagnetic transition of Ce and Yb-based compounds, the so-called "heavy fermion" materials).

A series of compounds, which a priori do not seem so different from the ones matching perfectly Hertz predictions, created the controversy. Some physicists believe that Hertz theory can be saved, and that provided one can derive a new extension that could take proper account of the complexity of the material, new experiments can be explained based on Hertz framework of quantum critical phenomena. However, none of these attempts have been convincing enough, and the "ultimate extension" of Hertz theory remains to be found.

Others argue that the discrepancy between the canonical theory and the recent experimental results comes from a failure of Hertz's original approximations. This failure can be attributed to an incomplete account of the realities of the materials (like, say, disorder), or to an unjustified assumption in the mathematical derivation. This is the point of view we develop in the first part of the present text, where we show that independently of its failures to explain experimental results, Hertz theory is bound to break down in the special case of a ferromagnetic quantum critical point.

Finally, a third possibility considers that a new starting point is needed for a proper examination of the fluctuations: a new framework for quantum phase transitions is required. If it were the case, such a new development would be quite remarkable, as the current conventional picture relies on two cornerstones of modern physics, namely the theory of classical critical phenomena and the quantum mechanics. In the second part of this work, we develop a new approach towards the understanding of the quantum critical behavior of heavy fermion materials. Motivated by the failures of Hertz theory to account for the recent experimental results for these compounds, we seek new insights from an unexplored route towards criticality. Such new elements may help in devising a new mean field theory for the quantum critical point in these systems.

5 Outline

The present dissertation is divided up into two parts.

In the first part, we study the stability of the ferromagnetic critical point in close relation with Hertz theory.

Chapter 1 is an introduction to the ideas and assumptions behind Hertz canonical theory of quantum critical phenomena. After reviewing some of the experimental successes of the latter, we focus on the main failures and the possible explanations advanced to account for them.

Chapter 2 presents the phenomenological model used as a starting point of our analysis. After a short treatment based on a perturbative expansion, we show what the crucial elements are for deriving a controllable scheme that could describe

the quantum critical behavior of itinerant ferromagnets. We then move on to this derivation, and alter verify that the various approximations made in the beginning at indeed justified.

Chapter 3 contains our main results. It presents the computation of the static spin susceptibility and shows that a non-analytic contribution arises, leading to a breakdown of the continuous transition towards ferromagnetism below a given energy scale. This same result is recast within the framework of Hertz theory. We further argue that the breakdown is a peculiarity of the ferromagnetic case and does not seem to appear in closely related models.

Chapter 4 recalls the main conclusions of this first part and presents the future work towards a better understanding of the ferromagnetic quantum critical point.

Some of the results of this first part have been published in a short letter (Publication 1) but most of the present work is unpublished at the moment and will give rise to a longer publication, still in preparation (Publication 2). For this reason, we chosoe to present all technical details either in the main text or in the appendices.

In the second part, we study a large-N approach of quantum impurity models based on a bosonic representation of the localized spin.

Chapter 5 is an introduction to the Kondo and Anderson models, and to their modern applications to the physics of quantum dots and heavy fermion materials.

Chapter 6 recalls the main results of the bosonic large-N approach to the description of the overscreened and underscreened Kondo impurity. We then prove that contrarily to the common wisdom, the same method can be used to describe the exactly screened case as well.

Chapter 7 presents an extension of the previous bosonic large-N approach to the case of two coupled impurities. Our results suggest that the approach is not only capable of handling magnetic correlations but also to describe the physics of the quantum critical point. They are in line with previous results for this system. The results of Chapters 6 and 7 have been grouped in Publication 4

Chapter 8 seeks a generalized method that could cure some of the failures of the original large-N method. We show that although this promising new approach do lead to a better description of the exactly screened single impurity, it does not account for the full physics of the Fermi liquid state. These results led to Publication 5

Chapter 9 concerns an extension of the large-N bosonic approach to the Kondo lattice model. Some of these results, along with technical derivations of an extended Luttinger-Ward description of this model, are presented in Publication 3.

Part I

Instability of a Ferromagnetic Quantum Critical Point

CHAPTER 1

Introduction and motivations

Contents

In this chapter, we review the canonical quantum critical theory for the itinerant electronic systems, the so-called Hertz-Millis-Moriya theory (HMM). We then present some of the experimental puzzles related to the ferromagnetic quantum critical point in these systems as well as some recent analytical studies questioning the validity of the HMM theory.

1.1 Quantum critical theory of itinerant ferromagnets

The simplest model of a metal is the non-interacting Fermi gas. In such a system, however, there is an equal number of electrons occupying either spin states in the

conducting band: the motion of up and down spin is uncorrelated, and there are no magnetic effect to be found. Introducing an interaction between the electrons leads to correlations and hence magnetism in the Fermi sea.

To be more concrete, we consider a lattice model with repulsion between the electrons, such as the Hubbard model [7], whose Hamiltonian writes:

$$H = \sum_{\mathbf{k}} \sum_{\sigma=\uparrow,\downarrow} (\epsilon_{\mathbf{k}} - \mu) c^{\dagger}_{\mathbf{k}\sigma} c_{\mathbf{k}\sigma} + U \sum_i n_{i\uparrow} n_{i\downarrow} \tag{1.1}$$

where we consider the system at low density (to stay far away from the Mott transition at half-filling). This model Hamiltonian is characterized by a competition between the kinetic term and the Coulomb interaction U, and as such is a good candidate for displaying a quantum phase transition between a Fermi liquid (where the kinetic term dominates) and a magnetically ordered state (where the repulsion is dominant).

The Coulomb repulsion term can be written in terms of the charge and spin density variables:

$$U \sum_i n_{i\uparrow} n_{i\downarrow} = \frac{U}{4} \sum_i (n_{i\uparrow} + n_{i\downarrow})^2 - \frac{U}{4} \sum_i (n_{i\uparrow} - n_{i\downarrow})^2 \tag{1.2}$$

where $(n_{i\uparrow} - n_{i\downarrow})/2 = \phi_i^z$ is the magnetization, and $N_i = n_{i\uparrow} + n_{i\downarrow}$ the total number of electrons at site i.

1.1.1 Mean-field theory and Stoner criterion

Let's assume that there exists a net magnetization $M_z = \langle \phi_i^z \rangle$ and ask under what condition this is energetically favorable compared to the unmagnetized state.

Treating this model in a mean-field way, each electron sees an effective magnetic field $B_{\text{eff}} = 2UM_z$ due to the magnetization of its fellow electrons, as well as a renormalization of the chemical potential:

$$-U \left(\phi_i^z\right)^2 \quad \underset{MF}{\longrightarrow} \quad U(-2M_z \phi_i^z + M_z^2) \tag{1.3}$$

$$\frac{U}{4} N_i^2 \quad \underset{MF}{\longrightarrow} \quad \frac{U}{4} \left(2\langle N \rangle N_i - \langle N \rangle^2\right) \tag{1.4}$$

The variational energy of the ground-state then writes:

$$\begin{aligned} E_{\text{var}}(M_z) &= \langle H_{\text{eff}} \rangle \\ &= E_{\text{kin}}(M_z) - M_z B_{\text{eff}} + U M_z^2 \end{aligned} \tag{1.5}$$

where $E_{\text{kin}}(M_z) = \sum_{\mathbf{k},\sigma} (\epsilon_k - \tilde{\mu}) \langle c^{\dagger}_{\mathbf{k}\sigma} c_{\mathbf{k}\sigma} \rangle$, and $\tilde{\mu}$ is the renormalized chemical potential.

As we are interested in the onset of ferromagnetism, the spontaneous magnetization M_z can be assumed to be small, so that one can treat the electron gas in the linear response regime. Introducing the Pauli susceptibility χ_0 of the non-interacting Fermi gas in zero magnetic field, one has:

$$E_{\rm kin}(M_z) = E_{\rm kin}(0) + \frac{M_z^2}{2\chi_0} \tag{1.6}$$

It follows that an instability towards the development of a spontaneous magnetization occurs when:

$$2U\chi_0 = 1 \tag{1.7}$$

which is known as the Stoner criterion [8] for the onset of ferromagnetism in metals.

1.1.2 Hertz-Millis-Moriya effective theory (HMM)

Now that we know from this simple mean field approach that a quantum critical point is expected as a function of the Coulomb interaction U, we turn to a more careful analysis of the behavior of the system as one approaches this QCP from the paramagnetic side.

□ Derivation

The derivation of the effective theory was first carried out by Béal-Monod and Hertz [9, 10, 3]. Starting from the Hubbard model, Eq. (1.2), and performing a Hubbard-Stratonovich decomposition on the interacting term in the spin channel, the partition function reads:

$$Z = Z_0 \int \mathcal{D}[c,\phi] exp\left[- \int_0^\beta d\tau \left(\phi_i^z(\tau)\phi_i^z(\tau) - \sqrt{U}\phi_i^z(\tau) c_{i\alpha}^\dagger(\tau)\sigma_{\alpha\beta}^z c_{i\beta}(\tau) \right) \right] \tag{1.8}$$

where we chiefly focused on the spin fluctuations and disregarded the charge ones, assuming they are unimportant close to the ferromagnetic QCP.

Integrating the fermionic degrees of freedom out of the partition function, one obtains a purely bosonic effective theory in terms of the order-parameter field $\phi(x,\tau)$, given by the Landau-Ginzburg-Wilson (LGW) free energy functional:

$$\begin{aligned}
\Phi[\phi] &= \int_0^\beta d\tau \int_0^\beta d\tau' \left[\phi_i(\tau)\phi_i(\tau)\delta(\tau-\tau') - {\rm Tr}\left(1 - \sqrt{U}\phi_i G_0^{ij}(\tau-\tau') \right) \right] \\
&= \sum_{\omega_n, q} \left(1 - U\chi_0(q, i\omega_n) \right) \phi(q, i\omega_n)\phi(-q, -i\omega_n) \\
&\qquad + T \sum_{\omega_i, q_i} u(1,2,3,4)\phi(q_1, i\omega_1)\phi(q_2, i\omega_2)\phi(q_3, i\omega_3)\phi(q_4, i\omega_4) \\
&\qquad\qquad \times \delta(q_1+q_2+q_3+q_4)\delta(\omega_1+\omega_2+\omega_3+\omega_4) + \dots
\end{aligned} \tag{1.9}$$

where we expanded in the last expression up to fourth power in ϕ, and used the notation G_0 for the conduction electron Green's functions at $U = 0$.

The bare dynamical susceptibility $\chi_0(q, i\omega_n)$ is given by a Lindhard expansion around $q = \omega = 0$ close to the ferromagnetic phase transition:

$$\chi_0(q, \omega_n) = \chi_0 - b\frac{q^2}{k_F^2} + a\frac{|\omega_n|}{v_F q} \tag{1.10}$$

The same kind of derivation can be extended to a vector order parameter, so that the spin rotation invariance is preserved. This only affects the numerical prefactors so that the effective bosonic theory we refer to in the rest of this chapter ultimately writes:

$$\begin{aligned}\Phi[\mathbf{S}] \;=\; & \sum_n \int \frac{d^d q}{(2\pi)^d}\left(\delta + q^2 + \frac{|\omega_n|}{q}\right)\mathbf{S}(\mathbf{q},\omega_n)\cdot\mathbf{S}(-\mathbf{q},-\omega_n) \\ & + uT \sum_{n_1,n_2,n_3,n_4} \int \frac{d^d q_1}{(2\pi)^d}\cdots\frac{d^d q_4}{(2\pi)^d}\;\delta(\mathbf{q_1}+\mathbf{q_2}+\mathbf{q_3}+\mathbf{q_4})\;\delta_{n_1+n_2+n_3+n_4} \\ & \times\left[\mathbf{S}(\mathbf{q_1},\omega_{n_1})\cdot\mathbf{S}(\mathbf{q_2},\omega_{n_2})\right]\left[\mathbf{S}(\mathbf{q_3},\omega_{n_3})\cdot\mathbf{S}(\mathbf{q_4},\omega_{n_4})\right]\end{aligned} \tag{1.11}$$

where, following Hertz, we assumed that the quartic term u can be approximated by a constant.

□ A few comments

▷ *Landau damping*

The dependence on $|\omega_n|$ of the quadratic term arises because the spin modes $\mathbf{S}$ lie inside the particle-hole continuum of the Fermi liquid (see Fig. 1.1) and are therefore overdamped: the decay mechanism is Landau damping [11]. In the ferromagnetic case, the conservation of the order parameter fluctuations enforces the damping rate, which appears in the denominator, to vanish as $q \to 0$. The overdamping leads, in the quantum critical regime, to a dynamic exponent $z > 1$.

▷ *Stoner criterion*

Note that the constant appearing in the quadratic term in ϕ vanishes when the Stoner criterion is satisfied, i.e. at the transition. This term thus measures the distance to the magnetic instability.

▷ *Assumptions*

In order to derive the effective bosonic action (1.11), one has to make a few assumptions:

- all other excitations are neglected with respect to the spin fluctuations. Indeed, in the derivation, we assumed the interaction in the charge channel was

unimportant, and disregarded any possible pairing instability. Making this assumption, we only exclude the case of bi-critical points, considering that close enough to the ferromagnetic QCP, all other excitations are gapped, and can be safely neglected. In practice, this is true for charge fluctuations. However, the spin fluctuations can lead to an effective attractive interaction between the electrons, and eventually to a $p-$wave superconducting instability.

- the bosonic modes are "slower" than the fermionic ones. This is a necessary condition to perform the integration over the fermionic degrees of freedom. In the Hertz derivation, this cannot be justified a priori. However, assuming this is true, the final result of Eq. (1.11) suggests that the typical bosonic momentum and frequency are related by $\omega \sim q^3$. Comparing this to the low-energy fermions, for which $\omega \sim |k - k_F|$, we see that there is no contradiction with the original assumption, which can be seen as an a posteriori justification.[1]

- the coefficient of the ϕ^4 term can be approximated by a constant. This is again unjustified a posteriori, and is related to the difficulty of treating this coefficient exactly. Hertz argued however from a Renormalization Group treatment (see the next paragraph for the main results) that this ϕ^4 is irrelevant in dimensions 2 and higher.

We argue later in the text (Section 3.1) that these last two approximations are actually questionable at criticality, and their violation leads, all at once, to the breakdown of both the HMM theory and the ferromagnetic QCP.

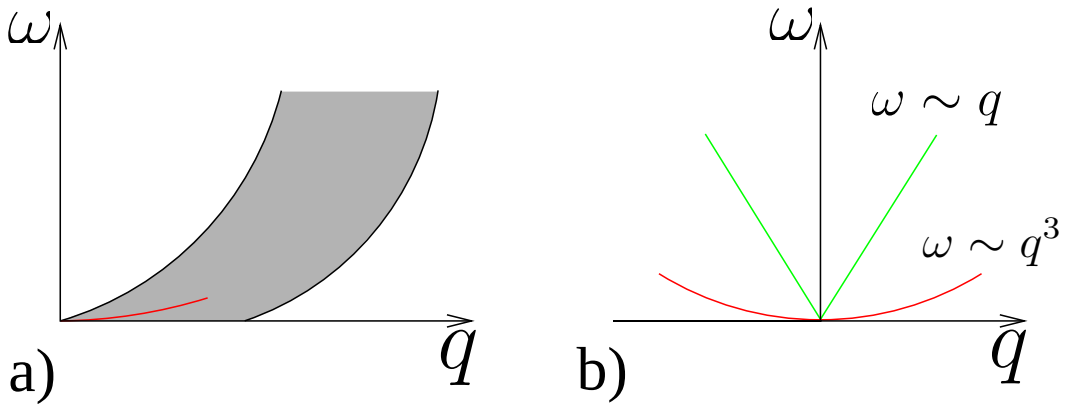

Figure 1.1: a) Particle-hole continuum (shaded region) and ferromagnetic modes (red line), b) Schematic view of the bosonic (red) and fermionic (green) dispersion.

[1] Further in the text, we refer to these regions of the $(d+1)$-dimensional space of frequency and momentum, as the fermionic and bosonic mass-shells.

□ Millis and Moriya additions

In order to obtain a quantitative description, Moriya and Kawabata developed a more sophisticated theory, the so-called self-consistent theory of spin fluctuations [12]. This theory is very successful in describing magnetic materials with strong spin fluctuations outside the quantum critical region. As for the quantum critical regime of itinerant ferromagnets, this leads to identical results to those of Hertz theory [13].

Later, Millis [14] revisited the theory developed by Hertz. He considered an additional scaling equation for the temperature, which allowed him to correct some of Hertz' results concerning the crossover behavior at finite temperature.

For these reasons, the quantum critical theory, associated to the effective action (1.11), is known as the Hertz-Millis-Moriya theory.

□ Results

We now present the main results of the HMM theory for the ferromagnetic QCP.

From the effective action (1.11), Hertz applied a Renormalization Group (RG) treatment. Eliminating the outer-shell defined as:

$$\left\{ \begin{array}{lll} e^{-l} & < q < & 1 \\ e^{-zl} & < \omega < & 1 \end{array} \right. \tag{1.12}$$

where z is the dynamic exponent and l an infinitesimal scaling factor, one can leave the quadratic and the quartic terms of the effective action unchanged by rescaling q, ω and $\mathbf{S}$, and imposing scaling conditions on the parameters δ and u. The rescaling of frequency and momentum requires that $z = 3$ in order for the q^2 term to scale like the Landau damping.

Incorporating the contribution of the outer-shell beyond the simple rescaling, this leads to the following:

$$\frac{d\delta}{dl} = 2\delta + 2uf(T,\delta) \tag{1.13a}$$

$$\frac{du}{dl} = (4-(d+z))\,u - 4u^2 g(T,\delta) \tag{1.13b}$$

$$\frac{dT}{dl} = zT \tag{1.13c}$$

where f and g are complicated integrals depending on T and δ. The last equation, missed by Hertz, was proved by Millis to be important for the finite temperature crossover regime.

The set of equations (1.13) already suggests the existence of an unstable Gaussian fixed point at $T = u = \delta = 0$. Moreover, close to this critical point, the interaction u is irrelevant if $d + z > 4$ (i.e. if $d > d_c^+ = 1$) , and one then expects the exponents to be those of the Gaussian model.

Solving the set of RG equations, one can extract the behavior in temperature of several physical properties in the quantum critical regime:

$$\text{Specific heat:} \quad C_v \sim T \log\left(\frac{T_0}{T}\right) \tag{1.14a}$$

$$\text{Resistivity:} \quad \rho(T) \sim T^{5/3} \tag{1.14b}$$

$$\text{Susceptibility:} \quad \chi(T) \sim \chi_0 - \chi_1 T^{4/3} \tag{1.14c}$$

$$\text{Critical temperature:} \quad T_c(\delta) \sim |\delta - \delta_c|^{3/4} \tag{1.14d}$$

1.2 Experiments

Magnetic quantum phase transitions are among the most studied ones experimentally. In this section, we present some experimental results concerning the quantum critical regime of some itinerant ferromagnetic compounds.

1.2.1 Successes

The behavior of many physical properties in the quantum critical regime of itinerant ferromagnets, as predicted by the Hertz-Millis-Moriya theory, was observed in several compounds.

□ $\mathbf{Ni}_x\mathbf{Pd}_{1-x}$

Pd is a strongly enhanced Pauli paramagnet, close to ferromagnetic order. It has long been known [15] that roughly 2.5% of nickel ions doped into palladium induce such a ferromagnetic order. Below 10% of doping, the induced structural and magnetic disorder is rather small and is believed to play only a minor role.

Nicklas and collaborators [16] studied samples of Ni_xPd_{1-x} for doping concentrations $0 \leq x \leq 1$. They observed the following:

- close to $x = 0.1$, a clear change of slope appears in the $\log T_c$ vs. $\log(x - x_c)$ plot, revealing a $(x - x_c)^{3/4}$ behavior at low doping (see Fig. 1.2). They could extract from these data that the critical concentration $x_c = 0.026 \pm 0.002$,
- at $x = 0.026$, the resistivity follows a $T^{5/3}$ dependence for more than two decades (see Fig. 1.2). The exponent changes quickly as one departs form x_c either way, signaling that the quantum critical behavior is limited to a narrow region around the critical doping,
- the heat capacity linear coefficient C_v/T increases logarithmically towards low temperature for a range of doping $0.022 \leq x \leq 0.028$ (see Fig. 1.3),

All these results match the predictions of the HMM theory for the quantum critical regime.

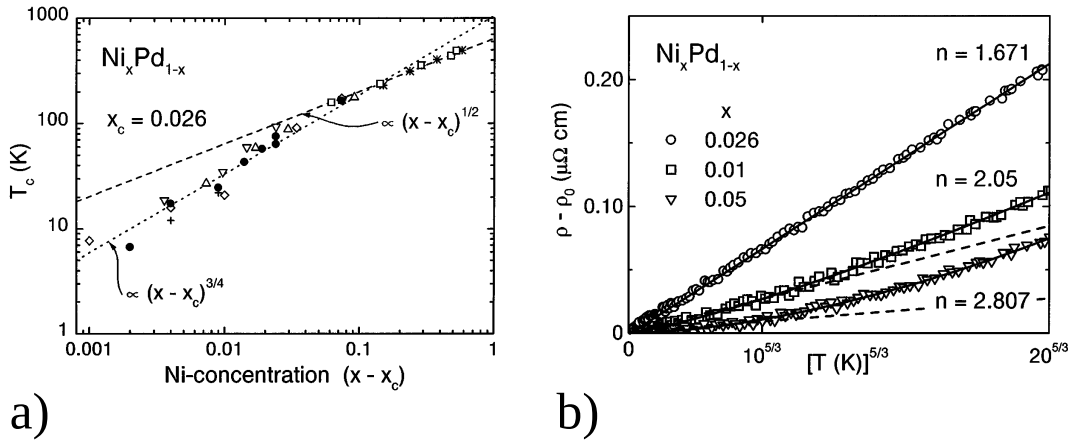

Figure 1.2: Ni_xPd_{1-x}, data from [16]: a) Curie temperature T_c as a function of $x-x_c$. The dashed line indicates $(x - x_c)^{1/2}$ and the doted line $(x - x_c)^{3/4}$; b) Resistivity as a function of temperature for three concentrations: in the paramagnet $x = 0.01$, in the ferromagnet $x = 0.05$, and at the critical doping $x_c = 0.026$. The solid lines stand for $\rho = \rho_0 + AT^n$.

□ $\mathbf{Zr_{1-x}Nb_xZn_2}$

Although it is made of non-magnetic constituents, $ZrZn_2$ is a ferromagnetic compound at low temperature. The Curie temperature at which the ferromagnetic ordering develops can be reduced towards zero by applying pressure (see next paragraph) or doping with niobium.

Sokolov and collaborators [17] studied the phase diagram of Nd-doped $ZrZn_2$, for concentrations $0 \leq x \leq 0.14$. They observed that upon doping, the critical temperature of the ferromagnetic transition continuously drops like a power-law: $T_c(x) \sim (x-x_c)^{3/4}$ (see Fig. 1.3). The critical concentration where the extrapolated critical temperature terminates is estimated to be $x_c = 0.083 \pm 0.002$.

They could also measure the susceptibility close to this critical doping, in the paramagnetic region. The temperature dependent part of the susceptibility behaves as $1/\chi^* = (\chi^{-1} - \chi_0^{-1}) = aT^{4/3}$ (see Fig. 1.3) close to the QCP. The temperature $T^*(x)$ below which this power-law behavior develops is maximum for $x = x_c$ and drops as one departs from it, ultimately vanishing at $x = 0.15$.

The quantum critical behavior documented by Sokolov et al. is in excellent agreement with the theoretical predictions of the HMM theory.

1.2.2 Departures from HMM results

Nevertheless, experimental studies have revealed notable differences from the standard second order behavior predicted by Hertz, Millis and Moriya.

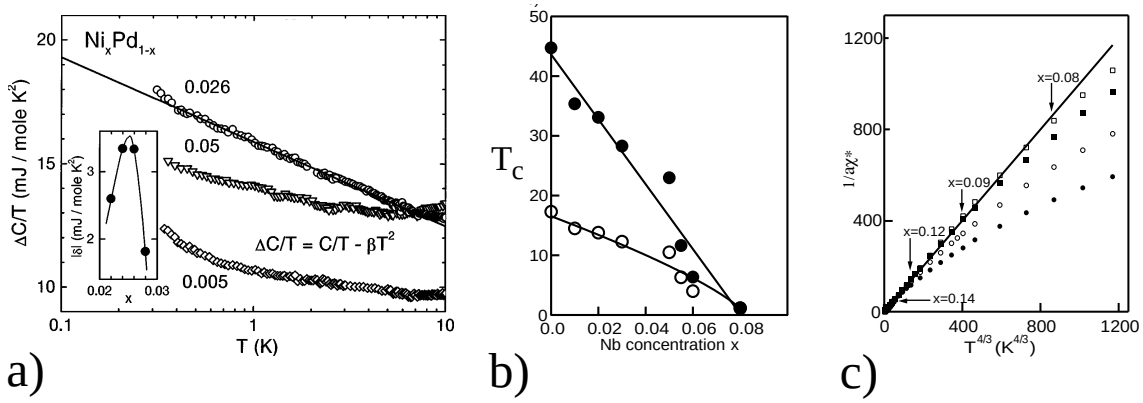

Figure 1.3: Ni_xPd_{1-x}, data from [16]: a) Specific heat vs. $\log T$ for three concentrations. The quadratic temperature dependence has been subtracted from these data, and the prefactor δ of the logarithmic term is shown in the inset. $Zr_{1-x}Nb_xZn_2$, data from [17]: b) Variation of the Curie temperature T_c (white dots) and $T_c^{4/3}$ (black dots) as a function of the Nb concentration. The solid lines are fits to $T_c \propto (x - x_c)$ and $T_c^{4/3} \propto (x - x_c)$; c) The inverse susceptibility $1/\chi^* = (\chi^{-1} - \chi_0^{-1})$ for $x \geq x_c$ is proportional to $T^{4/3}$ (solid line) for $T \leq T^*$.

□ Superconductivity

The first departure from the HMM results concerns the development of a superconducting instability. This is actually expected as in order to derive the effective bosonic action, we made the assumption that all excitations but the spin fluctuations could be neglected. As a result, it would be quite surprising that the HMM theory predicts the existence of a superconducting phase without including a possible instability towards that state from the very beginning.

A superconducting instability has been reported at very low temperature in several compounds, among which $ZrZn_2$ [18], UGe_2 [19] and URhGe [20] (see Fig. 1.4).

The existence of such a superconducting state generated a lot of interest as it seems to develop only inside the ferromagnetically ordered phase, and might have ties with the magnetic quantum critical point. We choose not to detail here the various aspects of the controversy these results created, since we will not discuss in this work the properties of the ordered state.

□ First order transition

The second and most interesting departure from the standard results of the HMM theory stands in the order of the transition towards the ferromagnetic state. Hertz, Millis and Moriya predicted a second order transition all the way down to the quantum critical point. However, a first order transition at low temperature has been

observed in almost all the itinerant materials investigated to date[2].

UGe_2, for example, shows in addition to a low temperature superconducting phase, a first order transition between the ferro- and the para-magnetic states close to the QCP (see Fig. 1.4). This first order transition was not predicted by the HMM theory, but this compound has a complicating factor: it is a strongly uniaxial (Ising) system.

$ZrZn_2$, however, is a straightforward itinerant ferromagnet, and the neutron diffraction is consistent with all the hallmarks of a three-dimensional itinerant ferromagnet. Although the ferromagnetic transition at ambient pressure is continuous, the ferromagnetism disappears in a first order fashion as pressure is increased beyond $p_c = 16.5kbar$. The experimental magnetization data suggest that a tricritical point separates a line of first order transitions from second order behavior at high pressure (see Fig. 1.4).

One last example of a first order transition close to the QCP is MnSi.

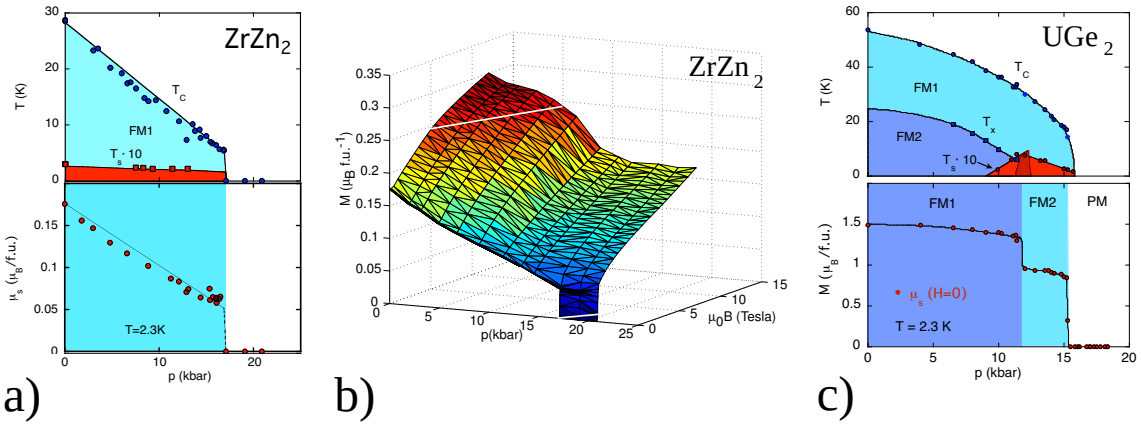

Figure 1.4: $ZrZn_2$, data from [18, 21]: a) (T, p) phase diagram, the ferromagnetic region appears in blue, and the superconducting phase in red; Magnetization as a function of pressure for $T = 2.3K$, the sudden drop at $p = 16.5kbar$ is characteristic of a first order transition towards the paramagnet; b) Magnetization as a function of pressure and magnetic field. UGe_2, data from [19, 22]: c) (T, p) phase diagram, the ferromagnetic regions appear in blue, and the superconducting phase in red; Magnetization as a function of pressure for $T = 2.3K$, the sudden drop at $p = 12.2kbar$ and $p = 15.8kbar$ are characteristic of a first order transition.

[2]Some argue that even the compounds which seem to perfectly match the HMM predictions do present a first order transition, but only at a temperature below the lowest temperature investigated experimentally.

1.2.3 The puzzling case of MnSi

For completeness, we present here some of the results associated to MnSi, which was one of the first itinerant magnet where a first order transition was discovered [23]. It turns out that the behavior of this compound deviates from the HMM picture in several aspects beyond the simple order of the transition [24, 25].

MnSi is a very well-known system, perhaps the most extensively studied itinerant electron magnet apart from iron, cobalt, nickel and chromium. At ambient pressure, the ground-state below the magnetic ordering temperature $T_c = 29.5K$ is a three-dimensional weakly spin-polarized Fermi-liquid state. As the pressure in increased, the critical temperature continuously approaches zero. The order of the transition, however, changes from second order at ambient pressure to first order below $p^* = 12kbar$.

The ordered state of MnSi is not a simple ferromagnet: the crystalline structure lacks an inversion symmetry, and weak spin-orbit interactions (of a Dzyaloshinsky-Moriya form) destabilizes the uniform ferromagnetic order and introduces a helical modulation. Further spin-orbit interactions lock the direction of the spiral in the direction $\mathbf{Q} = \langle 111 \rangle$.

The most surprising features of MnSi come from the region of the phase diagram above the critical pressure p_c where the transition temperature vanishes. This region of the phase diagram seems to be the cleanest example of an extended non-Fermi liquid (NFL) state in a three-dimensional metal: the bulk properties of MnSi suggest that sizable quasi-static magnetic moments survive far into the NFL phase. These moments are organized in an unusual pattern with partial long-range order. The resistivity displays a power-law behavior $\rho \sim T^{1.5}$, characteristic of the NFL state, up to the highest pressure achieved experimentally.

MnSi seems to question not only the results of the HMM theory, but the whole quantum criticality paradigm, and remains an understood puzzle to date.

1.3 Non-analytic static spin susceptibility

1.3.1 Long-range correlations

It is well known that in fluids, that is in interacting many-body systems, there are long-range correlations between the particles. For example, in classical fluids in thermal equilibrium, there are dynamical long-range correlations in time that manifest themselves as long-time tails. However long-range spatial correlations in classical systems in equilibrium are impossible due to the fluctuation-dissipation theorem.

In quantum statistical mechanics, though, statics and dynamics are coupled and need to be considered together, allowing long-range spatial correlations to develop. In return, this leads to non-analyticities in the limit of small momentum.

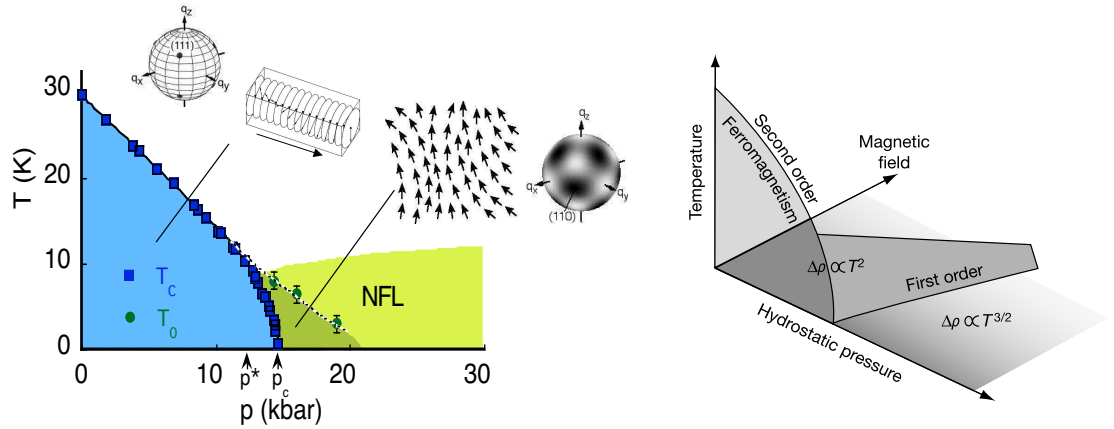

a) b)

Figure 1.5: a) Temperature vs. pressure phase diagram of MnSi. The insets qualitatively show the location and key features of elastic magnetic scattering intensity in reciprocal space. At high pressure, the neutron scattering signal disappears above a temperature T_0 represented by a dotted line. b) Schematic phase diagram with applied magnetic field in the third direction. The non-Fermi liquid behavior seems to extend to the region of finite magnetic field.

Following this idea, Belitz, Kirkpatrick and Vojta (BKV) [26] studied the long-wavelength properties of the spin-density correlation function (i.e. the spin susceptibility) of a Fermi liquid using a perturbative expansion in the interaction.

The existence of non-analytic corrections to the Fermi liquid theory has a long-standing history and it has been predicted that such non-analyticities occur in the specific heat coefficient [27] but was thought not to affect the spin and charge susceptibilities.

BKV proved that in a three-dimensional Fermi liquid, away from criticality, the leading long-wavelength dependence of the static susceptibility reads, up to second-order in perturbation theory:

$$\frac{\chi^{3D}(\mathbf{q})}{\chi^{3D}(\mathbf{0})} = 1 + c_3 \frac{|\mathbf{q}|^2}{k_F^2} \log\left(\frac{|\mathbf{q}|}{2k_F}\right) + O(|\mathbf{q}|^2) \tag{1.15}$$

where c_3 is a negative prefactor.

Later on, Chubukov and Maslov confirmed that a non-analytic dependence of the static spin susceptibility survives below $d = 3$ [28, 29], and writes in the two-dimensional case:

$$\frac{\chi^{2D}(\mathbf{q})}{\chi^{2D}(\mathbf{0})} = 1 + c_2 \frac{|\mathbf{q}|}{k_F} + O(|\mathbf{q}|^2) \tag{1.16}$$

where c_2 is, again, a negative prefactor.

Both groups of authors argued that these non-analytic corrections to the Fermi-liquid theory originate from the singularities in the dynamic particle-hole response function.

Following these results, Belitz and collaborators argued that the LGW functional, derived in the HMM approach, was formally ill-defined as the spin susceptibility enters the quadratic term in ϕ. The non-analyticities in the static susceptibility would then prevent a continuous quantum phase transition towards the ferromagnetic order. The authors argued that such a mechanism could explain the failures of the HMM approach, and the appearance of a first order ferromagnetic transition close to the QCP.

1.3.2 Effect on the quantum critical regime

It is a priori unclear, however, whether the results of Belitz et al. can be extended to the quantum critical regime. We emphasize that these results have been derived in a generic Fermi liquid, away from criticality.

Approaching the quantum critical point, one expects the effective four-fermion interaction to be strongly renormalized (which is consistent with a divergence of the effective mass at criticality). This would lead to a breakdown of the simple perturbative expansion performed by Belitz et al. Moreover, the Fermi liquid behavior does not seem to survive as one approaches the QCP [30, 31] which invalidates the results derived perturbatively for a Fermi liquid.

The first main motivation of our work is to clarify this issue and check whether the non-analytic behavior predicted in the Fermi liquid phase survives as one approaches the QCP (perhaps under a somewhat different form) or is washed out in the quantum critical regime.

In the next chapters, we re-analyze the problem of the quantum critical regime of itinerant ferromagnets. We build a controllable expansion close to the QCP, without integrating out the low-energy fermions, and analyze in details the stability of the ferromagnetic quantum critical point.

As one can see from (1.15) and (1.16), the effect of long-range correlations is more dramatic as the dimensionality is lowered. For that reason, we focus in all this work to the case of a two-dimensional system, close to criticality.

CHAPTER 2

Eliashberg theory of the spin-fermion model

Contents

In this chapter, we describe the starting model for our study of the ferromagnetic quantum critical point. After a direct perturbative treatment which justifies the need to include the curvature, we carry out a self-consistent approximate treatment (also known as "Eliahberg theory") and check a posteriori that the assumptions made for these computations are indeed justified.

2.1 Spin-fermion model

We argued in the previous chapter that integrating the fermions out of the partition function was a questionable way of studying the quantum critical regime, because of the possible non-analyticities that are missed in such a procedure.

Therefore, our starting point for the study of the ferromagnetic quantum critital point is a model describing low-energy fermions interacting with Landau overdamped collective bosonic excitations. These excitations are spin-fluctuations and become gapless at the quantum critical point.

2.1.1 Low-energy model

The general strategy to derive such a low-energy model is to start with a model describing the fermion-fermion interaction, and assume that there is only one low-energy collective degree of freedom near the QCP. This assumption is basically the same as one of the HMM assumptions: the idea is to exclude all excitations but the ferromagnetic spin fluctuations we are interested in. One then has to decouple the four-fermion interaction term using the critical bosonic field as an Hubbard-Stratonovich field, and integrate out of the partition function all high-energy degrees of freedom, with energies between the fermionic bandwidth W and some cutoff Λ [32].

If this procedure was performed completely we would obtain a full Renormalization Group treatment of the problem. Unfortunately, there is no controllable scheme to perform this procedure. It is widely believed, though that although the propagators of the remaining low-energy modes possess some memory of the physics at high energies, the integration of high-energy fermions does not give rise to anomalous dimensions for the bare fermionic and bosonic propagators in the low-energy model.

In practical terms, this assumption implies that the bare propagator of the relevant collective mode is an analytic function of momentum and frequency, and the fermionic propagator has the Fermi liquid form:

$$G(k,\omega) = \frac{Z_0}{i\omega - \epsilon_k}, \tag{2.1}$$

where $Z_0 < 1$ is a constant, and ϵ_k is the renormalized band dispersion.

Near the Fermi surface,

$$\epsilon_k = v_F k_\perp + \frac{k_\parallel^2}{2m_B}. \tag{2.2}$$

Here $\mathbf{k}$ is the momentum deviation from $\mathbf{k_F}$, the parallel and perpendicular components are with respect to the direction along the Fermi surface at $\mathbf{k_F}$, m_B is the band mass, the Fermi velocity $v_F = k_F/m$, and for a circular Fermi surface one has $m = m_B$.

Following this scheme, the original model of fermions interacting with themselves can be recast into an effective low-energy fermion-boson model. In the context of the magnetic QCP, this model is known as the "spin-fermion model" and was first suggested by Chubukov and collaborators [32].

Close to the ferromagnetic quantum critical point, the low-energy degrees of freedom are:

- fermions, whose propagator is given by Eq. (2.1));
- long-wavelength collective spin excitations whose propagator (in this case, the spin susceptibility) is analytic near $q = \Omega = 0$, and is given by:

$$\chi_{s,0}(q,\Omega) = \frac{\chi_0}{\xi^{-2} + q^2 + A\Omega^2 + O(q^4,\Omega^4)}. \tag{2.3}$$

In this last expression, A is a constant, and ξ is the correlation length of the magnetic spin fluctuations, which diverges at the QCP. We prove, further in this chapter, that the quadratic term in frequency does not play any role in our analysis. Indeed, one can argue that the interaction of these collective bosonic modes with fermions close to the Fermi surface generates a Landau damping of the spin fluctuations, as we demonstrate in the next section. As a consequence, we neglect from now on the Ω^2 term in the spin susceptibility, and approximate the above bare propagator by the static one $\chi_{s,0}(q)$.

The model can then be described by the following Hamiltonian:

$$H_{sf} = \sum_{k,\alpha} \epsilon_k c^\dagger_{k,\alpha} c_{k,\alpha} + \sum_q \chi^{-1}_{s,0}(q) \mathbf{S}_q \mathbf{S}_{-q} + g \sum_{k,q,\alpha,\beta} c^\dagger_{k,\alpha} \sigma_{\alpha\beta} c_{k+q,\beta} \cdot \mathbf{S}_q. \tag{2.4}$$

where $\mathbf{S}_q$ are vector bosonic variables, and g is the effective fermion-boson interaction. For convenience, we incorporated the fermionic residue Z_0 into g.

We emphasize that the above spin-fermion model cannot be derived in a true RG-like procedure, and has to be considered as a phenomenological model which captures the essential physics of the problem.

2.1.2 Forward scattering model

To illustrate how this effective Hamiltonian can, in principle, be derived from the microscopic model of interacting conduction electrons, we consider a model in which

the electrons interact with a short range four-fermion interaction $U(q)$ and assume that only the forward scattering is relevant ($U(0) = U$):

$$H = \sum_{k,\alpha} \epsilon_k c^\dagger_{k,\alpha} c_{k,\alpha} + \frac{1}{2} \sum_q U \sum_{k,k',\alpha,\beta} c^\dagger_{k,\alpha} c_{k+q,\alpha} c^\dagger_{k'\beta} c_{k'-q,\beta}, \tag{2.5}$$

In this situation, the interaction is renormalized independently in the spin and in the charge channels [33]. Using the identity for the Pauli matrices:

$$\sigma_{\alpha\beta} \cdot \sigma_{\gamma\delta} = -\delta_{\alpha\beta}\delta_{\gamma\delta} + 2\delta_{\alpha\delta}\delta_{\beta\gamma} \tag{2.6}$$

one can demonstrate [33] that in each of the channels, the Random Phase Approximation (RPA) summation is exact, and the fully renormalized four-fermion interaction $U^{full}_{\alpha\beta,\gamma\varepsilon}(q)$ is given by:

$$U^{full}_{\alpha\beta,\gamma\varepsilon}(q) = U \left[\delta_{\alpha\gamma}\delta_{\beta\varepsilon} \left(\frac{1}{2} + \mathcal{G}_\rho \right) + \sigma^a_{\alpha\gamma}\sigma^a_{\beta\varepsilon} \left(\frac{1}{2} + \mathcal{G}_\sigma \right) \right], \tag{2.7}$$

where $\sigma^a_{\alpha\beta}$ are Pauli matrices ($a = x, y, z$), and

$$\mathcal{G}_\rho \equiv \frac{1}{2} \frac{1}{1 - U\Pi(q)}; \qquad \mathcal{G}_\sigma \equiv -\frac{1}{2} \frac{1}{1 + U\Pi(q)}, \tag{2.8}$$

with $\Pi(q) = -\frac{m}{2\pi}(1 - a^2(q/k_F)^2)$ is the fermionic bubble made out of high-energy fermions, and $a > 0$.

For positive values of U satisfying $mU/2\pi \approx 1$, the interaction in the spin channel is much larger than the one in the charge channel. Neglecting then the interaction in the charge channel, we can simplify the Hamiltonian (2.5):

$$H = \sum_{k,\alpha} \epsilon_k c^\dagger_{k,\alpha} c_{k,\alpha} + \frac{1}{2} \sum_q U_{eff}(q) \sum_{k,k',\alpha,\beta,\gamma,\delta} c^\dagger_{k,\alpha} \boldsymbol{\sigma}_{\alpha\beta} c_{k+q,\beta} \cdot c^\dagger_{k'\gamma} \boldsymbol{\sigma}_{\gamma\delta} c_{k'-q,\delta}. \tag{2.9}$$

where $U_{eff}(q) = (1/2)U^2\Pi(q)/(1 + U\Pi(q))$. Performing a Hubbard-Stratonovich decomposition in the three fields $\mathbf{S}_q$, one recasts (2.9) into Eq. (2.4) with:

$$\begin{cases} g &= U\frac{a}{2} \\ \chi_0 &= 2\frac{k_F^2}{Ua^2} \\ \bar{g} &= g^2\chi_0 = (U/2)k_F^2 \\ \xi^{-2} &= \frac{k_F^2}{a^2}\left(\frac{2\pi}{mU} - 1\right) \end{cases} \tag{2.10}$$

The QCP is reached when $mU/2\pi = 1$, i.e., $\xi^{-2} = 0$. This coincides with the Stoner criterion for a ferromagnetic instability [8].

We emphasize that the bosonic propagator in Eq. (2.3) does not contain the Landau damping term. This is because we only integrated out the high-energy

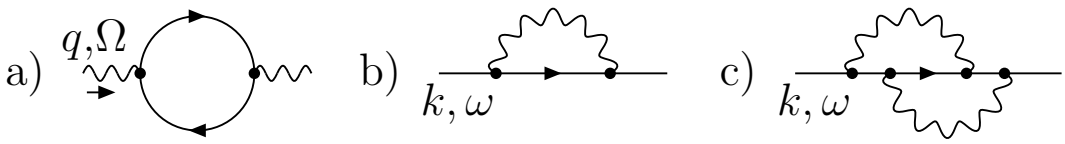

Figure 2.1: a) Polarization bubble b) One-loop fermionic self-energy c) Two-loop fermionic self-energy. The fermions are represented by straight lines and the bosons by wavy lines.

fermions, whereas the Landau damping of a collective mode of energy Ω comes from fermions of energy $\omega < \Omega$, and can only be generated within the low-energy theory. The dynamics of both the bosonic fields $\mathbf{S}_q$ and the fermionic c and $c^\dagger$ is determined self-consistently by treating both fluctuations on equal footing.

To put under control the computations carried out later in the text, it is necessary to extend the model by introducing N identical fermion species, while keeping the $SU(2)$ spin symmetry. The Hamiltonian (2.4) can then be rewritten as:

$$\begin{aligned} H_{sf} &= H_f + H_b + H_{int} \quad \text{where} \\ H_f &= \sum_{k,j,\alpha} \epsilon_k c^\dagger_{k,j,\alpha} c_{k,j,\alpha} \\ H_b &= \sum_q \chi^{-1}_{s,0}(q) \mathbf{S}_q \cdot \mathbf{S}_{-q} \\ H_{int} &= g \sum_{k,q,j,\alpha,\beta} c^\dagger_{k,j,\alpha} \boldsymbol{\sigma}_{\alpha\beta} c_{k+q,j,\beta} \cdot \mathbf{S}_q, \end{aligned} \tag{2.11}$$

where the index $j = 1 \dots N$ labels the fermionic species.

2.2 Direct perturbative results

In this section we compute the fermionic and bosonic self-energies for the model presented in Eq. (2.4) using a perturbative expansion around non-interacting fermions. Our goal here is three-fold: to relate the Landau damping coefficient to the fermion-boson coupling constant g, to evaluate the significance of the momentum-dependent part of the fermionic self-energy and to demonstrate the importance of the curvature of the Fermi surface.

We emphasize that this perturbative expansion is only used as a motivation for a further, more sophisticated approach detailed in the next sections, and for illustrative purposes. It is *not* a self-consistent computation, and most probably breaks down as one approaches the QCP.

2.2.1 Bosonic polarization

The full bosonic propagator depends on the self-energy $\Pi(q,\Omega)$ according to:

$$\chi_s(q,\Omega) = \frac{\chi_0}{\xi^{-2} + q^2 + \Pi(q,\Omega)}. \tag{2.12}$$

At the lowest order in the spin-fermion interaction, the bosonic self-energy is given by the first diagram in Fig. 2.1, and reads:

$$\Pi(\mathbf{q},\Omega) = 2N\bar{g} \int \frac{d^2k\ d\omega}{(2\pi)^3}\ G(\mathbf{k},\omega)\ G(\mathbf{k}+\mathbf{q},\omega+\Omega). \tag{2.13}$$

The curvature of the fermionic dispersion does not affect much the result of this computation as it only leads to small corrections in $q/m_B v_F$. Neglecting the quadratic term in the fermionic propagators, we introduce the angle θ defined as $\epsilon_{\mathbf{k}+\mathbf{q}} = \epsilon_{\mathbf{k}} + v_F q\cos\theta$ and perform the integration over $\epsilon_{\mathbf{k}}$, which gives us:

$$\begin{aligned}\Pi(\mathbf{q},\Omega) &= i\frac{N\bar{g}m}{2\pi^2}\int_{-\infty}^{+\infty} d\omega\ \ (\theta(\omega+\Omega)-\theta(\omega))\int_0^{2\pi} d\theta\ \frac{1}{i\Omega - v_F q\cos\theta} \\ &= \frac{Nm\bar{g}}{\pi}\frac{|\Omega|}{\sqrt{(v_F q)^2+\Omega^2}}.\end{aligned} \tag{2.14}$$

At the QCP, the bosonic mass-shell corresponds to the region of momentum and frequency space for which the terms in the inverse propagator are of the same order, i.e. near a mass shell q and Ω satisfies $\Pi(q,\Omega) \sim q^2$. It follows that, at the QCP, near the bosonic mass shell, $v_F q/\Omega \sim v_F(m\bar{g}v_F^2/\Omega^2)^{1/3} \gg 1$ at small enough frequency, so that $v_F q$ is the largest term in the denominator of $\Pi(q,\Omega)$. The expression of the bosonic self-energy then reduces to:

$$\Pi(\mathbf{q},\Omega) = \gamma\ \frac{|\Omega|}{q}, \tag{2.15}$$

where $\gamma = \dfrac{Nm\bar{g}}{\pi v_F}$.

We see that the lowest order bosonic self-energy recovers the form of the Landau damping presented in Chapter 1, with a prefactor depending on the fermion-boson coupling constant.

As explained earlier, this term is larger than a regular $O(\Omega^2)$ term, and fully determines the dynamics of the collective bosonic mode.

2.2.2 One-loop fermionic self-energy

We now turn to the fermionic self-energy, right at the QCP, where $\xi^{-1} = 0$. To the lowest order in the interaction, the fermionic self-energy contains one bosonic line,

as represented in Fig.2.1.b, and its analytic form writes:

$$\Sigma_1^{\rm free}(\mathbf{k},\omega) = 3ig^2 \int \frac{d^2q\ d\Omega}{(2\pi)^3} G_0(\mathbf{k}+\mathbf{q},\omega+\Omega)\chi(\mathbf{q},\Omega). \tag{2.16}$$

The superscript "free" implies that we use the free fermionic $G_0(k,\omega)$ in the integral for the self-energy.

In a direct perturbation theory in g, one would have to use the bare form of the bosonic propagator, Eq. (2.3), which leads to $\Sigma(\omega) \propto \log\omega$. However, this result is useless, as we already know that the Landau damping term completely overshadows a regular frequency dependence in (2.3). It makes more sense then to estimate the perturbative self-energy using the full bosonic propagator Eq. (2.12). This is *not* a fully self-consistent procedure, but we use it here to estimate the functional forms of the self-energy at various orders in perturbation around free fermions.

It is instructive to distinguish between $\Sigma(\mathbf{k_F},\omega) = \Sigma(\omega)$ and $\Sigma(\mathbf{k},0) = \Sigma(\mathbf{k})$. Indeed, there is an asymmetry in the behavior of the fermionic self-energy depending on whether one computes it at zero frequency or at zero momentum departure from the Fermi surface. This feature is one of the key elements of the self-sonsistent treatment presented in the next section.

□ Frequency dependence

Substituting the renormalized bosonic propagator with the Landau damping term into (2.16), the frequency-dependent self-energy reads:

$$\Sigma_1^{\rm free}(\omega) = \frac{3i\bar{g}}{(2\pi)^3} \int d\Omega\ qdq\ d\theta\ \frac{1}{q^2+\gamma\frac{|\Omega|}{q}} \frac{1}{i(\omega+\Omega)-v_F q\cos\theta}. \tag{2.17}$$

Here θ is the angle between $\mathbf{k_F}$ and $\mathbf{q}$, and we linearized the fermionic dispersion. Evaluating the integral over the angle, and using that the typical internal bosonic momentum $q \sim \Omega^{1/3}$ is much larger than $\Omega \sim \omega$, we obtain:

$$\begin{aligned} \Sigma_1^{\rm free}(\omega) &= \frac{3\bar{g}}{2\pi^2 v_F} \int_0^\omega d\Omega \int \frac{dqq}{q^3+\gamma|\Omega|} \\ &= \omega_0^{1/3}\omega^{2/3}, \end{aligned} \tag{2.18}$$

where

$$\omega_0 = \frac{3\sqrt{3}\bar{g}^3}{8\pi^3 v_F^3\gamma} = \frac{3\sqrt{3}\bar{g}^2}{8\pi^2 N m v_F^2}. \tag{2.19}$$

This result has been first obtained in Ref. [34, 35] when treating the interaction of low-energy fermions with singular gauge fields. It suggests that in $D = 2$, the interaction between bare fermions and critical bosons leads to a breakdown of the Fermi-liquid behavior: at low energies, the $\omega^{2/3}$ term in (2.18) is larger than the bare ω in the fermionic propagator. This obviously makes one wonder if higher order insertions lead to even more singular contributions.

□ **Momentum dependence**

Before looking at higher-order self-energy corrections, we compute the one-loop momentum-dependent self-energy $\Sigma(\mathbf{k})$, given by:

$$\begin{aligned}\Sigma_1^{\text{free}}(\mathbf{k}) &= \frac{3i\bar{g}}{(2\pi)^3}\int d\Omega\ qdq\ d\theta\ \frac{1}{q^2+\gamma\frac{|\Omega|}{q}}\frac{1}{i\Omega-\epsilon_k-v_Fq\cos\theta} \\ &= \frac{3\bar{g}}{(2\pi)^2}\epsilon_{\mathbf{k}}\int\frac{d\Omega\ dq}{q^2+\gamma\frac{|\Omega|}{q}}\frac{q|\Omega|}{(\Omega^2+(v_Fq)^2)^{3/2}}. \end{aligned} \tag{2.20}$$

One can make sure that the integral is infrared-convergent, i.e. $\Sigma^{\text{free}}(\epsilon_{\mathbf{k}}) \propto \epsilon_{\mathbf{k}}$, with an interaction dependent prefactor, which also depends on the upper cutoff of the theory, Λ.

This suggests that the momentum dependent part of the fermionic self-energy, unlike the frequency-dependent part derived earlier, is regular at the QCP and only leads to a finite mass renormalization.

2.2.3 Two-loop fermionic self-energy

As the one-loop frequency-dependent self-energy seems to dominate over the bare ω term of the fermionic propagator, one could wonder whether higher-order insertions lead to even more singular contributions.

To investigate this issue, we next calculate the contribution to the fermionic self-energy $\Sigma(\omega)$ from diagrams at the two-loop level, and focus, for illustrative purposes, on the diagram presented in Fig. 2.1.c, which writes:

$$\begin{aligned}\Sigma_2^{\text{free}}(\omega) \sim \bar{g}^2\int d\omega_1 d^2q_1\int d\omega_2 d^2q_2\ G(\mathbf{k_F}+\mathbf{q_1},\omega+\omega_1)\ G(\mathbf{k_F}+\mathbf{q_2},\omega+\omega_2) \\ \times\ G(\mathbf{k_F}+\mathbf{q_1}+\mathbf{q_2},\omega+\omega_1+\omega_2)\ \chi_s(\mathbf{q_1},\omega_1)\ \chi_s(\mathbf{q_2},\omega_2),\end{aligned} \tag{2.21}$$

where we use the full bosonic propagator, the free fermionic one, and we restrict ourselves to the frequency dependence of this contribution to the self-energy.

We first compute this integral expanding the dispersion of the internal fermions to linear order, since the quadratic term was not significant in the computation of the one-loop bosonic and fermionic self-energy. Choosing the x axis along the external $\mathbf{k} = \mathbf{k_F}$ and integrating over q_1^x and q_2^x, we are left with:

$$\begin{aligned}\Sigma_2^{\text{free}}(\omega) &\sim \frac{\bar{g}^2}{v_F^2\omega}\int_0^\omega\frac{d\omega_1 dq_{1y}}{q_{1y}^2+\frac{\gamma|\omega_1|}{q_{1y}}}\int_{\omega-\omega_1}^\omega\frac{d\omega_2 dq_{2y}}{q_{2y}^2+\frac{\gamma|\omega_2|}{q_{2y}}} \\ &\sim \omega_0^{2/3}\omega^{1/3}.\end{aligned} \tag{2.22}$$

where ω_0 is defined in (2.19).

At low-energy, this two-loop self-energy diverges faster than the one-loop self-energy obtained in (2.18). Estimating higher-order diagrams, we find that they form a series in powers of $(\omega_0/\omega)^{1/3}$, such that the perturbative expansion around free fermions breaks down at $\omega \sim \omega_0$.

This result is in line with the one obtained by Lawler et al. [36], in the context of a QCP in the charge channel using a two-dimensional bosonization scheme. The scale ω_0 is related by $\omega_0 = v_F/x_0$ to the spatial scale at which the equal time fermionic Green's function $G(x)$, obtained from bosonization, begins decaying exponentially ($G(x) \propto e^{-(x/x_0)^{1/3}}$).

However, the divergence of the perturbation theory can be cured once the curvature of the fermionic dispersion is included, as we now show. We re-evaluate the two-loop self-energy (2.21), using now the full fermionic dispersion, Eq. (2.2), without neglecting the quadratic term. After integrating over the momentum component q_1^x and q_2^x, one has:

$$\begin{aligned} \Sigma_2^{\text{free}}(\omega) &\sim \frac{\bar{g}^2}{v_F^2} \int_0^\omega \frac{d\omega_1 dq_{1y}}{q_{1y}^2 + \frac{\gamma|\omega_1|}{q_{1y}}} \int_{\omega-\omega_1}^\omega \frac{d\omega_2 dq_{2y}}{q_{2y}^2 + \frac{\gamma|\omega_2|}{q_{2y}}} \frac{1}{i\omega - \frac{q_{1y}q_{2y}}{m_B}} \\ &\sim \frac{m_B^2 \bar{g}^2}{\gamma^2 v_F^2}\, \omega \log^2 \omega. \end{aligned} \tag{2.23}$$

When the curvature of the fermionic dispersion is included, we see that the two-loop self-energy turns out to be small compared to its one-loop counterpart, at low energy. In a separate study [37], Chubukov and Khveshchenko reconsidered the bosonization procedure in the presence of the curvature and obtained the same results as in (2.23).

2.2.4 Conclusion

As a conclusion, this first crude approach suggests that both the fermionic and the bosonic self-energies are important at the QCP. The bosonic self-energy sets the dynamics of the bosons, while the fermionic self-energy is non-analytic and parametrically larger than the bare ω term at low energy, which implies a breakdown of the Fermi-liquid behavior at criticality.

We argued that only the frequency-dependent part of the self-energy matters, the momentum-dependent one only leads to a regular renormalization of the effective mass.

We also found that the curvature of the Fermi surface actually plays a very important role in regularizing the perturbative expansion, which was missed by previous studies in comparable low-energy models.

However, the full account of these effects cannot be obtained from this simple analysis. For example, we did not account here for the mutual effects of the self-energies onto each other. One has to develop a controllable way to treat the bosonic and fermionic self-energies on equal footing, in a self-consistent fashion.

Since we found that only the frequency-dependent $\Sigma(\omega)$ is relevant, a way to proceed is to verify whether an Eliashberg-like theory, similar to the one developed in the context of phonon superconductivity[38], may be such a controllable approximation.

2.3 Eliashberg theory

The Eliashberg procedure allows to compute the fermionic self-energy $\Sigma(\omega)$ and the bosonic polarization $\Pi(q,\Omega)$, by solving the self-consistent set of coupled Dyson's equations, neglecting all contributions coming from the vertex corrections and the momentum-dependent fermionic self-energy.

2.3.1 Self-consistent solution

Specifically the Eliashberg theory follows three steps:

- neglect both the vertex corrections and the momentum dependent part of the fermionic self-energy, i.e., approximate:

$$\begin{aligned} &\Sigma(\mathbf{k},\omega_n) = \Sigma(\omega_n) \\ &g_{\text{Tot}} = g + \Delta g = g \end{aligned} \tag{2.24}$$

- construct the set of self-consistent Dyson's equations:

$$\begin{aligned} &G^{-1}(k,\omega_n) = i\omega_n - v_F(k-k_F) + i\Sigma(\omega_n) \\ &\chi_s(q,\Omega_m)\frac{\chi_0}{\xi^{-2}+q^2+\Pi(q,\Omega_m)}, \end{aligned} \tag{2.25}$$

  with the following fermionic and bosonic self-energies:

$$\begin{aligned} i\Sigma(\omega_n) &= \\ \chi_0^{-1}\Pi(q,\Omega_m) &= \end{aligned} \tag{2.26}$$

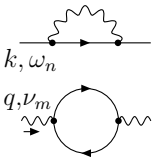

  The fermionic Green's functions in (2.26) are full (they are represented diagrammatically by a straight line) and $\chi_s(q,\Omega_m)$ is the full bosonic propagator (represented by a wavy line).

- check a posteriori that the neglected terms Δg and $\Sigma(\mathbf{k})$, are all parametrically small.

The evaluation of the momentum integral for the fermionic self-energy in the Eliashberg theory requires care. Since fermions are faster than bosons, the leading contribution to $\Sigma(\omega)$ is obtained if one integrates over the momentum component transverse to the Fermi surface only in the fermionic propagator and sets this component to zero in the bosonic propagator (this implies that the momentum integral is factorized).

One can show that the corrections that arise from keeping the transverse component of momentum in the bosonic propagator are small to the same parameter as $\Delta g/g$ and should therefore be neglected, as keeping them would be beyond the accuracy of the theory.

The evaluation of the bosonic and fermionic self-energies within the Eliashberg theory is presented in Appendices A and B. We list here the main results.

□ Away from the QCP

At large but finite correlation length ξ and for a bosonic momentum and frequency satisfying $v_F q \gg \Sigma(\Omega)$ we obtain:

$$\begin{cases} \Pi(q,\Omega) = \gamma \dfrac{|\Omega|}{q} \text{ , and} \\ \\ \Sigma(\omega) = \lambda \omega F\left(\gamma \omega \xi^3\right), \end{cases} \tag{2.27}$$

where $F(x \ll 1) = 1 + O(x)$, and $F(x \gg 1) = \frac{2}{\sqrt{3}} x^{-1/3}$. The parameter γ is the same as for free fermions,

$$\gamma = \frac{N m \bar{g}}{\pi v_F}, \tag{2.28}$$

and λ is the dimensionless coupling

$$\lambda = \frac{3\bar{g}}{4\pi v_F \xi^{-1}} \qquad \bar{g} = g^2 \chi_0 \tag{2.29}$$

At finite ξ^{-1} and vanishing ω, the self-energy has a Fermi liquid form:

$$\Sigma(\omega) = \lambda \omega. \tag{2.30}$$

The Fermi liquid theory is stable in this case, and the low-energy quasi-particles have a finite effective mass:

$$m^* = m(1+\lambda). \tag{2.31}$$

The effective mass diverges proportionally to ξ in the vicinity of the QCP.

□ **At criticality**

At $\omega \gg (\gamma\xi^3)^{-1}$, however, the system is in the quantum-critical regime. Here the Fermi liquid theory breaks down in the sense that the quasi-particles damping becomes comparable to its energy. We have:

$$\Sigma(\omega) = \omega_0^{1/3}|\omega|^{2/3}\text{sign}(\omega), \tag{2.32}$$

where $\omega_0 = 3\sqrt{3}\bar{g}^2/(8\pi^2 N m v_F^2)$ is the same as in (2.19).

At the QCP, $\xi^{-1} = 0$, the region of Fermi-liquid behavior collapses in frequency space, and the $\omega^{2/3}$ dependence of the self-energy extends down to the lowest frequencies. The expression for $\Sigma(\omega)$ is valid for all frequencies below the cutoff Λ.

However, only frequencies $\omega \leq \omega_0$ are actually relevant for the quantum critical regime, as at higher frequencies the system behaves as a nearly ideal Fermi gas.

2.3.2 A few comments

□ **General remarks**

One has to make a few remarks concerning the Eliashberg solution obtained at the QCP:

▷ Curvature

Note that the curvature of the fermionic dispersion is unimportant here for both self-energies, and only accounts for small corrections containing higher powers of frequencies.

▷ Direct perturbative expansion

Comparing (2.27) and (2.32) with (2.15) and (2.18), we see that the self-energies in the Eliashberg theory coincide with the one-loop perturbative results around free fermions that we carried out in the previous section. This arises from the fact that the full fermionic propagator appears in both self-energies only via the fermionic density of states (DOS):

$$N(\omega) = \frac{i}{\pi}\int d\epsilon_k \frac{1}{\omega + \Sigma(\omega) - \epsilon_k}. \tag{2.33}$$

This DOS reduces to $N(\omega) = \text{Sign}(\omega)$, independently on the self-energy: it remains the same as for free fermions.

▷ Bosonic momentum and frequency

Note that Eq. (2.27) for the bosonic self-energy is only valid as long as the interplay between the external momentum and frequency is such that $v_F q \gg \Sigma(\Omega)$. When this is verified, the Landau damping term no longer depends on

the fermionic self-energy, which explains why we recover the same expression for the self-consistent treatment and the direct perturbative expansion. In the opposite limit, the vertex corrections cannot be neglected as we argue in the next section.

□ Mass-shells

A lot of the computations we carry out in the further sections are estimated based on the typical bosonic and fermionic momenta and frequencies. Indeed, from inspecting the propagators, one can isolate a region of the three-dimensional momentum-frequency space where they are maximum. It follows that the quantities we compute are dominated by these regions of the phase space.

We thus distinguish two "mass shells", defined respectively as:

- the fermionic one is given by $G(\mathbf{k},\omega)^{-1} \simeq 0$, i.e. at the fermionic mass-shell, one has:
$$|\mathbf{k} - \mathbf{k_F}| \sim \frac{\omega + \Sigma(\omega)}{v_F} \tag{2.34}$$
- the bosonic mass-shell, on the other hand, is given by:
$$|\mathbf{q}| \sim (\gamma|\Omega|)^{1/3} \tag{2.35}$$

In the computations carried out in the next sections, we argue that the result strongly depends on the typical internal bosonic momentum and frequency. Depending whether one, two, or none of the components of this internal bosonic momentum vibrate on the bosonic mass-shell, we end up with very different results.

□ Factors of N

We argue in the next scetion that the extension of the model to N fermionic flavors is essential for the validity of the current approach. However, it can be readily seen from (2.27) and (2.32) that both self-energy contain factors of N through their prefators.

It follows that one cannot take the true infinite N limit, as the bosonic susceptibility trivially vanishes and the fermionic self-energy, although dominant because of its frequency dependence, would be washed out. Our approach has to be considered as an asymptotic expansion, where we keep N finite, but consider it is large enough to allow us to neglect higher-powers in N.

For further analysis of the corrections to the Eliashberg theory, it is then convenient to rescale N out of the formulas for $\Sigma(\omega)$ and for $\Pi(q,\Omega)$. This can be done by rescaling m and k_F leaving v_F intact:

$$m \to m/N \qquad k_F \to k_F/N. \tag{2.36}$$

We emphasize that the fermionic self-energy $\Sigma \propto \omega^{2/3}$ and the Landau damping term in the bosonic propagator do not contain N after rescaling, and therefore must be included into the new "zero-order" theory about which we then expand using $1/N$ as a small parameter. This zero-order theory includes:

$$\begin{cases} \chi(q,\Omega) &= \dfrac{\chi_0}{\xi^{-2}+q^2+\gamma|\Omega|/q} \\ G(k,\omega) &= \dfrac{1}{i(\omega+\Sigma(\omega))-\epsilon_k}. \end{cases} \tag{2.37}$$

We can reformulate the Eliashberg theory by introducing the following effective Lagrangian describing the fermion-boson interaction:

$$L = L_F + L_B + L_{int} \text{ , with}$$

$$\begin{aligned} L_B =& T\sum_{q,n} \mathbf{S}_{q,n}\chi^{-1}(q,\Omega_n)\mathbf{S}_{-q,-n}, \\ L_F =& T\sum_{k,n,\alpha,j} c^\dagger_{k,j,n,\alpha} G^{-1}(k,\omega_n) c_{k,j,n,\alpha}, \\ L_{int} =& gT^2 \sum_{n,m,k,q} \mathbf{S}_{q,m} c^\dagger_{k,j,n\alpha}\sigma_{\alpha\beta} c_{k-q,j,n-m,\beta}, \end{aligned} \tag{2.38}$$

where n, m number Matsubara frequencies, α, β are spin indices, j is a flavor index, and G and χ are given by (2.37). The upper limit of the frequency summation is the cutoff Λ.

We emphasize that there is no double counting in the bosonic propagator (2.37a). The integration of high-energy fermions, above the cutoff Λ leads to the momentum dependence of the static bosonic propagator, whereas the interaction at frequencies below Λ gives rise to the Landau damping, without affecting the static part.

To summarize, the Eliashberg-type theory at the QCP contains a non-analytic fermionic self-energy which scales as $\omega^{2/3}$ and breaks down the Fermi liquid description of fermions. At the same time, the bosonic propagator is regular – the only effect of the interaction with low-energy fermions is the appearance of a Landau damping.

We emphasize that the fully renormalized *bosonic* susceptibility does not necessary coincide with the one in (2.37) and may, in particular, acquire an anomalous dimension [39].

However, this can only be due to infra-red divergent corrections to Eliashberg theory, which are fully captured by the effective low-energy model of Eq. (2.38). An anomalous dimension was proved to emerge at the antiferromagnetic QCP in $d = 2$ [32, 39], but not in our case.

Expression	Definition	Eq.
v_F	Fermi velocity	(2.2)
m	bare quasiparticle mass, $m = k_F/v_F$	(2.2)
m^*	effective (renormalized) quasiparticle mass	(2.31)
m_B	band mass, determines the curvature of the Fermi surface	(2.2)
g	spin-fermion coupling constant	(2.4)
ξ	ferromagnetic correlation length	(2.3)
$\chi_0\xi^2$	value of the spin susceptibility at $q = 0$	(2.3)
N	number of fermionic flavors	
$\bar{g}=g^2\chi_0$	effective four-fermion interaction	(2.29)
$\gamma=\frac{Nm\bar{g}}{\pi v_F}$	Landau damping coefficient	(2.28)
$\lambda=\frac{3\bar{g}\xi}{4\pi v_F}$	dimensionless coupling constant, it measures the mass enhancement: $\lambda = \frac{m^*}{m} - 1$	(2.29)
$\omega_0=\frac{3\sqrt{3}\bar{g}^3}{8\pi^3\gamma v_F^3} \sim \frac{\bar{g}^2}{E_F}$	frequency up to which $\Sigma(\omega)$ dominates over ω in the fermionic propagator	(2.32)
$\omega_{\max}=\sqrt{\gamma v_F^3} \sim \sqrt{\bar{g}E_F}$	frequency up to which the fermionic and the bosonic mass-shells are well separated	(2.42)
$\alpha=\frac{\bar{g}^2}{\gamma v_F^3} \sim \frac{\bar{g}}{E_F}$	small parameter measuring the slowness of the bosonic modes compared to the fermionic ones; the same small parameter justifies the low-energy description	(2.39)
$\beta=\frac{m_B}{mN}$	small parameter related to the curvature of the fermionic dispersion	(2.53)

Table 2.1: List of the various parameters used in the text, their expression before the rescaling in N, and the reference equation where it is defined in the text.

2.4 Validity of the approach

The essential part of the Eliashberg procedure is an a posteriori verification that the neglected terms in the self-energies are small. Quite generally, the validity of this procedure is based on the idea that the fermions are fast excitations compared to the bosons, and hence the fermionic and bosonic mass shells are well separated in energy.

When scattering off physical mass-shell bosons, the fermions are forced to vibrate on the bosonic mass shell, which is far away from their own. The electronic spectral function near the bosonic mass-shell is then small and this reduces the self-energy that arises from true fermion-boson scattering. In the case of the electron-phonon interaction, this is known as the Migdal theorem, and ensures that the corrections to the electron-phonon vertex are small.

The computation of the fermionic self-energy $\Sigma(\omega)$ gives us an idea of what the typical intermediate momenta and frequencies are in the problem. One can make sure that at criticality the typical fermionic momenta $k - k_F$ are of order $\Sigma(\omega)/v_F = \omega_0^{1/3}\omega^{2/3}/v_F$. On the other hand, the typical bosonic momenta $q_\perp$ along the direction of $\mathbf{k}_F$ (i.e. transverse to the Fermi surface) are of the same order as the typical fermionic momenta, while the momenta $q_\parallel$ transverse to $\mathbf{k}_F$ (i.e. along the Fermi surface) are of order $(\gamma\omega)^{1/3} \gg \omega_0^{1/3}\omega^{2/3}/v_F$. We see that for a given frequency ω, the typical $|q| = \sqrt{q_\perp^2 + q_\parallel^2}$ are much larger than $k - k_F$, i.e. the effective boson velocity is much smaller than v_F. One then expects that the extension of Migdal theorem to our model holds.

The ratio of the typical fermionic $k - k_F$ and bosonic $|q|$ at the same frequency ω is $(\omega_0\omega/\gamma v_F^2)^{1/3}$. At $\omega \sim \omega_0$, this ratio then becomes:

$$\alpha = \left(\frac{\omega_0^2}{\gamma v_F^3}\right)^{1/3} \sim \frac{\bar{g}}{NE_F}, \tag{2.39}$$

and the slowness of the bosonic mode is then ensured in the quantum critical regime provided that $\alpha \ll 1$. This condition coincides, in our case, with the condition that the interaction should be smaller than the bandwidth. This is a necessary condition for the effective low-energy model to be valid, for if it is not satisfied, one cannot distinguish between contributions coming from low and from high energies.

However, the smallness of α is not sufficient. In the integral for the fermionic self-energy, only one component of the bosonic momentum, $q_\parallel$, is much larger than $k - k_F$, the other one is comparable: $q_\perp \sim k - k_F$. One needs to check whether the corrections to the Eliashberg theory scale as the ratio of $k - k_F$ to the modulus of $|q|$ or one of its components.

To address these issues, we explicitly compute the vertex corrections and the fermionic self-energy at the two-loop level.

2.4.1 Vertex corrections

We consider the vertex corrections due to the insertion of one bosonic propagator (three-leg vertex) and two bosonic propagators (four-leg vertex). The behavior of these vertex corrections strongly depends on the interplay between the internal and external momenta and frequencies. We present the results below and discuss technical details of the calculations in Appendix C.

In the case of the three-leg vertex, the result strongly depends on the interplay between external as well as internal momentum and frequency. We thus distinguish between three cases.

□ Three-leg vertex with zero external momentum and frequency

We begin with the simplest 3-leg vertex, with strictly zero incoming frequency Ω and momentum q. The one-loop vertex renormalization diagram contains one bosonic line and is presented in Fig. 2.2a. In analytic form, it writes:

$$\begin{aligned}\left.\frac{\Delta g}{g}\right|_{q=\Omega=0} &\sim g^2 \int d\omega d^2p\; G(\mathbf{k_F},\omega)^2\; \chi(\mathbf{p},\omega) \\ &\sim \bar{g} \int \frac{d\omega d^2p}{\frac{\gamma|\omega|}{p}+p^2}\; \frac{1}{\left(i\tilde{\Sigma}(\omega)-v_F p_x-\frac{p_y^2}{2m_B}\right)^2},\end{aligned} \tag{2.40}$$

where we defined $\tilde{\Sigma}(\omega)=\omega+\Sigma(\omega)$ and we have chosen $\mathbf{k}_F$ along the x axis, so that $p_x=p_\perp$ and $p_y=p_\parallel$.

Since the poles coming from the fermionic Green's functions are in the same half plane, the integral over q_x is only non-zero because of the branch cut in the bosonic propagator. At the branch cut $p_x\sim p_y$, so that we can safely drop the quadratic term in the fermionic propagators. Introducing polar coordinates, and integrating successively over the angle between $\mathbf{k_F}$ and $\mathbf{p}$, then over the modulus p, we obtain:

$$\left.\frac{\Delta g}{g}\right|_{q=\Omega=0} \sim \frac{\bar{g}}{\gamma v_F^3}\int_0^{\omega_{\max}} d\omega \frac{\tilde{\Sigma}(\omega)}{\omega}, \tag{2.41}$$

where $\omega_{\max}$ is the frequency up to which bosons are slow modes compared to fermions, i.e. up to which $\tilde{\Sigma}(\omega)/v_F \ll (\gamma\omega)^{1/3}$. This frequency exceeds ω_0, so to find it we have to use $\tilde{\Sigma}(\omega)\approx\omega$. We then obtain:

$$\omega_{\max}\sim\sqrt{\gamma v_F^3}\sim\sqrt{N\bar{g}E_F}. \tag{2.42}$$

Note that for small values of α, $\omega_{\max}\gg\omega_0$, and the maximum frequency up to which the bosons can be treated as slow modes well exceeds the upper limit of the quantum-critical behavior.

Substituting $\tilde{\Sigma}$ and $\omega_{\max}$ into (2.41), we obtain

$$\left.\frac{\Delta g}{g}\right|_{q=\Omega=0} \sim \sqrt{\alpha} \tag{2.43}$$

This correction to the vertex can then be neglected provided that α is small.

□ Three-leg vertex with finite external momentum

We now turn to the three-leg vertex with zero external frequency but a finite bosonic momentum $\mathbf{q}$. The one-loop renormalization is given in Fig.2.2, and its analytic form writes:

$$\begin{aligned}\left.\frac{\Delta g}{g}\right|_{q,\Omega=0} &\sim g^2 \int d\omega d^2p\; G(\mathbf{k_F}+\mathbf{p}+\mathbf{q},\omega)G(\mathbf{k_F}+\mathbf{p},\omega)\chi(\mathbf{p},\omega) \\ &\sim \bar{g}\int \frac{d\omega d^2p}{\frac{\gamma|\omega|}{p}+p^2}\;\frac{1}{i\tilde{\Sigma}(\omega)-v_F p_x-\frac{p_y^2}{2m_B}} \\ &\quad\times\frac{1}{i\tilde{\Sigma}(\omega)-v_F q_x-v_F p_x-\frac{p_y^2}{2m_B}-\frac{q_y p_y}{m_B}},\end{aligned} \tag{2.44}$$

where p_x is the projection of $\mathbf{p}$ along $\mathbf{k_F}$.

As before, the integral over p_x can be reduced to the contribution from only the branch cut in the bosonic propagator. At the branch cut, $p_x \sim p_y$, hence we can neglect the quadratic term in the fermionic Green's function, which then allows us to integrate over p_y. Expanding in q_x, and subtracting the constant term at zero momentum calculated in (2.41), we obtain:

$$\begin{aligned}\left.\frac{\Delta g}{g}\right|_{q,\Omega=0} - \left.\frac{\Delta g}{g}\right|_{q=\Omega=0} &\sim i\frac{q_x}{k_F}\int_{|v_F q_x|}\frac{d\omega}{|\omega|}\log[i\tilde{\Sigma}(\omega)] \\ &\sim \frac{q_x}{k_F}\log|q_x|,\end{aligned} \tag{2.45}$$

When not only the bosonic momentum q is finite but also the external fermionic momentum is away from k_F, the $q\times\log$ dependence of the static vertex correction survives, but the argument of the logarithm is the maximum of the bosonic q and fermionic $k-k_F$ (we directed both along x).

In general, the typical value of q_x is much smaller than k_F, hence the momentum dependent part of this vertex correction is small. However, we argue in the next chapter that because of the logarithmic term in (2.45), the insertion of this vertex correction into the static susceptibility gives rise to a non-analytic term.

We also emphasize that although the calculations of $\left.\frac{\Delta g}{g}\right|_{q=\Omega=0}$ and $\left.\frac{\Delta g}{g}\right|_{q,\Omega=0}$ look similar, the characteristic bosonic momenta are different for the two cases. At

$q = \Omega = 0$, the typical bosonic momenta in (2.40) are of order $(\gamma\omega)^{1/3}$, i.e. near the bosonic mass shell. On the other hand, the typical bosonic momenta in (2.44) are of order $\tilde{\Sigma}(\omega)/v_F$, i.e. near the fermionic mass shell. This is why only one of these two vertex corrections is small in α, as this parameter measures the slowness of the bosonic modes compared to the fermionic ones.

□ Generic three-leg vertex

We next consider the same vertex with small but finite external momentum q and frequency Ω. This diagram, presented in Fig. 2.2b, reads:

$$\begin{aligned}\left.\frac{\Delta g}{g}\right|_{q,\Omega} &\sim g^2 \int d\omega d^2p\; G(\mathbf{k_F}+\mathbf{p}+\mathbf{q},\omega+\Omega)G(\mathbf{k_F}+\mathbf{p},\omega)\;\chi(\mathbf{p},\omega) \\ &\sim \bar{g}\int \frac{d\omega d^2p}{\frac{\gamma|\omega|}{p}+p^2}\;\frac{1}{i\tilde{\Sigma}(\omega)-v_F p_x-\frac{p_y^2}{2m_B}} \\ &\qquad \times \frac{1}{i\tilde{\Sigma}(\omega+\Omega)-v_F q_x-v_F p_x-\frac{p_y^2}{2m_B}-\frac{q_y p_y}{m_B}},\end{aligned} \tag{2.46}$$

where we have chosen $\mathbf{k}_F$ along the x axis, so that $q_x = q_\perp$ and $q_y = q_\parallel$.

Integrating over p_x first, one obtains two contributions: one arising from the poles in the fermionic Green's functions (which now can be in different half-planes since Ω is finite), and the other from the branch cut in the bosonic propagator. The latter leads to the same result as (2.41), up to small corrections due to the finiteness of the external q and Ω.

Focusing on the other contribution, one has:

$$\left.\frac{\Delta g}{g}\right|_{q,\Omega} \sim i\frac{\bar{g}}{v_F}\int_0^\Omega d\omega \int dp_y \frac{|p_y|}{\gamma|\omega|+|p_y|^3}\frac{1}{i\tilde{\Sigma}(\Omega-\omega)+i\tilde{\Sigma}(\omega)-v_F q_x-\frac{q_y p_y}{m_B}}, \tag{2.47}$$

where the simplification of the frequency integral comes from the pole structure in p_x.

This generic correction to the vertex strongly depends on the interplay between the external q_x, q_y, and Ω.

When q and Ω are both finite,

$$\left.\frac{\Delta g}{g}\right|_{q,\Omega} = \mathcal{F}\left(\frac{v_F q}{\Sigma(\Omega)}\right), \tag{2.48}$$

where

$$\mathcal{F}(x) = \int_0^1 \frac{dz}{z^{1/3}}\frac{1}{(1-z)^{2/3}+z^{2/3}+ix} \tag{2.49}$$

has the following asymptotic behavior:

$$\left\{\begin{array}{rcl}\mathcal{F}(x\ll 1) &=& O(1) \\ \mathcal{F}(x\gg 1) &=& O\left(\frac{1}{x}\right)\end{array}\right. \tag{2.50}$$

If the typical external momentum q is on the bosonic mass shell, then $q \sim (\gamma\Omega)^{1/3}$, and one has:

$$\left.\frac{\Delta g}{g}\right|_{q,\Omega} \sim \frac{\Sigma(\Omega)}{v_F q_x} \sim \sqrt{\alpha}\ \left(\frac{\Omega}{\omega_{\max}}\right)^{1/3}. \tag{2.51}$$

This is obviously small in α.

It turns out that the behavior of the vertex correction is more complex and the result for $\Delta g/g$ strongly depends on the direction of q compared to the direction of $\mathbf{k}_F$.

This directional dependence is important for our purposes as we saw in previous computations that in the fermionic self-energy, only the y component of the internal bosonic momentum is near the bosonic mass shell and scales as $(\gamma\Omega)^{1/3}$, while the x component of the bosonic momentum is much smaller and is actually of the order of $\tilde{\Sigma}(\omega)/v_F$, i.e. is near the fermionic mass shell.

Let's take a more careful look at this vertex correction, depending on the direction of q.

For the case where $q_x \sim \tilde{\Sigma}(\Omega)/v_F$ and $q_y \sim (\gamma\Omega)^{1/3}$, one would argue from (2.51) that the vertex correction now becomes of order $O(1)$ and is no longer parametrically small. However, the computation that lead to (2.51) cannot be extended to the strongly anisotropic case as for external $q_x \sim \tilde{\Sigma}(\Omega)/v_F$ and $q_y \sim (\gamma\Omega)^{1/3}$, the curvature of the fermionic dispersion becomes relevant and changes the result.

The full dependence on q_x and q_y is rather complex and we restrict ourselves to the case when the importance of the curvature ensures that $\frac{1}{N}\frac{m_B}{m} \ll 1$. In this situation, $q_y^2/m_B \sim (v_F q_x)/\beta \gg v_F q_x$, so that the quadratic term in the fermionic propagator dominates.

Performing the integration, we then find that:

$$\begin{aligned}\left.\frac{\Delta g}{g}\right|_{q,\Omega} &\sim \beta^2 \left(\frac{\gamma\Omega}{q_y^3}\right)^{2/3} \log^2\left[\beta\frac{(\gamma\Omega)^{1/3}}{q_y}\right] \\ &\sim \beta^2 \log^2\beta,\end{aligned} \tag{2.52}$$

where

$$\beta = \frac{1}{N}\frac{m_B}{m} \ll 1. \tag{2.53}$$

It follows that even when only one component of the bosonic momentum is near the bosonic mass shell, the vertex correction is small if β is small. This is the second condition for the Eliashberg theory to be controllable at criticality.

The smallness of β can be ensured by either extending the theory to large values of N, or by considering a very strong curvature of the Fermi surface which implies that $m_B \ll m$. Even though the latter can hardly be satisfied for realistic Fermi surfaces, we emphasize that the curvature of the dispersion plays a crucial role in the theory, for even in the case of $N \gg 1$, the vertex correction is of order $O(1)$ without this very curvature.

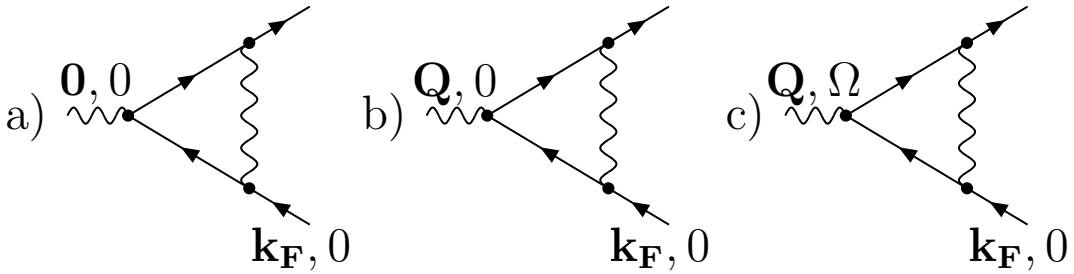

Figure 2.2: Three-leg vertices: a) zero external momentum and frequency b) finite momentum c) generic vertex.

□ Pairing vertex

By contrast to the previous vertices we studied, the pairing vertex in the Cooper channel is not sensitive to the curvature of the Fermi surface. This leads to a vertex of order $O(1)$ even in the large-N limit and the pairing problem then has to be carried out exactly within the Eliashberg theory.

This vertex renormalization is presented in Fig. 2.3 and its analytic form is given by:

$$\begin{aligned}\left.\frac{\Delta g}{g}\right|_{\text{Cooper}} &\sim g^2 \int d\omega d^2q\ \chi(\mathbf{q},\omega)\ G(\mathbf{k_F}+\mathbf{q},\omega)G(-\mathbf{k_F}-\mathbf{q},-\omega-\Omega) \\ &\sim \bar{g}\int \frac{d\omega d^2q}{\frac{\gamma|\omega|}{q}+q^2}\frac{1}{i\tilde{\Sigma}(\omega)-v_Fq_x-\frac{q_y^2}{2m_B}}\frac{1}{-i\tilde{\Sigma}(\omega+\Omega)-v_Fq_x-\frac{q_y^2}{2m_B}}.\end{aligned}$$

Integrating over q_x, restricting ourselves to the contribution from the fermionic poles (the one from the branch cut can be proved to be smaller), we find that the quadratic terms cancel out, leaving us with:

$$\left.\frac{\Delta g}{g}\right|_{\text{Cooper}} \sim \frac{\bar{g}}{v_F}\int_{|\Omega|}^{D}\frac{d\omega}{\tilde{\Sigma}(\omega+\Omega)+\tilde{\Sigma}(\omega)}\int_0^\infty \frac{dq_y\ q_y}{\gamma\omega+q_y^3}. \tag{2.54}$$

Performing the remaining integral, the prefactor simplifies and we obtain:

$$\begin{aligned}\left.\frac{\Delta g}{g}\right|_{\text{Cooper}} &\sim \frac{\bar{g}}{\gamma^{1/3}\omega_0^{1/3}v_F}\log\left|\frac{\Omega}{D}\right| \\ &\sim \log\left|\frac{\Omega}{D}\right|,\end{aligned} \tag{2.55}$$

where we assumed that we were in the quantum critical regime, i.e. $|\Omega| < \omega_0$.

We emphasize that the prefactor of the log in (2.55) is $O(1)$, even when one takes into account the curvature of the fermionic dispersion. The result of Eq. (2.55) confirms previous studies [40] advocating that the system at a ferromagnetic QCP can lead to a supersoncudcting instability.

□ **Four-leg vertex**

We consider now higher-order corrections to the vertex through the example of a four-leg vertex correction with two crossed bosonic lines, also called a Cooperon insertion. Analytically, the expression for this renormalized vertex, presented diagrammatically in Fig. 2.3, writes:

$$\Gamma_2(q,\Omega) \sim \bar{g}^2 \int d\omega d^2p\ \chi_s\left(\frac{\Omega+\omega}{2},\frac{\mathbf{p}+\mathbf{q}}{2}\right)\chi_s\left(\frac{\Omega-\omega}{2},\frac{\mathbf{q}-\mathbf{p}}{2}\right) \times G\left(\frac{\Omega+\omega}{2},\mathbf{k_F}+\frac{\mathbf{p}+\mathbf{q}}{2}\right)G\left(\frac{\Omega-\omega}{2},\mathbf{k_F}+\frac{\mathbf{q}-\mathbf{p}}{2}\right) \quad (2.56)$$

After integrating over p_x (projection of $\mathbf{p}$ along $\mathbf{k_F}$), and ω, were are left with:

$$\Gamma_2(q,\Omega) \sim \frac{\bar{g}^2}{v_F}\frac{\Omega}{|q_y|^3}\int dz \frac{\sqrt{\left(z^2+\frac{q_x^2}{q_y^2}\right)^2-4z^2}}{2i\Sigma\left(\frac{\Omega}{2}\right)-v_Fq_x-\frac{q_y^2}{4m}(1+z^2)} \times\frac{1}{\left(z^2+2z+\frac{q_x^2}{q_y^2}\right)^{3/2}+\frac{\gamma|\Omega|}{|q_y|^3}}\frac{1}{\left(z^2-2z+\frac{q_x^2}{q_y^2}\right)^{3/2}-\frac{\gamma|\Omega|}{|q_y|^3}}, \quad (2.57)$$

where we have changed p_y into $z=p_y/|q_y|$.

This renormalized 4-leg vertex $\Gamma_2(q,\Omega)$ has to be compared with the bare four-leg vertex, whose analytic form is given by the bosonic propagator multiplied by g^2:

$$\Gamma_1(q,\Omega) \sim \frac{\bar{g}}{q^2+\frac{\gamma|\Omega|}{q}}. \quad (2.58)$$

In the case of a typical external momentum $q_x \sim q_y \sim (\gamma\Omega)^{1/3}$, the ratio Γ_2/Γ_1 is of order α. For a typical $q_x \sim \tilde{\Sigma}(\omega)/v_F$ and $q_y \sim (\gamma\omega)^{1/3}$, we obtain, to logarithmic accuracy:

$$\frac{\Gamma_2}{\Gamma_1} \sim \beta \ll 1. \quad (2.59)$$

This last result again critically depends on the curvature of the Fermi surface: neglecting the quadratic terms in the fermionic propagators, one would obtain $\Gamma_2/\Gamma_1 = O(1)$. We see that likewise to the three-loop vertices, the smallness of the crossed vertex $\Gamma_2(q,\Omega)$ requires both α and β to be small.

2.4.2 Self-energy corrections

The second element one has to check in order to validate the Eliashberg procedure concerns the momentum-dependent self-energy. After verifying on the practical example of the two-loop self-energy, that the vertex correction analyzed above are indeed small, we turn to the computation of the momentum-dependent self-energy and the density of states.

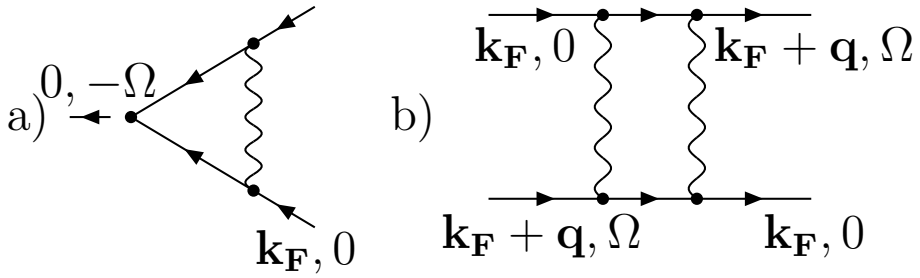

Figure 2.3: a) Cooper pairing vertex b) Four-leg vertex

□ **Corrections to the self-energy at the two-loop level**

We found in our analysis of the vertex corrections that the result depends on the interplay between the typical momentum and frequency. In our estimates, we considered two regions of external q and Ω, namely $q_x \sim q_y \sim (\gamma\Omega)^{1/3}$ and $q_x \sim \tilde{\Sigma}(\omega)/v_F$, $q_y \sim (\gamma\Omega)^{1/3}$. In both cases, we found that the vertex corrections are small.

We verify here that the two-loop self-energy, obtained by inserting vertex corrections into the one-loop self-energy diagram, is also small.

The two-loop self-energy diagram is presented in Fig. 2.1. We have:

$$\begin{aligned}\Sigma_2(\omega) \;\sim\; & \bar{g}^2 \int d\omega_1 d^2q_1 \int d\omega_2 d^2q_2 \; \chi(\mathbf{q_1},\omega_1)\; \chi(\mathbf{q_2},\omega_2)\; G(\mathbf{k_F}+\mathbf{q_1},\omega+\omega_1) \\ & \times G(\mathbf{k_F}+\mathbf{q_2},\omega+\omega_2)\; G(\mathbf{k_F}+\mathbf{q_1}+\mathbf{q_2},\omega+\omega_1+\omega_2) \\ \sim\; & \bar{g}^2 \int d\omega_1 d^2q_1 \int d\omega_2 d^2q_2 \frac{q_1}{\gamma|\omega_1|+q_1^3}\frac{q_2}{\gamma|\omega_2|+q_2^3} \\ & \times \frac{1}{i\tilde{\Sigma}(\omega+\omega_1)-v_F q_{1x}} \frac{1}{i\tilde{\Sigma}(\omega+\omega_2)-v_F q_{2x}-\frac{q_{2y}^2}{2m_B}} \\ & \times \frac{1}{i\tilde{\Sigma}(\omega+\omega_1+\omega_2)-v_F q_{1x}-v_F q_{2x}-\frac{q_{1y}^2}{2m}-\frac{q_{2y}^2}{2m_B}},\end{aligned} \tag{2.60}$$

where we recall $\tilde{\Sigma}(\omega) = \omega + \Sigma(\omega)$.

Integrating successively over q_{1x} and q_{2x}, and rescaling the remaining momentum components by introducing $x = q_{1y}/(\gamma|\omega_1|)^{1/3}$ and $y = q_{2y}/(\gamma|\omega_2|)^{1/3}$, we obtain:

$$\Sigma_2(\omega) \sim \frac{m_B\bar{g}^2}{v_F^2}\int_0^{\omega} d\omega_2 \int_{\omega-\omega_2}^{\omega} d\omega_1 \frac{1}{(\gamma^2\omega_1\omega_2)^{2/3}} \int_{-\infty}^{\infty} \frac{dxdy}{xy+i\zeta}\frac{|xy|}{(1+|x|^3)\,(1+|y|^3)} \tag{2.61}$$

where $\zeta = m_B \frac{\tilde{\Sigma}(\omega+\omega_1)+\tilde{\Sigma}(\omega+\omega_2)-\tilde{\Sigma}(\omega+\omega_1+\omega_2)}{(\gamma^2\omega_1\omega_2)^{1/3}}$.

As the typical frequencies ω_1 and ω_2 are of order ω, the typical value of ζ is of order $\beta \ll 1$. Expanding then in (2.61) to first order in ζ and performing the

remaining integrals, we obtain in the quantum-critical regime:

$$\begin{aligned}\Sigma_2(\omega) &\sim \frac{m\bar{g}^2}{v_F^2}\int_0^\omega d\omega_2 \int_{\omega-\omega_2}^{\omega} d\omega_1 \frac{\zeta \log^2 \zeta}{(\gamma^2\omega_1\omega_2)^{2/3}} \\ &\sim \Sigma(\omega)\ \beta^2 \log^2 \beta, \end{aligned} \tag{2.62}$$

where $\Sigma(\omega) = \Sigma_1(\omega) = \omega_0^{1/3}\omega^{2/3}$ is the self-energy in the Eliashberg theory.

This result agrees with the one obtained in [30], and shows that $\Sigma_2(\omega) \sim \Sigma_1(\omega) \times \frac{\Delta g}{g}\Big|_{\mathrm{q},\Omega}$ where $\frac{\Delta g}{g}\Big|_{\mathrm{q},\Omega}$ is given by (2.52). This last result implies that the typical internal q and Ω for the Eliashberg self-energy and for $\Sigma_2(\omega)$ are the same.

It is also instructive to compare these two-loop results, obtained as an expansion around the Eliashberg solution, to the perturbation expansion around free fermions. In the latter, we found in Eq. (2.23) that $\Sigma_2(\omega) \sim \omega \log^2 \omega$ whereas in the former we have $\Sigma_2(\omega) \propto \beta(\omega_0^{1/3}\omega^{2/3}) \log^2 \beta$, Eq. (2.62). The free-fermion result can be reproduced if we neglect the self-energy in (2.61). We see that the expansion around free fermions does not reproduce the correct frequency dependence of $\Sigma_2(\omega)$. This obviously implies that if one expands around free fermions, there exist higher-order terms associated with insertions of the self-energy $\Sigma(\omega)$ into the internal fermionic lines, which may overshadow the two-loop result around free fermions. Accordingly, near the QCP, the expansion around free fermions does not converge, even if the curvature of the fermionic dispersion is included. On the other hand, the expansion around the Eliashberg solution is regular and holds in powers of the small parameters α and β.

□ Momentum dependence of the self-energy and the density of states

Along with the vertex corrections, we also neglected the momentum dependence of the fermionic self-energy in order to proceed with the Eliashberg scheme. We now verify whether the momentum dependent part of the self-energy $\Sigma(\mathbf{k}, \omega = 0) = \Sigma(\mathbf{k})$ remains small when evaluated with the full fermionic propagator. The k dependent self-energy is given by:

$$\begin{aligned}\Sigma(\mathbf{k}, 0) &= 3ig^2 \int \frac{d^2q\ d\Omega}{(2\pi)^3} G(\mathbf{k}+\mathbf{q}, \Omega)\chi(\mathbf{q}, \Omega) \\ &= \frac{3i\bar{g}}{(2\pi)^3}\int \frac{d\Omega d^2q}{i\tilde{\Sigma}(\Omega) - \epsilon_{k+q}} \frac{q}{\gamma|\Omega| + q^3}. \end{aligned} \tag{2.63}$$

Defining the angular variable θ as $\epsilon_{k+q} = \epsilon_k + v_F q\cos\theta$, integrating over it, and expanding to linear order in $\epsilon_{\mathbf{k}}$ we obtain:

$$\Sigma(\mathbf{k}, 0) = -3i\epsilon_k \times \frac{\bar{g}}{2\pi^2}\int_0^\infty d\Omega\ \tilde{\Sigma}(\Omega) \int \frac{q^2 dq}{(q^3 + (\gamma|\Omega|))\left((v_F q)^2 + \tilde{\Sigma}(\Omega)^2\right)^{3/2}}. \tag{2.64}$$

A simple experimentation with the integrals shows that the integration over momentum is confined to $q \sim \tilde{\Sigma}(\Omega)/v_F$, while the frequency integral is confined to $\Omega < \omega_{max}$, where ω_{max}, defined in (2.42), is the scale where $(\gamma\Omega)^{1/3} = \tilde{\Sigma}(\Omega)/v_F$. The computation of $\Sigma(\mathbf{k})$ is given in the Appendix B, and the result is

$$\Sigma(\mathbf{k},0) = -i\epsilon_k \times \frac{3 \times 1.3308}{2\sqrt{2}\pi^{3/2}}\sqrt{\alpha} = -i\epsilon_k \; 0.253\sqrt{\alpha} \tag{2.65}$$

Plugging this back into the fermionic propagator, we then obtain that $\Sigma(\mathbf{k},0)$ gives rise to a small, regular correction to the quasiparticle mass $\epsilon_k - i\Sigma(\mathbf{k},0) = \epsilon_k^* = v_F^*(k-k_F)$, where

$$v_F^* = v_F \; \left(1 - 0.253\sqrt{\alpha}\right). \tag{2.66}$$

Like the vertex correction at zero external bosonic momentum and frequency, this small correction is of order $O(\sqrt{\alpha})$ and comes from frequencies of order $\omega_{\max}$.

The momentum dependent self-energy, unlike the frequency dependent part, generally gives rise to corrections to the fermionic density of states (DOS)

$$N(\omega) \sim -\int \frac{d\epsilon_k}{\pi} \mathrm{Im}G(\epsilon_k,\omega). \tag{2.67}$$

where N_0 is the DOS of free fermions.

Assuming that $\Sigma(k)$ is small and expanding in it in the fermionic propagator, we obtain, in real frequencies

$$N(\omega) \sim 1 - \mathrm{Im}\left(\left.\frac{\Sigma(\mathbf{k})}{\epsilon_k}\right|_{\epsilon_k = i\tilde{\Sigma}(-i\omega)}\right), \tag{2.68}$$

Substituting (2.65) into (2.68), we find that the density of states just shifts by a constant. It follows that in order to extract the frequency dependence of the density of states, one has to evaluate the momentum-dependent self-energy to next order in ϵ_k and on the mass shell, where $\epsilon_k = i\tilde{\Sigma}(\omega)$.

The evaluation of the self-energy near a mass shell generally requires extra caution as the self-energy may possess mass-shell singularities [33]. We, however, have checked in Appendix F that in our case the self-energy does not possess any mass-shell singularity, and the self-energy remains finite on the mass shell.

The calculation of the self-energy to order ϵ_k^2 is displayed in the Appendix B, and the result is

$$\Sigma(\mathbf{k},\omega) = i\epsilon_k \times \frac{0.45\bar{g}}{8\pi N}\frac{|\Sigma(\omega)|}{E_F}\log\frac{\omega_1}{|\omega|} \tag{2.69}$$

Substituting this self-energy into the expression for the DOS and converting to real frequencies, we find at small ω

$$N(\omega) \sim N_0\left(1 - \left(\frac{\omega}{\omega_1}\right)^{2/3}\log^2\frac{\omega_{max}}{\omega}\right), \tag{2.70}$$

where we explicitly defined

$$\omega_1 = \frac{128\pi^{5/2}}{0.45^{3/2}\ 3^{3/4}} \frac{N^2 E_F^2}{\bar{g}}. \tag{2.71}$$

2.4.3 Summary

We have shown in this section that there are two conditions for the validity of the Eliashberg theory that one can recast as the smallness of two parameters:

$$\alpha \sim \frac{\bar{g}^2}{\gamma v_F^3} \sim \frac{\bar{g}}{N E_F} \ll 1 \qquad \beta \sim \frac{m\bar{g}}{\gamma v_F} \sim \frac{m_B}{Nm} \ll 1. \tag{2.72}$$

The first condition is quite generic for a low-energy theory since it requires that the fermion-fermion interaction mediated by the exchange of a boson should be smaller than the Fermi energy. Otherwise, the physics is not restricted to the vicinity of the Fermi surface anymore. The parameter α plays the same role as the Migdal parameter for the electron-phonon interaction: it sets the condition that fermions are fast excitations compared to bosons. In the scattering processes that are small in α, fermions are forced by the interaction to vibrate at frequencies near the bosonic mass shell. They are then far from their own resonance and thus have a small spectral weight.

However, the condition $\alpha \ll 1$ is not sufficient to construct a fully controllable perturbative expansion around the non-Fermi liquid state at the QCP. In spatially isotropic systems there exist vertex corrections for which the external momentum has a component on the fermionic mass-shell. These corrections don't contain α. However, these corrections are sensitive to the curvature of the Fermi surface, and are small if β is small which can be achieved either by imposing $m_B \ll m$ or by extending the theory to a large number N of fermionic flavors.

In evaluating the renormalization of the static vertex, we silently assumed that $\sqrt{\alpha} \ll \beta$, i.e., $\bar{g}/E_F < (m_B/m)^2/N$. At very large N, this is no longer valid, but in this situation our estimates show that the static vertex is even smaller than $\sqrt{\alpha}$.

Finally, the pairing vertex in the Cooper channel stays of order $O(1)$, signaling the possibility of a pairing instability close to the quantum critical point. Nevertheless, we assume, based on explicit calculations worked out in [40], that the quantum critical behavior extends in the parameter space to a region where the superconductivity is not present.

CHAPTER 3

Static spin susceptibility

Contents

In this chapter, we revisit the Hertz-Millis-Moriya ϕ^4 theory using the solution of our Eliashberg scheme at criticality. We then turn to the computation of the static spin susceptibility, following the remarks of Belitz and collaborators: now that we

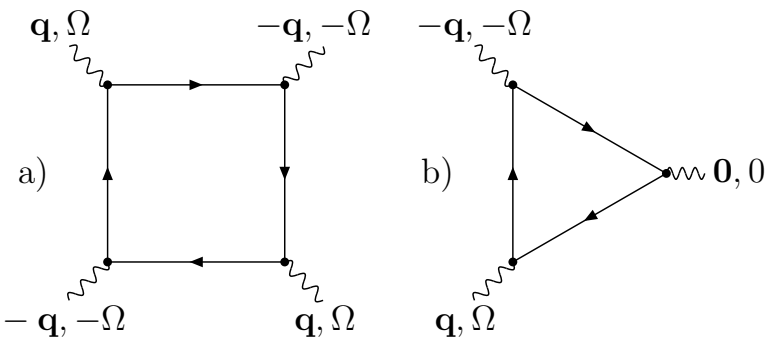

Figure 3.1: "ϕ^4" and "ϕ^3" type diagram

have derived a controllable way of describing the quantum critical regime, we can estimate whether the non-analytic corrections associated to the Fermi liquid regime survivies at criticality. We indeed prove that this non-analytic term does not survive at criticality but another one, weaker, is till present. Finally, we study whether this analysis is limited to the ferromagnetic QCP or can be extended to other physical models.

3.1 Revisiting the Hertz-Millis-Moriya theory

As we argued in the first chapter, it is widely believed that an itinerant fermionic system near a ferromagnetic QCP is adequately described by a phenomenological $2+1$D ϕ^4 bosonic theory (in our case, the role of ϕ is played by the vector field $\mathbf{S}$) with the dynamic exponent $z=3$ and a constant prefactor for the ϕ^4 term [3, 14, 13]. In dimensions $d \geq 4-z=1$, the model lies above its upper critical dimension and the ϕ^4 term is simply irrelevant.

In this section, we derive the effective ϕ^4 theory from the spin-fermion model Hamiltonian, and show that it contains two new elements absent from the phenomenological HMM approach. First, the prefactor of the ϕ^4 term strongly depends on the ratio between the external momenta and frequencies, and contains a non-analytic term in addition to the constant one. Second, there also exists a cubic ϕ^3 term whose prefactor, although vanishing in the static limit, also strongly depends on the interplay between the external momenta and frequencies.

3.1.1 ϕ^4 term

In order to derive a quantum critical ϕ^4 model, one has to integrate the fermions out of the partition function, noticing that the Lagrangian of the spin-fermion model is quadratic in the fermions.

Expanding then in the number of bosonic fields $\mathbf{S}$, the quartic term in the effective

action reads:

$$\int \frac{d^2q d^2p d^2p' \; d\Omega d\nu d\nu'}{(2\pi)^9} \; A(\mathbf{p},\mathbf{p}',\mathbf{q},\nu,\nu',\Omega) \left[\mathbf{S}_{p+q/2}\cdot\mathbf{S}_{q/2-p} \; \mathbf{S}_{p'-q/2}\cdot\mathbf{S}_{-p'-q/2} \right. \\ \left. + \; \mathbf{S}_{p+q/2}\cdot\mathbf{S}_{-p'-q/2} \; \mathbf{S}_{q/2-p}\cdot\mathbf{S}_{p'-q/2} \; - \; \mathbf{S}_{p+q/2}\cdot\mathbf{S}_{p'-q/2} \; \mathbf{S}_{-q/2-p'}\cdot\mathbf{S}_{q/2-p} \right] \tag{3.1}$$

where p, p', q are bosonic momenta, and ν, ν', Ω are bosonic frequencies.

Our goal here is to prove that the prefactor A is not a regular function of momenta and frequencies. To simplify the presentation, we choose to study only the dependence of A on q and Ω and set $\mathbf{p}, \mathbf{p}', \nu, \nu'$ to zero (see Fig 3.1).

The analytic form of this prefactor then writes (see Appendix B for the technical details):

$$A(q,\Omega) \sim Ng^4 \int d\omega \; \int d^2k \; G(\mathbf{k},\omega)^2 \; G(\mathbf{k}+\mathbf{q},\omega+\Omega)^2. \tag{3.2}$$

Defining θ as the angle between $\mathbf{k}$ and $\mathbf{q}$, and performing the integration over ϵ_k,and the angular variable, we find:

$$A(q,\Omega) \sim \frac{Nmg^4}{\omega_0\Omega} \int_0^1 dz \frac{\left[\left(\frac{v_F q}{\Sigma(\Omega)} \right)^2 - 2\left(z^{2/3} + (1-z)^{2/3} \right)^2 \right]}{\left[\left(\frac{v_F q}{\Sigma(\Omega)} \right)^2 + \left(z^{2/3} + (1-z)^{2/3} \right)^2 \right]^{5/2}}, \tag{3.3}$$

where we defined $z = \omega/\Omega$, and neglected at this stage a regular part that comes from large values of ϵ_k and for which the curvature is relevant.

We see that $A(q,\Omega)$ depends on the interplay between the momentum and frequency. We can identify two regimes

- If $|q| \sim (\gamma|\Omega|)^{1/3}$, i.e. if the bosonic momenta are near the bosonic mass shell, the self-energy in the denominator can be neglected. The frequency factors in the numerator and the denominator then cancel out, and we obtain:

$$A(\Omega) \sim \frac{Nmg^4}{\gamma v_F^3} \sim \frac{1}{\chi_0^2} \; \alpha m \; , \tag{3.4}$$

  We see that A can be safely replaced by a constant $O(\alpha)$. This is consistent with the previous works of Hertz, Millis and Moriya. The agreement is not surprising as the relation $q \sim (\gamma|\Omega|)^{1/3}$ is assumed in the power counting based on the fact that the dynamic exponent $z = 3$. Note that the condition $|q| \sim (\gamma|\Omega|)^{1/3}$ only specifies the magnitude of q, one of its components (e.g., q_x) can be much smaller.

- If $q \sim \tilde{\Sigma}(\omega) \sim \omega_0^{1/3}\Omega^{2/3} v_F$ (at $\omega < \omega_0$), i.e. when a boson resonates near a fermionic mass shell, the scaling arguments of the $z = 3$ theory are no longer

applicable. We have in this regime:

$$A(q,\Omega) \sim \frac{Nmg^4}{\omega_0 \Omega} \sim \frac{Nm}{\chi_0^2} \frac{1}{\sqrt{\alpha}} \frac{\omega_{\max}}{\Omega}. \tag{3.5}$$

In this case, $A(\Omega)$ is a singular function of frequency, and cannot be replaced by a constant.

We see therefore that the pre-factor of the ϕ^4 term is actually singular outside the scaling regime of a $z = 3$ theory.

3.1.2 ϕ^3 term

In the similar spirit, one can construct a cubic term in the bosonic fields.

$$\int \frac{d^2q d^2p d\Omega d\nu}{(2\pi)^9} B(\mathbf{p},\mathbf{q},\nu,\Omega)\ \mathbf{S}_p \cdot (\mathbf{S}_{q-p/2} \times \mathbf{S}_{-q-p/2}), \tag{3.6}$$

where the pre-factor B is a convolution of three fermionic Green's functions as presented in Fig.3.1, and is given by:

$$B(\mathbf{q},\mathbf{p},\Omega,\nu) \sim Ng^3 \int d\omega \int d^2k\, G(\mathbf{k}-\mathbf{p},\omega-\nu) G\left(\mathbf{k}-\frac{\mathbf{p}}{\mathbf{2}}-\mathbf{q},\omega-\frac{\nu}{2}-\Omega\right) G(\mathbf{k},\omega)$$

Proceeding as for the quartic term, we set for simplicity $\mathbf{p} = \mathbf{0}$, $\nu = 0$, and integrate over ϵ_k and the angular variable, leading to:

$$B(q,\Omega) \sim \frac{Nmg^3}{\omega_0^{2/3}\Omega^{1/3}} \int_0^1 dz \frac{\left(z^{2/3}+(1-z)^{2/3}\right)}{\left[\left(\frac{v_F q}{\Sigma(\Omega)}\right)^2 + \left(z^{2/3}+(1-z)^{2/3}\right)^2\right]^{3/2}}, \tag{3.7}$$

where we again introduced the rescaled frequency $z = \omega/\Omega$.

We can again identify two regimes.

- In the $z = 3$ regime where $q \sim (\gamma\Omega)^{1/3}$, one can expand for large $\frac{v_F q}{\Sigma(\Omega)}$, which leads to:

$$B(q,\Omega) \sim \frac{Nmg}{\chi_0}\ \alpha \left(\frac{\Omega}{\omega_{\max}}\right)^{2/3}, \tag{3.8}$$

  where ω_{max} is given by (2.42). This term is small in the quantum critical regime where $\Omega < \omega_0 \sim \omega_{max}\alpha^{3/2}$, and can be safely neglected.

- For $q \sim \Sigma(\Omega)$, the remaining integral is of order $O(1)$ and the result writes:

$$B(q,\Omega) \sim \frac{Nmg}{\chi_0}\ \frac{1}{\sqrt{\alpha}} \left(\frac{\omega_{\max}}{\Omega}\right)^{1/3}, \tag{3.9}$$

  which is large and cannot be neglected.

We demonstrate in the next section how the singular behavior of the ϕ^3 and ϕ^4 terms leads to a non-analytic contribution to the static spin susceptibility.

3.2 Static spin susceptibility

We found that the Eliashberg theory for fermions interacting with gapless long-wavelength bosons is stable and controlled by two small parameters. We verified this by calculating the fermionic self-energy in a two-loop expansion around the Eliashberg solution

One may wonder whether the same conclusions hold for the bosonic self-energy as well. In particular, what are the corrections to the static susceptibility $\chi_s(q,0)$?

For a ferromagnetic $SU(2)$ QCP, for which the massless bosons are spin fluctuations, we show in this section that the corrections to the static spin susceptibility are non-analytic: they scale like $q^{3/2}$, and *do not* contain any prefactor except for a proper power of k_F. Such terms obviously overshadow the regular q^2 of the bare susceptibility at small enough momenta.

The physics behind the $q^{3/2}$ term in $\chi(q,0)$ at a ferromagnetic QCP is, by itself, not directly related to criticality: far away from the QCP, the spin susceptibility also contains negative, non-analytic $|q|$ term as we argued in the first chapter. This term gradually evolves as the correlation length ξ increases, and transforms into the $q^{3/2}$ term at the QCP. Both these non-analyticities, at and away from the QCP, emerge because the boson-mediated interaction between fermions contain a long-range dynamic component, generated from the Landau damping.

We now estimate the effect of these singularities on physical quantities. Both the ϕ^3 and ϕ^4 terms in the effective action give rise to corrections to the ϕ^2 term, i.e. to the spin susceptibility. These corrections are obtained diagrammatically by contracting the external legs of the ϕ^3 and ϕ^4 terms, as shown in Fig. 3.2. The computations are described in detail in Appendix D.

The contributions from the ϕ^4 terms have been considered in Publication 1. The contributions from cubic terms were missed, and were first considered in [41] in the analysis of the spin susceptibility in the paramagnetic phase, away from a QCP.

Using the bosonic Dyson's equation:

$$\chi(q,0) = \frac{\chi_0}{(\xi^{-2} + q^2 + \Pi(q,0))} \tag{3.10}$$

we define the static polarization bubble at this order by $\Pi = \Pi_1(q,0) + \Pi_2(q,0) + \Pi_3(q,0) + \Pi_4(q,0)$, where the individual contributions are presented in Fig. 3.2, and

write:

$$\Pi_1(q,0) = \frac{\Gamma_1^S N\bar{g}^2}{(2\pi)^6\chi_0}\int d^2k d\omega d^2l d\Omega\ \chi_s(l,\Omega)\ G(\omega,k)\ G(\omega+\Omega,k+l) \times G(\omega+\Omega,k+q+l)\ G(\omega,k+q) \tag{3.11a}$$

$$\Pi_2(q,0) = \frac{\Gamma_2^S N\bar{g}^2}{(2\pi)^6\chi_0}\int d^2k d\omega d^2l d\Omega\ \chi_s(l,\Omega)\ G(\omega,k)^2\ G(\omega+\Omega,k+l) \times G(\omega,k+q) \tag{3.11b}$$

$$\Pi_3(q,0) = \frac{\Gamma_3^S N^2\bar{g}^3}{(2\pi)^9\chi_0^2}\int d^2k d\omega d^2k' d\omega' dl d\Omega\ \chi_s(l,\Omega)\ \chi_s(q+l,\Omega)\ G(\omega,k) \times G(\omega+\Omega,k+l+q)\ G(\omega',k')\ G(\omega'+\Omega,k'+l+q) \times G(\omega,k+q)\ G(\omega',k'+q) \tag{3.11c}$$

$$\Pi_4(q,0) = \frac{\Gamma_4^S N^2\bar{g}^3}{(2\pi)^9\chi_0^2}\int d^2k d\omega d^2k' d\omega' dl d\Omega\ \chi_s(l,\Omega)\ \chi_s(l,\Omega)\ G(\omega,k) \times G(\omega,k+q)\ G(\omega+\Omega,k+l+q)\ G(\omega',k') \times G(\omega'+\Omega,k'+l)\ G(\omega'+\Omega,k'+l+q) \tag{3.11d}$$

The factors of N come from the fermionic loops and the numerical prefactors from the following spin summations:

$$\Gamma_1^S = \sum_{\alpha,\beta,\gamma,\delta}\sigma^Z_{\alpha\beta}\boldsymbol{\sigma}_{\beta\gamma}\sigma^Z_{\gamma\delta}\boldsymbol{\sigma}_{\delta\alpha} = -2 \tag{3.12a}$$

$$\Gamma_2^S = \sum_{\alpha,\beta,\gamma,\delta}\sigma^Z_{\alpha\beta}\boldsymbol{\sigma}_{\beta\gamma}\cdot\boldsymbol{\sigma}_{\gamma\delta}\sigma^Z_{\delta\alpha} = 6 \tag{3.12b}$$

$$\Gamma_3^S = \sum_{\alpha,\beta,\gamma,\delta,\epsilon,\zeta}\sigma^Z_{\alpha\beta}\left(\boldsymbol{\sigma}_{\beta\gamma}\cdot\boldsymbol{\sigma}_{\delta\epsilon}\right)\left(\boldsymbol{\sigma}_{\gamma\alpha}\cdot\boldsymbol{\sigma}_{\zeta\delta}\right)\sigma^Z_{\epsilon\zeta} = 8 \tag{3.12c}$$

$$\Gamma_4^S = \sum_{\alpha,\beta,\gamma,\delta,\epsilon,\zeta}\sigma^Z_{\alpha\beta}\left(\boldsymbol{\sigma}_{\beta\gamma}\cdot\boldsymbol{\sigma}_{\epsilon\delta}\right)\left(\boldsymbol{\sigma}_{\gamma\alpha}\cdot\boldsymbol{\sigma}_{\delta\zeta}\right)\sigma^Z_{\zeta\epsilon} = -8 \tag{3.12d}$$

These four diagrams are related by pairs. To verify this, it is useful to expand the products of Green's functions according to:

$$G(\omega_1,k_1)G(\omega_2,k_2) = \frac{G(\omega_1,k_1)-G(\omega_2,k_2)}{G^{-1}(\omega_2,k_2)-G^{-1}(\omega_1,k_1)}. \tag{3.13}$$

Applying this to $\Pi_2(q,0)$, we find that it splits into two parts. In one part, the poles in ϵ_k are located in the same half-plane, leading to a vanishing contribution. The remaining term in $\Pi_2(q,0)$ is related to $\Pi_1(q,0)$ in such a way that:

$$\Pi_1(q,0) = -\frac{2\Gamma_1}{\Gamma_2}\Pi_2(q,0). \tag{3.14}$$

(see Appendix D for details).

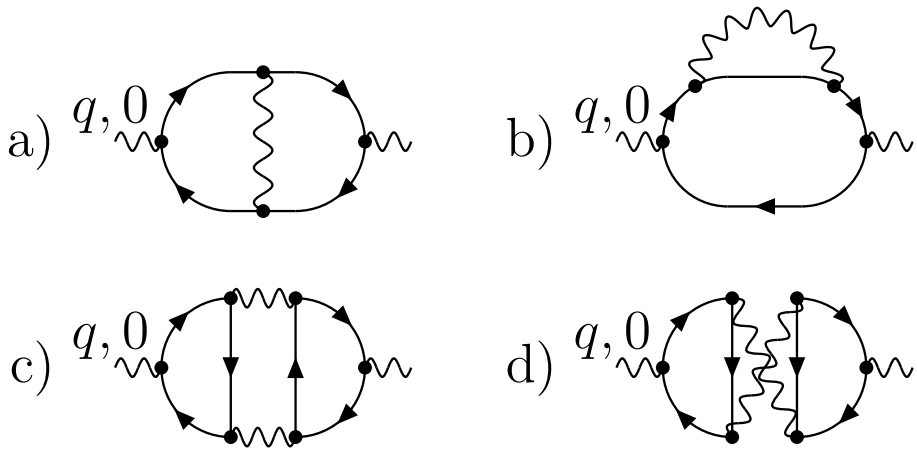

Figure 3.2: Corrections to the polarization bubble from diagrams with one and two extra bosonic lines

Similarly, $\Pi_3(q,0)$ and $\Pi_4(q,0)$ are related as

$$\Pi_3(q,0) = -\frac{\Gamma_3}{\Gamma_4}\Pi_4(q,0). \tag{3.15}$$

Collecting all four contributions and using the relations between prefactors, we obtain:

$$\begin{aligned}
\Pi(q,0) &= \Pi_A(q,0) + \Pi_B(q,0)\ , && (3.16)\\
\Pi_A(q,0) &= \Pi_1(q,0) + 2\Pi_2(q,0)\\
&= 16\frac{N\bar{g}^2}{(2\pi)^6}\int d^2K d\omega d^2l d\Omega\ \chi_s(l,\Omega)G(\omega,k)^2G(\omega+\Omega,k+l)G(\omega,k+q)\\
\Pi_B(q,0) &= \Pi_3(q,0) + \Pi_4(q,0)\\
&= 16\frac{N^2\bar{g}^3}{(2\pi)^9\chi_0^2}\int d^2k d\omega d^2k' d\omega' dl d\Omega\ \chi_s(l,\Omega)\ \chi_s(q+l,\Omega)\ G(\omega,k)\\
&\quad \times G(\omega,k+q)\ G(\omega+\Omega,k+l+q)\ G(\omega',k'+q)\\
&\quad \times G(\omega',k')\ G(\omega'+\Omega,k'+l+q) && (3.17)
\end{aligned}$$

3.2.1 Away from the QCP

Away from criticality, the correlation length ξ is finite, and at low frequency, the system is in the Fermi-liquid regime. The fermionic self-energy is given by $\Sigma(\omega) = \lambda\omega$, Eq. (2.30).

The spin susceptibility in this regime has been analyzed in [42, 43, 29, 44, 45, 46, 41]. It was shown there that to the lowest order in the interaction, $\Pi_B(q,0) = \Pi_A(q,0)$, i.e., $\Pi(q,0) = 2\Pi_A(q,0)$. Beyond leading order, $\Pi_B(q,0)$ and $\Pi_A(q,0)$ are not equivalent but are of the same sign and of comparable magnitude. For

simplicity, we assume that the relation $\Pi_B(q,0) = \Pi_A(q,0)$ holds in the whole Fermi liquid regime. We will see below that even at the QCP, $\Pi_B(q,0)$ and $\Pi_A(q,0)$ are quite similar (at criticality $\Pi_B(q,0) \simeq 1.3\Pi_A(q,0)$).

Introducing $\cos\theta = \frac{\mathbf{k}\cdot\mathbf{l}}{|\mathbf{k}||\mathbf{l}|}$ and $\cos\theta' = \frac{\mathbf{k}\cdot\mathbf{q}}{|\mathbf{k}||\mathbf{q}|}$, and successively integrating over $|\mathbf{k}|$, ω and θ', (3.16) can be rewritten as:

$$\begin{aligned}\Pi(q,0) &= \frac{8\bar{g}|q|}{\pi^3(1+\lambda)v_F}\int_0^\infty dz \int_0^{\frac{\pi}{2}} d\phi \int_0^\pi d\theta \frac{1}{\frac{1}{\tilde{\gamma}\xi^2}+\tan\phi} \\ &\times \frac{\cos\phi\sin\phi}{(i\sin\phi-\cos\theta\cos\phi)^2}\,\frac{z}{\sqrt{1+z^2(\sin\phi+i\cos\phi\cos\theta)^2}} \end{aligned} \tag{3.18}$$

where we defined $\tilde{\gamma} = \frac{\gamma v_F}{1+\lambda}$, and introduced the new variables z and ϕ, which satisfy $z\cos\phi = \frac{l}{q}$ and $z\sin\phi = \frac{(1+\lambda)\Omega}{v_F q}$.

The universal part of $\Pi(q,0)$ can be isolated by subtracting from it the constant part $\Pi(0,0)$. The integral over z then becomes convergent. Integrating successively over z, ϕ and θ, we obtain:

$$\delta\Pi(q,0) = \Pi(q,0) - \Pi(0,0) = -\frac{4}{\pi^2}\frac{\bar{g}}{v_F(1+\lambda)}|q|\ \mathcal{H}\left(\frac{1+\lambda}{\tilde{\gamma}\xi^2}\right), \tag{3.19}$$

where $\mathcal{H}(0) = \frac{1}{3}$, and $\mathcal{H}(x \gg 1) \approx 2/(3x^2)$. We do recover the non-analytic $|q|$ correction to the static spin susceptibility in $D = 2$, as obtained in earlier studies [26, 29, 42, 43, 44].

Note that Eq. (3.21) does not contradict the Fermi liquid relation:

$$\chi_s(q \to 0, \omega = 0) \propto \frac{(1+F_{1,s})}{(1+F_{0,a})} \tag{3.20}$$

where $F_{1,s}$ and $F_{0,a}$ are Landau parameters. The Fermi liquid theory only implies that the static spin susceptibility saturates to a constant value as $q \to 0$, but does not impose any formal constraint on the $q-$dependence of $\chi_s(q,\omega)$.

As one gets closer to the QCP, $\lambda = 3\bar{g}/(4\pi v_S\xi^{-1})$ diverges and the prefactor of the $|q|$ term vanishes as:

$$\delta\Pi(q,0) = -\frac{16}{9\pi}\xi^{-1}|q|. \tag{3.21}$$

This is not surprising since the Fermi liquid regime extends on a region of the phase diagram that shrinks and ultimately vanishes as one approaches the QCP.

Now, two different scenarios are possible:

- the divergence of ξ at the QCP completely eliminates the non-analyticity and the expansion of $\Pi(q,0)$ begins as q^2, like in a bare spin susceptibility,
- the self-energy $\Sigma(\omega) \propto \omega^{2/3}$ at the QCP still leads to a non-analytic term $\Pi(q,0) \propto |q|^\delta$, with $1 < \delta < 2$, which dominates over the bare q^2 term.

We show in the next subsection that the second scenario is realized, and at the QCP, one has $\Pi(q,0) \propto |q|^{3/2}$.

3.2.2 At criticality

At the QCP, we have to take into account two new elements: the bosonic propagator is massless ($\xi^{-1} = 0$) and the fermionic self-energy is no longer Fermi-liquid-like, it is given by (2.32).

The full calculation of $\Pi_A(q,0)$ and $\Pi_B(q,0)$ is presented in Appendix D. We just outline here the main steps of the computation and show where the $q^{3/2}$ term comes from.

Consider first $\Pi_A(q,0)$. Using (3.16) as a starting point, and substituting the full form of the spin susceptibility[1], Eq. (A.8), we then expand $\epsilon_{\mathbf{k+l}}$ and $\epsilon_{\mathbf{k+q}}$, and integrate successively over l_y (projection of $\mathbf{l}$ perpendicular to $\mathbf{k_F}$) and ϵ_k, leading to:

$$\begin{aligned}\Pi_A(q,0) &= 16i\frac{m\bar{g}^2}{(2\pi)^5}\int_0^{2\pi}d\theta\int_{-\infty}^{+\infty}dl_x\int_{-\infty}^{+\infty}d\Omega\int_{-\Omega}^{0}d\omega\frac{(\gamma|\Omega|)^{-1/3}}{\left(i\Sigma(\omega+\Omega)-i\Sigma(\omega)-v_F l_x\right)^2}\\ &\quad h\left(\frac{\sqrt{l_x^2+c^2\Sigma^2(\Omega)}}{(\gamma|\Omega|)^{1/3}}\right)\frac{1}{i\Sigma(\omega+\Omega)-i\Sigma(\omega)-v_F l_x+v_F q\cos\theta},\end{aligned} \tag{3.22}$$

where $c \simeq 1.19878$ (see A.6), and $h(x)$ is the bosonic propagator integrated over the momentum component l_y. The asymptotic behavior of $h(x)$ is given by:

$$\begin{cases} h(x\gg 1) = \frac{\pi}{x} \\ h(x\ll 1) = \frac{4\pi}{3\sqrt{3}} + (\log 2 - 1)x^2 - \frac{x^2\log x^2}{2}\end{cases} \tag{3.23}$$

Since the integrand in (3.22) has poles in l_x located in the same half-plane, the only non-vanishing contributions to Π comes from the non-analyticities in $h(x)$.

There are two non-analyticities in $h(x)$. The first one comes from the $1/x$ behavior at large x, which extends to $x \sim 1$. This is a conventional non-analyticity associated with bosons vibrating near their own mass shell, since at $x \sim 1$, $l_x \sim l_y \sim (\gamma|\Omega|)^{1/3}$.

Subtracting the universal $\Pi_A^{(a)}(0,0)$, expanding in q in (3.22) and substituting $l_x \sim (\gamma|\Omega|)^{1/3}$, we find for this contribution to Π:

$$\begin{aligned}\delta\Pi_A^{(a)} &\propto q^2\frac{m\bar{g}^2}{v_F^3\gamma^{5/3}}\int_0^{\Omega_{\max}}\frac{d\Omega}{\Omega^{2/3}} \\ &\propto \sqrt{\alpha}q^2,\end{aligned} \tag{3.24}$$

where $\Omega_{\max} \sim \sqrt{\gamma v_F^3}$.

We see that the integration over the momentum range relevant to the $z = 3$ scaling regime yields a regular q^2 contribution to the static susceptibility. Not only

[1] To account for a possible contribution from bosonic momentum near the fermionic mass-shell, we have computed in Appendix A, the one-loop bosonic polarization in the regime where $v_F q \sim \tilde{\Sigma}(\omega)$. This is the expression we use here.

this contribution is regular in q, but it is also small in α. This result is similar to the one we obtained in (2.41) for the static vertex at a vanishing momentum.

However, Eq. (3.23) shows that $h(x)$ has a non-analytic $x^2 \log x$ term already at small x, i.e. far from the bosonic mass shell: the branch cut associated with the logarithmic term emerges at $v_F l_x \sim \Sigma(\omega)$. The typical value of l_y in the integral that leads to this $x^2 \log x$ term is also of the same order, although larger in the logarithmic sense. This implies that this second non-analyticity comes from a process in which the bosons are vibrating near a fermionic mass shell and far from their own.

Furthermore, this logarithmic term in (3.23) comes exclusively from the Landau damping term in the bosonic propagator – the q^2 term in $\chi(l, \Omega)$ can be safely omitted. Indeed, one has:

$$\int_{-\Lambda}^{\Lambda} dl_y \frac{1}{\frac{\gamma|\Omega|}{\sqrt{l_x^2+l_y^2}}} = f(\Lambda) - \frac{l_x^2 \log l_x^2}{2\gamma\Omega}. \tag{3.25}$$

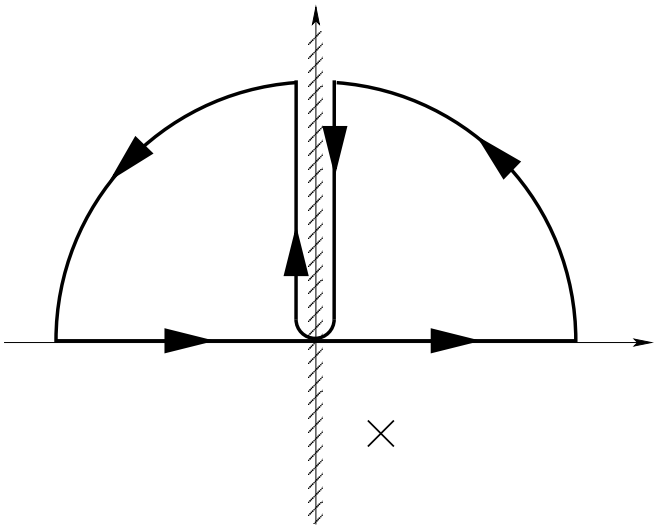

Figure 3.3: Integration contour: the hatched region stands for a branch cut, and the cross for a pole.

Substituting the logarithmic term from (3.23) into (3.22), we subtract the non-universal constant term $\Pi_A^{(b)}(0,0)$, which makes the integral over l_x convergent. Introducing $z = l_x/(c\Sigma(\Omega))$, one can perform the integral over z over the contour of

Fig. 3.3, which leads to the following contribution to Π:

$$\begin{aligned}\Pi_A^{(b)}(q,0)-\Pi_A^{(b)}(0,0) &= \frac{4Nm\bar{g}^2}{c^2\pi^4\gamma v_F}q^2\int_0^{\pi/2}d\theta\int_1^{+\infty}dy\int_0^{+\infty}\frac{d\omega}{\Sigma(\Omega)^2}\\ &\int_0^1 dw\frac{\cos^2\theta}{\left[c^{-1}\left((1-w)^{2/3}+w^{2/3}\right)+y\right]^3}\\ &\frac{1-y^2}{\left[y+c^{-1}\left((1-w)^{2/3}+w^{2/3}\right)\right]^2+\left(\frac{v_F q\cos\theta}{c\Sigma(\Omega)}\right)^2},\end{aligned} \tag{3.26}$$

where we defined $w=\omega/\Omega$. Introducing the new variables $t=\left(\frac{c\Sigma(\Omega)}{v_F q\cos\theta}\right)^{3/2}$ and $v=t\left[y+c^{-1}\left((1-w)^{2/3}+w^{2/3}\right)\right]$, it becomes possible to separate the integrals, leading to the following final result:

$$\begin{aligned}\Pi_A^{(b)}(q,0)-\Pi_A^{(b)}(0,0) &= -0.8377q^{3/2}\frac{Nm\bar{g}^2}{\pi^4\gamma v_F^{3/2}\omega_0^{1/2}}\\ &= -0.1053\ \sqrt{k_F}\ q^{3/2}.\end{aligned} \tag{3.27}$$

We emphasize that this dependence comes from bosonic modes vibrating at the fermionic mass-shell. This explains why the result of (3.27) is not small in α, as this small parameter measures the softness of the mass-shell bosons compared to the mass-shell fermions.

The integrals for $\Pi_B(q,0)$ cannot be exactly evaluated analytically, but an approximate calculation, detailed in Appendix E, yields:

$$\Pi_B^{(b)}(q,0)-\Pi_B^{(b)}(0,0)=-0.14q^{3/2}\sqrt{p_F}, \tag{3.28}$$

such that the total contribution of all four diagrams reads:

$$\Pi(q,0)-\Pi(0,0)=-0.25\ q^{3/2}\sqrt{k_F}. \tag{3.29}$$

We see that $\Pi(q,0)$ is still non-analytic in q and the prefactor is negative. At small q, the negative $q^{3/2}$ term well exceeds the regular q^2 term in the static spin susceptibility, which reads at criticality:

$$\chi_s(q,0)=\frac{\chi_0}{q^2-0.25\ q^{3/2}\sqrt{k_F}} \tag{3.30}$$

This implies that *the static spin susceptibility is negative at small momenta, i.e. a ferromagnetic QCP is unstable*. We discuss the consequences of this instability in the concluding chapter. The momentum q_{min} below which χ_s is negative is determined by:

$$\chi_s^{-1}(q_{min})\propto q_{min}^2-0.25q_{min}^{3/2}\sqrt{k_F}=0, \tag{3.31}$$

which gives $q_{min} = 0.06 k_F$.

Parametrically, q_{min} is of order k_F, which is the largest momentum scale in our problem. Strictly speaking, this suggests that the whole quantum-critical theory for the ferromagnetic case is not valid, since the quantum critical behavior extends up to energies of order ω_0, i.e. up to momenta of order $q \leq \omega_0/v_F \sim \alpha^2 k_F \ll k_F$. Numerically, however, q_{min} is much smaller than k_F. This implies that for reasonable values of α, there exists an intermediate momentum and energy range $q_{min} < q < \omega_0/v_F$ where the system is in the quantum-critical regime, but the static spin susceptibility is still positive.

The $q^{3/2}$ non-analyticity can also be viewed as emerging from the momentum dependence of the static vertex analyzed in the previous chapter. Using Eq. (2.45), one can rewrite:

$$\Pi(q,0) \sim N\bar{g} \int d^2k d\omega \frac{1}{i\Sigma(\omega) - \epsilon_k} \frac{\left.\frac{\Delta g}{g}\right|_{q,\Omega=0}}{i\Sigma(\omega) - \epsilon_{k+q}} \tag{3.32}$$

Performing the contour integration over ϵ_k, and changing variables into $y = \epsilon_k/\Sigma\omega$ and $t = \sqrt{\omega_0}\omega/((v_F q)^{3/2})$, we obtain:

$$\Pi(q,0) \sim \sqrt{k_F} q^{3/2} \tag{3.33}$$

We note in this regard that the non-analytic momentum dependence of the fermion-boson static vertex also comes from bosons vibrating near the fermionic mass shell, i.e. it emerges due to the same physics as we outlined above.

3.3 Related results

3.3.1 Finite temperature result

We can also prove that the non-analyticity appears in the temperature-dependent uniform static susceptibility $\chi_s(T)$. We show below that $\chi_s^{-1}(T) \propto T|\log T|$, again with a negative prefactor.

In this section, we show that the static uniform susceptibility is negative at finite temperature above a ferromagnetic QCP. To demonstrate this, we compute the static uniform $\Pi_A(q = 0, \omega = 0, T) = \Pi_A(T)$, assuming that $\xi^{-1} = 0$. The contribution from $\Pi_B(T)$ is of the same sign and comparable in magnitude. We have

$$\Pi_A(0,T) = 16iN \frac{m\bar{g}^2}{(2\pi)^3} T \sum_{p\neq 0} \Omega_p \int d^2q \frac{1}{q^2 + \frac{\gamma|\Omega_p|}{q}} \frac{1}{\left(i\Sigma(\Omega_p) - v_F q_x - \frac{q_y^2}{2m}\right)^3}. \tag{3.34}$$

Since the poles in q_x from the fermionic Green's functions are all in the same half-plane, one expects that $q_x^{\text{Typ}} \sim (\gamma\Omega)^{1/3}$ and thus dominates over the q_y^2 term,

which in turn can be neglected in the fermionic Green's functions. It then becomes possible to perform the integral over q_y, which gives

$$\Pi_A(0,T) = 2iN\frac{m\bar{g}^2}{\pi^3\gamma v_F^3}T\sum_{p\neq 0}\frac{\Omega_p}{|\Omega_p|}\int_0^{(\gamma\Omega_p)^{1/3}} dq_x\ \frac{q_x^2\log|q_x|}{(i\tilde{\Sigma}(\Omega_p)-v_Fq_x)^3} \tag{3.35}$$

Integrating over the half-space where there is no triple pole, we find that the integral is determined by the branch cut in $\log|q_x|$. Evaluating the integral we obtain

$$\int\frac{dq_xq_x^2\log|q_x|}{(i\tilde{\Sigma}(\Omega_p)-v_Fq_x)^3} = \mathrm{Sign}(\Omega_p)\ \frac{i\pi}{v_F^3}\log\left(\frac{E_F}{|\tilde{\Sigma}(\Omega_p)|}\right)\ . \tag{3.36}$$

Thus

$$\Pi_A(0,T) = \frac{2N}{3}\frac{m\bar{g}^2}{\pi^2\gamma v_F^3}T\sum_{p\neq 0}\log\frac{E_F}{|\Omega_p|} \tag{3.37}$$

To perform the summation over p, we notice that when the summand does not depend on p

$$T\sum_{-\Lambda/T}^{\Lambda/T} A = 2A\Lambda\ , \tag{3.38}$$

is independent on T. Then the same sum but without the term at $p=0$ will be $2A\Lambda - AT$. Using this, we obtain with logarithmic accuracy

$$T\sum_{p\neq 0}\log\frac{E_F}{|\Omega_p|} = -T\log\frac{E_F}{T} + ... \tag{3.39}$$

where dots stand for $O(T)$ terms. Substituting this into (3.37), we obtain the final result:

$$\Pi_A(0,T) = -\frac{2k_F^2}{3\pi^2}\alpha\frac{T}{E_F}\log\left(\frac{E_F}{T}\right). \tag{3.40}$$

Although small, because of the prefactor in α, this term dominates at low temperature over any regular T^2 term. The sign of this $T\log E_F/T$ term is opposite to the sign of a conventional correction to the HMM theory, which comes from a constant part of the prefactor of the ϕ^4 term. In the HMM theory the temperature dependence of the spin susceptibility is $bT^{d+z-2}z$, $b>0$, which in $d=2$ leads to a linear in T contribution with positive prefactor. The negative sign of the non-analytic temperature correction in (3.40) implies that the static spin susceptibility is negative right above the QCP. This is another indication that the ferromagnetic QCP is unstable.

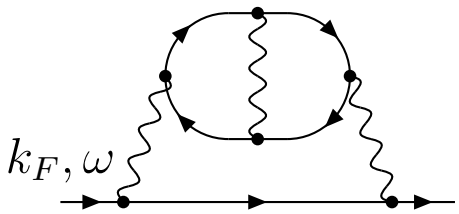

Figure 3.4: Three-loop contribution to the fermionic self-energy

3.3.2 Three-loop fermionic self-energy

Finally, we show how one can detect the instability of a ferromagnetic QCP from an analysis of higher order self-energy diagrams. This analysis is complimentary to the calculations that we have already done in the previous subsections. We show that upon inserting the contributions from the diagrams presented in Fig. 3.2 into the fermionic self-energy, we obtain series of singular corrections in powers of ω_{min}/ω, where $(\gamma\omega_{min})^{1/3} = q_{min}$, and q_{min} is the scale at which the static susceptibility $\chi_s(q)$ becomes negative, Eq. (3.31).

To illustrate this, we consider one of the three-loop diagrams, represented in Fig. 3.4. In the case of a spin interaction, we obtained a finite result after collecting the various diagrams, so we restrict ourselves here with just one of these contributions. The analytic form of the diagram in Fig. 3.4 writes:

$$\Sigma_3(\omega) \sim \bar{g} \int d\omega_1 d^2q_1 \frac{A(q_1,\omega_1)}{i\Sigma(\omega-\omega_1) - v_F q_{1x} - \frac{q_{1y}^2}{2m}} \left(\frac{1}{q_1^2 + \frac{\gamma|\omega_1|}{q_1}} \right)^2, \tag{3.41}$$

where $A(q_1,\omega_1)$ is the dynamic fermionic bubble given by:

$$\begin{aligned} A(q_1,\omega_1) \;\sim\; & N\bar{g}^2 \int d^2k d\Omega \int d^2q_2 d\omega_2 \frac{1}{q_2^2 + \frac{\gamma|\omega_2|}{q_2}} \; \frac{1}{i\Sigma(\Omega) - \epsilon_k} \; \frac{1}{i\Sigma(\Omega-\omega_1) - \epsilon_{k+q_1}} \\ & \times \frac{1}{i\Sigma(\Omega+\omega_1+\omega_2) - \epsilon_{k+q_1+q_2}} \; \frac{1}{i\Sigma(\Omega+\omega_2) - \epsilon_{k+q_2}}. \end{aligned} \tag{3.42}$$

Approximating $A(q_1,\omega_1)$ by its singular static part $q_1^{3/2}\sqrt{k_F}$ and substituting into (3.4) we obtain:

$$\Sigma_3(\omega) \sim \bar{g}\sqrt{k_F} \int d\omega_1 d^2q_1 \left(\frac{q_1}{q_1^3 + \gamma|\omega_1|} \right)^2 \frac{q_1^{3/2}}{i\Sigma(\omega-\omega_1) - v_F q_{1x} - \frac{q_{1y}^2}{2m}}. \tag{3.43}$$

A simple analysis of this expression shows that the dominant contribution to $\Sigma_3(\omega)$ comes from $q_{1x} \sim q_{1y} \sim (\gamma\omega_2)^{1/3}$ since the integral over q_{1x} is determined by the branch cut in the bosonic propagator. One can then safely drop the quadratic

term in the fermionic propagator and integrate over the angle θ between $\mathbf{k_F}$ and $\mathbf{q_1}$. This leads to:

$$\begin{aligned}\Sigma_3(\omega) &\sim \bar{g}\sqrt{k_F}\int_0^{\omega} d\omega_1 \int dq_1 \, \frac{q_1^{9/2}}{(q_1^3+\gamma\omega_1)} \frac{1}{\sqrt{(v_F q_1)^2+\Sigma(\omega)^2}} \\ &\sim \frac{\bar{g}\sqrt{k_F}}{v_F\sqrt{\gamma}}\int_0^{\omega}\frac{d\omega_1}{\sqrt{\omega_1}}. \end{aligned} \tag{3.44}$$

Collecting the prefactors, we find:

$$\Sigma_3(\omega) \sim (\bar{g}\omega)^{1/2}. \tag{3.45}$$

We see that the non-analyticity in the static spin susceptibility feeds back into the fermionic self-energy leading to a contribution from the three loop self-energy whose frequency dependence is more singular than the $\omega^{2/3}$ dependence that we obtained assuming that the static susceptibility is regular. Comparing these two contributions, we see that they become comparable at a frequency:

$$\omega_0^{1/3}\omega_{min}^{2/3} \sim \sqrt{\bar{g}\omega_{min}} \implies \omega_{min} \sim \frac{q_{min}^3}{\gamma} \sim \frac{E_F^2}{\bar{g}}. \tag{3.46}$$

where q_{min} is given by (3.31). Parametrically, q_{min} is not small since $q_{min} \sim k_F$, and $\omega_{min} \sim E_F/\alpha$ is larger than E_F. However, $q_{min} \sim 0.06 k_F$ is small numerically so that ω_{min} is four orders of magnitude smaller than E_F/α.

3.3.3 Conclusion

To summarize, we found that the Eliashberg theory for an $SU(2)$ symmetric ferromagnetic QCP has to be extended to include extra singular terms into both the spin susceptibility and the fermionic self-energy. These terms originate from the "anti-Migdal" processes in which slow bosons are vibrating near the fermionic mass shell. Physically, these extra processes originate from the dynamic long-range interaction between fermions, which is still present at the QCP despite the fact that fermions are no longer good quasi-particles.

We demonstrated that these extra non-analytic terms can be understood in the framework of HMM ϕ^4 theory of quantum criticality. We showed that the prefactor for the ϕ^4 term is non-analytic and depends on the interplay between momentum and frequency. The non-analytic bosonic self-energy is the feedback from the non-analytic ϕ^4 term to the quadratic ϕ^2 term.

We found that these extra terms in the Eliashberg theory make a ferromagnetic QCP unstable below a certain momentum/energy scale. We detected the instability by analyzing the momentum and temperature dependence of the spin susceptibility, and also the fermionic self-energy at three-loop order.

3.4 Non-$SU(2)$ symmetric case

3.4.1 Discussion

The low-energy model used to describe the ferromagnetic quantum critical point is actually quite similar to other models. The problem of fermions interacting with bosonic collective modes with a propagator similar to the one we considered, is quite general, and one can wonder to what extent our analysis for a ferromagnetic case can be extended to these systems.

Indeed, even though it arises from very different underlying microsopic models, one can use an effective Hamiltonian comparable to the spin-fermion one in other problems, namely:

- fermions interacting with singular gauge fields (as studied in [34, 35, 30]);
- a quantum critical point in the charge channel;
- a quantum critical point towards a nematic-type ordering [47, 36, 48, 49, 50];
- a ferromagnetic QCP with Ising symmetry;

The essential difference between these cases and the ferromagnetic one lies in the symmetry of the order parameter. In an SU(2) spin-symmetric ferromagnetic case, the order parameter (magnetization) is a three-dimensional vector, while in the other cases, it is a scalar.

As we already discussed, the Eliashberg theory, and the analysis of its validity at the two-loop level can be carried out equally for systems with vector and with scalar order parameter: the only unessential difference is in the numerical prefactors. On the other hand, the evaluation of the corrections to the static susceptibility leads to different results for scalar and vector order parameters, as we now demonstrate.

3.4.2 Ising case

Consider first the situation of a magnetically-mediated interaction, where we change the spin symmetry of the bosons from SU(2) to Ising. The Ising case was argued to be relevant for metamagnetic quantum critical points [51].

The use of Ising spins doesn't change the expression for the Green's functions but replaces the Pauli matrix $\boldsymbol{\sigma}$ at the fermion-boson vertex by σ^z. As a consequence, the computations performed for the SU(2) case still hold, but the interplay between different diagrams changes because of a change in the numerical prefactors. In particular, instead of Eq. (3.12) we now have:

$$\begin{aligned} \Gamma_1^{\text{Ising}} &= \Gamma_2^{\text{Ising}} = 2, \\ \Gamma_3^{\text{Ising}} &= \Gamma_4^{\text{Ising}} = 0. \end{aligned} \tag{3.47}$$

Under these circumstances, the non-analytic contributions from the diagrams in Fig. 3.2 cancel each other out. As a result, the static spin susceptibility remains analytic and scales as $\chi^{-1}(q) \propto q^2$ with a positive prefactor at the QCP.

This result can be extended to the case of a nematic instability, following the same arguments.

3.4.3 Charge channel

For a charge vertex, one has to replace the Pauli matrices present at the vertex by Kronecker symbols $\delta_{\alpha\beta}$. We then have:

$$\begin{aligned}\Gamma_1^{\text{Charge}} &= \Gamma_2^{\text{Charge}} = \sum_{\alpha,\beta,\gamma,\delta} \delta_{\alpha\beta}\delta_{\beta\gamma}\delta_{\gamma\delta}\delta_{\delta\alpha} = 2,\\ \Gamma_3^{\text{Charge}} &= \Gamma_4^{\text{Charge}} = \sum_{\alpha,\beta,\gamma,\delta,\epsilon,\zeta} \delta_{\alpha\beta}\delta_{\beta\gamma}\delta_{\delta\epsilon}\delta_{\gamma\alpha}\delta_{\zeta\delta}\delta_{\epsilon\zeta} = 4.\end{aligned}$$

Substituting these Γ^{Charge} into the expressions for Π, we find that the diagrams Π_1 and Π_2, as well as Π_3 and Π_4 cancel each other out. This leaves only a regular q^2 term in the static charge susceptibility.

3.4.4 Physical arguments

The cancellation of the non-analytic terms in the charge susceptibility is not a direct consequence of the conservation laws. These laws impose constraints on the behavior of the susceptibilities in the opposite limit $q = 0$, $\omega \neq 0$ ($\chi_c(q = 0, \omega)$ vanishes as a uniform perturbation cannot affect a time independent, conserved quantity).

Instead, the absence of the non-analytic terms in the charge channel is related to the fact that this susceptibility measures the response of the system to a change in the chemical potential. We showed that the origin of the singular behavior of the static spin susceptibility lies in the Landau damping term in the bosonic propagator (see (3.25), (3.29)). The Landau damping does not depend in a singular way on k_F (i.e. on the density of electrons), and therefore there is no singular response of the system to a change in the chemical potential.

Conversely, the effect of a magnetic field on the Landau damping is singular. For a fermionic bubble with opposite spin projections of the two fermions, one has, in the presence of a small magnetic field H:

$$\Pi_{\pm} \sim \frac{|\Omega|}{\sqrt{(\Omega + 2i\mu_B H)^2 + (v_F l)^2}} \tag{3.48}$$

instead of the usual $\Pi_{\pm} \sim |\Omega|/\sqrt{\Omega^2 + (v_F l)^2}$.

As a consequence, taking the second derivative of $\Pi_\pm$ over H and setting $H = 0$ later, one obtains, for $v_F l \gg \Omega$, the following non-analytic term:

$$\frac{d^2\Pi_\pm}{dH^2} \sim \frac{\mu_B}{v_F^3}\frac{\Omega}{l^3}. \tag{3.49}$$

This non-analyticity ultimately gives rise to the $q^{3/2}$ term in the static spin susceptibility [46, 41]. For an Ising ferromagnet, this effect does not exist as there are no bubbles with opposite spin projections in the theory.

The above reasoning shows that the non-analyticity appears in the spin response but not in the charge one. To further verify this argument, we computed the subleading, three-loop diagrams for the charge susceptibility and found that the non-analytic contributions from individual diagrams all cancel out. We present the calculations in Appendix E.

The same argument holds for the self-energy at the three-loop and higher orders. The singular $\omega^{1/2}$ term obtained in Eq. (3.45) appears in individual diagrams, but in the case of a QCP in the charge channel (or an Ising QCP in the spin channel) the total singular contribution cancel out.

CHAPTER 4

Conclusions and perspectives

We have constructed a fully controllable quantum critical theory describing the interaction of fermions with gapless long-wavelength collective bosonic modes. Our approach, similar but not identical to the Eliashberg theory for the electron-phonon interaction, allows us to perform detailed calculations of the fermionic self-energy and the vertex corrections at the QCP.

We constructed a controllable expansion at the QCP as follows: we first created a new, non Fermi-liquid "zero-order" theory by solving a set of coupled equations for the fermionic and the bosonic propagators, neglecting the vertex corrections as well as the momentum dependence of the fermionic self-energy, and then analyzed the residual interaction effects in a perturbative expansion around this new zero-order theory.

We have proved that this approach is justified under two conditions:

(i) the interaction $\bar{g}$ should be smaller than the fermionic bandwidth (which we assumed for simplicity to be of the same order as E_F),

(ii) either the band mass m_B should be smaller than $m = p_F/v_F$, or the number of fermionic flavors N should be large. When $N = O(1)$ and $m_B \sim m$, the corrections are of order $O(1)$.

We found that the corrections that are small in $\bar{g}/E_F$ come from bosons near their resonance, as in the Eliashberg theory for the electron-phonon interaction. The corrections small in $m_B/(Nm)$ come from bosons for which one of the momentum component (the larger one) is near the bosonic resonance, while the other component is close to the fermionic mass-shell.

For an SU(2)-symmetric quantum critical point towards ferromagnetic ordering, we found that there exists an extra set of singular renormalizations which come from bosons with both momentum components vibrating near the fermionic mass-shell. These processes can be understood as a consequence of an effective long-range dynamic interaction between quasi-particles, generated by the Landau damping term. They give rise to a negative non-analytic $q^{3/2}$ correction to the static spin susceptibility, signaling that the ferromagnetic QCP is unstable.

We also demonstrated that the non-analytic $q^{3/2}$ term can be understood in the framework of Hertz-Millis-Moriya ϕ^4 theory of quantum criticality. We showed how the effective long-range dynamic interaction between fermions affects the structure of the ϕ^4 theory, once fermions are integrated out: we found that the prefactors of the ϕ^3 and ϕ^4 terms appearing in the effective action are non-analytic and depend on the interplay between the typical external momentum and frequency.

We showed that the non-analytic corrections to the bosonic propagator are specific to the SU(2)-symmetric case when the order parameter is a vector. For systems with a scalar order parameter, like a QCP in the charge channel, a nematic QCP, or a ferromagnetic QCP with Ising symmetry, the $q^{3/2}$ contributions from individual diagrams cancel out in the full expression of the susceptibility.

The consequences of the instability of the ferromagnetic QCP still needs to be fully understood. There are two possible scenarios for the behavior of the system: either the ferromagnetic transition becomes first order [52, 53], or the instability occurs at a finite q, leading to a second order transition towards an incommensurate state [54, 55]. The full analysis of these two scenarios is clearly called on.

Note however that in all the experimental examples presented in Chapter 1 where a first order transition has been observed, the latter usually appear at very low temperature, well below the typical energy scale where the quantum critical behavior is observed. Such features do strongly suggest that a first order transition is the most likely to occur in our case.

PUBLICATION 1

Instability of the Quantum Critical Point of itinerant ferromagnets

Phys. Rev. Lett. **92**, 147003 (2004)

PUBLICATION 2

Quantum critical behavior of itinerant ferromagnets

Unpublished

Appendices

APPENDIX A

Bosonic self-energy

In this section, we compute the bosonic self-energy at the one-loop level, in the case of both free and fully renormalized fermions. We prove that for an external bosonic momentum on the bosonic mass-shell, this self-energy becomes independent on the actual form of the fermionic self-energy, and reduces to the usual Landau damping term, whereas an extra term has to be included if this same external momentum is on the fermionic mass shell.

After performing the sum over spin matrices, we are left with the following expression:

$$\Pi(\mathbf{q},\Omega) = 2N\bar{g}\int \frac{d^2k\ d\omega}{(2\pi)^3}\ G(\mathbf{k},\omega)\ G(\mathbf{k}+\mathbf{q},\omega+\Omega). \tag{A.1}$$

Introducing the angle θ defined by $\epsilon_{k+q} = \epsilon_k + v_F q\cos\theta$, this writes:

$$\begin{aligned}\Pi(\mathbf{q},\Omega) = N\frac{\bar{g}m}{4\pi^3}\int d\omega\ d\epsilon_k\ d\theta\ \frac{1}{i(\omega+\Sigma(\omega))-\epsilon_k} \\ \times\frac{1}{i(\omega+\Omega+\Sigma(\omega+\Omega))-\epsilon_k-v_F q\cos\theta}.\end{aligned} \tag{A.2}$$

Proceeding with a contour integration over ϵ_k, and noticing that ω and $\Sigma(\omega)$ have the same sign, we get:

$$\begin{aligned}\Pi(\mathbf{q},\Omega) = iN\frac{\bar{g}m}{2\pi^2}\int_{-\infty}^{+\infty} d\omega\ \int_0^{2\pi} d\theta\ (\theta(\omega+\Omega)-\theta(\omega)) \\ \times\frac{1}{i(\Omega+\Sigma(\Omega+\omega)-\Sigma(\omega))-v_F q\cos\theta}.\end{aligned} \tag{A.3}$$

Performing the integration over θ, and rearranging a little bit the integration over Ω, we are left with:

$$\Pi(\mathbf{q},\Omega) = N\frac{m\bar{g}}{\pi v_F}\int_0^{\Omega} d\omega\ \frac{\mathrm{Sign}(\Omega)}{\sqrt{(v_F q)^2 + (\Omega + \Sigma(\Omega-\omega) + \Sigma(\omega))^2}}. \tag{A.4}$$

We know from direct perturbative calculation that the fermionic self-energy goes like $\Sigma(\omega) = \omega_0^{1/3}\omega^{2/3}$, where $\omega_0 \sim \alpha\bar{g}$. It follows that if the external bosonic momentum is on the bosonic mass-shell, i.e. if $q \sim \Omega^{1/3}$, it dominates over the frequency-dependent term in the integral, so that:

$$\begin{aligned}\Pi(\mathbf{q},\Omega) &= N\frac{m\bar{g}}{\pi}\int_0^{\Omega} d\omega\ \frac{\mathrm{Sign}(\Omega)}{v_F q} \\ &= N\frac{m\bar{g}}{\pi v_F}\ \frac{|\Omega|}{q}.\end{aligned} \tag{A.5}$$

We recover here the expression of the Landau damping term with a prefactor depending on the details of the interaction considered in our model. This result is independent on the fermionic self-energy provided that $v_F q \gg (\Omega + \Sigma(\Omega))$.

However, if the external bosonic momentum is on the fermionic mass shell, i.e. if $v_F q \sim \Sigma(\Omega)$, the frequency-dependent term can no longer be neglected. Defining $z = \frac{\omega}{\Omega}$, one then has:

$$\Pi(\mathbf{q},\Omega) = N\frac{m\bar{g}}{\pi}\ \left|\frac{\Omega}{\Sigma(\Omega)}\right| \int_0^1 dz\ \frac{1}{\sqrt{\left(\frac{v_F q}{\Sigma(\Omega)}\right)^2 + \left(z^{2/3} + (1-z)^{2/3}\right)^2}}. \tag{A.6}$$

This formula is of limited use as it is modified by vertex corrections. For the calculations of the static spin susceptibility, we will actually only need the leading $O(1/q)$ and the subleading, $O(1/q^3)$ terms in $\Pi(q,\Omega)$ We will show in Appendix C that these two terms still can be evaluated without vertex corrections (see Eq. (C.21) below). Expanding (A.6) in $1/q$ to first two orders, we find, at $\Omega < \omega_0$,

$$\Pi(q,\Omega) = \gamma\frac{|\Omega|}{q}\ \left(1 - \frac{c^2\Sigma^2(\Omega)}{v^2 q^2}\right) \tag{A.7}$$

where $c \sim 1.19878$. To simplify writing, we will be using the expression for the polarization operator with Ω dependence in the denominator, i.e., plug Σ^2 term back into denominator, i.e.,

$$\Pi(\mathbf{q},\Omega) = N\frac{m\bar{g}}{\pi}\ \frac{|\Omega|}{\sqrt{(v_F q)^2 + c^2\Sigma(\Omega)^2}}, \tag{A.8}$$

but one should keep in mind that we will actually only need $1/q$ and $1/q^3$ terms in the calculations.

APPENDIX B

Fermionic self-energy

In this section, we compute the fermionic self-energy at the one, two and three loop levels, for an external momentum taken to be on the Fermi surface. We also analyze the momentum dependence of the one-loop fermionic self-energy.

B.1 One-loop

B.1.1 At the Fermi level

After summing over the spin matrices, the fermionic self-energy at the one-loop level is given by:

$$\begin{aligned}\Sigma(\omega) &= 3ig^2 \int \frac{d^2q\ d\Omega}{(2\pi)^3} G(\mathbf{k_F}+\mathbf{q}, \omega+\Omega)\chi(\mathbf{q},\Omega) \\ &= \frac{3i\bar{g}}{(2\pi)^3}\int d\theta\ \frac{d\Omega\ dq}{\xi^{-2}+q^2+\gamma\frac{|\Omega|}{q}} \frac{q}{i(\omega+\Omega+\Sigma(\omega+\Omega))-v_F q\cos\theta}, \quad \text{(B.1)}\end{aligned}$$

where we defined θ as the angle between $\mathbf{k}$ and $\mathbf{q}$, and considered an external fermionic momentum $k \simeq k_F$. The i prefactor comes from the convention $G^{-1} = G_0^{-1} + i\Sigma$.

Since the pole in q from the fermionic propagator is in a definite half-plane, the integral in q is dominated by poles coming from the bosonic Green's function, so that one can perform the integral over the angular variable and simplify the result

as follows:

$$\begin{aligned}\Sigma(\omega) &= -\frac{3g^2}{(2\pi)^2}\int d\Omega\; dq\; \frac{\chi_0}{q^3+\gamma|\Omega|+q\xi^{-2}}\frac{q^2\mathrm{Sign}(\omega+\Omega)}{\sqrt{(v_Fq)^2+(\omega+\Omega+\Sigma(\omega+\Omega))^2}} \\ &= -\frac{3\bar{g}}{(2\pi)^2}\int_{-\infty}^{+\infty} d\Omega\; \int_0^{+\infty} dq\; \frac{q^2\mathrm{Sign}(\omega+\Omega)}{v_Fq}\frac{1}{q^3+\gamma|\Omega|+q\xi^{-2}}. \qquad \text{(B.2)}\end{aligned}$$

Defining the new variables $z=\frac{\Omega}{\omega}$ and $u=\frac{v_Fq}{\omega}$, this leads to:

$$\Sigma(\omega)=\frac{3\bar{g}}{2\pi^2}\;\frac{\omega^2}{\gamma v_F^3}\int_0^1 dz\;\int_0^{+\infty} du\;\frac{u}{z+au+bu^3}, \qquad \text{(B.3)}$$

where we have used $a=\dfrac{1}{\gamma v_F\xi^2}$ and $b=\dfrac{\omega^2}{\gamma v_F^3}$

Let's denote by I the last double integral, and define the new variables $y=\sqrt{\frac{b}{a^3}}z=(\omega\gamma\xi^3)z$ and $t=\sqrt{\frac{b}{a}}u=\frac{\xi\omega}{v_F}u$. Now I reduces to:

$$\begin{aligned}I &= \left(\frac{v_F}{\xi\omega}\right)^2\int_0^{\gamma\omega\xi^3} dy\;\int_0^{+\infty} dt\;\frac{t}{t^3+t+y} \\ &= \left(\frac{v_F}{\xi\omega}\right)^2 h(\gamma\omega\xi^3). \qquad \text{(B.4)}\end{aligned}$$

Substituting this back into our expression for the self-energy:

$$\Sigma(\omega)=\frac{3}{2\pi m\xi^2}\mathcal{I}(\gamma\omega\xi^3), \qquad \text{(B.5)}$$

with the following asymptotic behavior: $\mathcal{I}(x\to 0)\frac{\pi x}{2}$ and $h(x\to\infty)=\frac{\pi x^{2/3}}{\sqrt{3}}$.

In the two regimes we are interested in, this last result can be rewritten as:

$$\Sigma(\omega)=\begin{cases}\lambda\omega & \text{for } \xi^{-1}\gg 1,\\ \omega_0^{1/3}\omega^{2/3} & \text{for } \xi^{-1}\to 0,\end{cases} \qquad \text{(B.6)}$$

where the constant prefactors are defined as:

$$\begin{cases}\lambda &= \dfrac{3}{4\pi}\dfrac{\bar{g}\xi}{v_F},\\ \omega_0 &= \dfrac{3\sqrt{3}}{8\pi^3}\dfrac{\bar{g}^3}{\gamma v_F^3}.\end{cases} \qquad \text{(B.7)}$$

B.1.2 Momentum dependence

For definiteness, we set $\xi^{-1} = 0$. We first compute the momentum-dependent part of the one-loop fermionic self-energy at zero external frequency:

$$\begin{aligned}\Sigma(\mathbf{k}, \omega = 0) &= 3ig^2 \int \frac{d^2q\ d\Omega}{(2\pi)^3} G(\mathbf{k}+\mathbf{q}, \Omega)\chi(\mathbf{q}, \Omega) \\ &= \frac{3i\bar{g}}{(2\pi)^3} \int \frac{d\Omega d^2q}{i\tilde{\Sigma}(\Omega) - \epsilon_{k+q}} \frac{q}{\gamma|\Omega| + q^3}\ . \end{aligned} \tag{B.8}$$

Expanding $\epsilon_{k+q} = \epsilon_k + v_F q\cos\theta$ and integrating over θ, we obtain

$$\Sigma(\mathbf{k}, 0) = \frac{3\bar{g}}{4\pi^2} \int d\Omega\ \mathrm{Sign}(\Omega) \int \frac{q^2 dq}{q^3 + \gamma|\Omega|} \frac{1}{\left((v_F q)^2 + (\tilde{\Sigma}(\Omega) + i\epsilon_k)^2\right)^{1/2}}. \tag{B.9}$$

At $\epsilon_k = 0$, the integral vanishes by parity. Expanding to linear order in ϵ_k we obtain:

$$\Sigma(\mathbf{k}, 0) = -3i\epsilon_k \times \frac{\bar{g}}{2\pi^2} \int_0^\infty d\Omega\ \tilde{\Sigma}(\Omega) \int \frac{q^2 dq}{(q^3 + (\gamma|\Omega|)) \left((v_F q)^2 + \tilde{\Sigma}(\Omega)^2\right)^{3/2}}. \tag{B.10}$$

Simple estimates show that the result depends on the interplay between $(\gamma\Omega)^{1/3}$ and $\tilde{\Sigma}(\Omega)/v_F$. Introducing the scale ω_{Max}, defined as the frequency at which $(\gamma\Omega)^{1/3} = \tilde{\Sigma}(\Omega)/v_F$ (see (2.42), and rescaling variables as $q = (\gamma\omega_{\mathrm{Max}})^{1/3} y$, $\Omega = \omega_{\mathrm{Max}} x$, we rewrite (B.10) as

$$\Sigma(\mathbf{k}, 0) = -3i\epsilon_k \times \frac{\bar{g}\omega_{\mathrm{Max}}}{2\pi^2 v_F^3 \gamma} I \tag{B.11}$$

where

$$I = \int_0^\infty dx \int_0^\infty dy \frac{xy^2}{(x^2+y^2)^{3/2}(x+y^3)} \simeq 1.3308 \tag{B.12}$$

Substituting $\omega_{\mathrm{Max}} = (\gamma v_F^3)^{1/2}$, we obtain (2.65).

To obtain the frequency dependence of the fermionic density of states at small ω, we have to evaluate the second order term in ϵ_k at the mass shell, where $\epsilon_k = i\tilde{\Sigma}(\omega)$ and convert the result to real frequencies. We therefore will keep both ω and ϵ_k finite, and use

$$\Sigma(\mathbf{k}, \omega) = \frac{3i\bar{g}}{(2\pi)^3} \int d\Omega d^2q \frac{q}{\gamma|\Omega| + q^3} \frac{1}{i\tilde{\Sigma}(\omega+\Omega) - \epsilon_{k+q}}. \tag{B.13}$$

Writing, as before, $\epsilon_{k+q} = \epsilon_k + v_F q\cos\theta$ and integrating over θ, we obtain

$$\Sigma(\mathbf{k}, \omega) = \frac{3\bar{g}}{4\pi^2} \int \frac{d\Omega q^2 dq}{\gamma|\Omega| + q^3} \frac{\mathrm{sign}(\omega+\Omega)}{\sqrt{(\tilde{\Sigma}(\omega+\Omega) + i\epsilon_k)^2 + (v_F q)^2}}. \tag{B.14}$$

We assume and then verify that internal $v_F q$ are still larger than $\tilde{\Sigma}(\omega+\Omega)$ and ϵ_k, and expand

$$\Sigma(\mathbf{k},\omega) = -\frac{3\bar{g}}{8\pi^2 v_F^3}\int d\Omega\ \mathrm{Sign}(\omega+\Omega)\int \frac{dq}{q(\gamma|\Omega|+q^3)}\left(\tilde{\Sigma}(\omega+\Omega)+i\epsilon_k\right)^2 \quad \text{(B.15)}$$

The lower limit of the momentum integral is $(\tilde{\Sigma}(\omega+\Omega)+i\epsilon)k)/v_F$. At the mass shell, $i\epsilon_k = \tilde{\Sigma}(\omega)$. Substituting we find

$$\Sigma(\mathbf{k},\omega) = -\frac{3\bar{g}}{8\pi^2 v_F^3}\int d\Omega\ \mathrm{Sign}(\omega+\Omega)\int \frac{dq}{q(\gamma|\Omega|+q^3)}\left(\tilde{\Sigma}(\omega+\Omega)-\tilde{\Sigma}(\omega)\right)^2 \quad \text{(B.16)}$$

We will need the contributution which is confined to $\Omega\sim\omega$. The contributions from $|\Omega| >> |\omega|$ diverge in our expansion procedure, and account for the regular $O(\epsilon_k)$ term in the self-energy, and also for regular $O(\omega)$ term. The last term is even smaller in α than the regular (ϵ_k) term and is totally irrelevant. As $\Omega\sim\omega$ is small, $\tilde{\Sigma}(\Omega)\approx\Sigma(\Omega)=\Omega^{2/3}\omega_0^{1/3}$.

Because of sign factor in the numerator of (B.14), there are two distinct contributions from $\Omega\sim\omega$. For both of them, the momentum integral is logarithnic (this justifies the expansion) and yields $(1/3)\log(\omega_1/\omega)$, where $\omega_1\sim N^2E_F^2/\bar{g}$. The first contribution comes from $|\Omega|\le|\omega|$ and to logarithmical accuracy is

$$\Sigma(\mathbf{k},\omega)_A = -\frac{\bar{g}}{8\pi^2 v_F^3\gamma}\mathrm{sign}(\omega)\int_{-\omega}^{|\omega|}\frac{d\Omega}{|\Omega|}\left(\Sigma(|\omega|+\Omega)-\Sigma(|\omega|)\right)^2\ \log\frac{\omega_1}{|\omega|} \quad \text{(B.17)}$$

Rescaling the frequency, we obtain from (B.17)

$$\Sigma(\mathbf{k},\omega)_A = -\frac{\bar{g}I_1}{4\pi^2 v_F^3\gamma}\Sigma(\omega)|\Sigma(\omega)|\log\frac{\omega_1}{\omega}. \quad \text{(B.18)}$$

where

$$I_1 = \frac{1/2}{\int_{-1}}^{1}\frac{dx}{|x|}\left((1+x)^{3/2}-1\right)^2 = 0.254 \quad \text{(B.19)}$$

Another comes from $|\Omega|>|\omega|$, and is

$$\Sigma(\mathbf{k},\omega)_B = \frac{\bar{g}\Sigma(\omega)}{4\pi^2 v_F^3\gamma}\ \log\frac{\omega_1}{|\omega|}\int_{|\omega|}^{\infty}\frac{d\Omega}{\Omega}\left(\Sigma(|\omega|+\Omega)+\Sigma(\Omega-|\omega|-2\Sigma(\Omega))\right) \quad \text{(B.20)}$$

Rescaling, we obtain

$$\Sigma(\mathbf{k},\omega)_B = \frac{\bar{g}I_2}{4\pi^2 v_F^3\gamma}\Sigma(\omega)|\Sigma(\omega)|\log\frac{\omega_1}{\omega}. \quad \text{(B.21)}$$

where

$$I_2 = \int_1^\infty\frac{dx}{|x|}\left((1+x)^{2/3}+(x-1)^{2/3}-2x^{2/3}\right) = -0.195 \quad \text{(B.22)}$$

Combining $\Sigma(\mathbf{k},\omega)_A$ and $\Sigma(\mathbf{k},\omega)_B$, we obtain

$$\Sigma(\mathbf{k},\omega)_= - \frac{0.45\bar{g}}{4\pi^2 v_F^3 \gamma}\Sigma(\omega)|\Sigma(\omega)| \log\frac{\omega_1}{\omega}. \tag{B.23}$$

where

The neglected terms are either regular in ϵ_k or contain a simple $\log\epsilon_k$ additional contribution, which justifies that we only focus on the most divergent $\log^2\epsilon_k$ term.

B.2 Two-loop

We here compute one of the contributions to the two-loop self-energy, as given by fig. 2.1, which originates from the insertion of the vertex correction into the Eliashberg self-energy.

We have:

$$\begin{aligned}\Sigma_2(\omega) \sim \bar{g}^2 \int d\omega_1 d^2q_1 \int d\omega_2 d^2q_2 \; \chi(\mathbf{q_1},\omega_1)\; \chi(\mathbf{q_2},\omega_2)\; G(\mathbf{k_F}+\mathbf{q_1},\omega+\omega_1) \\ \times G(\mathbf{k_F}+\mathbf{q_2},\omega+\omega_2)\; G(\mathbf{k_F}+\mathbf{q_1}+\mathbf{q_2},\omega+\omega_1+\omega_2),\end{aligned} \tag{B.24}$$

which gives, once we replace each propagator by its full expression:

$$\begin{aligned}\Sigma_2(\omega) \;\sim\; & \bar{g}^2 \int d\omega_1 d^2q_1 \int d\omega_2 d^2q_2 \frac{q_1}{\gamma|\omega_1|+q_1^3}\frac{q_2}{\gamma|\omega_2|+q_2^3} \\ & \times \frac{1}{i\tilde{\Sigma}(\omega+\omega_1)-v_F q_{1x}} \frac{1}{i\tilde{\Sigma}(\omega+\omega_2)-v_F q_{2x}-\frac{q_{2y}^2}{2m_B}} \\ & \times \frac{1}{i\tilde{\Sigma}(\omega+\omega_1+\omega_2)-v_F q_{1x}-v_F q_{2x}-\frac{q_{1y}^2}{2m_B}-\frac{q_{2y}^2}{2m_B}},\end{aligned} \tag{B.25}$$

where we use the shorter notation $\tilde{\Sigma}(\omega)=\omega+\Sigma(\omega)$.

Integrating successively over q_{1x} and q_{2x}, closing each contour on the upper half-plane, one has:

$$\begin{aligned}\Sigma_2(\omega) \;\sim\; & \frac{m_B\bar{g}^2}{v_F^2}\int d\omega_1 \int d\omega_2 \; \Theta(\omega,\omega_1,\omega_2) \int dq_{1y}\frac{|q_{1y}|}{|q_{1y}|^3+\gamma|\omega_1|} \\ & \times \int dq_{2y}\frac{|q_{2y}|}{|q_{2y}|^3+\gamma|\omega_2|}\frac{1}{\left(\gamma^2\omega_1\omega_2\right)^{1/3}}\frac{1}{\frac{q_{1y}q_{2y}}{\left(\gamma^2\omega_1\omega_2\right)^{1/3}}+i\zeta}\end{aligned} \tag{B.26}$$

where $\zeta = m_B\dfrac{\tilde{\Sigma}(\omega+\omega_1)+\tilde{\Sigma}(\omega+\omega_2)-\tilde{\Sigma}(\omega+\omega_1+\omega_2)}{\left(\gamma^2\omega_1\omega_2\right)^{1/3}}$ and $\Theta(\omega,\omega_1,\omega_2)$ comes from the choice of a contour for the integration and is given in our case by:

$$\begin{aligned}\Theta(\omega,\omega_1,\omega_2) = & \left(\theta(\omega+\omega_1)-\theta(\omega+\omega_1+\omega_2)\right) \\ & \times\Big(\theta(\omega+\omega_2)-\theta(\tilde{\Sigma}(\omega+\omega_1+\omega_2)-\tilde{\Sigma}(\omega+\omega_1))\Big).\end{aligned} \tag{B.27}$$

It is convenient at this stage to rescale the perpendicular components of the bosonic momenta. Introducing $x = q_{1y}/(\gamma|\omega_1|)^{1/3}$ and $y = q_{2y}/(\gamma|\omega_2|)^{1/3}$, we obtain:

$$\Sigma_2(\omega) \sim \frac{m\bar{g}^2}{v_F^2} \int d\omega_2 \int d\omega_1 \int_0^\infty dxdy \; \frac{\Theta(\omega,\omega_1,\omega_2)}{(\gamma^2\omega_1\omega_2)^{2/3}} \times \frac{i\zeta}{x^2y^2+\zeta^2} \frac{xy}{(1+x^3)\,(1+y^3)}, \tag{B.28}$$

where we rearranged the double integral over x and y to make it real.

Since all internal frequencies typically go like ω, the typical value of ζ is given by the small parameter β given in (2.53). Expanding the double integral for small values of ζ, the leading contribution from the integral over x and y reads:

$$\int_0^\infty dxdy \; \frac{1}{x^2y^2+\zeta^2} \frac{xy}{(1+x^3)\,(1+y^3)} \sim \log^2\zeta. \tag{B.29}$$

If one considers now free fermions, it becomes possible to reduce the expression of the two-loop self-energy to:

$$\begin{aligned} \Sigma_2^{\rm free}(\omega) &\sim \frac{m_B^2\bar{g}^2}{v_F^2} \int_0^\omega d\omega_2 \int_{\omega-\omega_2}^\omega d\omega_1 \frac{\log^2\left(\frac{m_B\omega}{(\gamma^2\omega_1\omega_2)^{2/3}}\right)}{\gamma^2\omega_1\omega_2} \\ &\sim \frac{m_B^2\bar{g}^2}{\gamma v_F^2}\omega \int_0^1 dz_2 \int_{1-z_2}^1 dz_1 \frac{\log^2\left(\frac{m_B^3\omega}{\gamma z_1 z_2}\right)}{z_1 z_2} \\ &\sim \beta^2\omega\log^2\omega, \end{aligned} \tag{B.30}$$

where we only kept the leading contribution in the last expression, and $\beta = m_B/mN$ is one of the small parameters defined in the text.

Now, in the case of dressed fermions, we need to take $\tilde{\Sigma}(\omega) = \omega_0^{1/3}\omega^{2/3}$. The procedure is identical to the free fermion case, but the final expression is a bit more complicated:

$$\begin{aligned} \Sigma_2^{\rm Dressed}(\omega) &\sim \frac{m^2\bar{g}^2}{\gamma^2 v_F^2}\omega_0^{1/3}\omega^{2/3} \int_0^1 dz_2 \int_{1-z_2}^1 dz_1 \frac{1}{z_1 z_2} \\ &\quad \times \left[(1-z_1)^{2/3} + (1-z_2)^{2/3} + (z_1+z_2-1)^{2/3}\right] \\ &\quad \times \log^2\left(\frac{(1-z_1)^{2/3} + (1-z_2)^{2/3} + (z_1+z_2-1)^{2/3}}{\frac{\gamma^{2/3}}{m\omega_0^{1/3}} z_1^{1/3} z_2^{1/3}}\right). \end{aligned} \tag{B.31}$$

Expanding the $\log^2$, one is left with a double integral that only contributes as a numerical prefactor, and the dominant term is then given by:

$$\Sigma_2(\omega) \sim \Sigma_1(\omega)\; \beta^2\log^2\beta, \tag{B.32}$$

where $\Sigma_1(\omega) = \omega_0^{1/3}\omega^{2/3}$ is the self-energy in the Eliashberg theory.

B.3 Three loop

We now turn to the computation of the three-loop self energy. We are only interested here in one diagram, given in fig. 3.4, where we try to analyze the feedback of the non-analytic susceptibility into the the higher-order diagrams for the fermionic self-energy. For spin interaction, there is no cancellation between different diagrams for the static susceptibility, which justifies that we restrict ourselves to just one contribution.

The analytic expression for this diagram is:

$$\Sigma_3(\omega) \sim \bar{g} \int d\omega_1 d^2q_1 \frac{A(q_1,\omega_1)}{i\Sigma(\omega-\omega_1) - v_F q_{1x} - \frac{q_{1y}^2}{2m_B}} \left(\frac{1}{q_1^2 + \frac{\gamma|\omega_1|}{q_1}} \right)^2, \tag{B.33}$$

where $A(q_1,\omega_1)$ is the factor from the fermionic bubble:

$$\begin{aligned} A(q_1,\omega_1) &\sim N\bar{g}^2 \int d^2k d\Omega \int \frac{d^2q_2 d\omega_2}{q_2^2 + \frac{\gamma|\omega_2|}{q_2}} \frac{1}{i\Sigma(\Omega+\omega_1+\omega_2) - \epsilon_{k+q_1+q_2}} \\ &\times \frac{1}{i\Sigma(\Omega) - \epsilon_k} \frac{1}{i\Sigma(\Omega-\omega_1) - \epsilon_{k+q_1}} \frac{1}{i\Sigma(\Omega+\omega_2) - \epsilon_{k+q_2}}. \end{aligned} \tag{B.34}$$

Approximating $A(q_1,\omega_1)$ by its singular static part $q_1^{3/2}\sqrt{k_F}$ and substituting into the expression of Σ_3 we obtain:

$$\Sigma_3(\omega) \sim \bar{g}\sqrt{k_F} \int d\omega_1 d^2q_1 \left(\frac{q_1}{q_1^3 + \gamma|\omega_1|} \right)^2 \frac{q_1^{3/2}}{i\Sigma(\omega-\omega_1) - v_F q_{1x} - \frac{q_{1y}^2}{2m_B}}. \tag{B.35}$$

The integral over q_{1x} is determined by the branch-cut in the bosonic propagator and one then expects that this very integral is dominated by $q_{1x} \sim (\gamma\omega_1)^{1/3}$. It follows that the term in q_{1x} dominates inside the fermionic propagator allowing us to neglect the curvature term. Defining the angle θ between $\mathbf{k_F}$ and $\mathbf{q_1}$, and integrating over it, this leads to:

$$\Sigma_3(\omega) \sim \frac{\bar{g}\sqrt{k_F}}{v_F} \int \frac{d\omega_1 dq_1 \ \mathrm{sign}(\omega-\omega_1)}{\sqrt{q_1^2 + \frac{\Sigma(\omega-\omega_1)^2}{v_F^2}}} \frac{q_1^{9/2}}{(q_1^3 + \gamma|\omega_1|)^2}. \tag{B.36}$$

Since the dominant contribution comes from $q_1 \sim (\gamma\omega_1)^{1/3}$, one can neglect the fermionic self-energy in the denominator. This in turn allows to simplify the frequency integral, which then writes:

$$\begin{aligned} \Sigma_3(\omega) &\sim \frac{\bar{g}\sqrt{k_F}}{v_F} \int_0^\omega d\omega_1 \int dq_1 \frac{q_1^{7/2}}{(q_1^3 + \gamma\omega_1)^2} \\ &\sim \frac{\bar{g}\sqrt{k_F}}{\sqrt{\gamma} v_F} \int_0^\omega \frac{d\omega_1}{\sqrt{\omega_1}}, \end{aligned} \tag{B.37}$$

where we introduced $z = q_1/(\gamma\omega_1)^{1/3}$, so that the integral over z just contribute to the numerical prefactor.

Collecting prefactors, one finally has:

$$\Sigma_3(\omega) \sim \sqrt{\bar{g}\omega}. \tag{B.38}$$

APPENDIX C

Vertex corrections

In this section, we compute the various vertex corrections analyzed in the text.

C.1 $q = \Omega = 0$

Consider first the simplest 3-leg vertex, with strictly zero incoming frequency Ω and momenta q, as presented in fig. 2.2a. Its analytic expression writes:

$$\begin{aligned}\left.\frac{\Delta g}{g}\right|_{q=\Omega=0} &\sim g^2 \int d\omega d^2p \; G(\mathbf{k_F},\omega)^2 \; \chi(\mathbf{p},\omega) \\ &\sim \bar{g} \int \frac{d\omega d^2p}{\frac{\gamma|\omega|}{p}+p^2} \; \frac{1}{\left(i\tilde{\Sigma}(\omega) - v_F p_x - \frac{p_y^2}{2m_B}\right)^2},\end{aligned}$$

where we defined $\tilde{\Sigma}(\omega) = \omega + \Sigma(\omega)$ and we have chosen $\mathbf{k}_F$ along the x axis.

Since both poles coming from the fermionic Green's functions are in the same half plane, the integral over q_x is finite only because of the branch cut in the bosonic propagator. Since at the branch cut p_x and p_y are of the same order, we can drop the curvature term in the fermionic propagators and introduce polar coordinates for the internal bosonic momentum. Defining θ as the angle between $\mathbf{k_F}$ and $\mathbf{p}$, and integrating over it, one has:

$$\left.\frac{\Delta g}{g}\right|_{q=\Omega=0} \sim \bar{g} \int \frac{d\omega dp}{p^3+\gamma|\omega|} \frac{p^2|\tilde{\Sigma}(\omega)|}{\left((v_F p)^2 + \tilde{\Sigma}(\omega)^2\right)^{3/2}}. \tag{C.1}$$

Introducing the frequency $\omega_{\max}$ up to which bosons are slow modes compared to fermions, i.e. up to which $(\gamma\omega)^{1/3} > \tilde{\Sigma}(\omega)/v_F$, one can split the frequency integral into two parts, and define in each of them the reduced momentum $z = p/\mathrm{Min}((\gamma\omega)^{1/3}, \tilde{\Sigma}(\omega)/v_F)$ so that the integral over z only contributes to the numerical prefactor, leading to:

$$\left.\frac{\Delta g}{g}\right|_{q=\Omega=0} \sim \bar{g}\int_0^{\omega_{\max}} d\omega \frac{\tilde{\Sigma}(\omega)}{\gamma v_F^3 \omega} \sim \frac{\bar{g}}{\gamma v_F^3}\tilde{\Sigma}(\omega_{\max}) \tag{C.2}$$

One can easily make sure that the frequency $\omega_{\max}$ at which $(\gamma\omega)^{1/3} = \tilde{\Sigma}(\omega)/v_F$ exceeds ω_0, such that one should use $\tilde{\Sigma}(\omega) = \omega$ to find $\omega_{\max}$. Substituting, we obtain $\omega_{max} \sim (N\bar{g}E_F)^{1/2}$, and

$$\left.\frac{\Delta g}{g}\right|_{q=\Omega=0} \sim \sqrt{\alpha} \tag{C.3}$$

C.2 $q = 0$, Ω finite

Considering the same vertex, now with a finite external frequency, one has:

$$\begin{aligned}\left.\frac{\Delta g}{g}\right|_{q=0,\Omega} &\sim g^2 \int d\omega d^2p\; G(\mathbf{k_F}+\mathbf{p},\omega+\Omega)G(\mathbf{k_F}+\mathbf{p},\omega)\chi(\mathbf{p},\omega) \\ &\sim \bar{g}\int \frac{d\omega d^2p}{\frac{\gamma|\omega|}{p}+p^2}\,\frac{1}{i\tilde{\Sigma}(\omega)-v_F p_x-\frac{p_y^2}{2m_B}}\frac{1}{i\tilde{\Sigma}(\omega+\Omega)-v_F p_x-\frac{p_y^2}{2m_B}},\end{aligned} \tag{C.4}$$

where we chose the x axis along $\mathbf{k_F}$.

From the pole structure in p_x of this expression, one expects two contributions to this integral. A first term comes from the branch cut in the bosonic propagator, however this contribution ultimately leads to the same result as the $q = \Omega = 0$ vertex, up to small corrections from the finiteness of Ω. The second contribution arises from taking the poles in the fermionic propagators. At zero external frequency, these two poles were in the same half-plane of p_x, so we could close the integration contour over a different half-plane and only consider the contribution from the branch but in the bosonic propagator. At a finite Ω, there is a range where ω and $\omega + \Omega$ have different signs, and the two poles are in different half-planes of p_x. The result after integration reads:

$$\left.\frac{\Delta g}{g}\right|_{q=0,\Omega} \sim \frac{\bar{g}}{v_F}\int_0^{\Omega} d\omega \int dp_y \frac{|p_y|}{\gamma|\omega|+|p_y|^3}\frac{1}{\tilde{\Sigma}(\Omega-\omega)+\tilde{\Sigma}(\omega)}, \tag{C.5}$$

where we slightly rearranged the frequency integral.

Performing the integration over p_y, we are left with:

$$\begin{aligned}\left.\frac{\Delta g}{g}\right|_{q=0,\Omega} &\sim \frac{\bar{g}}{\gamma^{1/3} v_F}\int_0^{\Omega} d\omega \frac{\omega^{-1/3}}{\tilde{\Sigma}(\Omega-\omega)+\tilde{\Sigma}(\omega)} \\ &\sim \frac{\bar{g}}{(\omega_0 \gamma v_F^3)^{1/3}} \\ &\sim \text{Const.},\end{aligned} \tag{C.6}$$

where we assumed that Ω is small, i.e. $\tilde{\Sigma}(\Omega) = \omega_0^{1/3}\Omega^{2/3}$. This vertex thus reduces to a numerical constant, that does not contain any small parameter.

C.3 q finite, $\Omega = 0$

Conversely, the same vertex taken at finite external momentum q, but zero external frequency writes:

$$\begin{aligned}\left.\frac{\Delta g}{g}\right|_{q,\Omega=0} &\sim g^2 \int d\omega d^2p \; G(\mathbf{k_F}+\mathbf{p}+\mathbf{q},\omega) G(\mathbf{k_F}+\mathbf{p},\omega)\chi(\mathbf{p},\omega) \\ &\sim \bar{g}\int \frac{d\omega d^2p}{\frac{\gamma|\omega|}{p}+p^2}\; \frac{1}{i\tilde{\Sigma}(\omega) - v_F p_x - \frac{p_y^2}{2m_B}} \\ &\quad \times \frac{1}{i\tilde{\Sigma}(\omega) - v_F q_x - v_F p_x - \frac{p_y^2}{2m_B} - \frac{q_y p_y}{m_B}},\end{aligned} \tag{C.7}$$

where p_x is the projection of $\mathbf{p}$ along $\mathbf{k_F}$.

Like its $q = 0$ counterpart, this vertex is characterized by poles in p_x from the fermionic propagators lying in the same half-plane. The only nonzero contribution then comes from the branch cut in the bosonic propagator. At the branch cut, $p_x \sim p_y$ which allows us to neglect the quadratic curvature terms in the fermionic Green's functions.

This makes possible a direct integration over p_y. This integral can be separated from the rest of the expression, and reads:

$$\begin{aligned}\int dp_y \frac{p}{\gamma|\omega| + p^3} &= \frac{1}{|p_x|}\int_{-\infty}^{+\infty} dz \; \frac{\sqrt{1+z^2}}{(1+z^2)^{3/2} + \gamma\frac{|\omega|}{|p_x|^3}} \\ &= \frac{2p_x^2}{\gamma|\omega|}\int_0^{+\pi/2} du \; \frac{1}{\frac{|p_x|^3}{\gamma|\omega|} + (\cos u)^3},\end{aligned} \tag{C.8}$$

where we successively defined $z = p_y/|p_x|$ and $z = \tan u$.

This last integral can be approximated by its asymptotic form, namely:

$$\int \frac{dp_y\ p}{\gamma|\omega| + p^3} = \begin{cases} \frac{\pi}{|p_x|},\ \text{if } |p_x|^3 \gg \gamma\omega \\ \frac{4\pi}{3\sqrt{3}} \frac{1}{(\gamma|\omega|)^{1/3}} - \frac{1}{2}\frac{p_x^2}{\gamma|\omega|} \log \frac{p_x^2}{(\gamma|\omega|)^{2/3}} \\ \quad + \left(\log 2 - \frac{1}{2}\right) \frac{p_x^2}{\gamma|\omega|},\ \text{if } |p_x|^3 \ll \gamma\omega \end{cases} \tag{C.9}$$

The only non-vanishing contribution once we take the integral over p_x comes from the log term. After expanding in q_x, this contribution reads:

$$\left.\frac{\Delta g}{g}\right|_{q,\Omega=0} - \left.\frac{\Delta g}{g}\right|_{q=\Omega=0} \sim \frac{\bar{g} v_F}{\gamma} q_x \int \frac{d\omega}{|\omega|} \int dp_x \frac{p_x^2 \log p_x^2}{\left(i\tilde{\Sigma}(\omega) - v_F p_x\right)^3}. \tag{C.10}$$

Defining the scaled momentum $z = v_F p_x / \tilde{\Sigma}(\omega)$ and performing the integration over z, one obtains two terms, the dominant one being:

$$\left.\frac{\Delta g}{g}\right|_{q,\Omega=0} - \left.\frac{\Delta g}{g}\right|_{q=\Omega=0} \sim i \frac{\bar{g}}{\gamma v_F^2} q_x \int_{|v_F q_x|} \frac{d\omega}{\omega} \log[i\tilde{\Sigma}(\omega)], \tag{C.11}$$

where the frequency integral runs over $|\tilde{\Sigma}(\omega)| > |v_F q_x|$ since as we expanded in $v_F q_x$, we assumed that it was smaller than $|\tilde{\Sigma}(\omega)|$.

Performing the remaining integral, one finds:

$$\left.\frac{\Delta g}{g}\right|_{q,\Omega=0} - \left.\frac{\Delta g}{g}\right|_{q=\Omega=0} \sim \frac{q_x}{k_F} \log |q_x|. \tag{C.12}$$

C.4 q, Ω finite

Finally, we consider the general vertex where both external bosonic momentum and frequency are non-zero. In analytic form, this writes:

$$\begin{aligned} \left.\frac{\Delta g}{g}\right|_{q,\Omega} &\sim g^2 \int d\omega d^2p\ G(\mathbf{k_F} + \mathbf{p} + \mathbf{q}, \omega + \Omega) G(\mathbf{k_F} + \mathbf{p}, \omega) \chi(\mathbf{p}, \omega) \\ &\sim \bar{g} \int \frac{d\omega d^2p}{\frac{\gamma|\omega|}{p} + p^2} \frac{1}{i\tilde{\Sigma}(\omega) - v_F p_x - \frac{p_y^2}{2m_B}} \\ &\qquad \times \frac{1}{i\tilde{\Sigma}(\omega + \Omega) - v_F q_x - v_F p_x - \frac{p_y^2}{2m_B} - \frac{q_y p_y}{m_B}}, \end{aligned}$$

where p_x is defined as $p_x = \mathbf{p} \cdot \mathbf{k_F}$.

Integrating over p_x first, there are two contributions. One comes from the branch cut in the bosonic propagator, and gives similar results to the $(q = 0, \Omega = 0)$ and the (q finite, $\Omega = 0$) vertices up to small correction from the finiteness of the external

frequency. We neglect it here and focus on the other contribution which comes from the poles in the fermionic propagators:

$$\left.\frac{\Delta g}{g}\right|_{q,\Omega} \sim i\frac{\bar{g}}{v_F}\int_0^\Omega d\omega \int dp_y \frac{|p_y|}{\gamma|\omega|+|p_y|^3} \times \frac{1}{i\tilde{\Sigma}(\Omega-\omega)+i\tilde{\Sigma}(\omega)-v_F q_x-\frac{q_y p_y}{m_B}}, \tag{C.13}$$

where the simplification of the frequency integral comes from the poles in p_x.

This vertex correction strongly depends on the interplay between the external q_x, q_y and Ω, and is in particular quite sensitive to the momentum anisotropy. We now analyze the various possibilities.

For the generic case where $q_x \sim q_y$ (we use the notation q to designate them), one can neglect the quadratic term in the fermionic dispersion, allowing to perform the integration over p_y, leaving us with:

$$\left.\frac{\Delta g}{g}\right|_{q,\Omega} \sim i\frac{\bar{g}}{v_F\gamma^{1/3}}\int_0^\Omega \frac{d\omega\ \omega^{-1/3}}{i\tilde{\Sigma}(\Omega-\omega)+i\tilde{\Sigma}(\omega)-v_F q}. \tag{C.14}$$

Restricting ourselves to the quantum-critical regime (i.e. $\Omega \leq \omega_0$) for which $\tilde{\Sigma}(\omega) = \omega_0^{1/3}\omega^{2/3}$, one has:

$$\left.\frac{\Delta g}{g}\right|_{q,\Omega} = \mathcal{F}\left(\frac{v_F q}{\Sigma(\Omega)}\right), \tag{C.15}$$

where $\mathcal{F}(x) = \int_0^1 \frac{dz}{z^{1/3}}\frac{1}{(1-z)^{2/3}+z^{2/3}+ix}$, has the following asymptotic behavior:

$$\begin{cases} \mathcal{F}(x \ll 1) &= O(1) \\ \mathcal{F}(x \gg 1) &= O\left(\frac{1}{x}\right) \end{cases} \tag{C.16}$$

If the typical q is on the bosonic mass shell, then $q \sim (\gamma\Omega)^{1/3}$, and one has:

$$\left.\frac{\Delta g}{g}\right|_{q,\Omega} \sim \frac{\Sigma(\Omega)}{v_F q} \sim \sqrt{\alpha}\ \left(\frac{\Omega}{\omega_{\max}}\right)^{1/3}. \tag{C.17}$$

However, we encountered in previous computations (e.g. self-energies) that a strong anisotropy can be observed between the components of the bosonic momentum, with $q_y \gg q_x$. In this case, the full expression of the vertex correction is a bit complicated and we choose to present here the most relevant case for which the curvature term dominates over $v_F q_x$ in the fermionic propagator. The vertex correction then no longer depends on q_x and writes:

$$\left.\frac{\Delta g}{g}\right|_{q,\Omega} \sim \frac{\bar{g}}{v_F}\int_0^\Omega d\omega \int_0^\infty dp_y \frac{p_y}{\gamma\omega+p_y^3}\frac{\tilde{\Sigma}(\Omega-\omega)+\tilde{\Sigma}(\omega)}{\left(\tilde{\Sigma}(\Omega-\omega)+\tilde{\Sigma}(\omega)\right)^2+\left(\frac{q_y p_y}{m_B}\right)^2}, \tag{C.18}$$

Defining $u = p_y/(\gamma\omega)^{1/3}$ and $z = \omega/\Omega$, it is possible to rewrite the vertex correction in this regime as:

$$\left.\frac{\Delta g}{g}\right|_{q,\Omega} \sim \mathcal{G}\left(\beta\frac{(\gamma\Omega)^{1/3}}{q_y}\right) \tag{C.19}$$

where $\beta = \frac{m_B}{Nm}$ and $\mathcal{G}(x)$ is the following double integral:

$$\begin{aligned}\mathcal{G}(x) &= \int_0^\infty \frac{du\ u}{1+u^3}\int_0^1 \frac{dz\ z^{-1/3}\ \left((1-z)^{2/3}+z^{2/3}\right)}{\left((1-z)^{2/3}+z^{2/3}\right)^2+\frac{u^2z^{2/3}}{x^2}} \\ &\sim x^2\log^2 x \qquad \text{if } x \ll 1.\end{aligned} \tag{C.20}$$

Finally, for the computations of the full dynamic polarization bubble will also need the vertex averaged over the directions of q. The generic structure of this vertex, which we define as $< \Delta g/g >$ is the same as in (C.15), i.e.,

$$\begin{aligned}&\langle\frac{\Delta g}{g}\rangle\Big|_{\mathrm{q},\Omega}\tilde{\mathcal{F}}\left(\frac{v_F q}{\tilde{\Sigma}(\Omega)}\right), \\ &\tilde{\mathcal{F}}(0) = O(1), \quad \tilde{\mathcal{F}}(x >> 1)O\left(\frac{1}{x}\right)\end{aligned} \tag{C.21}$$

However, it will be essential for our further analysis that the expansion of $\tilde{\mathcal{F}}(x)$ at large x holds in odd powers of $1/x$, i.e., $\tilde{\mathcal{F}}(x >> 1) = a_1/x + a_3/x^3 + ...$ In particular, there is no term $O(1/x^2)$, which we found in the polarization operator without vertex corrections (see (A.7)).

C.5 4-leg vertex

In this paragraph, we compute the renormalized 4-leg vertex $\Gamma_2(q,\Omega)$ presented in Fig 2.3, which reads:

$$\begin{aligned}\Gamma_2(q,\Omega) \sim \bar{g}^2\int d\omega\ \int d^2p\ \chi_s\left(\frac{\Omega+\omega}{2},\frac{\mathbf{p}+\mathbf{q}}{2}\right)\ \chi_s\left(\frac{\Omega-\omega}{2},\frac{\mathbf{q}-\mathbf{p}}{2}\right) \\ \times G\left(\frac{\Omega+\omega}{2},\mathbf{k_F}+\frac{\mathbf{p}+\mathbf{q}}{2}\right)\ G\left(\frac{\Omega-\omega}{2},\mathbf{k_F}+\frac{\mathbf{q}-\mathbf{p}}{2}\right).\end{aligned} \tag{C.22}$$

Performing the integration over p_x, projection of $\mathbf{p}$ along $\mathbf{k_F}$, we obtain:

$$\begin{aligned}\Gamma_2(q,\Omega) &\sim \frac{\bar{g}^2}{v_F}\int_0^\Omega \frac{d\omega\ dp_y}{\gamma(\Omega-\omega)+(q^2+p_y^2-2q_yp_y)^{3/2}} \\ &\times\frac{1}{i\tilde{\Sigma}\left(\frac{\Omega+\omega}{2}\right)+i\tilde{\Sigma}\left(\frac{\Omega-\omega}{2}\right)-v_Fq_x-\frac{q_y^2+p_y^2}{4m_B}} \\ &\times\frac{\sqrt{(q^2+p_y^2)^2-4q_y^2p_y^2}}{\gamma(\Omega+\omega)+(q^2+p_y^2+2q_yp_y)^{3/2}}.\end{aligned} \tag{C.23}$$

It is convenient at this stage to define the reduced variables $z = \omega/\Omega$ and $y = p_y/|q_y|$:

$$\begin{aligned}\Gamma_2(q,\Omega) &\sim \bar{g}\frac{(\gamma\Omega)^{1/3}}{|q_y|^3}\int_0^1 \frac{dz\ dy}{\frac{\gamma\Omega}{|q_y|^3}(1-z)+|1-y|^3}\frac{|1-y^2|}{\frac{\gamma\Omega}{|q_y|^3}(1+z)+|1+y|^3} \\ &\times\frac{1}{i\left[(1-z)^{2/3}+(1+z)^{2/3}\right]-\frac{v_F q_x}{\Sigma(\Omega)}-\frac{1+y^2}{\beta}\left(\frac{|q_y|^3}{\gamma\Omega}\right)^{2/3}}\end{aligned} \tag{C.24}$$

where we assumed that $\Omega \leq \omega_0$, and we used that in all our computations, the perpendicular component of the bosonic momentum is always either dominant or comparable to the parallel one, so that one has $q_y \sim q$.

Comparing this renormalized vertex with the bare one given by $\Gamma_1(q,\Omega) \sim \frac{\bar{g}q_y^{-2}}{1+\frac{\gamma|\Omega|}{|q_y|^3}}$, one has for the ratio of the two:

$$\begin{aligned}\frac{\Gamma_2}{\Gamma_1} &\sim \frac{(\gamma\Omega)^{1/3}}{|q_y|}\int_0^1 \frac{dz\ dy}{\frac{\gamma\Omega}{|q_y|^3}(1-z)+|1-y|^3}\frac{|1-y^2|}{\frac{\gamma\Omega}{|q_y|^3}(1+z)+|1+y|^3} \\ &\times\frac{1}{i\left[(1-z)^{2/3}+(1+z)^{2/3}\right]-\frac{v_F q_x}{\Sigma(\Omega)}-\frac{1+y^2}{\beta}\frac{|q_y|^2}{(\gamma\Omega)^{2/3}}}\end{aligned} \tag{C.25}$$

which only depends on two parameters: the ratios $\frac{v_F q_x}{\Sigma(\Omega)}$ and $\frac{|q_y|^3}{\gamma\Omega}$.

In the generic case of an external bosonic momentum on the mass shell, i.e. $q_x \sim q_y \sim (\gamma\Omega)^{1/3}$ one has:

$$\frac{\Gamma_2}{\Gamma_1} \sim \frac{\Sigma(\Omega)}{v_F q_x} \sim \sqrt{\alpha}\left(\frac{\Omega}{\omega_{\max}}\right)^{1/3}. \tag{C.26}$$

On the contrary, for a typical $q_x \sim \Sigma(\Omega)/v_F$ and $q_y \sim (\gamma\Omega)^{1/3}$:

$$\frac{\Gamma_2}{\Gamma_1} \sim \beta, \tag{C.27}$$

up to logarithmic factors.

APPENDIX D

Static spin susceptibility

D.1 Diagrams

In this Appendix we present the details of our calculations of the singular terms in the static spin susceptibility. We discuss in great detail the calculation of the first two diagrams in Fig. 3.2 (vertex and self-energy correction diagrams). These two diagrams can be computed explicitly both away from QCP and at QCP. We labeled the total contribution from these two diagrams as $\Pi_A(q,0)$. The remaining two diagrams (their total contribution is $\Pi_B(q,0)$) cannot be computed explicitly at QCP, and we compute them in an approximate scheme.

In explicit form, the first two diagrams in Fig. 3.2 are given by:

$$\Pi_{1a}(q,0) = \Gamma_a \frac{\bar{g}^2}{(2\pi)^6} \int d^2K d\omega d^2l d\Omega \; G(\omega,k)^2 \times \; G(\omega+\Omega,k+l)G(\omega,k+q)\chi_s(l,\Omega) \tag{D.1}$$

$$\Pi_{1b}(q,0) = \Gamma_b \frac{\bar{g}^2}{(2\pi)^6} \int d^2K d\omega d^2l d\Omega \; \chi_s(l,\Omega)G(\omega,k)G(\omega,k+q) \times G(\omega+\Omega,k+l)G(\omega+\Omega,k+q+l) \tag{D.2}$$

where $\Gamma_{a,b}$ are numerical prefactors coming from spin summation. Note that for symmetry reasons, one has to count the first diagram twice, so that the total contribution reads:

$$\Pi_A(q,0) = 2\Pi_{1a}(q,0) + \Pi_{1b}(q,0). \tag{D.3}$$

D.1.1 First diagram

To prove our point, we try to expand the products of fermionic Green's functions into a simpler form:

$$G(\omega,k)^2G(\omega+\Omega,k+l)G(\omega,k+q) = \frac{G(\omega,k)^2G(\omega,k+q)}{\kappa(l,\omega,\Omega)} - \frac{G(\omega,k)G(\omega,k+q)}{\kappa(l,\omega,\Omega)^2} + \frac{G(\omega+\Omega,k+l)G(\omega,k+q)}{\kappa(l,\omega,\Omega)^2}, \quad \text{(D.4)}$$

where $\kappa(l,\omega,\Omega)i(\Sigma(\omega+\Omega)-\Sigma(\omega))-v_Fl_x$

The interest of such a splitting up is that one can reduce this drastically by performing the integration over k. In fact:

$$\int d\varepsilon_k G(\omega,k)G(\omega,k+q) = 0, \quad \text{(D.5)}$$

since all the poles in ε_k are in the same half-plane.

For this reason, we are left with:

$$\Pi_{1a}(q,0) = 2\Gamma_a\frac{\bar{g}^2}{(2\pi)^6}\int d^2Kd\omega d^2ld\Omega\ \chi_s(l,\Omega)\frac{G(\omega+\Omega,k+l)G(\omega,k+q)}{\kappa(l,\omega,\Omega)^2}. \quad \text{(D.6)}$$

Let's keep this expression as it is for the moment and move on to the second diagram.

D.1.2 Second diagram

Following the same path, we can rewrite the product of fermionic Green's functions as:

$$\begin{aligned} G(\omega,k)G(\omega+\Omega,k+l)G(\omega+\Omega,k+l+q)G(\omega,k+q) = \\ \frac{G(\omega,k)G(\omega,k+q)-G(\omega,k)G(\omega+\Omega,k+l+q)}{\kappa(l,\omega,\Omega)^2} \\ + \frac{G(\omega+\Omega,k+l)G(\omega+\Omega,k+l+q)}{\kappa(l,\omega,\Omega)^2} \\ - \frac{G(\omega+\Omega,k+l)G(\omega,k+q)}{\kappa(l,\omega,\Omega)^2}, \end{aligned} \quad \text{(D.7)}$$

with the expression of κ defined above.

Once again, the integration over ε_k may give zero if the poles are in the same

half-plane, which reduces our previous expression to:

$$\Pi_{1b}(q,0) = -\Gamma_b \frac{\bar{g}^2}{(2\pi)^6} \int d^2K d\omega d^2l d\Omega \ \chi_s(l,\Omega) \times \left(\frac{G(\omega+\Omega,k+l)G(\omega,k+q)}{\kappa(l,\omega,\Omega)^2} + \frac{G(\omega,k)G(\omega+\Omega,k+l+q)}{\kappa(l,\omega,\Omega)^2} \right). \quad \text{(D.8)}$$

Changing k into $k-q$ in the second part of the integral, we have:

$$\Pi_{1b}(q,0) = -\Gamma_b \frac{\bar{g}^2}{(2\pi)^6} \int d^2K d\omega d^2l d\Omega \ \chi_s(l,\Omega) \times \left(\frac{G(\omega+\Omega,k+l)G(\omega,k+q)}{\kappa(l,\omega,\Omega)^2} + \frac{G(\omega,k-q)G(\omega+\Omega,k+l)}{\kappa(l,\omega,\Omega)^2} \right). \quad \text{(D.9)}$$

One can then notice that $\varepsilon_{k-q} = \varepsilon_k - v_F q \cos\theta$ changes to ε_{k+q} if one changes θ into $\theta - \pi$. This finally leads to:

$$\Pi_{1b}(q,0) = -2\Gamma_b \frac{\bar{g}^2}{(2\pi)^6} \int d^2K d\omega d^2l d\Omega \ \chi_s(l,\Omega) \frac{G(\omega+\Omega,k+l)G(\omega,k+q)}{\kappa(l,\omega,\Omega)^2}. \quad \text{(D.10)}$$

From what precedes, we have:

$$\Pi_A(q,0) = 2\left(1 - \frac{\Gamma_b}{\Gamma_a}\right) \Pi_{1a}(q,0). \quad \text{(D.11)}$$

Spin summation prefactors can be easily computed, and are given by:

$$\left\{ \begin{array}{rcl} \Gamma_a &=& \sum_{\alpha,\beta,\gamma,\delta} \sigma^Z_{\alpha\beta} \boldsymbol{\sigma}_{\beta\gamma} \cdot \boldsymbol{\sigma}_{\gamma\delta} \sigma^Z_{\delta\alpha} \\ \Gamma_b &=& \sum_{\alpha,\beta,\gamma,\delta} \sigma^Z_{\alpha\beta} \boldsymbol{\sigma}_{\beta\gamma} \sigma^Z_{\gamma\delta} \boldsymbol{\sigma}_{\delta\alpha} \end{array} \right. \begin{array}{c} = \\ = \end{array} \begin{array}{c} 6 \\ -2 \end{array}$$

This finally leads to:

$$\Pi_A(q,0) = \frac{8}{3} \Pi_{1a}(q,0). \quad \text{(D.12)}$$

D.2 Away from the QCP

In the Fermi-liquid regime we have

$$\begin{aligned} \Pi_A(q,0) &= \frac{16N\bar{g}^2}{(2\pi)^6} \int d^2K d\omega d^2l d\Omega \ \frac{1}{(i(1+\lambda)\omega - \epsilon_k)^2} \frac{1}{\xi^{-2} + l^2 + \gamma\frac{|\Omega|}{l}} \\ &\times \frac{1}{i(1+\lambda)(\omega+\Omega) - \epsilon_{k+l}} \ \frac{1}{i(1+\lambda)\omega - \epsilon_{k+q}} \end{aligned} \quad \text{(D.13)}$$

where we used for the fermionic self-energy $\Sigma(\omega) = \lambda\omega$, since we are deep in the Fermi liquid phase in this case.

Defining $\cos\theta = \frac{\mathbf{k}\cdot\mathbf{l}}{|\mathbf{k}||\mathbf{l}|}$ and $\cos\theta' = \frac{\mathbf{k}\cdot\mathbf{q}}{|\mathbf{k}||\mathbf{q}|}$, and integrating over k and ω, one has:

$$\begin{aligned}\Pi_A(q,0) &= i\frac{16Nm\bar{g}^2}{(2\pi)^5}\int_0^{2\pi}d\theta\int_0^{2\pi}d\theta'\int_{-\infty}^{+\infty}d\Omega\int_0^{\infty}\frac{dl\ l}{\xi^{-2}+l^2+\frac{\gamma|\Omega|}{l}} \\ &\times\frac{\Omega}{\left(i(1+\lambda)\Omega - v_F l\cos\theta\right)^2}\ \frac{1}{i(1+\lambda)\Omega - v_F q\cos\theta' - v_F l\cos\theta}. \quad \text{(D.14)}\end{aligned}$$

The integral over θ' then gives:

$$\begin{aligned}\Pi_A(q,0) &= -\frac{4Nm\bar{g}^2}{\pi^4}\int_0^{\pi}d\theta\int_0^{\infty}d\Omega\int_0^{\infty}dl\ \frac{l}{\xi^{-2}+l^2+\frac{\gamma\Omega}{l}} \\ &\frac{\Omega}{\left((1+\lambda)\Omega + iv_F l\cos\theta\right)^2}\ \frac{1}{\sqrt{(v_F q)^2+\left(\Omega(1+\lambda)+iv_F l\cos\theta\right)^2}}. \quad \text{(D.15)}\end{aligned}$$

It is convenient to rescale the variables at this stage, introducing $\Omega' = \frac{(1+\lambda)\Omega}{v_F q}$ and $l' = \frac{l}{q}$, so that the previous expression reduces to:

$$\begin{aligned}\Pi_A(q,0) &= -\frac{4Nm\bar{g}^2}{\pi^4 v_F(1+\lambda)^2}|q|\int_0^{\pi}d\theta\int_0^{+\infty}d\Omega'\int_0^{\infty}dl'\ \frac{l}{\xi^{-2}+\frac{\gamma v_F}{1+\lambda}\frac{\Omega'}{l'}} \\ &\times\ \frac{\Omega'}{\left(\Omega'+il'\cos\theta\right)^2}\ \frac{1}{\sqrt{1+\left(\Omega'+il'\cos\theta\right)^2}}, \quad \text{(D.16)}\end{aligned}$$

where we kept only the leading order in q.

Defining z and ϕ as $z\cos\phi = l'$ and $z\sin\phi = \Omega'$, one is left with:

$$\begin{aligned}\Pi_A(q,0) &= -\frac{4Nm\bar{g}^2}{\pi^4 v_F(1+\lambda)^2}|q|\int_0^{\pi}d\theta\int_0^{\infty}dz\int_0^{\pi/2}d\phi\ \frac{\cos\phi}{\xi^{-2}+\frac{\gamma v_F}{1+\lambda}\tan\phi} \\ &\times\frac{z\sin\phi}{\left(\sin\phi+i\cos\phi\cos\theta\right)^2}\ \frac{1}{\sqrt{1+z^2\left(\sin\phi+i\cos\phi\cos\theta\right)^2}}. \quad \text{(D.17)}\end{aligned}$$

Subtracting the constant part $\Pi_A(0,0)$ (and neglecting it), and integrating over z, this leads to:

$$\Pi_A(q,0) = \frac{4Nm\bar{g}^2}{\pi^4 v_F(1+\lambda)^2}|q|\int_0^{\pi/2}\frac{d\phi\ \cos\phi\sin\phi}{\xi^{-2}+\frac{\gamma v_F}{1+\lambda}\tan\phi}\int_0^{\pi}\frac{d\theta}{\left(\sin\phi+i\cos\phi\cos\theta\right)^4}. \quad \text{(D.18)}$$

The angular integration over θ can be done explicitly and gives:

$$\int_0^{\pi}\frac{d\theta}{\left(\sin\phi+i\cos\phi\cos\theta\right)^4} = \frac{\pi}{2}\sin\phi(5\sin^2\phi-3). \quad \text{(D.19)}$$

Substituting this into the expression of $\delta\Pi_A$, we are left with the following final result:

$$\Pi_A(q,0) = -\frac{2\bar{g}}{\pi^2 v_F(1+\lambda)}\ |q|\ \mathcal{H}\left(\frac{1+\lambda}{\gamma v_F \xi^2}\right), \tag{D.20}$$

where $\mathcal{H}$ is defined as:

$$\mathcal{H}(x) = \int_0^{\pi/2} d\phi \frac{\cos\phi \sin^2\phi(3-5\sin^2\phi)}{\tan\phi + x}. \tag{D.21}$$

In the two limits,

$$\mathcal{H}(0) = \frac{1}{3}, \quad \mathcal{H}(x \gg 1) \approx \frac{2}{3x^2} \tag{D.22}$$

As one approaches the QCP, ξ gets bigger, and one can take the asymptotic form of $\mathcal{H}(x)$ for small x: $\mathcal{H}(0) = 1/3$. Rearranging the prefactor for this limit, we are left with:

$$\Pi_A(q,0) \underset{\xi\to\infty}{=} -\frac{8}{9\pi}\xi^{-1}\ |q|. \tag{D.23}$$

D.3 At criticality

At the QCP, we have:

$$\begin{aligned}\Pi_A(q,0) &= \frac{16N\bar{g}^2}{(2\pi)^6}\int d^2K d\omega d^2l d\Omega\ \frac{1}{l^2+\gamma\frac{|\Omega|}{l}}\ \frac{1}{(i\Sigma(\omega)-\epsilon_k)^2} \\ &\times \frac{1}{i\Sigma(\omega+\Omega)-\epsilon_{k+l}}\ \frac{1}{i\Sigma(\omega)-\epsilon_{k+q}}\end{aligned} \tag{D.24}$$

where we considered that, close to criticality, the self-energy dominates completely the bare ω term in the fermionic propagators.

We expand both energies as $\epsilon_{k+l} = \epsilon_k + v_F l_x + \frac{l_y^2}{2m_B}$ and $\epsilon_{k+q} = \epsilon_k + v_F q\cos\theta$, and perform the integration over ϵ_k, leading to:

$$\begin{aligned}\Pi_A(q,0) = i\frac{16Nm\bar{g}^2}{(2\pi)^5}\int_0^{2\pi} d\theta \int_{-\infty}^{+\infty} dl_x \int_{-\infty}^{+\infty} d\Omega \int_0^{\Omega} d\omega \\ \int_{-\infty}^{\infty} \frac{dl_y\ l}{\gamma|\Omega|+l^3} \frac{1}{\left(i\Sigma(\Omega-\omega)+i\Sigma(\omega)-v_F l_x - \frac{l_y^2}{2m_B}\right)^2} \\ \times\ \frac{1}{i\Sigma(\Omega-\omega)+i\Sigma(\omega)+v_F q\cos\theta - v_F l_x - \frac{l_y^2}{2m_B}}.\end{aligned} \tag{D.25}$$

The integration over l_x brings two contributions. One comes from the poles in the fermionic propagator, and can be neglected here since both poles are in the same half-plane. The other contribution comes from the branch cut in the bosonic

propagator, and since at the branch cut $q_x \sim q_y$, one can safely drop the quadratic term in the fermionic propagators. This allows us to integrate over l_y. Out of the terms arising from this integral, the only non-vanishing ones come from the non-analyticities of the integrated bosonic propagator defined as:

$$\int dl_y \chi(\mathbf{l}, \Omega) = \int dl_y \frac{1}{l^2 + \frac{\gamma v_F |\Omega|}{\sqrt{(v_F l)^2 + c^2 \Sigma(\Omega)^2}}}, \tag{D.26}$$

We use here the full form of the polarization operator, Eq. (A.8) as we will see that typical $v_F l_x \geq \Sigma(\Omega)$, and typical l_y are only larger in logarithmic sense.

This integral was performed in a slightly different form in (C.9), but the method is the same: introducing u such that $\tan u = \frac{v_F l_y}{\sqrt{(v_F l_x)^2 + \Sigma(\Omega)^2}}$, one has:

$$\int dl_y \chi(\mathbf{l}, \Omega) = \frac{(v_F l_x)^2 + c^2 \Sigma(\Omega)^2}{\gamma v_F^2 |\Omega|} \int_0^{\pi/2} \frac{du}{\cos^3 u - \delta \ \cos^2 u + \epsilon}, \tag{D.27}$$

where we introduced $\delta = \frac{c^2 \Sigma(\Omega)^2 ((v_F l_x)^2 + c^2 \Sigma(\Omega)^2)^{1/2}}{\gamma v_F^3 |\Omega|}$ and $\epsilon = \frac{((v_F l_x)^2 + c^2 \Sigma(\Omega)^2)^{3/2}}{\gamma v_F^3 |\Omega|}$.

In the process of integrating over l_x, two non-analytic contributions arise from (D.27). One comes from $l_x \gtrsim (\gamma \Omega)^{1/3}$ and goes like $\frac{\pi}{(\gamma |\Omega|)^{1/3}}$, Plugging this back into Π_A and subtracting (and neglecting) a constant term, we obtain

$$\Pi_A^{(1)}(q, 0) N \sim m \bar{g}^2 v_F^2 q^2 \int_{-\infty}^{+\infty} \frac{dl_x}{|l_x|} \int_{-\infty}^{+\infty} d\Omega \int_0^{\Omega} \frac{d\omega}{\left(i\Sigma(\Omega - \omega) + i\Sigma(\omega) - v_F l_x\right)^5}$$

where we subtracted $\Pi_A(0, 0)$ (hence the notation $\delta\Pi_A$) and expanded in q.

We further simplify the integrals, noticing that the fermionic propagator is dominated by $v_F l_x$ since $l_x \sim (\gamma \Omega^{1/3})$:

$$\begin{aligned} \Pi_A^{(1)}(q, 0) &\sim q^2 \frac{N m \bar{g}^2}{v_F^3} \int_0^{\omega_{\max}} d\Omega \int dl_x \frac{\Omega}{l_x^6} \\ &\sim q^2 \frac{N m \bar{g}^2}{v_F^3 \gamma^{5/3}} \int_0^{\omega_{\max}} \frac{d\Omega}{\Omega^{2/3}} \\ &\sim \sqrt{\alpha} q^2, \end{aligned} \tag{D.28}$$

where we substituted $l_x \sim (\gamma \Omega^{1/3})$ in the last steps.

The other non-analytic contribution from (D.27) comes from typical $v_F l_x \sim \Sigma(\Omega)$. It can be seen from an expansion of (D.27) for small values of both δ and ϵ, and goes like:

$$-\frac{(v_F l_x)^2 + c^2 \Sigma(\Omega)^2}{2 v_F^2 \gamma |\Omega|} \log\left((v_F l_x)^2 + c^2 \Sigma(\Omega)^2\right).) \tag{D.29}$$

One can explicitly verify that to get the logarithm, we only need the polarization operator $\Pi(l, \Omega)$ to order $1/l^3$. Like we said in Appendix C, to this order, polarization

bubble can be evaluated with the full fermionic Green's functions but without vertex corrections.

Substituting (D.29) into the expression for Π_A and subtracting a constant part, we obtain:

$$\begin{aligned}\Pi_A^{(2)}(q,0) = i\frac{8Nm\bar{g}^2}{(2\pi)^5\gamma v_F}q\int_0^{2\pi}d\theta\int_{-\infty}^{+\infty}dl_x\int_{-\infty}^{+\infty}\frac{d\Omega}{|\Omega|}\\ \int_0^{\Omega}d\omega\frac{\cos\theta\left[(v_Fl_x)^2+c^2\Sigma(\Omega)^2\right]}{\left(i\Sigma(\Omega-\omega)+i\Sigma(\omega)-v_Fl_x\right)^3}\\ \times\ \frac{\log\left((v_Fl_x)^2+c^2\Sigma(\Omega)^2\right)}{i\Sigma(\Omega-\omega)+i\Sigma(\omega)+v_Fq\cos\theta-v_Fl_x}.\end{aligned} \tag{D.30}$$

Using the $\theta\longleftrightarrow-\theta$ symmetry, and splitting the integral over Ω into two parts, one can rearrange this expression as:

$$\begin{aligned}\Pi_A^{(2)}(q,0) &= i\frac{Nm\bar{g}^2}{c\pi^5\gamma v_F^2}q\int_0^{\pi}d\theta\int_{-\infty}^{+\infty}dz\int_0^{+\infty}\frac{d\Omega}{\Omega}\int_0^{\Omega}d\omega\frac{1}{\Sigma(\Omega)}\\ &\times\frac{\cos\theta(1+z^2)}{\left(i\frac{\Sigma(\Omega-\omega)+\Sigma(\omega)}{c\Sigma(\Omega)}-z\right)^3}\ \frac{\log\left(1+z^2\right)}{i\frac{\Sigma(\Omega-\omega)+\Sigma(\omega)}{c\Sigma(\Omega)}+\frac{v_Fq\cos\theta}{c\Sigma(\Omega)}-z},\end{aligned} \tag{D.31}$$

where we defined $z=v_Fl_x/(c\Sigma(\Omega))$.

Let's now isolate the integral over z, given by:

$$J=\int_{-\infty}^{+\infty}dz\frac{(1+z^2)\log(1+z^2)}{(ia-z)^3(ia+b-z)}, \tag{D.32}$$

where $a=\frac{\Sigma(\Omega-\omega)+\Sigma(\omega)}{c\Sigma(\Omega)}$ and $b=\frac{v_Fq\cos\theta}{c\Sigma(\Omega)}$, and $a\geq 0$.

Performing the contour integration in the lower half-plane (where lies the branch-cut), one gets:

$$\begin{aligned}J &= -2\pi\int_1^{\infty}dy\frac{1-y^2}{(y+a)^3(y+a-ib)}\\ &= -2\pi\int_1^{\infty}dy\frac{(1-y^2)(y+a+ib)}{(y+a)^3\left((y+a)^2+b^2\right)}.\end{aligned} \tag{D.33}$$

Once (D.33) is plugged back into (D.31), only the imaginary term survives due to the symmetry of the integral in θ. We are left with:

$$\begin{aligned}\Pi_A^{(2)}(q,0) = \frac{4Nm\bar{g}^2}{c^2\pi^4\gamma v_F}q^2\int_0^{\pi/2}d\theta\int_1^{+\infty}dy\int_0^{+\infty}d\Omega\\ \int_0^1dw\frac{1}{\Sigma(\Omega)^2}\frac{\cos^2\theta}{\left[c^{-1}\left((1-w)^{2/3}+w^{2/3}\right)+y\right]^3}\\ \times\ \frac{1-y^2}{\left[y+c^{-1}\left((1-w)^{2/3}+w^{2/3}\right)\right]^2+\left(\frac{v_Fq\cos\theta}{c\Sigma(\Omega)}\right)^2},\end{aligned} \tag{D.34}$$

where we changed variables, defining $w = \omega/\Omega$.

Introducing the new variable $t = \left(\frac{c\Sigma(\Omega)}{v_F q \cos\theta}\right)^{3/2}$, this rewrites:

$$\begin{aligned}\Pi_A^{(2)}(q,0) = & \frac{4Nm\bar{g}^2}{c^{3/2}\pi^4\gamma v_F^{3/2}\omega_0^{1/2}} q^{3/2} \int_0^{\pi/2} d\theta \ (\cos\theta)^{3/2} \\ & \times \int_1^{+\infty} dy \int_0^1 dw \frac{1}{\left[c^{-1}\left((1-w)^{2/3}+w^{2/3}\right)+y\right]^3} \\ & \times \int_0^{+\infty} dt \frac{1-y^2}{1+t^{4/3}\left[y+c^{-1}\left((1-w)^{2/3}+w^{2/3}\right)\right]^2}. \end{aligned} \tag{D.35}$$

A final change in variables leads to:

$$\begin{aligned}\Pi_A^{(2)}(q,0) &= \frac{4Nm\bar{g}^2}{c^{3/2}\pi^4\gamma v_F^{3/2}\omega_0^{1/2}} q^{3/2} \int_0^{\pi/2} d\theta \ (\cos\theta)^{3/2} \int_0^{+\infty} dv \ \frac{1}{1+v^{4/3}} \\ & \times \int_1^{+\infty} dy \int_0^1 dw \frac{1-y^2}{\left[c^{-1}\left((1-w)^{2/3}+w^{2/3}\right)+y\right]^{9/2}} \end{aligned} \tag{D.36}$$

where $v = t\left[y + c^{-1}\left((1-w)^{2/3}+w^{2/3}\right)\right]^{3/2}$

Performing the integral over y, one is left with three independent integrals contributing to the numerical prefactor:

$$\begin{aligned}\Pi_A^{(2)}(q,0) &= -\frac{32Nm\bar{g}^2}{105\pi^4\gamma v_F^{3/2}\omega_0^{1/2}} q^{3/2} \int_0^{\pi/2} d\theta \ (\cos\theta)^{3/2} \int_0^{+\infty} dv \ \frac{1}{1+v^{4/3}} \\ & \times \int_0^1 dw \ \frac{5c + 2\left((1-w)^{2/3}+w^{2/3}\right)}{\left(c+(1-w)^{2/3}+w^{2/3}\right)^{5/2}} \end{aligned} \tag{D.37}$$

These integrals can be performed separately and read:

$$\begin{aligned}\int_0^{\pi/2} d\theta \ (\cos\theta)^{3/2} &= \frac{\sqrt{2}\pi^{3/2}}{6\left[\Gamma\left(\frac{3}{4}\right)\right]^2} \simeq 0.8740 \\ \int_0^{+\infty} \frac{dv}{1+v^{4/3}} &= \frac{3\pi\sqrt{2}}{4} \simeq 3.3322 \\ \int_0^1 dw \ \frac{5c+2s(w)}{\left(c+s(w)\right)^{5/2}} &\simeq 0.9438 \end{aligned} \tag{D.38}$$

and we used the notation $s(w) = (1-w)^{2/3} + w^{2/3}$.

Collecting all integrals, and rearranging the prefactor, the final result for the contribution of the first two diagrams then writes:

$$\Pi_A^{(2)}(q,0) = -0.1053 \ \sqrt{k_F} \ q^{3/2}. \tag{D.39}$$

D.4 Other two diagrams

The computation of the other two diagrams in Fig. 3.2 proceeds along the same way. Far away from criticality, when $\gamma v_F \xi^2/(1+\lambda)$ is small, and one can just expand perturbatively in the interaction, the sum of these two "drag" diagrams, which we label here and in the main text as Π_B, was shown in [41] to be equal to $\Pi_A(q,0)$ to the leading order in $\bar{g}$ (which in our model is $\bar{g}^3$, see (D.20 -D.22). Near criticality such simple relation no longer holds, but $\Pi_A(q,0)$ and $\Pi_B(q,0)$ remain of the same sign and of comparable magnitude.

At criticality, we obtained for $\Pi_B(q,0)$

$$\Pi_B(q,0) = \frac{\sqrt{2}}{43^{3/4}\pi^4}\, q^{3/2}\sqrt{k_F} I \tag{D.40}$$

where in rescaled variables (e.g., momentum is in units of q)

$$I = \int d\Omega dx x \int_0^{2\pi} d\theta \frac{S^2(x,\Omega,\theta)}{S_1(x,\Omega) S_1(x+\cos\theta,\Omega)} \tag{D.41}$$

and $S(x,\Omega,\theta)$ and $S_1(x,\Omega)$ are given by

$$\begin{aligned} S(x,\Omega,\theta) &= \int_0^{\Omega} d\omega \int_0^{2\pi} \frac{d\theta_1}{i\Sigma^* - x\cos(\theta_1)} \\ &\quad \times \frac{1}{i\Sigma^* - \cos(\theta+\theta_1) - x\cos\theta_1} \end{aligned} \tag{D.42}$$

$$S_1(x,\Omega) = \int_0^{\Omega} \frac{d\omega}{x^2 + (\Sigma^*)^2} \tag{D.43}$$

where we introduced $\Sigma^* = \Sigma^*(\omega,\Omega) = (\Omega-\omega)^{2/3} + \omega^{2/3}$.

We could not evaluate this integral explicitly, and we compute it under two simplifying assumptions

- we compute $S_1(x,\Omega)$ by expanding to leading order in $(\Sigma^*/x)^2$, evaluating the frequency integral and plugging the result back into denominator. This way, we approximated $S_1(x,\Omega)$ by

  $$S_1(x,\Omega) \approx \frac{\Omega}{x^2 + (c\Omega^{2/3})^2} \tag{D.44}$$

  where $c \approx 1.2$ (see (A.6) This procedure is similar to the one which led to (A.8), but here we cannot justify that only $1.x$ and $1/x^3$ terms are relevant.

- We replace Σ^* by the same $c\Omega^{2/3}$ in the integrand for $S(x,\Omega,\theta)$

- We assume that internal momenta are larger than the external one, i.e $x \gg 1$ (x is measured in units of q), neglected terms $O(1)$ compared to $O(x)$ and set the lower limit of the integration over x at some number b.

- We choose b by applying the same approximate computation scheme to the first part $\Pi_A(q,0)$ and requesting that the result coincide with the exact expression, Eq. (D.39).

Carrying out this calculation for $\Pi_B(q,0)$ we obtain

$$\Pi_A^{(2)}(q,0) \approx -0.14\ \sqrt{k_F}\ q^{3/2}. \tag{D.45}$$

This is the result that we cited in the text.

APPENDIX E

Two-loop renormalization of the charge susceptibility

In this Appendix we show that the singular contributions to the static charge susceptibility from individual diagrams cancel out in the full expression of $\chi_c(q)$.

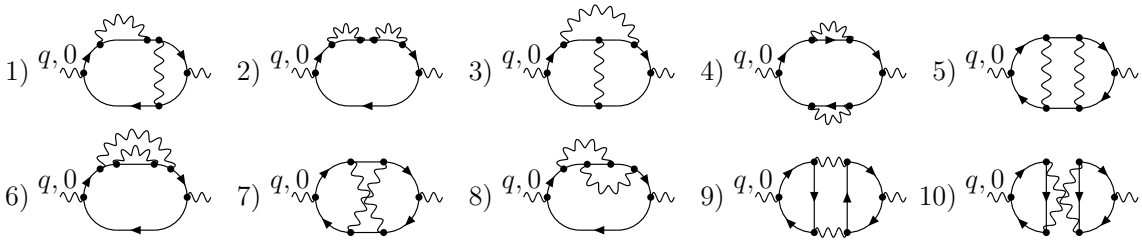

Figure 5.1: The 10 two-loop diagrams for the charge susceptibility.

There are 10 different two-loop diagrams for the charge susceptibility, presented in Fig. 5.1. The last two diagrams are identical to the ones we considered in the main text. We already argued there that these two diagrams cancel out in the case of a QCP in the charge channel.

The other eight diagrams have to be considered together. We demonstrate that the total contribution from these eight diagrams vanishes once one linearizes the dispersion of the intermediate fermions. This still leaves out the contributions from

non-linear terms in the dispersion, but one can show that these contributions are regular.

To begin, consider one of these diagrams, e.g., diagram 7 in Fig. 5.1. In analytic form, the contribution from this diagram is:

$$\Pi_7(q) = 2\int d^2q_1 d\omega_1 d^2q_2 d\omega_2 \; G_k G_{k+q} G_{k+q_1} G_{k+q_2+q} \times G_{k+q_1+q_2} G_{k+q_1+q_2+q} \chi_{q_1}\chi_{q_2}, \tag{E.1}$$

where we labeled $q_i = (\mathbf{q}_i, \omega_i)$, and the combinatoric factor 2 comes from the summation over spin indices.

Introduce now

$$G_k G_{k+q_i} = \frac{1}{\alpha_{q_i}} \; (G_k - G_{k+q_i}), \tag{E.2}$$

where

$$\alpha_{q_i} = i\omega_i - q_i \cos\theta_i, \tag{E.3}$$

and θ_i is the angle between $\mathbf{k} \approx \mathbf{k}_F$ and $\mathbf{q}_i$. Shortening the notations further as $q_1 \equiv 1$ and $q_2 \equiv 2$, using the symbolic notation $\int_{1,2}$ for the 6-dimensional integral over q_1 and q_2, and applying (E.2), we obtain:

$$\Pi_7(q) = 2\int_{1,2} \chi_1\chi_2 \left[\frac{G_{k+q}G_{k+1+2}}{\alpha_1^2\alpha_2^2} - \frac{G_{k+q}G_{k+1+2}}{\alpha_1\alpha_2(\alpha_1+\alpha_2)^2} - 2\frac{G_{k+q}G_{k+1}}{\alpha_2^2(\alpha_1^2-\alpha_2^2)}\right] \tag{E.4}$$

Similarly,

$$\Pi_8(q) = 2\int_{1,2} \chi_1\chi_2 \left[\frac{G_{k+q}G_{k+1+2}}{\alpha_1\alpha_2(\alpha_1+\alpha_2)^2} - 2\frac{G_{k+q}G_{k+1}}{\alpha_1^2(\alpha_1^2-\alpha_2^2)}\right] \tag{E.5}$$

and further

$$\Pi_5(q) = 2\int_{1,2} \chi_1\chi_2 \left[\frac{G_{k+q}G_{k+1+2}}{\alpha_1\alpha_2(\alpha_1+\alpha_2)^2} + 2\frac{G_{k+q}G_{k+1}}{\alpha_1^2(\alpha_1^2-\alpha_2^2)}\right] \tag{E.6}$$

$$\Pi_3(q) = 2\int_{1,2} \chi_1\chi_2 \left[-\frac{G_{k+q}G_{k+1+2}}{\alpha_1^2\alpha_2^2} + 2\frac{G_{k+q}G_{k+1}}{\alpha_1^2\alpha_2^2}\left(\frac{\alpha_1^2+\alpha_2^2}{\alpha_1^2-\alpha_2^2}\right)\right] \tag{E.7}$$

$$\Pi_2(q) = 4\int_{1,2} \chi_1\chi_2 \frac{G_{k+q}G_{k+1}}{\alpha_1^2\alpha_2^2}\left(\frac{\alpha_2^2}{\alpha_1^2-\alpha_2^2}\right) \tag{E.8}$$

$$\Pi_1(q) = 4\int_{1,2} \frac{\chi_1\chi_2}{\alpha_1^2\alpha_2^2} \left[G_{k+q}G_{k+1+2}\frac{\alpha_2^2}{\alpha_1^2-\alpha_2^2} - G_{k+q}G_{k+1}\frac{3\alpha_2^2-\alpha_1^2}{\alpha_1^2-\alpha_2^2}\right] \tag{E.9}$$

$$\Pi_4(q) = \int_{1,2} \frac{\chi_1\chi_2}{\alpha_1^2\alpha_2^2} \left[G_{k+q}G_{k+1+2} - 2G_{k+q}G_{k+1}\right] \tag{E.10}$$

and finally,

$$\Pi_6(q) = \int_{1,2} \frac{\chi_1\chi_2}{\alpha_1^2\alpha_2^2} \left[G_{k+q}G_{k+1+2}\frac{\alpha_1^2+\alpha_2^2}{(\alpha_1+\alpha_2)^2} - 2G_{k+q}G_{k+1}\right] \tag{E.11}$$

Collecting the prefactors for $G_{k+q}G_{k+1+2}$ and $G_{k+q}G_{k+1}$ from all of the eight contributions we find that they cancel out.

APPENDIX F

Mass-shell singularity

In this Appendix, we analyze in more detail the form of the self-energy near the fermionic mass shell. The interest to the mass-shell behavior of the self-energy was triggered by recent studies of the self-energy near a mass shell in a 2D Fermi liquid [33] and for 2D Dirac fermions [56]. In both cases, the lowest-order self-energy diverges at the mass-shell, which forces to re-sum the perturbative series.

At first glance, the same situation holds in our analysis at the QCP. Evaluating the self-energy in a two-loop expansion *around free fermions* and using the fermionic dispersion with the curvature, we obtain near the mass shell [57]

$$\Sigma(k,\omega) \sim \frac{1}{N^2}(i\omega - \epsilon_k) \left[N \log \frac{i\omega - \epsilon_k}{\epsilon_k} \right]^2 . \tag{F.1}$$

This result implies that the quasiparticle residue $Z \propto d\Sigma/d\epsilon_k$ logarithmically diverges on the mass shell of free fermions. Without the curvature of the dispersion, the divergence would be stronger than logarithm.

The issue we now have to address is whether Z still diverges on the mass shell if we expand around the Eliashberg solution, i.e., around fermions with

$$G_0(k,\omega) = \frac{1}{i\tilde{\Sigma}(\omega) - \epsilon_k}, \tag{F.2}$$

where, we remind, $\tilde{\Sigma}(\omega) = \omega + \Sigma(\omega)$.

It turns out that this is not the case: the expansion around the Eliashberg solution leads to a finite residue Z.

At the two-loop order, we obtain, instead of (F.1):

$$\Sigma(k,\omega) \sim \frac{1}{N^2}\int_0^1 dz \int_{1-z}^1 dz' \left(i\Sigma(\omega)\psi_{z,z'} - \epsilon_k\right) \left[\log\frac{N(i\Sigma(\omega)\psi_{z,z'} - \epsilon_k)}{\epsilon_k}\right]^2 \quad \text{(F.3)}$$

where

$$\psi_{z,z'} = (1-z)^{2/3} + (1-z')^{2/3} + (z+z'-1)^{2/3}. \quad \text{(F.4)}$$

For simplicity, we restricted ourselves to the quantum critical regime where $\tilde{\Sigma}(\omega) \approx \Sigma(\omega)$. If $\psi_{z,z'}$ were equal to a constant, as it is when the system is in the Fermi liquid regime, and $\Sigma(\omega) = \lambda\omega$, Z would diverge at $\omega = \epsilon/(1+\lambda)$. However, since $\Sigma(\Omega-\omega)+\Sigma(\omega)$ does not reduce to $\Sigma(\Omega)$, we have two additional integrations over z and z', and the logarithmic singularity is washed out. In particular, at $\epsilon_k = i\Sigma(\omega)$, i.e. at the "Matsubara mass shell", we have

$$Z_{eff} \sim \frac{1}{N^2}\left[\frac{\pi^2}{6}\log^2 N - 4.08\log N + 2.88\right], \quad \text{(F.5)}$$

in which case Z_{eff} is just a constant. Combining this with our earlier result that the renormalization of ϵ_k is also finite, Eq. (2.65), we obtain for the full fermionic Green's function at the smallest ω and ϵ_k

$$G(k,\omega) = \frac{Z_{eff}}{i\tilde{\Sigma}(\omega) - \epsilon_k^*}, \quad \text{(F.6)}$$

where ϵ_k^* differs from ϵ_k by a constant factor.

Part II

Bosonic approach to quantum impurity models

CHAPTER 5

Introduction and motivations

Contents

This first chapter is a general introduction to the Kondo model. After briefly recalling the history and the physics behind the Kondo effect, we review some of the experiments where the Kondo effect plays a major role. This experimental relevance is used to motivate the present work.

5.1 Kondo and Anderson models: a brief review

5.1.1 History of the Kondo effect

The Kondo effect was explained by Jun Kondo in 1964. It solved a 30 year old experimental puzzle, known as the resistance minimum. Kondo's theory however was incomplete, and one had to wait the work of Wilson, ten years later, to fully understand the low-temperature physics of the Kondo effect.

□ Resistance minimum

For electrons in a perfect lattice, the conductivity at low temperature diverges as there is no scattering, and consequently no current dissipation. At finite temperature, the essential mechanism for current dissipation lies in the scattering off phonons. At low enough temperature, the contributions from the phonons decay rapidly, and the scattering by defects and impurities in the metal host become the main source of dissipation. The low-temperature resistance saturates in this case at a finite value which depends on the number of defects in the material: adding more of them increases the residual resistance but does not affect the character of the temperature dependence.

However, since the pioneering work of de Hass et al. [58], there have been many observations of a low temperature increase in the resistance of metals, leading to a minimum of resistance (see Fig. 5.1). The later observation that the minimum depended on the concentration of impurities indicating it as being an impurity phenomenon.

In 1964, Kondo considered the interaction between a single magnetic ion, embedded inside a non-magnetic metal, and the conduction electrons of the latter [59]. He was motivated by a recent experimental work by Sarachik and collaborators [60] who observed a correlation between the existence of a Curie-Weiss term in the impurity susceptibility (signaling the existence of local moments) and the occurrence of the resistance minimum. Convinced that the magnetic character of the impurity was responsible for the resistance minimum, rather than crystal field effects or the impurity charge, he considered the following Hamiltonian[1]:

$$H = \sum_{\mathbf{k}} \sum_{\alpha=\pm} \epsilon_{\mathbf{k}} c^{\dagger}_{\mathbf{k}\alpha} c_{\mathbf{k}\alpha} + J_K \sum_{\mathbf{k},\mathbf{k}'} \sum_{\alpha\beta} \mathbf{S} \cdot \left(c^{\dagger}_{\mathbf{k}\alpha} \frac{\boldsymbol{\sigma}_{\alpha\beta}}{2} c_{\mathbf{k}'\beta} \right) \tag{5.1}$$

where $c^{\dagger}_{\mathbf{k}\alpha}$ and $c_{\mathbf{k}\alpha}$ are creation and annihilation operators for the conduction electrons, with momentum $\mathbf{k}$ and spin σ. While the first term is a generic kinetic term for the band of electrons, the second term describes the interaction between the impurity spin $\mathbf{S}$ and the local density of spin of the conduction electrons.

[1] This Hamiltonian, often called the "Kondo Hamiltonian", was not introduced by Kondo but by Zener [61]. Kondo is however the first one to have found the log term in the resistivity.

Treating the coupling between the localized impurity spin and the sea of conduction electrons up to third order in perturbation theory, he found that the resistivity associated to such magnetic impurities read:

$$\rho(T) = \rho_{\text{host}}(T) + a\rho_0 J_K^2 + b\rho_0^2 J_K^3 \log\left(\frac{D}{T}\right) \tag{5.2}$$

where $\rho_{\text{host}}(T)$ is the resistivity of the metal in absence of the impurities, ρ_0 is the density of states at the Fermi level, D is the bandwidth and a, b are constants proportional to the impurity density.

It follows that for an antiferromagnetically coupled impurity spin, Kondo's theory correctly describes the observed minimum of resistivity: it can be attributed to the log term which overshadows the phonon contribution to the resistivity at low enough temperature (see Fig. 5.1).

Physically, the interacting term in (5.1) generates local inter-exchange of spins between the magnetic impurity and the conduction band. This induces strong correlations between the electrons and ultimately leads to an increase in the resistivity. The Kondo effect is a true many-body problem: a first electron scattering off the impurity flips its spin, so that a second electron interacting with the impurity now sees an impurity whose spin changed because of the first electron: the electrons are now correlated due to the impurity.

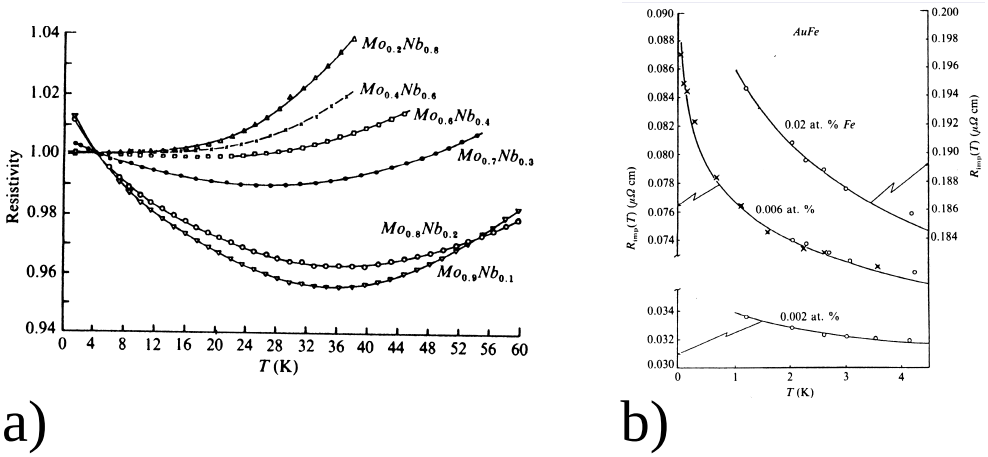

Figure 5.1: a) Data from [60] showing the minimum of resistance for Fe impurities in Mo-Nb alloys; b) Resistivity fits from Kondo's original paper [59] using the expression he derived, Eq. 5.2.

□ The Kondo problem

Although Kondo's theory explains the resistance minimum, it also makes the unphysical prediction that the resistance diverges at even lower temperatures. This

divergence signals the breakdown of Kondo's perturbative treatment. Resumming the logarithmically divergent terms, a natural scale appears, below which any kind of perturbative expansion is bound to fail. This temperature scale is known as the Kondo temperature T_K, and is given by:

$$T_K \sim D e^{-1/(\rho_0 J_K)} \tag{5.3}$$

as one can argue from (5.2), by comparing the two terms depending on the Kondo coupling.

Anderson's work on the so-called "poor man's scaling" [62] inferred that a ground-state with an infinite coupling develops, the impurity being bound to a conduction electron in a singlet state. The behavior at low-temperature would then be similar to that of a non-magnetic impurity, the impurity spin being compensated.

Wilson's numerical renormalization group confirmed this hypothesis [63]. He could obtain definitive results for the ground-state and low-temperature behavior of the system. Wilson highlighted the existence of a dynamically generated temperature scale, corresponding to the Kondo temperature T_K, where the systems enters a cross-over towards a strong-coupling regime for the case of an antiferromagnetic coupling J_K. The system is then characterized by the formation of a Kondo singlet.

At high temperature, $T \gg T_K$, the impurity spin and the electrons are only weakly coupled: one can compute the properties of the system from a perturbative expansion around the free impurity regime. At low temperature, $T \ll T_K$, one enters the strong coupling regime: the conduction electrons screen out the impurity spin, forming with it a spin singlet state. Note that in this respect, the Kondo effect is a simple example of asymptotic freedom: the theory is trivial at high energy (free local moment), but much more complex at low energy (many-body object).

5.1.2 Anderson model

The Anderson model [64] is a generalization of the simple model used by Kondo, which takes into account charge fluctuations. In this model, the magnetic impurity is a localized electronic orbital, whose charge can now fluctuate. The associated Hamiltonian writes:

$$H = \sum_{\mathbf{k}} \sum_{\sigma=\pm} \epsilon_{\mathbf{k}} c^\dagger_{\mathbf{k}\sigma} c_{\mathbf{k}\sigma} + V \sum_{\mathbf{k}\sigma} \left(c^\dagger_{\mathbf{k}\sigma} f_\sigma + f^\dagger_\sigma c_{\mathbf{k}\sigma} \right) + \epsilon_f \sum_\sigma f^\dagger_\sigma f_\sigma + U n_{f\uparrow} n_{f\downarrow} \tag{5.4}$$

where $n_{f\sigma} = f^\dagger_\sigma f_\sigma$.

This model takes into account the generic kinetic term for the band of conduction electrons, an hybridization V between the localized orbital and the metallic host, the energy ϵ_f of the orbital, and finally a Coulomb repulsion term on the site of the impurity.

To get some insight into this model, let's consider the case $V = 0$, the so-called "atomic limit" (where the localized states are uncoupled from the conduction

electrons). In this situation, there are three energy configurations for the states of the localized f electrons:

- zero occupation, with a total energy $E_0 = 0$
- single occupation by a spin σ, with an energy $E_{1,\sigma} = \epsilon_f$
- double occupation with a spin $\uparrow$ and a spin $\downarrow$, with energy $E_2 = 2\epsilon_f + U$

If the ground-state corresponds to single occupation, then the system has two-fold degeneracy corresponding to spin $\frac{1}{2}$, and displays an associated magnetic moment. The other two configurations are non-degenerate and therefore non-magnetic.

It follows that in the atomic limit, the condition for the formation of a local moment is that the singly-occupied configuration lies lowest in energy. Turning on the hybridization with the conduction band, we expect that for $V \ll U$ the ground-state of the ion is essentially the same as in the atomic limit. Therefore, the Kondo model can be seen as a limiting case of the Anderson one, where the valence fluctuations of the localized orbital can be neglected.

Schrieffer and Wolf [65] used a canonical transformation (which amounts to generalizing the second-order perturbation theory to encompass off-diagonal matrix elements) to prove that if the singly occupied state is the ground-state in the atomic limit, then the effective Hamiltonian for a small hybridization is obtained by taking into account virtual excitations to the zero and double occupied states. This effective Hamiltonian reduces to the one used by Kondo, in the local moment regime defined as $U + \epsilon_f > E_F$ and $\epsilon_f < E_F$.

This can be readily seen from (5.4) by taking the limit of infinitely low energy for the orbital and the Coulomb repulsion: $\epsilon_f = -U/2 \to \infty$. In this regime, only the singly-occupied states survive, and they couple to the conduction electrons via an antiferromagnetic coupling $J_K \sim 4V^2/U$ which comes from virtual hopping onto the high-energy states of valence 0 and 2.

Note finally that because of the possibility of valence fluctuations, the physics of the Anderson model is richer than that of the Kondo model (which cannot treat, e.g., the mixed valent regime). Quite often, the theoretical formulation of experimental setups makes use of the Anderson model, and later reduces to a Kondo model in the local moment regime.

5.1.3 Experimental and theoretical relevance: the revival

Why would anyone still want to study a physical phenomenon that was explained more than 30 years ago? Although the Kondo effect is a well-known and widely studied phenomenon, it continues to capture the interest of both theorists and experimentalists [66].

Among the examples of the revival of the Kondo effect (some of which we detail in the next sections), one of the most interesting ones comes from the experimental

observation of the Kondo resonance. Due to the formation of the Kondo singlet state, which involves conduction electrons close to the Fermi surface, the Kondo effect results in the presence of an acute perturbation in the renormalized density of states at the Fermi energy: the "Kondo resonance".

Until very recently, physicists could only infer the role of the Kondo effect by measuring bulk properties like the resistance or the magnetic susceptibility. With the development of nanotechnology and one of its central tools – the Scanning Tunneling Microscopy or STM – it is now possible to image a surface with atomic resolution, and measure the Kondo resonance from the current versus voltage characteristics.

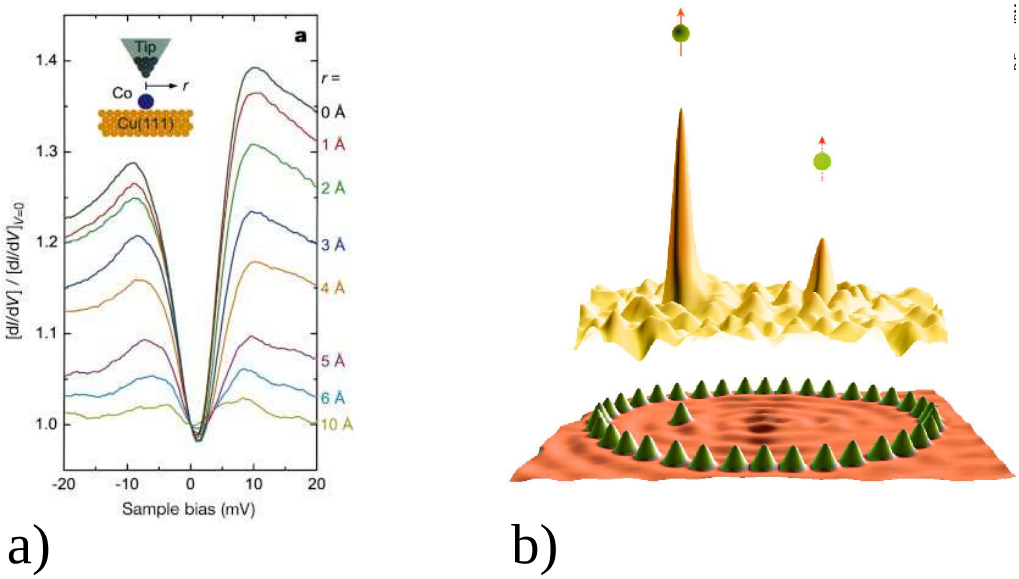

Figure 5.2: a) Differential tunnel conductance of the tip at various distances r from the impurity, taken from [67]. The anti-resonance close to zero bias is a hallmark of the Kondo effect. b) Ellipse of atoms with an impurity at one of the foci. The top part is a plot of the measured density of states on the surface, revealing a sharp peak located at both foci, even where the impurity is not present.

This has been done experimentally by two groups [68, 69] who measured the differential tunnel conductance at the site of the impurity (an atom of Co deposited on gold surface, and Ce on silver). Manoharan and collaborators [67] took it the the next level by building an ellipse of atoms around a cobalt impurity placed at one of the focal points. The STM-measured energy spectrum revealed the existence of a Kondo resonance at the site of the impurity but also at the second focus, despite the absence of any magnetic impurity at that location. Since then, this phenomenon, labeled as "quantum mirage", has led to many other experimental and theoretical studies [70].

The development of nanotechnology has rekindled interest in the Kondo effect. However, the study of these systems is limited by construction as one cannot modify the properties of the magnetic impurity or its coupling to the bulk electrons. This is precisely the next step physicists are aiming at, with the so-called "quantum dots".

5.2 Quantum dots

The ambition of this section is not to give a detailed review of the quantum dot physics[2], but rather to introduce the main concepts, explain the relevance of the Kondo effect in these systems and provide a motivation for our current work.

5.2.1 Charge quantization

Quantum dots are small semiconductor devices, man-made "droplets of charge" ranging from 10 to 1000 nm in size, where the number of trapped electrons can be tuned precisely by varying external parameters, from one to several thousand. They are made of an isolated patch containing an electron gas, coupled via tunnel barriers to one or two leads, and capacitively to a gate electrode, allowing to change the electrostatic potential of the dot (see Fig. 5.3).

These devices are often referred to as "artificial atoms", as the confinement of electrons leads quantized energy levels as in an atom. The tremendous difference being that quantum dots allow one to scan through the entire periodic table by simply changing a voltage.

The electronic states in the dot can be probed by transport when a small tunnel coupling is allowed between the dot and the surrounding reservoir of electrons: the so-called source and drain leads. The key idea behind the study of quantum dots, is to create devices where quantum effects, such as the quantization of charge, are important. In order to do so, one has to fulfill two conditions:

- work at low temperature: $\frac{e^2}{C} \gg k_B T$ (where C is the capacitance of the dot)

  When tunneling occurs between the dot and the leads, the charge on the island suddenly changes by the quantized amount e. The associated change in the Coulomb energy is conveniently expressed in terms of the capacitance C of the island so that the electrostatic potential increases by an amount $E_c = e^2/C$, known as the charging energy[3]. This charging energy plays a significant role only at temperatures much below it, when states of different charge are well separated in energy.

[2] See [71] for a complete review of the subject, or [72, 66] for a friendly introduction to this field.

[3] For that, we assumed that the Coulomb interaction between the electrons is independent on the number N of electrons in the island. This is known as the "constant-interaction" model. Despite its simplicity, this model is remarkably accurate and allows to describe the measurements. For a detailed justification of the model, see the review of Aleiner et al. [73].

- restrict to the weak conductance regime: $G \ll \frac{e^2}{h}$

  This means that the tunnel barriers must be sufficiently opaque such that the electrons are located either in the dot or in the leads, and not delocalized over the whole circuit.

The first criterion can be met by making the dot small (recall that the capacitance of an object scales with its typical radius), and the second by weakly coupling the dot to the leads.

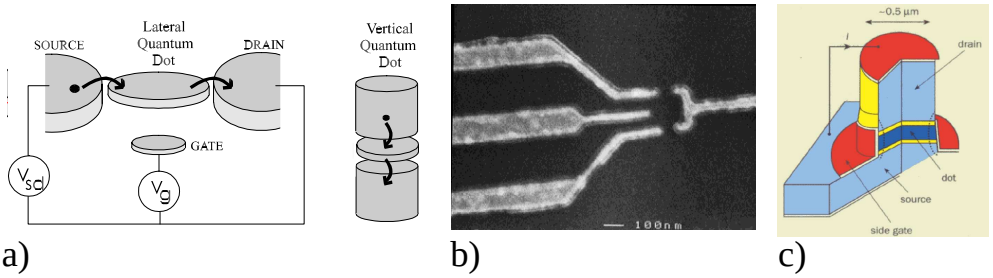

Figure 5.3: a) Schematic diagram of the lateral and vertical quantum dots (from [71]); b) Top surface of the SET used in the experiments of Goldhaber-Gordon et al. [74]; c) Vertical dot structure (from [75]).

5.2.2 Coulomb blockade

In the regime of quantized charge tunneling mentioned above, the energy of a dot containing $N+1$ electrons is greater than one containing N electrons: extra energy is therefore needed to add an electron to the dot and no current will flow until this energy is provided by increasing the voltage. This phenomenon is known as the "Coulomb blockade".

Indeed, a voltage V_g applied to the gate can change continuously the island's electrostatic energy: it lowers the energy of electrons in the droplet relative to the Fermi level in the leads. If we sweep V_g, the build up of electrostatic energy is compensated by tunneling of discrete charges onto the dot. Formally, the potential energy of a dot with N electron and a gate voltage V_g is given, in first approximation, by:

$$E = \frac{Q^2}{2C} + QV_g = \frac{1}{2}E_c N\left(N - 2\frac{CV_g}{e}\right) \tag{5.5}$$

Starting from a dot with N electrons and increasing V_g, one reaches a point where the energy of the two configurations with and N and $N+1$ electrons are degenerate. Because of this charge degeneracy, the allowed fluctuation in the number of electrons

on the dot leads to a current flow and results in peaks of the conductance as a function of the gate voltage: the so-called "Coulomb oscillations" (see Fig. 5.4).

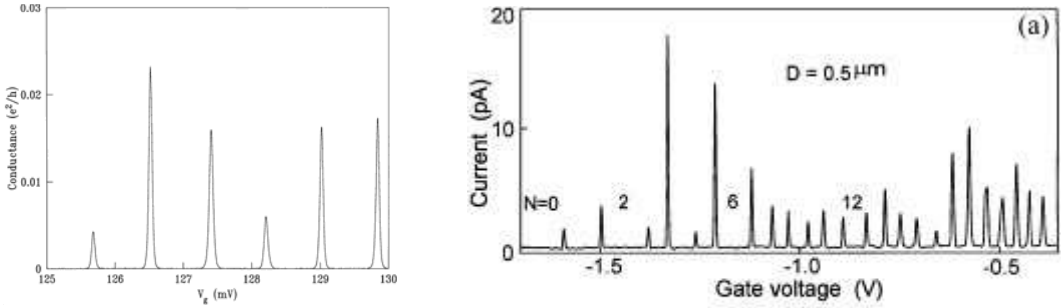

Figure 5.4: Conductance in the Coulomb blockade regime: a) for a lateral quantum dot [76], showing sharp periodically spaced peaks; b) for a vertical quantum dot [77], showing the appearance of multiplets corresponding to shell filling.

This mechanism allows one to control the current through the dot via a small change in the gate voltage V_g. For this reason, this device is also called a "single-electron transistor" (SET).

Refining a bit the model used to derive (5.5), one can take into account the energy spectrum ϵ_p of the states trapped on the dot, and consider the case where the energy spacing cannot be neglected compared to the charging energy. In this case, the energy one has to pay to add an electron to the state p is given by the charging energy. As soon as this state is filled, the energy cost increases in order to account for the energy difference between the ates p and $p+1$, in addition to the charging energy. This leads to Coulomb oscillations organized in multiplets separated by an energy $E_c + \epsilon_{p+1} - \epsilon_p$, where the peaks inside a given multiplet are separated by an energy E_c. This shell structure has been observed in vertical quantum dots [77] and clearly justifies the name "artificial atoms" for these devices (see Fig. 5.4).

5.2.3 Kondo physics in quantum dots

□ Conventional Kondo effect

We have just seen that a voltage applied to the gate electrode controls the number N of electrons on the dot. If an odd number of electrons is trapped within the island, the total spin of the dot S is necessarily non-zero. This localized spin, embedded between large reservoirs of electrons, is susceptible to undergo a Kondo effect. The relevance of the Kondo physics for these systems was predicted theoretically by Glazman and Raikh [78] and Ng and Lee [79]. The basic punch-line is that the formation of a Kondo singlet between this localized spin and the electrons of the

leads, is responsible for the development of a peak in the density of states of the localized spin (the so-called "Kondo resonance") pinned at the Fermi energy of the leads. Since the transport properties are determined by electrons with energies close to the Fermi level, the Kondo resonance is expected to have a dramatic influence on, e.g., the conductance of the dot.

For small dots, the quantized energy difference between different electronic states (for a given number of electrons N on the island) becomes important. When the temperature becomes lower than this energy spacing, a system with an odd number of electrons on the dot effectively behaves as a spin-1/2, coupled to a gas of free fermions (the two leads), and can be described by an Anderson model with the following Hamiltonian:

$$H = \sum_{\mathbf{k},\sigma} \sum_{a=L,R} \epsilon_{\mathbf{k}} c^{\dagger}_{a\mathbf{k}\sigma} c_{a\mathbf{k}\sigma} + E_c n_{d\uparrow} n_{d\downarrow} + \epsilon_0 \sum_{\sigma} d^{\dagger}_{\sigma} d_{\sigma} + \sum_{\mathbf{k},\sigma} \sum_{a=L,R} V_a \left(c^{\dagger}_{a\mathbf{k}\sigma} d_{\sigma} + d^{\dagger}_{\sigma} c_{a\mathbf{k}\sigma} \right) \tag{5.6}$$

where we introduced the $c^{\dagger}_{a\mathbf{k}\sigma}$ fermionic fields to describe the electrons of the leads, as well as the fermionic $d^{\dagger}_{\sigma}$ for the localized spin of the dot.

When the temperature is larger than the coupling Γ between the leads and the dot, one recovers the Coulomb oscillations and the conductance shows periodically spaced peaks (not very sharp if Γ is not small enough). As the temperature is lowered, one eventually goes below the Kondo temperature. In this regime, the development of the Kondo resonance strongly enhances the conductance of the dot provided that the number of electrons on the dot is odd (as we have just argued in the previous paragraph). This leads to an even-odd effect on the dot: if the number of trapped electrons is even, the conductance drops towards zero, whereas if it is odd, it increases dramatically and eventually reaches the unitary value of $2e^2/h$ at low temperature. The Kondo effect not only suppresses the Coulomb blockade, but is also able to make the dot completely transparent (the conductance is maximal in the zero temperature limit).

These consequences of the Kondo effect have been observed experimentally [74, 80].

□ New directions

The quantum dots provide new opportunities to control the Kondo effect, and although the results described thus far resemble what happens for an impurity in a metal, these devices allow to study regimes inaccessible with magnetic impurities, bringing the Kondo effect to a whole new level.

Although quantum dots have provided new opportunities to control the Kondo effect, the results described thus far resemble what happens for an impurity in a metal.

To name a few examples of these new directions for the Kondo effect, one has:

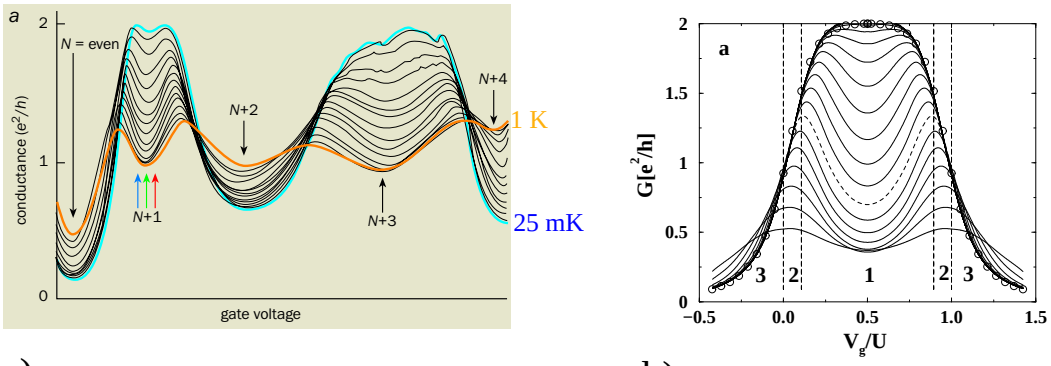

Figure 5.5: a) Experimental observation of the effect of the Kondo resonance on the conductance of a dot [80]; b) These lineshapes could be recovered theoretically using a numerical renormalization group approach [81].

- the effect of a magnetic field (singlet-triplet transition and associated two-stage screening) [82];
- the experimental realization of a two-impurity Kondo system using double quantum dots [83, 84];
- the physics out-of-equilibrium (high voltage, three-terminal SET,...);
- the coupling of a quantum dot to magnetic leads;
- the proposed experimental setups to explore the two-channel Kondo effect [85]

A lot of these effects require a better theoretical understanding of the Anderson and the Kondo models, in particular out of equilibrium, where very powerful tools like the Bethe ansatz are not so easy to extend [86]. We believe that some of the unanswered questions that these new directions raise can be, if not solved, at least better formulated, thanks to simple approaches capturing the low-temperature behavior of the Kondo effect, generalized to encompass the physics out of equilibrium. This is one of our main motivation for the present work.

5.3 Heavy fermions and the Kondo lattice

Another important application of the Kondo effect comes not from the single impurity physics, but from dense ordered lattices of impurities, and its relevance for a whole family of compounds known as "heavy fermion systems".

5.3.1 Kondo lattice

In a system containing many dilute impurities, the conduction electrons form with the network of localized spins, a set of Kondo singlets roughly independent from each other. When the density of impurity increases, correlations appear between them, due to the Kondo interaction with the conduction band.

□ RKKY interaction

As early as 1940, Frölich and Nabarro [87] discussed the possibility of a ferromagnetic interaction between nuclear spins mediated by the hyperfine coupling with the surrounding cloud of electrons. Later on, Ruderman and Kittel [88] computed from a second-order perturbation expansion the effective coupling between nuclear spins. Kasuya [89] and Yosida [90] proposed an extension of this mechanism to localized inner d-electron spins, coupled via an indirect exchange mediated by the conduction electrons. This long-range spin-spin interaction is now known as the Ruderman-Kittel-Kasuya-Yosida or "RKKY interaction".

When a magnetic moment is introduced into a metal, it polarizes the surrounding carriers by means of the Kondo interaction and induces Freidel oscillations in the spin density around the magnetic ion [91]. If another local moment is introduced, it couples with the first one, giving rise to the following long-range interaction:

$$J_{RKKY}(\mathbf{x}-\mathbf{x}') = -J_K^2 \chi(\mathbf{x}-\mathbf{x}') \quad \text{where} \quad \chi(\mathbf{q}) = 2\sum_{\mathbf{k}} \frac{f(\epsilon_{\mathbf{k}}) - f(\epsilon_{\mathbf{k}+\mathbf{q}})}{\epsilon_{\mathbf{k}+\mathbf{q}} - \epsilon_{\mathbf{k}}} \tag{5.7}$$

At zero temperature, for a parabolic band, one has:

$$J_{RKKY}(r) \sim -J_K^2 \rho_0 \frac{\sin(2k_F r) - 2k_F r \cos(2k_F r)}{2(2k_F r)^4} \tag{5.8}$$

where ρ_0 is the density of states at the Fermi level, and r is the distance from the impurity (see Fig. 5.6). The oscillating part with a period $2k_F$ is characteristic of Freidel oscillations. As a consequence, the sign of the RKKY interaction depends on the distance between the impurities, and the typical strength of the coupling is $E_{RKKY} \sim J_K^2 \rho_0$.

□ Donicah's picture

Comparing the typical energy scale associated to the Kondo ($T_K \sim De^{-1/(\rho_0 J_K)}$) and the RKKY ($T_{RKKY} \sim \rho_0 J_K^2$) interactions, one expects for the low temperature regime:

- for large values of the Kondo coupling constant, $T_K \gg T_{RKKY}$. One then expects the Kondo effect to be the dominant interaction, leading to the formation of local singlets roughly independent of one another. This suggests the formation of a Fermi liquid ground-state,

- for small values of J_K, $T_{RKKY} \gg T_K$. A magnetically ordered state is favored in this case. This magnetic order prevents spin-flip processes to occur, and the Kondo resonance to develop.

As one varies the Kondo coupling continuously, the system is expected to go from a magnetically ordered to a Fermi liquid ground-state, with a quantum critical point separating the two at zero temperature. These arguments and the associated pictorial phase diagram that emerges from them (see Fig. 5.6), are known as the Doniach picture [92].

However, it is important to keep in mind the crudeness of these arguments: this description is only qualitative. First of all, the exponential form of the Kondo temperature used in this discussion comes from the single-impurity physics, and may very well change substantially once we treat the lattice model. Second, and more importantly, both the expressions for T_K and J_{RKKY} relies on the assumption of a somewhat large electronic bandwidth. It follows that for $J_K \sim D$, these expressions should not be taken too seriously. It turns out that, as they stand, the Kondo coupling for which both scales are of the same order of magnitude corresponds to $J_K \sim D$.

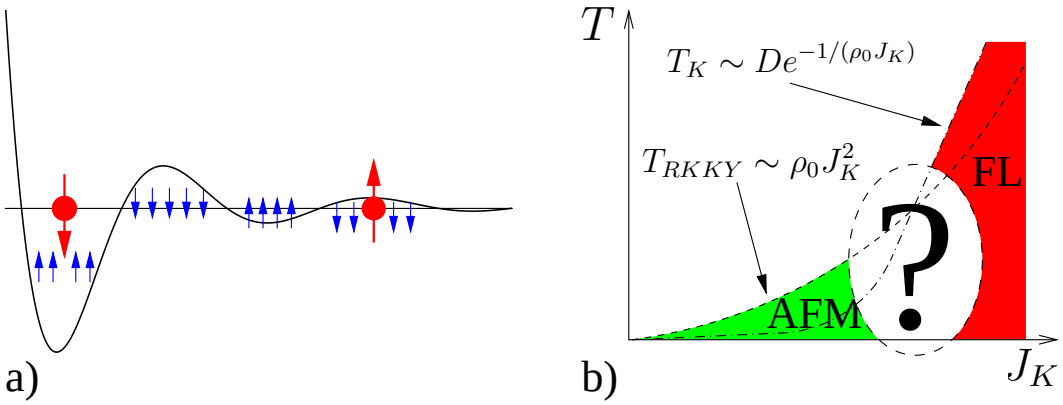

Figure 5.6: a) Illustration of the electron spin polarization (in blue) around a magnetic impurity (in red) giving rise to Freidel oscillations and inducing an RKKY interaction between impurity spins; b) Doniach phase diagram, with an antiferromagnetically ordered phase (AFM) at low J_K and a Fermi liquid phase (FL) at large J_K.

5.3.2 Heavy fermion: a prototypical Kondo lattice

There exists a whole family of compounds that can be thought of a dense lattice of local moments embedded in a metallic host. They are known as "heavy fermions".

□ Heavy fermions

In 1975, Andres, Graebner and Ott [93] pointed out that the low-temperature properties of $CeAl_3$ are those of a metal, with strongly renormalized physical properties. They had just discovered one of the first examples of heavy fermion metal.

Heavy fermion materials are rare-earth or actinide-based compounds, containing f-electron elements (U, Ce, Yb). They are distinguished at low temperatures by an anomalously large specific heat coefficient, with correspondingly large Pauli paramagnetic susceptibility (here "large" means 2 to 4 orders of magnitude larger than, say, Cu). These properties can be described within the framework of Landau's Fermi liquid theory, by considering a large renormalized mass, as big as 10^4 bare electronic mass, hence the name "heavy fermion" associated to these compounds (see Fig. 5.7).

Microscopically, one of the most important properties of the 4-f and 5-f elements is the small spatial extent of their radial probability. One can thus consider that heavy fermion materials are made of localized f orbitals arranged in a periodic lattice, interacting with delocalized conduction electrons.

For this reason, the heavy fermion compounds are thought to be described by the periodic Anderson model, whose Hamiltonian writes:

$$H = \sum_{\mathbf{k}} \sum_{\sigma=\pm} \epsilon_{\mathbf{k}} c^{\dagger}_{\mathbf{k}\sigma} c_{\mathbf{k}\sigma} + V \sum_{i,\sigma} \left(c^{\dagger}_{i\sigma} f_{i\sigma} + f^{\dagger}_{i\sigma} c_{i\sigma} \right) + \epsilon_f \sum_{i,\sigma} f^{\dagger}_{i\sigma} f_{i\sigma} + U n_{fi\uparrow} n_{fi\downarrow} \quad (5.9)$$

where the f electrons hybridize with the conduction electrons c.

In practice, due to the large local repulsion, and the weak hybridization of the $4-f$ and $5-f$ shells, most lanthanides and actinides-based compounds have stable valence states and concomitant local magnetic moments, which allows the reduction of the previous Hamiltonian, Eq. (5.9), to the one of the Kondo lattice model.

□ QCP and Non-Fermi liquid

Heavy fermion materials offer a unique opportunity to study quantum criticality under controlled conditions: by applying pressure, doping, or magnetic field, it is possible to tune the ground-state of the system from a magnetically ordered state to a Fermi liquid, through a quantum critical point.

A wide body of evidence suggests that the effective mass m^* of the fermionic quasiparticles in the paramagnetic Fermi liquid diverges as one approaches the QCP. This divergence leads to a breakdown of Landau's Fermi liquid theory, and the state which forms above the QCP is referred to as a non-Fermi liquid[4].

[4]This designation, already used in the text for MnSi, actually encompasses a broad range of different behaviors. Quoting Altshuler: "The difference between a Fermi liquid and a non-Fermi liquid is like the difference between a banana and a non-banana".

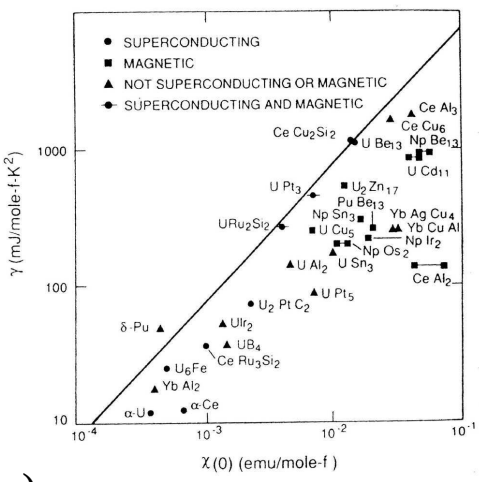

a)

Compound	C_v/T	$\rho(T)$
$YbRh_2Si_2$	$\log T$	T
$CeCoIn_5$		T
$CeCu_{6-x}Au_x$	$\log T$	T
$CeCu_{6-x}Ag_x$	$\log T$	$T^{1.1}$
$CeNi_2Ge_2$	$\log T$	$T^{1.4}$
$CeCu_2Si_2$	$\log T$	$T^{1.5}$
YbAgGe	$\log T$	T
$CePd_2Si_2$	$T^{-0.5}$	$T^{1.2}$

b)

Figure 5.7: a) Specific heat coefficient and Pauli susceptibility of a few heavy fermion materials in the Fermi liquid regime; b) Selected list of heavy fermion compounds, and their associated properties in the quantum critical regime.

Among the wide range of physical properties that departs from the Fermi liquid behavior at criticality, one sees many common features[5] (see Fig. 5.7):

- diverging specific heat coefficient at the QCP:

$$\frac{C_v}{T} \sim c \log\left(\frac{T_0}{T}\right) \quad \text{or, more rarely} \quad \sim T^{-1+\lambda} \tag{5.10}$$

  with $0.5 \leq \lambda \leq 0.9$. This suggests that the effective mass $m^* \to \infty$ at the QCP.

- quasi-linear resistivity:

$$\rho(T) \sim \rho_0 + AT^{1+\epsilon} \tag{5.11}$$

  where $0 \leq \epsilon \leq 0.6$ at the QCP. This quasi-linear behavior is seen on a temperature range going from half a decade up to three decades (for Ge-doped $YbRh_2Si_2$ [95]).

- a non-Curie spin susceptibility:

$$\chi^{-1}(T) = \chi_0^{-1} + CT^a \tag{5.12}$$

  where $a < 1$.

[5] For a review of the experimental data of the non-Fermi liquid behavior of f-electron metals, see e.g. [94].

In addition to this non-Fermi liquid behavior, scaling properties could be measured for a few compounds: in $YbRh_2Si_2$, the differential susceptibility exhibits H/T scaling [96] and in $CeCu_{6-x}Au_x$, neutron scattering measurements showed E/T scaling in the dynamical spin susceptibility [97].

None of the theoretical approaches devised to date, could explain all of these features (though some could recover partial results). The key ingredient that is generally missing is the competition between the Kondo effect and the development of magnetic correlations: most approaches have focused on one or the other unsuccessfully.

The bosonic scheme we develop in the next chapters of this manuscript is an attempt at bridging this gap. As we argue in Chapter 6 and 7, such a procedure does recover the Fermi liquid behavior (at least the expected thermodynamics) and allows one to study the effect of magnetic correlations. The extension to the lattice - though not yet achieved - could lead to extremely useful insights in building a mean-field theory susceptible to describe the quantum phase transition between antiferromagnetism and the heavy electron fluid.

CHAPTER 6

Single impurity multichannel Kondo model

Contents

In this chapter, we introduce and analyze the antiferromagnetic multichannel Kondo model for a single impurity. After deriving the saddle-point equations and recalling the results known for the overscreened and the underscreened regime, we study in details the physical properties of the exactly screened scenario.

6.1 Background

6.1.1 Generalized Kondo model

As a starting point, we consider the generalized Kondo model as introduced by Coqblin and Schrieffer [98]. This model is a generalization of the original one studied by Kondo, where the $SU(2)$ symmetry group has been extended to $SU(N)$. The Hamiltonian then writes:

$$H = \sum_{\mathbf{k}} \sum_{\sigma=1}^{N} \epsilon_{\mathbf{k}} c^{\dagger}_{\mathbf{k}\sigma} c_{\mathbf{k}\sigma} + \frac{J_K}{N} \sum_{\mathbf{k},\mathbf{k}'} \sum_{\alpha,\beta} S_{\alpha\beta} c^{\dagger}_{\mathbf{k}\beta} c_{\mathbf{k}'\alpha} \tag{6.1}$$

where the spin flavor now runs from 1 to N, and the antiferromagnetic Kondo coupling has been rescaled to preserve the same scaling in N for the kinetic and the interacting part of the Hamiltonian. The $c^{\dagger}_{\mathbf{k}\sigma}$ and $c_{\mathbf{k}\sigma}$ fields correspond respectively to the creation and annihilation of a conduction electron with momentum $\mathbf{k}$ and spin index σ.

The impurity spin $S_{\alpha\beta}$ now satisfies the commutation rules of the $su(N)$ algebra, namely:

$$[S_{\alpha\beta}, S_{\gamma\delta}] = \delta_{\beta\gamma} S_{\alpha\delta} - \delta_{\alpha\delta} S_{\gamma\beta} \tag{6.2}$$

□ Representation

While any irreducible representation of $SU(N)$ could be used to describe the impurity spin, historically, two representations retained attention:

- Schwinger bosons [99]

  This amounts to introducing N bosonic fields b_α, whose total number is constrained to be related to the size S of the impurity spin via the relation:

  $$\sum_{\alpha} b^{\dagger}_{\alpha} b_{\alpha} = P = 2S \tag{6.3}$$

  The $S_{\alpha\beta}$ operator is then defined as:

  $$S_{\alpha\beta} = b^{\dagger}_{\alpha} b_{\beta} - \frac{P}{N} \delta_{\alpha\beta} \tag{6.4}$$

where one can easily check that the commutation rule is satisfied, and the second term is introduced to make the operator traceless. Such a representation corresponds, in terms of Young tableaux, to a single line of P boxes (see fig.6.1a). Note that in the case of a line representation, there is no upper boundary for P.

- Abrikosov pseudo-fermions [100]

  This is the fermionic counterpart of the previous one. One introduces here a set of fermionic operators f_α, verifying:

$$S_{\alpha\beta} = f_\alpha^\dagger f_\beta - \frac{Q}{N}\delta_{\alpha\beta} \tag{6.5}$$

$$\sum_\alpha f_\alpha^\dagger f_\alpha = Q \tag{6.6}$$

  In terms of Young tableaux, this representation corresponds to a column of Q boxes, where by construction $0 \leq Q \leq N$ (see fig.6.1b).

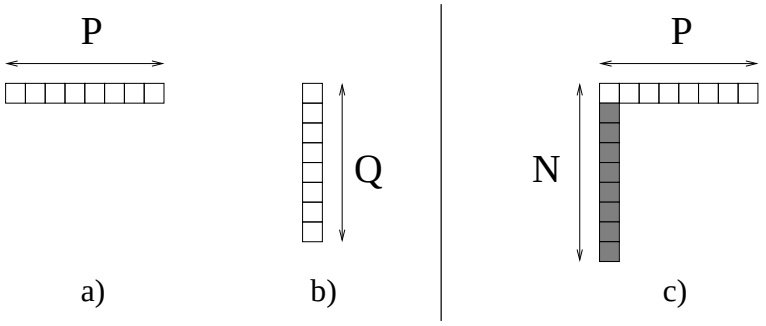

Figure 6.1: a) and b) Two examples of representation of $SU(N)$, c) Strong coupling limit of the single channel model. The white boxes correspond to the bosonic line representation and the gray ones to the conduction electrons.

One of our ultimate goals is to describe the competition between magnetism and the Kondo effect. It turns out that a fermionic description is not well suited to describe local moment magnetism [101, 102], so that we focus in the rest of this text only on Schwinger boson representation of the impurity spins.

□ Channel index

One can use Young tableaux to investigate the strong coupling solution of the generalized Kondo model: one combines the first box of the line representation with a column of boxes representing the conduction electrons to form a spin singlet. One then notices from fig. 6.1c, that unless $P = 1$, this model describes an underscreened impurity, where only a fraction of the original spin is screened by the conduction

electrons, leaving a residual spin of size $S = \frac{P-1}{2}$. In order to overcome this, Parcollet and Georges [103] introduced a multichannel version of the generalized Kondo model. The idea is to multiply the number of electronic flavors by introducing a channel index μ that runs from 1 to K. The Kondo interaction is left unchanged as no channel anisotropy is introduced. The new Hamiltonian, which now has the symmetry $SU(N) \times SU(K)$, is given by:

$$H = \sum_{\mathbf{k}} \sum_{\sigma=1}^{N} \sum_{\mu=1}^{K} \epsilon_{\mathbf{k}} c^{\dagger}_{\mathbf{k}\sigma\mu} c_{\mathbf{k}\sigma\mu} + \frac{J_K}{N} \sum_{\mathbf{k},\mathbf{k}'} \sum_{\alpha,\beta} \sum_{\mu} b^{\dagger}_{\alpha} b_{\beta} c^{\dagger}_{\mathbf{k}\beta\mu} c_{\mathbf{k}'\alpha\mu} \tag{6.7}$$

where we have replaced the impurity spin operator by the Schwinger boson representation, and dropped the constant term proportional to the total number of electrons at the site of the impurity.

This Hamiltonian is the starting point for all the work presented in this chapter.

6.1.2 Strong coupling limit

The multichannel Kondo Hamiltonian allows us to tune separately the parameters P and K, i.e. the size of the impurity spin and the total number of channels. This gives access to three regimes with very different physics. In order to get a first flavor of the physics associated to these regimes, we study the strong coupling behavior of the model using arguments due to Nozières and Blandin [104].

□ Nozières-Blandin analysis

In the strong coupling limit, the kinetic energy of the conduction electrons is negligible, and finding the ground state then amounts to minimizing the Kondo energy. In this limit, the impurity tends to trap as many electrons as possible (i.e. one per channel) with spin opposite to the one sitting at the impurity site. This results in a local effective spin of size $S - \frac{K}{2} = \frac{P-K}{2}$, hence three possibilities:

- $K < P$: Underscreened

  The trapped electrons cannot quench completely the impurity spin, so that the dressed impurity remains magnetic with a spin of reduced size. Virtual hopping to the first layer of neighbors with strength t generates a new Kondo effect between the residual spin and the conduction electrons with a weak ferromagnetic coupling $J_{\text{eff}} \sim \frac{t^2}{J_K}$ which vanishes in the infinite coupling limit, suggesting that the $J_K \to \infty$ fixed point is stable.

- $K = P$: Exactly screened

  The ground state is non degenerate and the strong coupling fixed point is attractive: the usual Fermi liquid picture applies.

- $K > P$: Overscreened

  Like the underscreened case, this leads to a finite residual spin, weakly coupled to the conduction electrons. However, the sign of this residual spin is opposite to the starting impurity spin S, so that the effective Kondo coupling between this residual spin and the conduction electrons is now antiferromagnetic: the $J_K \to \infty$ fixed point is now unstable.

The strong coupling arrangement of spins for the impurity and the trapped electrons for the various cases is presented in fig. 6.2.

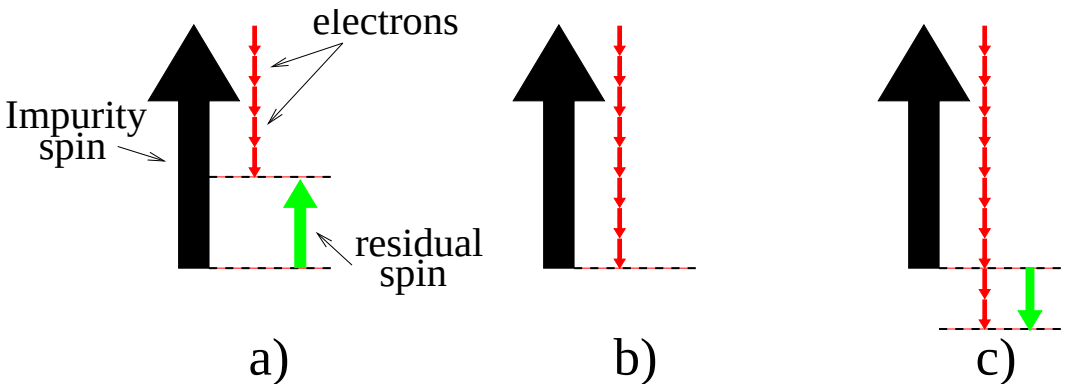

Figure 6.2: Schematic view of the three screening regimes: a) Underscreened case, b) Exactly screened case, c) Overscreened case. The large black arrow corresponds to the impurity spin, the small red ones to the electrons and the green arrow to the residual spin

□ Using Young tableaux

As one extends the original symmetry to $SU(N)$, the same kind of arguments hold but the derivation is more involved. However, there is a much easier and more convenient way of describing the physics of the strong coupling limit by using Young tableaux.

The idea is that for any given line representation of the impurity spin, each box can combine with a column of $N-1$ boxes representing the conduction electrons in order to form a spin singlet (the Pauli principle imposes that the total number of boxes per column cannot be greater than the spin degeneracy N). For a single channel, this is represented by fig.6.1c. As soon as one increases the number of channels, it becomes possible to form a singlet between the second box of the line representation and a column of conduction electrons taken in another channel.

For a given size of the impurity spin, i.e. a given length P of the line representation, one can identify three regimes depending on the total number of channels, just like in the $SU(2)$ case. One expects the following strong-coupling limits:

- Underscreened: $P > K$

  The conduction electron screens part of the impurity spin, leaving behind a residual spin of size $S = \frac{P-K}{2}$. The expected low-energy physics is then the one of a local moment, decoupled from the conduction electron band at zero temperature. As one departs slightly from this strong-coupling fixed point, a weak ferromagnetic effective Kondo interaction is restored signaling the stability of this fixed point.

- Exactly screened: $P = K$

  The impurity spin is totally screened in this case and forms an antiferromagnetic singlet. The impurity site is then locked and acts as a scattering center for the conduction electrons. One expects the low-energy physics to be Fermi-liquid like with a finite phase shift on the site of the impurity.

- Overscreened: $P < K$

  The number of screening channels is too important. A residual spin of size $S = \frac{K-P}{2}$ now remains. However, a small departure from this fixed point leads to a residual antiferromagnetic Kondo interaction, so that the strong-coupling fixed point is unstable and the system flows towards a stable infra-red fixed point. One expects from other investigations that this fixed point is non-Fermi-liquid like.

It follows that the generalization of the Kondo model to the $SU(N)$ symmetry gives qualitatively similar results to the $SU(2)$ case, which motivates the study of the generalized multichannel Kondo model in the large-N limit.

These three regimes are represented in fig.6.3, where the impurity spin is described by white boxes and the conduction electrons by gray ones.

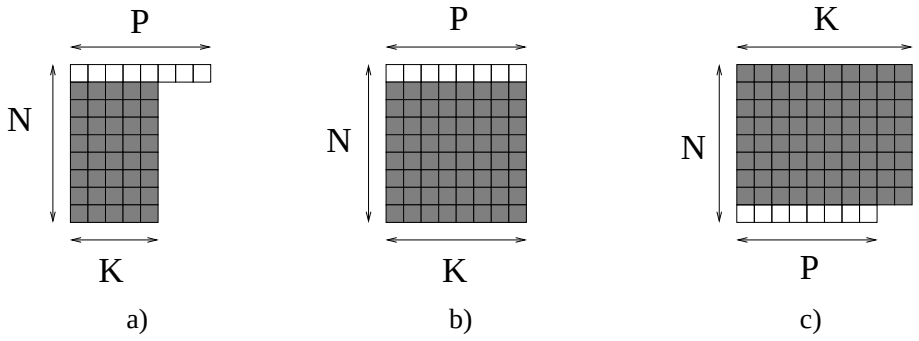

Figure 6.3: a) Underscreened case, b) Exactly screened case, c) Overscreened case. The impurity spin is described by a line of white boxes and the conduction electrons by a column of gray ones.

6.1.3 Saddle-point equations

In order to derive the large-N equations, we consider the multichannel Hamiltonian with a bosonic representation of the impurity spin, where we explicitly include the constraint on the total number of Schwinger bosons via a Lagrange multiplier. The action then reads:

$$\begin{aligned} S &= \int_0^\beta d\tau \sum_{\mathbf{k},\sigma,\mu} c^\dagger_{\mathbf{k}\sigma\mu}(\tau)\left(\partial_\tau + \epsilon_{\mathbf{k}}\right) c_{\mathbf{k}\sigma\mu}(\tau) + \int_0^\beta d\tau \sum_\alpha b^\dagger_\alpha(\tau)\left(\partial_\tau - \lambda(\tau)\right) b_\alpha(\tau) \\ &\quad + \frac{J_K}{N}\sum_{\alpha,\beta,\mu}\int_0^\beta d\tau\ \psi^\dagger_{\beta\mu}(\tau)\psi_{\alpha\mu}(\tau)b^\dagger_\alpha(\tau)b_\beta(\tau) \\ &\quad + p_0 N\int_0^\beta d\tau\ \lambda(\tau) - \frac{p_0 J_K}{N}\int_0^\beta d\tau \sum_{\alpha,\mu}\psi^\dagger_{\alpha\mu}(\tau)\psi_{\alpha\mu}(\tau) \end{aligned} \tag{6.8}$$

where $\psi^\dagger_{\alpha\mu} = \frac{1}{\sqrt{N}}\sum_{\mathbf{k}} c^\dagger_{\mathbf{k}\alpha\mu}$ creates an electron in the Wannier state at the impurity site.

Taking the limit of infinite N, one has to rescale the parameters P and K with N in order to describe a non-trivial case. We then define the following rescaled parameters:

$$P = p_0 N \qquad K = \gamma N \tag{6.9}$$

It is important to notice that this rescaling in N preserves the distinction between the three regimes: $p_0 > \gamma$ corresponds to the underscreened case, $p_0 = \gamma$ to the exactly screened case and $p_0 < \gamma$ to the overscreened case.

The first step is to integrate out of the partition function all of the conduction electrons, apart from the ones at the impurity site. We then decouple the interacting term by introducing an auxiliary grassmanian field[1] $\chi_\mu(\tau)$ for every channel index, which leaves us with the following action:

$$\begin{aligned} S &= -\int_0^\beta d\tau d\tau' \sum_{\sigma,\mu}\psi^\dagger_{\sigma\mu}(\tau)G^{-1}_{c0}\left(\tau-\tau'\right)\psi_{\sigma\mu}(\tau') - \frac{1}{J_K}\int_0^\beta d\tau \sum_\mu \chi^\dagger_\mu(\tau)\chi_\mu(\tau) \\ &\quad + p_0 N\int_0^\beta d\tau\ \lambda(\tau) + \int_0^\beta d\tau \sum_\alpha b^\dagger_\alpha(\tau)\left(\partial_\tau - \lambda(\tau)\right) b_\alpha(\tau) \\ &\quad + \frac{1}{\sqrt{N}}\sum_{\alpha,\mu}\int_0^\beta d\tau\ \left(\psi^\dagger_{\alpha\mu}(\tau)b_\alpha(\tau)\chi_\mu(\tau) + \chi^\dagger_\mu(\tau)b^\dagger_\alpha(\tau)\psi_{\alpha\mu}(\tau)\right) \end{aligned} \tag{6.10}$$

where we have dropped the $\frac{p_0 J_K}{N}\psi^\dagger\psi$ term since it only contributes to the local electronic Green's function to the order $1/N$.

[1] Note that the fields χ_μ contain no time derivative, so that instantaneously they behave as inert neutral fields.

The bare local conduction electron Green's function G_{c0} is given by:

$$G_{c0}(i\omega_n) = \sum_{\mathbf{k}} \frac{1}{i\omega_n - \epsilon_{\mathbf{k}}} \tag{6.11}$$

The actual choice of the conduction band does not matter much as long as we are interested in a regime of temperature much smaller than the bandwidth: we only probe the low-energy excitations, and only the density of states at the Fermi level really matters.

There are two different ways of obtaining the saddle-point equations for the Green's functions. First, we choose to derive them following the work of [103]. Then, we derive them from a Luttinger-Ward[105, 106, 107] perspective, as this will turn out to be useful in many aspects in the rest of the text.

□ Derived from the action

The first step is to integrate the remaining conduction electrons out of the partition function to end up with an effective action depending only on the Schwinger bosons and the χ fermions:

$$\begin{aligned} S &= \int_0^\beta d\tau \ \sum_\alpha b_\alpha^\dagger(\tau)\left(\partial_\tau - \lambda(\tau)\right) b_\alpha(\tau) - \frac{1}{J_K}\int_0^\beta d\tau \ \sum_\mu \chi_\mu^\dagger(\tau)\chi_\mu(\tau) \\ &\quad -\frac{1}{N}\int_0^\beta d\tau d\tau' \ \sum_\mu \chi_\mu(\tau')\chi_\mu^\dagger(\tau) \ G_{c0}(\tau-\tau') \ \sum_\alpha b_\alpha(\tau')b_\alpha^\dagger(\tau) \\ &\quad +p_0 N\int_0^\beta d\tau \ \lambda(\tau) \end{aligned} \tag{6.12}$$

It is useful at this stage to introduce the following precursors to the Green's functions:

$$N_\chi(\tau,\tau') = \sum_\mu \chi_\mu(\tau')\chi_\mu^\dagger(\tau) \qquad\qquad N_b(\tau,\tau') = \sum_\alpha b_\alpha(\tau')b_\alpha^\dagger(\tau) \tag{6.13}$$

One now introduces two new fields labeled $Q(\tau,\tau')$ and $\bar{Q}(\tau,\tau')$,conjugated respectively to $N_\chi(\tau,\tau')$ and $N_b(\tau,\tau')$. The idea is to generalize to a path-integral formulation the following result:

$$\int dX dY \ e^{-AXY + X\phi + Y\psi} = \text{Const.} \times e^{\phi A^{-1}\psi} \tag{6.14}$$

The partition function can be rewritten as $Z = \int \mathcal{D}Q\mathcal{D}\bar{Q}\mathcal{D}\lambda \ e^{-S(Q,\bar{Q},\lambda)}$ with the effective action expressed in terms of these new fields:

$$\begin{aligned} S(Q,\bar{Q},\lambda) &= N\int_0^\beta d\tau d\tau' \ \bar{Q}(\tau,\tau')G_{c0}^{-1}(\tau-\tau')Q(\tau,\tau') + p_0 N\int_0^\beta d\tau \ \lambda \\ &\quad -N\log Z_b(Q,\bar{Q},\lambda) - K\log Z_\chi(Q,\bar{Q},\lambda) \end{aligned} \tag{6.15}$$

where the partial partition functions are defined as:

$$\begin{aligned} Z_b &= \int \mathcal{D}b^\dagger \mathcal{D}b \; e^{-\int_0^\beta d\tau \; b^\dagger(\tau)(\partial_\tau - \lambda(\tau))b(\tau) + \int d\tau d\tau' Q(\tau,\tau') b(\tau') b^\dagger(\tau)} \\ Z_\chi &= \int \mathcal{D}\chi^\dagger \mathcal{D}\chi \; e^{-\int_0^\beta d\tau \; \chi^\dagger(\tau)(\partial_\tau - \lambda(\tau))\chi(\tau) + \int d\tau d\tau' \bar{Q}(\tau,\tau') \chi(\tau') \chi^\dagger(\tau)} \end{aligned} \tag{6.16}$$

The important element here is that every term in $S(Q, \bar{Q}, \lambda)$ scales like N, so that in the large-N limit one can apply the method of steepest descent. The saddle-point is such as the derivatives of $S(Q, \bar{Q}, \lambda)$ with respect to its variables all vanish:

$$\begin{aligned} \frac{\delta S(Q,\bar{Q},\lambda)}{\delta Q(\tau,\tau')} = 0 \quad &\Longrightarrow \quad \bar{Q}(\tau,\tau') = -G_{c0}(\tau - \tau') G_b(\tau' - \tau) \\ \frac{\delta S(Q,\bar{Q},\lambda)}{\delta \bar{Q}(\tau,\tau')} = 0 \quad &\Longrightarrow \quad Q(\tau,\tau') = -\gamma G_{c0}(\tau - \tau') G_\chi(\tau' - \tau) \\ \frac{\delta S(Q,\bar{Q},\lambda)}{\delta \lambda(\tau)} = 0 \quad &\Longrightarrow \quad p_0 = -G_b(\tau = 0^-) \end{aligned} \tag{6.17}$$

where we use the conventional definition of the Green's functions as:

$$\left\{ \begin{array}{rclcl} G_b(\tau) &=& -\langle T b(\tau) b^\dagger(0) \rangle_Z &=& -\langle T b(\tau) b^\dagger(0) \rangle_{Z_b} \\ G_\chi(\tau) &=& -\langle T \chi(\tau) \chi^\dagger(0) \rangle_Z &=& -\langle T \chi(\tau) \chi^\dagger(0) \rangle_{Z_\chi} \end{array} \right. \tag{6.18}$$

A careful look at (6.18) and (6.16) suggests that $Q(\tau,\tau')$ (resp. $\bar{Q}(\tau,\tau')$) is trivially related to the self-energy $\Sigma_b(\tau - \tau')$ (resp. $\Sigma_\chi(\tau - \tau')$):

$$\Sigma_b(\tau) = \gamma G_{c0}(\tau) G_\chi(-\tau) \qquad \Sigma_\chi(\tau) = -G_{c0}(\tau) G_b(-\tau) \tag{6.19}$$

where the self-energies are defined as:

$$G_b^{-1}(i\nu_n) = i\nu_n + \lambda - \Sigma_b(i\nu_n) \qquad G_\chi^{-1}(i\omega_n) = J_K - \Sigma_\chi(i\omega_n) \tag{6.20}$$

These saddle-point equations are valid for any shape of the conduction band, in particular there is no need to impose particle-hole symmetry. The striking feature of these saddle-point equations is that they are expressed in terms of the one-particle Green's functions only, so that once the solution is achieved, one gets access to all the correlation functions of the model (Susceptibility, free energy, entropy, ...).

□ Derived from a Luttinger-Ward picture

It is possible to derive the self-consistent equations for the self-energies starting from the free energy of the model. In the Baym-Kadanoff[108, 109] formalism, the free

energy can be recast as a functional of the various Green's functions one has to consider[2]:

$$\begin{aligned} F &= NT\sum_n \log(-G_b^{-1}(i\nu_n)) - KT\sum_n \log(-G_\chi^{-1}(i\omega_n)) \\ &\quad -NKT\sum_n \log(-G_c^{-1}(i\omega_n)) + NT\sum_n \Sigma_b(i\nu_n)G_b(i\nu_n) \\ &\quad -KT\sum_n \Sigma_\chi(i\omega_n)G_\chi(i\omega_n) - NKT\sum_n \Sigma_c(i\omega_n)G_c(i\omega_n) \\ &\quad +Np_0\lambda + \Phi_{LW}[G_b, G_\chi, G_c] \end{aligned} \tag{6.21}$$

The Luttinger-Ward functional $\Phi_{LW}[G_b, G_\chi, G_c]$ is given by the sum of all 2-particle irreducible diagrams. Some of these diagrams are presented in fig. 6.4, where we use straight lines for the conduction electron, wiggly lines for the Schwinger boson and dashed lines for the $\chi-$fermion full propagators. This sum ultimately reduces to the first leading order diagram, once we take the large-N limit.

$\Phi_{LW}[G_b, G_\chi, G_c] =$

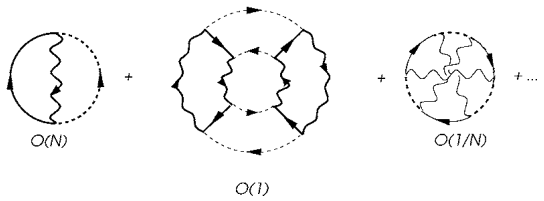

Figure 6.4: Some of the skeleton diagrams contributing to the Luttinger-Ward functional.

Using the stationarity of the free energy functional with respect to the Green's functions G_b, G_χ and G_c, one can see that at the saddle-point, the self-energies associated to these fields can be expressed as a derivative of the Luttinger-Ward functional, leading to:

$$\begin{aligned} \Sigma_b(\tau) &= \frac{-1}{N}\frac{\delta\Phi_{LW}}{\delta G_b(\beta-\tau)} = \\ \Sigma_\chi(\tau) &= \frac{-1}{K}\frac{\delta\Phi_{LW}}{\delta G_\chi(\beta-\tau)} = \\ \Sigma_c(\tau) &= \frac{-1}{NK}\frac{\delta\Phi_{LW}}{\delta G_c(\beta-\tau)} = \end{aligned} \tag{6.22}$$

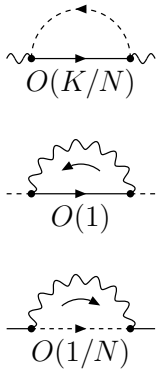

[2]The actual derivation of this expression for a single impurity Kondo model is given in Appendix A.

Each of these terms contains a factor $O(1/N)$ from the vertices, but the first two self-energies contain summations over the internal channel or spin indices, elevating Σ_b and Σ_χ to terms of order $O(1)$. However, in the leading order large N approximation, $\Sigma_c \sim O(1/N)$, so that a consistent large N approximation is produced by leaving the conduction electron lines un-dressed.

This provides an alternative diagrammatic derivation of the Parcollet-Georges approach.

□ Causality

It is interesting, now that we have derived the self-consistent equations for the Green's functions, to check that they respect the causality rules, i.e. that the imaginary part of the retarded self-energies and Green's functions have the right sign as a function of frequency.

In order to do so, we start expressing the imaginary part of the retarded self-energy and Green's function for the Schwinger boson:

$$G_b''(\nu + i\delta) = \frac{\Sigma_b''}{\left|\omega + \lambda - \Sigma_b(\omega + i\delta)\right|^2} \tag{6.23}$$

$$\Sigma_b''(\nu + i\delta) = \pi\gamma J_K^2 \int d\Omega \rho_c(\Omega + \nu)\rho_\chi(\Omega)\left[f(\Omega + \nu) - f(\Omega)\right] \tag{6.24}$$

where $f(\omega)$ is the temperature dependent Fermi function.

From this, it follows that G_b respects the causality rules provided that Σ_b does. It is then obvious that $[f(\Omega + \nu) - f(\Omega)]$ has the sign of ν for any given value of Ω, so that, assuming both fermionic fields respect causality, one has:

$$\Sigma_b''(\nu + i\delta) \propto -\mathrm{Sgn}(\nu) \tag{6.25}$$

which is one would expect if G_b were causal.

The same kind of reasoning extends to the $\chi-$fermion: the causality of G_χ is ensured by the causality of Σ_χ, since it is preserved by the Dyson's equation. Its imaginary part is given by:

$$\Sigma_\chi''(\omega + i\delta) = -\pi J_K^2 \int d\Omega \rho_c(\Omega + \omega)\rho_b(\Omega)\left[f(\Omega + \omega) + f(\Omega)\right] \tag{6.26}$$

It is easy to rewrite $[f(\Omega + \omega) + f(\Omega)]$ as a positive function of both frequencies divided by $\tanh\left(\frac{\beta\Omega}{2}\right)$ which obviously has the sign of Ω for any given value of ω. If both G_c and G_b respects causality, one has $\Sigma_\chi''(\omega + i\delta) < 0$ over the whole range of frequency, so that G_χ is also causal.

As a conclusion, the causality is built into the self-consistent equations, so that recursively, these rules are respected provided that the starting point at high-temperature is itself causal.

□ Set of equations

Here is a reminder of the whole set of equations we will refer to, in the rest of this text:

$$\text{Dyson's equations:} \quad G_b^{-1}(i\nu_n) = i\nu_n + \lambda - \Sigma_b(i\nu_n) \tag{6.27a}$$

$$G_\chi^{-1}(i\omega_n) = J_K - \Sigma_\chi(i\omega_n) \tag{6.27b}$$

$$\text{Schwinger boson:} \quad \Sigma_b(\tau) = -\gamma J_K^2 G_c(\tau) G_\chi(\beta - \tau) \tag{6.27c}$$

$$\chi\text{−fermion:} \quad \Sigma_\chi(\tau) = -J_K^2 G_c(\tau) G_b(\beta - \tau) \tag{6.27d}$$

$$\text{Conduction electron}^3\text{:} \quad \rho_c(\omega) = \rho_0 \Theta\left(D^2 - \omega^2\right) \tag{6.27e}$$

$$\text{Constraint:} \quad -G_b(\tau = 0^-) = \int d\omega \rho_b(\omega) n(\omega) = p_0 \tag{6.27f}$$

where all the spectral functions are defined as $\rho(\omega) = \frac{-1}{\pi}\text{Im}G(\omega + i\delta)$, and $n(\omega)$ is the Bose function.

To conclude, the Kondo problem reduces to this set of coupled integral equations in the large-N limit. Once these equations are solved, their solution gives access to all physical quantities, from the thermodynamics to the correlation functions.

6.2 Known results

The saddle-point equations (6.27c) and (6.27d) have been studied in great details for both the overscreened and the underscreened cases [103, 110]. It is actually rather hard to solve them exactly: even though these self-consistent equations are nothing but convolutions, the Dyson's equations make the self-consistency much more difficult to handle analytically than one would expect. It is quite interesting that the same set of integral equations gives very different results as one tunes the impurity spin from $p_0 > \gamma$ to $p_0 < \gamma$. This feature is still not well understood from the analytical point of view.

Nevertheless, one can explore some of the properties of these two regimes thanks to two methods:

1. A partial analytic solution at low-temperature. This allows to explore the low-energy behavior, in particular for the overscreened case where conformal field theory helps in the derivation of the scaling function in temperature, the behavior of the entropy and the specific heat.

2. A full numerical solution. This allows to explore the whole range in temperature and in particular the cross-over between the high and the low temperature regimes.

[3] We choose a flat band of conduction electron for simplicity but the saddle-point equations are independent on the actual form of the band. Moreover, as argued before, the actual shape of the density of states does not matter at low temperature.

In the next paragraphs, we recall some of the established results concerning the high-temperature and the low-temperature limit for all three regimes of screening.

6.2.1 High temperature regime

At high temperature, the system behaves as a free spin of size $s = p_0/2$: both self-energies are negligible compared to the free part of the Green's functions. This is independent on the number of channels since the Kondo interaction is too small to affect the impurity spin at high temperature.

It follows that the bosonic spectral function is given by a single $\delta-$peak:

$$\rho_b(\omega) = \delta(\omega + \lambda) \tag{6.28}$$

where the chemical potential λ is set by the constraint (6.27f). It follows that $n(-\lambda) = p_0$, so that one can rewrite the chemical potential as:

$$\lambda^{\text{High T}} = -T \log\left(\frac{1+p_0}{p_0}\right) \tag{6.29}$$

Replacing the expression for the bosonic Green's function into the free energy (6.21), and neglecting all self-energies with respect to the bare propagators, one has for the impurity free energy:

$$\begin{aligned} F_{\text{imp}}^{\text{High T}} &= F - F_{\text{bulk}} = NT \sum_n \log(-i\nu_n - \lambda) + Np_0\lambda(T) && (6.30)\\ &= NT\left[p_0 \log p_0 - (p_0+1)\log(p_0+1)\right] && (6.31)\end{aligned}$$

where we have subtracted the contribution from the conduction electron band to the free energy, labeled F_{bulk}.

From this, one can easily deduce that the high-temperature limit of the impurity entropy per spin flavor is:

$$s_{\text{imp}}^{\text{High T}} = -\frac{1}{N}\frac{\partial F_{\text{imp}}}{\partial T} = (p_0+1)\log(p_0+1) - p_0 \log p_0 \tag{6.32}$$

Finally, one can compute the local susceptibility: this quantity is defined as the susceptibility of the system when only the impurity is coupled to the external magnetic field (see Appendix B for more details about the difference between local and impurity susceptibility). The local susceptibility then writes:

$$\begin{aligned} \chi_{\text{loc}} &= \frac{1}{N^2}\int_0^\beta d\tau \sum_{\alpha\beta} \langle S_{\alpha\beta}(\tau) S_{\beta\alpha}(0)\rangle = \int_0^\beta d\tau G_b(\tau) G_b(\beta-\tau) \\ \chi_{\text{loc}}^{\text{High T}} &= \frac{p_0(p_0+1)}{T} && (6.33)\end{aligned}$$

which, as expected, gives a Curie law with a Curie constant κ depending on the size of the spin: $\kappa = p_0(p_0+1)$.

As the temperature is lowered, all these quantities cross-over to their low-T counterpart which now strongly depends on the screening regime considered.

6.2.2 Overscreened case: $p_0 < \gamma$

This section is devoted to the results of the overscreened regime. All the analytical results presented in this section have been derived in [103] and [110]. However, all the numerical data have been recomputed for illustrative purposes and as a test for our new set of programs.

□ Spectral functions

It is possible to extract the low-energy behavior of the Green's functions in the zero temperature limit. This derivation rests on a numerical observation, namely that as the temperature is reduced towards zero, both Green's functions seem to diverge at zero energy. This can be recast as:

$$\lambda - \Sigma_b(0 + i\delta) \underset{T\to 0}{\longrightarrow} 0 \tag{6.34}$$

$$J_K - \Sigma_\chi(0 + i\delta) \underset{T\to 0}{\longrightarrow} 0 \tag{6.35}$$

as one can see from the numerical data presented in fig. 6.5.

Using this as a hint, and a power-law ansatz for the Green's functions, one can perform a low-energy analysis identical in spirit to the one in [111]. The idea is to plug the ansatz into the self-energy equations and to identify the results self-consistently with the starting functions. This analysis leads to the following power-laws for the Green's functions:

$$G_b(\omega + i\delta) \sim \frac{A_+\theta(\omega) + A_-\theta(-\omega)}{|\omega|^{\frac{\gamma}{1+\gamma}}} \tag{6.36}$$

$$G_\chi(\omega + i\delta) \sim \frac{B_+\theta(\omega) + B_-\theta(-\omega)}{|\omega|^{\frac{1}{1+\gamma}}} \tag{6.37}$$

where $A_\pm$ and $B_\pm$ are constants.

Both Green's functions are singular at zero frequency, with a power-law divergence whose exponent does not depend on the size of the spin. This exponent is the same on both side of the singularity, but the prefactor is different: there is a spectral asymmetry that can be parametrized through the argument $\theta_\pm$ of $A_\pm$ (the self-consistency ensures that $B_\pm$ can be expressed in terms of $|A_\pm|$ and $\theta_\pm$).

Thanks to a procedure similar in many aspects to the proof of the Luttinger theorem for Fermi liquids [105, 106], one can relate the size of the spin to the low-energy parameters $\theta_\pm$, which ultimately leads to:

$$\begin{cases} \sin\theta_+ &= \sin\left(\dfrac{\pi(\gamma - p_0)}{1+\gamma}\right) \\ \sin\theta_- &= -\sin\left(\dfrac{\pi p_0}{1+\gamma}\right) \end{cases} \tag{6.38}$$

Finally, it is important to notice that the singularity at zero frequency is actually regularized at finite temperature. From this observation, Parcollet et al. [110] could infer a finite temperature ansatz for the Green's functions that satisfies the saddle-point equations. In the low-energy, low temperature limit, one can see ω/T scaling in the spectral functions, so that at the leading order in temperature:

$$\rho_b(\omega) \propto T^{-\frac{\gamma}{1+\gamma}} \phi_b\left(\frac{\omega}{T}\right) \qquad \rho_\chi(\omega) \propto T^{-\frac{1}{1+\gamma}} \phi_\chi\left(\frac{\omega}{T}\right) \tag{6.39}$$

where the $\phi_{b,\chi}$ scaling functions have a complicated expression in terms of Γ functions. This feature can be seen numerically from inspecting the zero-energy inverse Green's function as a function of temperature, which turn out to behave as the expected power-laws (see Fig. 6.5).

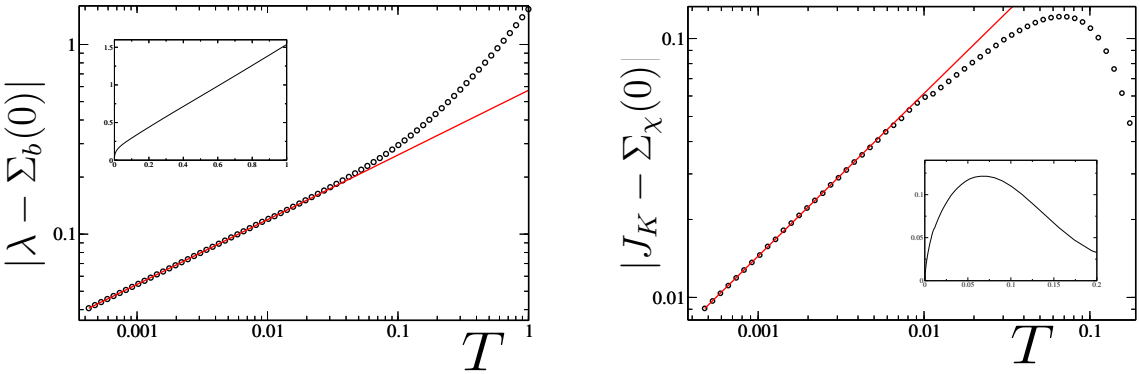

Figure 6.5: Inverse Green's functions at zero energy as a function of temperature on a double-log plot. The dots correspond to numerical data, and the straight lines to power-law fits, with an exponent of 0.341 and 0.628 for $|\lambda - \Sigma_b(0)|$ and $|J - \Sigma_\chi(0)|$. The corresponding exponents predicted by the analytic treatment are 1/3 and 2/3, respectively. The insets show the same data on a linear scale to stress out the vanishing of both quantities at low temperature.

□ Entropy and specific heat

From the scaling function in temperature, it is possible to compute the free energy at low temperature, at the saddle point, and from there to extract the residual entropy of the impurity. This turns out to be much more difficult than it seems, since because of the ω/T scaling of the spectral function, a small temperature Sommerfeld-like expansion is not possible here.

In the overscreened regime, the residual entropy per spin flavor of the impurity is given by:

$$s_{\text{imp}}^{\text{Res}} = \frac{1+\gamma}{2\pi} \text{Im}\left[\text{Li}_2\left(e^{2i\frac{\pi p_0}{1+\gamma}}\right) + \text{Li}_2\left(e^{2i\frac{\pi}{1+\gamma}}\right) - \text{Li}_2\left(e^{2i\frac{\pi(1+p_0)}{1+\gamma}}\right)\right] \tag{6.40}$$

where $\text{Li}_2(x)$ is the dilogarithm function.

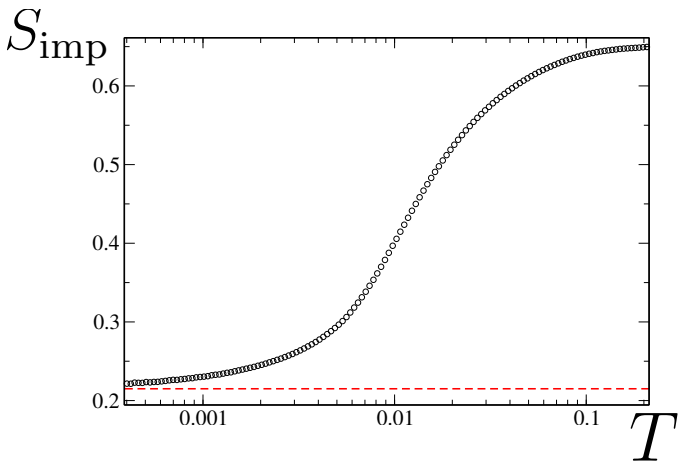

Figure 6.6: Entropy as a function of temperature in the overscreened case ($p_0 = 0.3, \gamma = 0.4$). The red dotted line correponds to the residual entropy computed with the expression given in the text, Eq. (6.40).

To access the specific heat coefficient, the expression of the spectral functions to the leading-order in temperature is not sufficient, and one has to push the low-temperature expansion to higher order. This allows to take the second derivative of the impurity free energy, which leads to the following result for the specific heat coefficient:

$$\begin{aligned} \gamma > 1: \quad \frac{C_v}{T} &\sim \left(\frac{1}{T}\right)^{\frac{\gamma-1}{\gamma+1}} \\ \gamma = 1: \quad \frac{C_v}{T} &\sim \log\left(\frac{1}{T}\right) \\ \gamma < 1: \quad \frac{C_v}{T} &\sim \text{const.} \end{aligned} \tag{6.41}$$

The asymmetry between the $\gamma < 1$ and the $\gamma > 1$ regimes is an artifact of the Kondo model. In the Anderson model, the symmetry is restored and one finds a diverging specific heat coefficient for $\gamma < 1$, namely $C_v/T \sim (1/T)^{\frac{1-\gamma}{\gamma+1}}$.

□ Susceptibility

It is possible from a conformal field theory point of view to derive the temperature dependence of the local spin susceptibility at low temperature. The latter turns out

to behave as a function of temperature just like the specific heat coefficient, i.e.:

$$\begin{aligned} \gamma > 1: \quad \chi_{\rm loc} &\sim \left(\frac{1}{T}\right)^{\frac{\gamma-1}{\gamma+1}} \\ \gamma = 1: \quad \chi_{\rm loc} &\sim \log\left(\frac{1}{T}\right) \\ \gamma < 1: \quad \chi_{\rm loc} &\sim \text{const.} \end{aligned} \tag{6.42}$$

For $\gamma \geq 1$, this can be easily re-derived from the expression of the local susceptibility in terms of the bosonic Green's functions, and the scaling form in temperature of G_b[4]. For $\gamma < 1$, however, the prefactor of the divergent term vanishes so that only a constant term remains in the low temperature limit. Again, this is a peculiarity of the Kondo model and the divergence with the expected power in T is recovered in the Anderson model.

6.2.3 Underscreened case: $p_0 > \gamma$

This section is devoted to the results of the underscreened regime. Again, all the analytical results presented in this section have been derived in [103] and [112], and the numerical data have been recomputed for illustrative purposes and as a test for our new set of programs.

□ Spectral functions

We know from the strong coupling analysis that the underscreened regime leads to a partially screened impurity spin, so that we expect the physics to look like a residual spin of size $p_0 - \gamma$, weakly ferromagnetically coupled to a bath of conduction electrons.

It follows that the expected bosonic spectral function looks like the one of a local moment, with sub-leading terms:

$$\rho_b(\omega) = \delta(\omega + \mu T) + \Phi_b(\omega) \tag{6.43}$$

where $\mu = -\log\left(\frac{p_0-\gamma+1}{p_0-\gamma}\right)$ as one expects for the chemical potential associated to a spin of size $p_0 - \gamma$.

Of course, in order to maintain the constraint as well as the normalization of this spectral function, one would expect that:

$$\int d\omega \Phi_b(\omega) = 0 \qquad \int d\omega \Phi_b(\omega) n(\omega) = \gamma \tag{6.44}$$

[4]The integral brings a power of T and the two powers of G_b a term in $T^{\frac{2\gamma}{1+\gamma}}$.

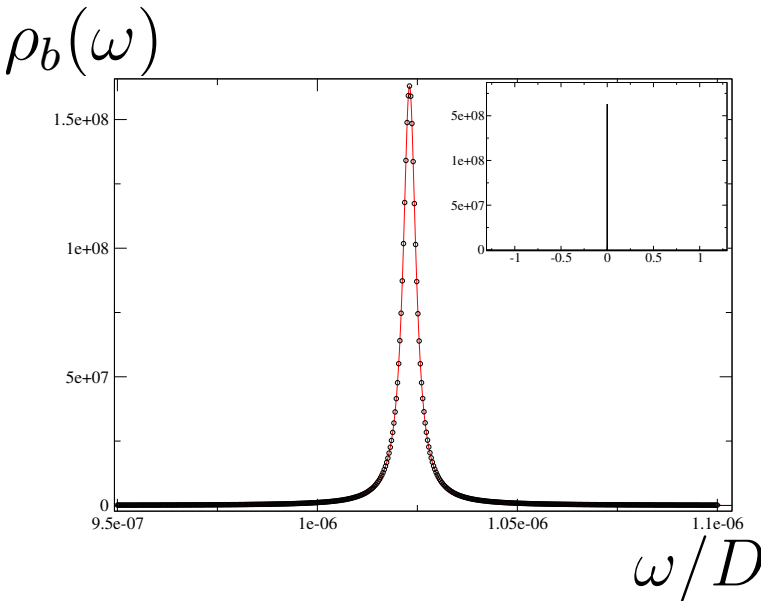

Figure 6.7: Bosonic spectral function at $T \sim 10^{-3} T_K$. The fit is a Lorentzian whose width decreases with temperature, consistent with a δ-peak in the zero temperature limit. In the inset, we show the same spectral function on the scale D.

The self-consistency imposes that upon substituting (6.43) into the self-energy equation for the $\chi-$fermion, one has:

$$\begin{aligned}\Sigma_\chi(\omega) &= \Phi_\chi(\omega) + \rho_0 J_K^2 (p_0 - \gamma)\left[\log\left|\frac{D+\omega-\mu T}{D-\omega+\mu T}\right| - i\pi\Theta(D^2-(\omega-\mu T)^2)\right] \\ &\quad + \rho_0 J_K^2 \log\left(\frac{D}{2\pi T}\right) - \rho_0 J_K^2\left[\Psi\left(\frac{1}{2} - i\frac{\omega-\mu T}{2\pi T}\right) + i\frac{\pi}{2}\right] \qquad (6.45)\end{aligned}$$

where $\Phi_\chi(\omega)$ is a sub-leading term arising from $\Phi_b(\omega)$, and $\Psi(x)$ is the di-gamma function.

Noticing that this diverges as $\log T$ as $T \to 0$, and plugging it back into the bosonic self-energy, one has: $\Sigma_b(\omega) - \Sigma_b(0) \sim -\gamma \dfrac{\omega}{\log T} + \ldots$, so that our ansatz is consistent.

This finally leaves us with the following inverse Green's functions at zero energy:

$$\lambda - \Sigma_b(0) \sim \mu T + \ldots \qquad (6.46)$$

$$J_K - \Sigma_\chi(0) \sim \rho_0 J_K^2 \log T + \ldots \qquad (6.47)$$

The divergence of the inverse $\chi-$fermion propagator at zero energy prevents a low-energy analysis like the one carried out for the overscreened case. This logarithmic divergence can be interpreted physically as arising from the effective ferromagnetic coupling between the residual spin and the electronic bath. Since we

introduced the χ fermion to decouple the Kondo interaction, the associated Green's function describes the effective Kondo coupling J_K^* between the residual spin and the conducting bath: as $T \to 0$, this coupling becomes negative and vanishes like $1/\log T$, consistent with a marginally irrelevant ferromagnetic coupling.

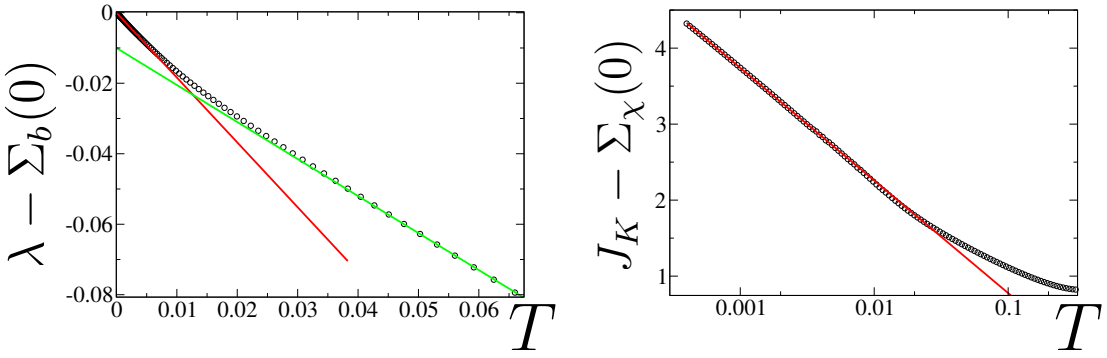

Figure 6.8: Inverse Green's functions at zero energy as a function of temperature. The dots correspond to numerical data, and the straight lines to fits: linear in the case of $\lambda - \Sigma_b(0)$ and logarithmic for $J - \Sigma_\chi(0)$.

The validity of our ansatz is verified from the numerical solution (see Figs. 6.8 and 6.7) where one sees the $\log T$ dependence of J_K^*, as well as the linear behavior of the renormalized bosonic chemical potential both in the high and low temperature regime with a change of slope related to the change in the size of the effective impurity spin.

□ Entropy and Susceptibility

The low-temperature physics is dominated by the local moment physics, since the effective coupling between the residual spin and the conduction band vanishes as $T \to 0$. As a consequence, both the entropy and the local susceptibility at zero temperature look like the ones of an isolated spin.

One then expects that the underscreened case at low temperature gives the same behavior as the ones we obtained for the high-temperature regime only for a spin of size $p_0 - \gamma$ instead of p_0. It follows that the residual entropy of the underscreened Kondo model is given by:

$$s_{\text{imp}} = (p_0 - \gamma + 1)\log(p_0 - \gamma + 1) - (p_0 - \gamma)\log(p_0 - \gamma) \tag{6.48}$$

and the local susceptibility at low-temperature is Curie-like, with a Curie constant $\kappa = (p_0 - \gamma)(p_0 - \gamma + 1)$:

$$\chi_{\text{loc}}^{\text{Low T}} \sim \frac{(p_0 - \gamma)(p_0 - \gamma + 1)}{T} \tag{6.49}$$

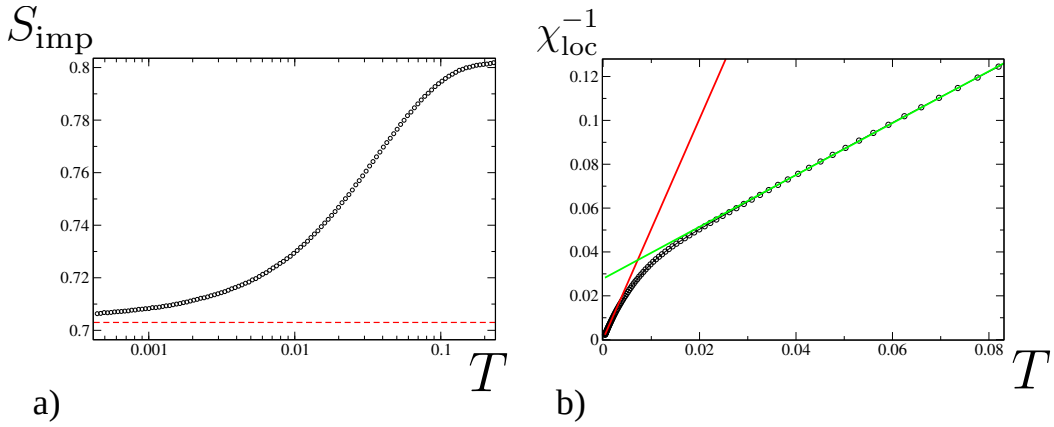

Figure 6.9: a) Entropy as a function of temperature on a logarithmic scale. The residual entropy at the lowest temperature achieved is very close to the theoretical value (red dotted line). b) The inverse local susceptibility is linear in both the high and low-temperature regime, with a net change in slope.

which we could verify numerically, as one can see from Fig. 6.9.

As one takes the $\gamma \to p_0$ limit, the residual entropy vanishes, as one would expect from the exactly screened case.

6.3 Exactly screened case: $p_0 = \gamma$

In this section we study the perfectly screened case which was thought to be a trivial non-interacting Fermi-liquid as an artifact of the large-N limit. We prove, helped by a numerical solution of the saddle-point equations, that this is not the case: even though the transport properties are indeed trivial in the large-N limit, one can recover the thermodynamics of a truly interacting Fermi liquid. The main results of this section have been published in the Publication 4, the rest is presented here for the first time.

6.3.1 General belief and counter-arguments

Previous works [103] on this large-N limit of the multichannel Kondo model focused on both the overscreened and the underscreened regimes, leaving the perfectly screened case aside. The general belief was that although the Kondo screening occurs at the leading order in N for the impurity, it only happens at a sub-leading order for the conduction electrons, so that the impurity doesn't seem to affect any properties of the Fermi liquid, even at the impurity site and one ends up describing a trivial non-interacting Fermi liquid.

This argument was backed up by the results of the Friedel sum rule [113] which predicts that the conduction electron phase shift on the impurity is given by $\delta_c = \frac{\pi}{N}$

so that both the phase shift and the $T-$matrix vanish in the large-N limit.

Although this argument is correct, the conclusions concerning the trivial Fermi liquid are not. Indeed, a vanishing phase shift only implies that the transport properties of the Fermi liquid cannot be recovered in the large-N limit. What was originally missed is that although the conduction electron self-energy is of order $O(1/N)$, it does participate to the thermodynamics because its effect is multiplied by the N spin components and the K scattering channels producing an $O(N)$ overall contribution.

This statement is not that obvious if one looks at the impurity free energy. The latter is defined as the difference between the total free energy and the bulk one (i.e. the one of the free conduction band). Starting from eq. 6.21 and removing the bulk free energy $F_{\rm bulk} = -NKT\sum_n \log\left(G_{c0}^{-1}(i\omega_n)\right)$, one can expand the conduction electron Green's function in $1/N$, so that the remaining terms look like:

$$\begin{aligned} F_{\rm imp} &= NT\sum_n \log(-G_b^{-1}(i\nu_n)) - KT\sum_n \log(-G_\chi^{-1}(i\omega_n)) \\ &\quad + NT\sum_n \Sigma_b(i\nu_n)G_b(i\nu_n) - KT\sum_n \Sigma_\chi(i\omega_n)G_\chi(i\omega_n) \\ &\quad + Np_0\lambda + \Phi_{LW}[G_b, G_\chi, G_c] \end{aligned} \tag{6.50}$$

This does not contain any explicit dependence on the conduction electron self-energy. However, it is possible from this expression to derive a closed form expression for the impurity entropy. This derivation is presented in Appendix A in the case of a single impurity and we only recall the result here:

$$\begin{aligned} \frac{S_{\rm imp}}{N} &= -\int \frac{d\omega}{\pi}\left[\frac{\partial n(\omega)}{\partial T}\left(\mathrm{Im}\log\left(-G_b^{-1}(\omega)\right) + G_b'(\omega)\Sigma_b''(\omega)\right)\right. \\ &\quad \left. +\gamma\frac{\partial f(\omega)}{\partial T}\left(\mathrm{Im}\log\left(-G_\chi^{-1}(\omega)\right) + G_\chi'(\omega)\Sigma_\chi''(\omega) - G_{c0}''(\omega)\tilde{\Sigma}_c'(\omega)\right)\right] \end{aligned} \tag{6.51}$$

where the notation $G'(\omega)$ and $G''(\omega)$ stands for the real and imaginary parts of the retarded Green's function $G(\omega + i\delta)$, and $\tilde{\Sigma}(\omega) = N\Sigma(\omega) = O(1)$.

It is obvious from (6.51) that the conduction electron self-energy plays a role in the thermodynamics even though it does not enter the self-consistent saddle-point equations. This motivated a careful analysis of the exactly screened regime despite the arguments related to the vanishing phase shift.

6.3.2 Spectral functions

□ Existence of a gap

The first interesting feature of the numerical solution of the saddle-point equations is the existence of a gap in both the bosonic and fermionic spectral functions at low temperature (see Fig. 6.10).

Even though we have no way of proving analytically that a gapped solution is favored in the case of a perfectly screened impurity, it is possible to show that a gapped solution is compatible with the saddle-point equations.

The imaginary parts of the self-energies, written in terms of real frequencies and taken at zero temperature, are given by:

$$\left\{\begin{array}{rcl} \Sigma_b''(\omega+i\delta) &=& -\pi\gamma J_K^2 \displaystyle\int_0^{-\omega} d\Omega\ \rho_c(\omega+\Omega)\rho_\chi(\Omega) \\ \\ \Sigma_\chi''(\omega+i\delta) &=& \pi J_K^2 \displaystyle\int_0^{-\omega} d\Omega\ \rho_c(\omega+\Omega)\rho_b(\Omega) \end{array}\right. \tag{6.52}$$

Assume that the bosonic spectral functions is gapped over the range of frequency $[-g_-, g_+]$, then the $\chi-$fermion self-energy and – upon a substitution in the Dyson's equation – the spectral function are both gapped, over a range of frequency that is now $[-g_+, g_-]$. Conversely, a gap in ρ_χ leads because of the self-consistency to a "mirrored" gap in ρ_b. This analysis is independent on the actual shape of the conduction band. Note finally that we couldn't extract a self-consistent equation for the gap starting from these equations.

The gap in the bosonic spectral function leads to a degenerate choice of the Lagrange parameter λ in the case of the exactly screened spin: when this effective chemical potential lies within the gap, the ground-state Schwinger boson occupancy[5] locks into the value $n_b = p_0 = \gamma$. Numerically, this manifests itself by a plateau in the bosonic occupancy as a function of λ, at low temperature (see Fig. 6.10). Such a picture suggests that starting from a solution of the saddle point equations, a small change $\delta\lambda$ in the bosonic chemical potential leads to another solution, apparently given by the same set of Green's functions only shifted rigidly in frequency by an amount $\delta\lambda$.

Just like the stability of the gap, this last feature is also built into the equations. Assume that $\Sigma_\chi(\omega, \lambda+\delta\lambda) = \Sigma_\chi(\omega-\delta\lambda, \lambda)$, then thanks to the Dyson's equation, this property is also verified by G_χ. It follows that, at zero temperature:

$$\begin{array}{rcl} \Sigma_b(\omega, \lambda+\delta\lambda) &=& \rho_0\gamma J_K^2 \left(\displaystyle\int_{-D}^{-\omega} d\Omega G_\chi'(\Omega-\delta\lambda, \lambda) + i \int_{-\omega}^{0} d\Omega G_\chi''(\Omega-\delta\lambda, \lambda) \right) \\ &=& \Sigma_b(\omega+\delta\lambda, \lambda) - \rho_0\gamma J_K^2 \displaystyle\int_{-\delta\lambda}^{0} d\Omega G_\chi''(\Omega, \lambda) \\ &=& \Sigma_b(\omega+\delta\lambda, \lambda) \end{array} \tag{6.53}$$

where we used that in the large bandwidth limit $D+\delta\lambda \simeq D$, and the extra term vanishes because of the gap in the $\chi-$fermion spectral function. The rest of the proof is identical: from the rigid shift of Σ_b it is easy to prove that G_b follows the

[5]The bosonic occupancy is defined as $n_b = -G_b(\tau = 0^-)$, which is set by the constraint to be equal to p_0.

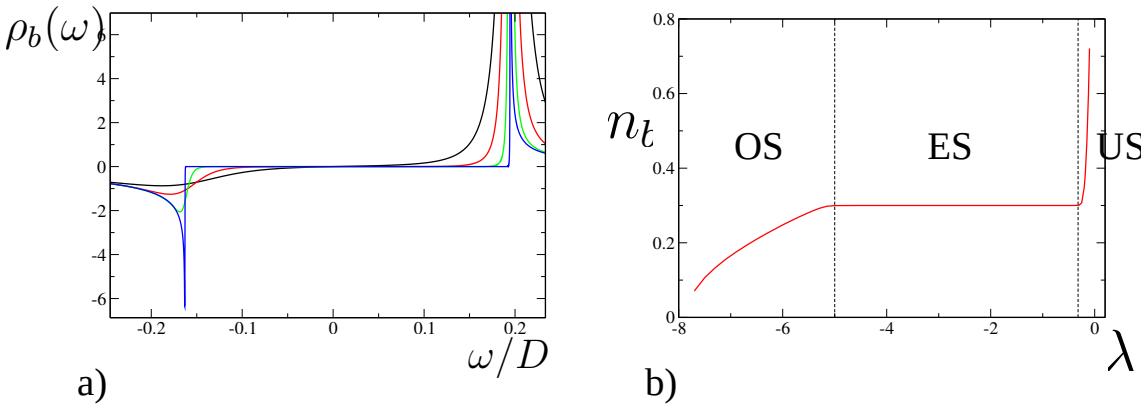

Figure 6.10: a) Bosonic spectral function as a function of frequency for decreasing temperature. As the gap opens at low energy, both peaks sharpen on the edges of the gapped region. b) Computed bosonic occupancy for $\gamma = 0.3$ when the chemical potential λ is varied (p_0 not being fixed). The plateau corresponds to an exactly screened case (ES).

same property, which transmits to $\Sigma_c hi$ via the saddle-point equation in the exact same way as we just proved, so that ultimately, on has at zero temperature:

$$\begin{aligned} G_b(\omega, \lambda + \delta\lambda) &= G_b(\omega + \delta\lambda, \lambda) \\ G_\chi(\omega, \lambda + \delta\lambda) &= G_\chi(\omega - \delta\lambda, \lambda) \end{aligned} \tag{6.54}$$

It is legitimate to wonder whether the presence of a gap in the spectral functions is an artifact of the large-N limit or if it has a deeper physical meaning in which case it would extend down to $N = 2$. We do not, at this stage, have any evidence to support either scenarios. However, we can argue that if a gap in the bosonic spectral function exists in the $SU(2)$ case, it could be revealed from inspecting the energy spectrum of the bosonic states, e.g. by ways of the Density Matrix Renormalization Group.

□ Renormalized chemical potential

As a consequence of the gapped bosonic spectral function, in the case of the exactly screened impurity, the renormalized chemical potential $\lambda^* = \lambda - \Sigma_b(0)$ does not vanish as a function of temperature unlike the overscreened and underscreened regimes. The bosonic Green's function taken at zero energy is given by $G_b(0) = 1/\lambda^*$ and can be expressed as:

$$G_b(0) = G_b'(0) = -\!\!\!\!\!\!\int d\Omega \, \frac{\rho_b(\Omega)}{\Omega} \tag{6.55}$$

which is protected by the low-energy gap, and is thus made finite.

Another feature that comes from the numerical investigation is the development of a $\delta-$peak in the bosonic spectral function at the boundary of the gapped region

at positive frequency. Unlike the underscreened case, the position of this peak does not evolve as the temperature is lowered, and one can make the following ansatz for the bosonic spectral function:

$$\rho_b(\omega) = A\delta(\omega - \eta) + \Phi_b(\omega) \tag{6.56}$$

where A and η are positive constants, and Φ_b is assumed to be a sub-leading term.

Of course, this ansatz is not enough to capture most of the properties of the perfectly screened impurity but it is sufficient here to self-consistently extract the low-energy behavior of the Green's functions. Substituting this ansatz into the equation for the fermionic self-energy, one has:

$$\begin{aligned} \Sigma_\chi(\omega) &= \Phi_\chi(\omega) + A\rho_0 J_K^2 \left[\log\left(\frac{D}{2\pi T}\right) - \Psi\left(\frac{1}{2} + \frac{\omega+\eta}{2i\pi T}\right) - i\frac{\pi}{2} \right] \\ &\underset{T\to 0}{\sim} \Phi_\chi(\omega) - A\rho_0 J_K^2 \log\left(\frac{|\omega+\eta|}{D}\right) \end{aligned} \tag{6.57}$$

This leads to the following contribution once plugged back into the bosonic self-energy:

$$\Sigma_b(\omega) - \Sigma_b(\eta) \sim B\frac{|\omega-\eta|}{\log|\omega-\eta|} \tag{6.58}$$

so that our ansatz is consistent.

As a conclusion, the inverse Green's functions at zero energy read:

$$\lambda - \Sigma_b(0) \underset{T\to 0}{\longrightarrow} \text{Const.} \tag{6.59}$$

$$J_K - \Sigma_\chi(0) \underset{T\to 0}{\longrightarrow} \text{Const.} \tag{6.60}$$

where both these constants are finite, which prevents any kind of low-energy analysis like the one carried out for the overscreened impurity. This is verified numerically (see fig. 6.11) where the saturation is observed over more than a decade in temperature.

6.3.3 Entropy and specific heat

The gap in both the bosonic and fermionic spectral functions removes the effect of both fields at low temperature. Indeed, as the temperature is lowered, one can only probe the low-energy spectrum of each field: the low-temperature physics is then completely dominated by the conduction electrons so that the emergence of the gap ultimately reveals a Fermi liquid.

The consequences of a gapped solution on the low-energy physics can readily be obtained from the impurity entropy defined in (6.51). In the low-temperature regime, it is useful to replace the derivative of the fermionic and bosonic distributions

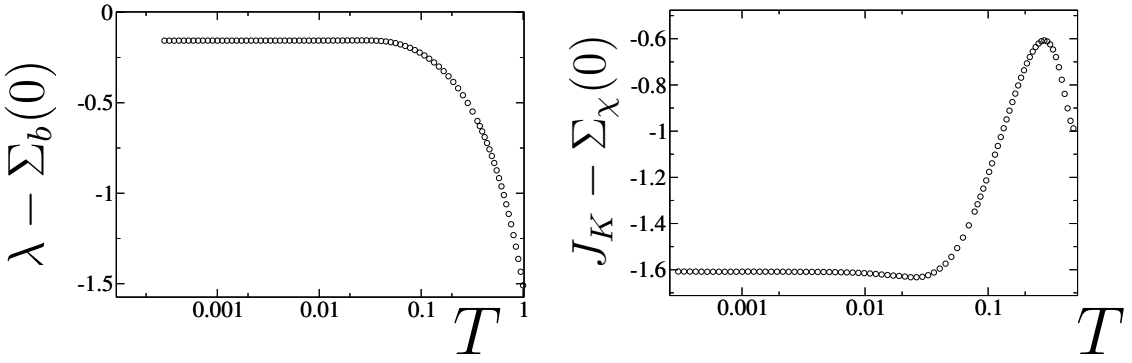

Figure 6.11: Inverse Green's functions at zero energy as a function of temperature. The dots correspond to numerical data. The logarithmic scale in temperature is used to underline the saturation at low T.

with respect to temperature by their derivative with respect to frequency. Using that $\frac{\partial n(\omega)}{\partial T} = \frac{-\omega}{T}\frac{\partial n(\omega)}{\partial \omega}$ and $\frac{\partial f(\omega)}{\partial T} = \frac{-\omega}{T}\frac{\partial f(\omega)}{\partial \omega}$, one can rewrite the impurity entropy as:

$$\begin{aligned} \frac{S_{\rm imp}^{{\rm Low}T}}{N} &= \frac{1}{T}\int d\omega \left[\frac{\partial n}{\partial \omega} s_b(\omega) + \frac{\partial f}{\partial \omega} s_f(\omega)\right] \\ &= \frac{-1}{T}\int d\omega \left[\frac{ds_b}{d\omega} n(\omega) + \frac{ds_f}{d\omega} f(\omega)\right] \end{aligned} \tag{6.61}$$

where we define

$$\left\{ \begin{array}{rcl} s_b &=& \frac{\omega}{\pi}\left({\rm Im}\log\left(-G_b^{-1}\right) + G_b'\Sigma_b''\right) \\ s_f &=& \frac{\gamma\omega}{\pi}\left({\rm Im}\log\left(-G_\chi^{-1}\right) + G_\chi'\Sigma_\chi'' - G_{c0}''\tilde{\Sigma}_c'\right) \end{array} \right.$$

One can then perform a Sommerfeld expansion at low temperature, which gives:

$$\frac{S_{\rm imp}^{{\rm Low}T}}{N} = -\frac{\pi^2}{6}T\left(2\left.\frac{d^2 s_b}{d\omega^2}\right|_{\omega=0} + \left.\frac{d^2 s_f}{d\omega^2}\right|_{\omega=0}\right) \tag{6.62}$$

It turns out that because of the causality properties of the bosonic Green's functions, one has $G_b''(0) = 0$ and $\Sigma_b''(0) = 0$, which then imposes, after some minor rearrangement, that $\left.\frac{d^2 s_b}{d\omega^2}\right|_{\omega=0} = 0$.

Taking the second derivative of s_f and rearranging the remaining terms, noticing that $\left.\frac{dG_{c0}''}{d\omega}\right|_{\omega=0} = 0$, one has:

$$\left.\frac{d^2 s_f}{d\omega^2}\right|_{\omega=0} = \frac{2\gamma}{\pi}\left(\left.\frac{dG_\chi'}{d\omega}\right|_{\omega=0}\Sigma_\chi''(0) - G_\chi''(0)\left.\frac{d\Sigma_\chi'}{d\omega}\right|_{\omega=0} + \pi\rho_0\left.\frac{d\tilde{\Sigma}_c'}{d\omega}\right|_{\omega=0}\right) \tag{6.63}$$

Recalling that the fermionic spectral function is gapped, this leads to the final expression of the low-temperature impurity entropy:

$$\frac{S_{\rm imp}^{{\rm Low}T}}{N} = -\frac{\pi^2}{3}\gamma\rho_0 T \left.\frac{d\tilde{\Sigma}_c'}{d\omega}\right|_{\omega=0} \tag{6.64}$$

which is linear in T as one would expect from a Fermi liquid.

Note in particular that the specific heat coefficient, defined as $\frac{C_v}{T} = \frac{dS_{\rm imp}}{dT}$, not only saturates at a constant value at low temperature, but also this constant depends on the renormalized number of channels γ.

The exponential decay of the Fermi and Bose function derivatives imposes that at a given temperature T, only the frequency range $\omega \in [-T, T]$ contributes to the entropy. As a consequence, as one reaches a temperature of the order of the gap in the spectral functions, the contributions to the entropy coming from both the Schwinger bosons and the $\chi-$fermions identically vanish. It follows from this derivation that the typical energy scale over which the Fermi liquid develops (some kind of effective Fermi temperature T^*) is given by the size Δ_g of the gap.

Numerically, one sees a cross-over from the high-temperature regime where the entropy is dominated by the local moment physics and is thus given by a constant, to the low-temperature regime where it becomes Fermi-liquid like and vanishes linearly with temperature (see Fig. 6.12).

6.3.4 Susceptibility and Wilson ratio

Using the numerical solution of the saddle-point equations, we could compute the local magnetic susceptibility, which shows a crossover from a high-temperature Curie law to a saturation at low-temperature characteristic of a screening process (see Fig. 6.12). This saturation defines the scale of the Kondo temperature in this regime since one has:

$$\chi_{\rm loc} \underset{T\to 0}{\sim} \frac{p_0(p_0+1)}{T_K} \tag{6.65}$$

This saturation is consistent with the Fermi liquid picture at low temperature. However, the dynamic susceptibility, defined as $\langle S(t)S(0)\rangle$, vanishes exponentially because of the gap in the bosonic spectral function. We expect the $1/t^2$ variation, characteristic of a Fermi-liquid, to be only present at the order $1/N$.

From the specific heat and the impurity susceptibility, we could compute the Wilson ratio, defined as:

$$W = \lim_{T\to 0} \frac{\pi^2}{3}\frac{\chi}{C_v/T} \tag{6.66}$$

where the numerical prefactor is chosen so that $W = 1$ for a non-interacting Fermi liquid.

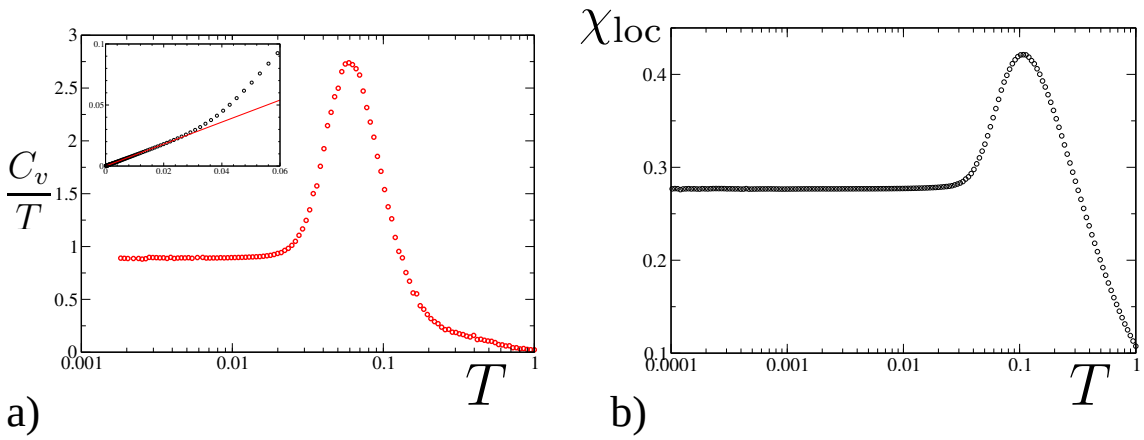

Figure 6.12: a) Specific heat coefficient for $\gamma = 0.1$ as a function of temperature on a log scale. Inset: the low temperature entropy shows a linear behavior. b) Temperature variation of the local spin susceptibility for $\gamma = 0.1$. The saturation of both quantitites is consistent with a Fermi liquid behavior.

Numerically, the Wilson ratio seems to grow linearly with the number of channels γ, which is confirmed by an analytical computation, similar in spirit to the one of Nozières and Blandin [104]. This amounts to expressing the phase shift of the local Fermi liquid at the impurity site and inspecting its response to variations of the fields coupled to the spin and channel magnetization, which ultimately leads to a relation between the spin, charge, and channel susceptibilities on one hand, and the specific heat coefficient on the other hand. The complete derivation is presented in Appendix C.

As a result of this analysis, we expect the Wilson ratio to be given by $W = 1+\gamma$, which is the behavior we recover in our numerical solution (see Fig. 6.13). This form is consistent with the Bethe ansatz results [114], taken in the limit of large values of N.

Such a Wilson ratio suggests, as we already argued from the entropy, that the exactly screened solution of the saddle-point equations describe an interacting local Fermi liquid in the large-N limit.

6.3.5 Scales

We argued, when dealing with the impurity entropy, that the typical energy scale over which the Fermi liquid develops is given by the size of the gap. From various other approaches we expect the crossover scale between the high-temperature local moment physics, and the low-temperature Fermi liquid behavior to be given by the Kondo temperature[6].

[6]As one can see, e.g. from the local susceptibility which diverges in $1/T$ until it reaches the Kondo temperature where it just saturates at a constant going like $1/T_K$.

From this reasoning, one expects that the gap roughly goes like the Kondo temperature. However, we could not find any analytic derivation that would confirm this result. One has to stress out that the ansatz we have made concerning the bosonic Green's functions is not sufficient here to fully explore the relation between the gap and the Kondo temperature, as one would need an explicit form for the subleading function $\Phi_b(\omega)$.

Numerically, there is quite a striking correspondence between the size of the gap and the Kondo temperature, as can be seen on fig. 6.13.

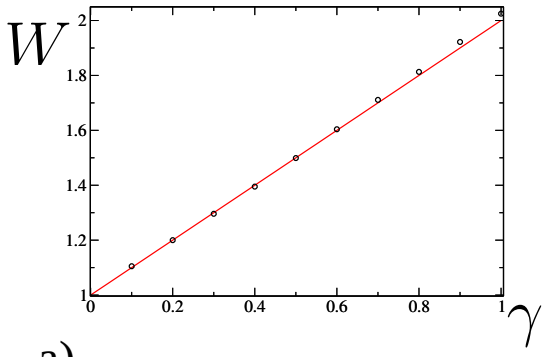

a)

Number of channels γ	Kondo temperature T_K extracted from χ_{imp}	Gap Δ_g in the spectral functions
0.1	0.506	0.397
0.2	0.446	0.372
0.3	0.390	0.346
0.4	0.355	0.322
0.5	0.321	0.299
0.6	0.286	0.277
0.7	0.257	0.256
0.8	0.230	0.236
0.9	0.208	0.218

b)

Figure 6.13: a) Wilson ratio computed for various values of γ (black circles) and compared with the behavior extracted from our Nozières-Blandin analysis (red line), b) Numerical values of the low-T gap and the Kondo temperature for a given Kondo coupling J_K and various γ.

6.4 Conclusion

In this chapter, we rederived the saddle-point equations associated to the large-N limit of the multichannel Kondo model using an extension of the Luttinger-Ward formalism. After recalling the main results of the overscreened and underscreened regimes, we studied in details the perfectly screened case. We proved that contrary to the common knowledge, this regime does not correspond to a trivial Fermi liquid. Instead, we showed that despite vanishing transport properties due to an artifact of the large-N limit, one can recover the thermodynamics of an interacting Fermi liquid.

The application of this method to the description of, e.g. quantum dot physics, is made difficult by the vanishing T-matrix in the limit of $N \to \infty$. An attempt to cure this issue is presented in Chapter 8.

However, an interesting application of this approach lies in the extension to many impurities. The first step towards this route is presented in Chapter 7, with the study of a two-impurity system.

CHAPTER 7

Two-impurity multichannel Kondo model

Contents

Having demonstrated that the large-N bosonic approach captures the thermodynamic properties of the Fermi liquid behavior for the perfectly screened impurity, we show in this section that it can also handle magnetic correlations within the two-impurity Kondo model. In this chapter, we explore the phase diagram of the two-impurity Kondo-Heisenberg model and discuss the similarities with the so-called "Varma-Jones" [115] fixed point in $N = 2$. The main results of this chapter have been published in the Publication 4, the rest is presented here for the first time.

7.1 Large-N equations

7.1.1 The model

We now consider two identical impurities coupled to the same sea of conduction electrons, and include for generality a Heisenberg-like interaction between the two localized spins, generated by other exchange processes not involving the conduction electrons. The Kondo interaction is the same as we described in the previous chapter.

Motivated by an extension to the lattice, and its relevance for the heavy fermion problem, we choose to limit ourselves to the case of an antiferromagnetic Heisenberg coupling between the two impurity spins. Moreover, we choose to follow the arguments of Read and Sachdev [116] and describe this Heisenberg interaction in terms of the boson pair operator $B_{12} = \sum_{m,\sigma} \sigma b_{1,m,\sigma} b_{2,m,-\sigma}$, where we recast the N spin indices under the form $\alpha = (m, \sigma)$ (m running from 1 to $\frac{N}{2}$, and $\sigma = \pm$).

Following this choice, the Hamiltonian describing the system is now invariant under spin transformation in the symmetry group $SP(N)$, subgroup of $SU(N)$ and writes:

$$\begin{aligned} H &= H_{\text{band}} + H_K^{(1)} + H_K^{(2)} + H_H \\ & H_{\text{band}} = \sum_{\mathbf{k}} \sum_{m,\sigma} \sum_{\mu=1}^{K} \epsilon_{\mathbf{k}} c^{\dagger}_{\mathbf{k}m\sigma\mu} c_{\mathbf{k}m\sigma\mu} \\ & H_K^{(i)} = \frac{J_K}{N} \sum_{m,m'} \sum_{\sigma,\sigma\prime} \sum_{\mu} b^{\dagger}_{i,m,\sigma} b_{i,m',\sigma'} \psi^{\dagger}_{im'\sigma'\mu} \psi_{im\sigma\mu} \\ & H_H = \frac{J_H}{N} \left(\sum_{m,\sigma} \sigma b^{\dagger}_{1,m,\sigma} b^{\dagger}_{2,m,-\sigma} \right) \left(\sum_{m',\sigma'} \sigma' b_{1,m',\sigma'} b_{2,m',-\sigma'} \right) \end{aligned} \tag{7.1}$$

where $\psi_{im\sigma\mu}$ creates an electron in the Wannier state with spin $\alpha = N + \sigma m + \frac{1-\sigma}{2}$ at the site i.

The number of bosons for each site is enforced by the constraint:

$$H_{\text{Constraint}} = - \sum_{i=(1,2)} \lambda_i \left(\sum_{m,\sigma} b^{\dagger}_{i,m,\sigma} b_{i,m,\sigma} - p_0 N \right) \tag{7.2}$$

and we focus in the rest of this chapter on perfectly screened impurities, so that we restrict ourselves to the case where $p_0 = \gamma$.

One would expect to see different screening regimes for this model, but we limit ourselves to the exactly screened case, fixing the number of channels to match the size of the impurity spins. There is now a new parameter one can tune, namely the Heisenberg coupling, which now competes with the Kondo interaction giving access to two different regimes, pictured in fig. 7.1:

- For a weak Heisenberg coupling, the two impurity spins prefer to form a singlet with the surrounding conduction electrons. We expect to see two perfectly screened impurities only weakly coupled to each other. The low-energy physics is then expected to be Fermi-liquid like.
- Whereas for a strong Heisenberg coupling, a spin singlet between the two impurity spins is favored. The impurities are locked in a singlet state and act as a scattering center for the conduction electrons, so that the low-energy physics is again Fermi-liquid like, but qualitatively different than the regime of weak Heisenberg coupling.

The most interesting region of the phase diagram turns out to be the crossover region between these two regimes.

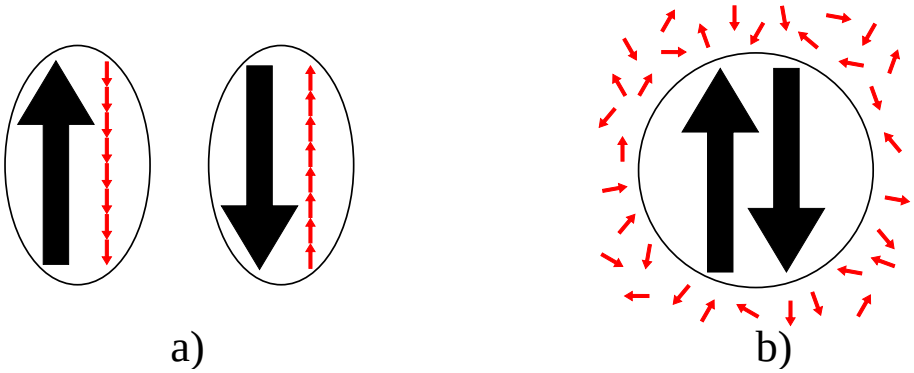

Figure 7.1: Schematic diagram illustrating the two limiting regimes: a) corresponds to the case of a dominant Kondo interaction and b) to a strong Heisenberg coupling. The large black arrows stand for the impurities, the red ones for the electrons.

7.1.2 Saddle-point equations

In order to study the phase diagram of the two-impurity Kondo-Heisenberg model in the large-N limit, we derive a set of saddle-point equations which we then study by means of numerical as well as analytical investigation when possible. The derivation of the saddle-point equations is quite similar to the one already presented for the single impurity case.

□ Derivation

As a first step, we decouple the Kondo interaction term for both impurities by introducing two sets of Grassmanian fields $\chi_{1,\mu}$ and $\chi_{2,\mu}$, where μ is the channel index, running from 1 to K. After integrating the conduction electrons out of the partition function, the action reads:

$$\begin{aligned} S &= \int_0^\beta d\tau \sum_{i,m,\sigma} b^\dagger_{i,m,\sigma}(\tau)\left(\partial_\tau - \lambda_i(\tau)\right) b_{i,m,\sigma}(\tau) - \frac{1}{J_K}\int_0^\beta d\tau \sum_{i,\mu} \chi^\dagger_{i,\mu}(\tau)\chi_{i,\mu}(\tau) \\ &-\frac{1}{N}\sum_{i,j}\int_0^\beta d\tau d\tau' \sum_\mu \chi_{j,\mu}(\tau')\chi^\dagger_{i,\mu}(\tau)\; G_{c0}(i-j;\tau-\tau') \sum_{m,\sigma} b_{j,m,\sigma}(\tau')b^\dagger_{i,m,\sigma}(\tau) \\ &+\sum_i \int_0^\beta d\tau \left(\Delta^\dagger_{i,\bar{i}}(\tau)\sum_{m,\sigma}\sigma b_{i,m,\sigma}(\tau)b_{\bar{i},m,-\sigma}(\tau) + \text{h.c.}\right) \\ &+\frac{N}{J_H}\sum_i\int_0^\beta d\tau\; \Delta^\dagger_{i,\bar{i}}(\tau)\Delta_{i,\bar{i}}(\tau) + p_0 N\sum_i\int_0^\beta d\tau\; \lambda_i(\tau) \end{aligned} \tag{7.3}$$

where we have decoupled the Heisenberg interaction by introducing a "bond" operator $\Delta_{i,\bar{i}}$, and $\bar{i}$ is defined as:

$$\bar{i} = \begin{cases} 2 & \text{if} \quad i=1 \\ 1 & \text{if} \quad i=2 \end{cases} \tag{7.4}$$

Using the symmetry under the exchange $1 \leftrightarrow 2$, one can argue that the Lagrange multipliers λ_1 and λ_2 are equal: if a solution is obtained with different values of λ_1 and λ_2, then the symmetry leads to another solution where these values are exchanged, suggesting that they are most likely equal. The same kind of reasoning suggests that the bond operators are also trivially related to one another via $\Delta_{12} = -\Delta_{21}$. This allows us to define λ and Δ as:

$$\begin{cases} \lambda_i &= \lambda \\ \Delta_{i,\bar{i}} &= \text{Sgn}(\bar{i}-i)\Delta \end{cases} \tag{7.5}$$

It is useful at this stage to introduce a spinor notation for the Schwinger bosons $\hat{b}^\dagger_{i,m} = (b^\dagger_{i,m,+}, b_{i,m,-})$ in order to rewrite the action under the following matrix form:

$$\begin{aligned} S &= \sum_{i,j}\int_0^\beta d\tau \sum_m \hat{b}^\dagger_{i,m}(\tau)\begin{bmatrix} \left(\partial_\tau - \lambda(\tau)\right)\delta_{ij} & 2\text{Sgn}(\bar{i}-i)\Delta(\tau)\delta_{j\bar{i}} \\ -2\text{Sgn}(\bar{i}-i)\Delta^\dagger(\tau)\delta_{j\bar{i}} & \left(-\partial_\tau - \lambda(\tau)\right)\delta_{ij} \end{bmatrix}\hat{b}_{j,m}(\tau) \\ &-\frac{1}{N}\int_0^\beta d\tau d\tau' \sum_{i,j} N_\chi(i,j,\tau,\tau')G_{c0}(i-j;\tau-\tau')N_b(i,j,\tau,\tau') \\ &-\frac{1}{J_K}\int_0^\beta d\tau \sum_{i,\mu}\chi^\dagger_{i,\mu}(\tau)\chi_{i,\mu}(\tau) + 2\frac{N}{J_H}\int_0^\beta d\tau\; \Delta^\dagger(\tau)\Delta(\tau) \\ &+2p_0 N\int_0^\beta d\tau\; \lambda(\tau) \end{aligned} \tag{7.6}$$

where the matrix is given in the σ-space, and N_b and N_χ are the precursors of the Schwinger boson and $\chi-$fermion Green's function defined as:

$$N_b(i,j,\tau,\tau') = \sum_{m,\sigma} b_{j,m,\sigma}(\tau') b^\dagger_{i,m,\sigma}(\tau) \qquad N_\chi(i,j,\tau,\tau') = \sum_{\mu} \chi_{j\mu}(\tau') \chi^\dagger_{i\mu}(\tau) \tag{7.7}$$

The method is then similar to the one used for the single impurity problem: one introduces the new fields $Q(i,j,\tau,\tau')$ and $\bar{Q}(i,j,\tau,\tau')$ conjugated to $N_\chi(i,j,\tau,\tau')$ and $N_b(i,j,\tau,\tau')$. This leads to an effective action $S(Q,\bar{Q},\lambda,\Delta)$ expressed in terms of these new fields, where every term scales like N so that one can apply the method of steepest descent. The saddle-point equations now write:

$$\begin{aligned}
\bar{Q}(i,j,\tau,\tau') &= -G_{c0}(i-j;\tau-\tau')\left(G_b^{(++)}(j-i;\tau'-\tau) + G_b^{(--)}(j-i;\tau'-\tau)\right) \\
Q(i,j,\tau,\tau') &= -\gamma G_{c0}(i-j;\tau-\tau') G_\chi(j-i;\tau'-\tau) \\
p_0 &= -\frac{1}{2}\left(G_b^{(++)}(i=j;\tau=0^-) + G_b^{(--)}(i=j;\tau=0^+)\right) \\
\frac{\Delta}{J_H} &= \frac{1}{2}\sum_{i=1,2} G_b^{(-+)}(i-\bar{i};\tau=0^-)
\end{aligned} \tag{7.8}$$

where the Green's functions are now defined as:

$$\begin{aligned}
G_b(i-j;\tau) &= \begin{bmatrix} G_b^{(++)}(i-j;\tau) & G_b^{(+-)}(i-j;\tau) \\ G_b^{(-+)}(i-j;\tau) & G_b^{(--)}(i-j;\tau) \end{bmatrix} \\
&= \begin{bmatrix} -\langle T b_{i,+}(\tau) b^\dagger_{j,+}(0)\rangle & -\langle T b_{i,+}(\tau) b_{j,-}(0)\rangle \\ -\langle T b^\dagger_{i,-}(\tau) b^\dagger_{j,+}(0)\rangle & -\langle T b^\dagger_{i,-}(\tau) b_{j,-}(0)\rangle \end{bmatrix} \qquad (7.9) \\
G_\chi(i-j;\tau) &= -\langle T\chi_i(\tau)\chi^\dagger_j(0)\rangle \qquad (7.10)
\end{aligned}$$

□ RKKY interaction

It is possible to relate the fields Q and $\bar{Q}$ to the self-energies of the Schwinger boson and the $\chi-$fermion. From the saddle-point equations, one can see that the Kondo interaction is responsible for local terms arising from $i=j$, but also for a cross-term that couples the two impurities to one another. This cross-term will give rise to a bosonic self-energy in the $SU(N)$ channel, i.e. that renormalizes the $-\langle T b_{i,\pm}(\tau) b^\dagger_{j,\pm}(0)\rangle$ term (with $i \neq j$).

This is known as the RKKY interaction [88, 89, 90]. This effective interaction between the impurities is mediated by the conduction band and can be tuned by adjusting the distance between the two impurities. However, we assume here that this distance is always big enough to neglect the RKKY interaction compared to the Heisenberg coupling between the impurities[1].

[1]This assumption is motivated by the fact that the RKKY interaction is known to drop very rapidly with the distance between impurities.

Qualitatively, the RKKY and the Heisenberg interactions, although arising from a completely different physics, play the same role as they lead to the establishment of short-range antiferromagnetic correlations between the impurities. Moreover, they are both tunable thanks to an external parameter: the distance R between impurities for the RKKY interaction, and the coupling J_H for the Heisenberg one. Our choice of favoring an Heisenberg-like rather than an RKKY interaction is motivated by real materials (where the overlap between orbitals of neighboring atoms is generally taken into account via an Heisenberg coupling), and by the fact that the Heisenberg coupling is conceptually easier to tackle as no retardation effects are present in the large-N limit (whereas one expects the cross-site bosonic self-energy to develop an imaginary part due to the RKKY interaction).

□ Set of equations

From this, it follows that the only non-local terms in our Green's functions are present in the "free" bosonic propagator, and come from the Heisenberg coupling between the impurities.

Since the $\chi-$fermion only sees the Kondo interaction, its propagator – along with both self-energies – is local within our approximation. It then becomes possible to reduce the full set of equations to only local propagators, where the non-locality of the Heisenberg interaction manifests itself through a dependence on Δ of the local bosonic Green's function.

The problem then reduces to the following set of equations:

$$G_b(i\nu_n) = \frac{-i\nu_n + \lambda - \Sigma_b(-i\nu_n)}{(i\nu_n + \lambda - \Sigma_b(i\nu_n))\,(-i\nu_n + \lambda - \Sigma_b(-i\nu_n)) - 4\Delta^2} \tag{7.11}$$

$$\Sigma_b(\tau) = -\gamma J_K^2 G_c(\tau) G_\chi(\beta - \tau) \tag{7.12}$$

$$G_\chi(i\omega_n) = \frac{1}{J_K - \Sigma_\chi(i\omega_n)} \tag{7.13}$$

$$\Sigma_\chi(\tau) = -J_K^2 G_c(\tau) G_b(\beta - \tau) \tag{7.14}$$

with the following constraint on λ and Δ:

$$\begin{cases} p_0 = \displaystyle\int d\omega\; n(\omega)\rho_b(\omega) \\ \dfrac{\Delta}{J_H} = 2\Delta \displaystyle\int \frac{d\omega}{\pi} n(\omega) \mathrm{Im}\left(\frac{1}{(\omega + \lambda - \Sigma_b(\omega))\,(-\omega + \lambda - \Sigma_b(-\omega))^* - 4\Delta^2} \right) \end{cases} \tag{7.15}$$

where we chose not to simplify the factors of Δ to account for the case where it vanishes.

Note that, just like the single impurity case, these constraints are not invertible and cannot be written as a simple equality directly involving λ or Δ: one needs the knowledge of the bosonic propagator over the whole range of frequency in order to meet these constraints.

7.1.3 General remarks

Before trying to solve eqns (7.11)-(7.14), let us analyze some of their properties.

□ **Causality**

The equations ruling the evolution of the $\chi-$fermion propagator as a function of frequency are the same as the ones derived in the case of a single impurity, so that the causality of the $\chi-$fermion self-energy and Green's function can be proved following the exact same reasoning.

The same argument holds for the bosonic self-energy. The proof of causality for the bosonic propagator requires some extra work on (7.11), from which one can extract the following imaginary part:

$$\begin{aligned} G_b''(\omega) &= \mathrm{Im}\left(\frac{(-\omega+\lambda-\Sigma_b(-\omega))^*}{(\omega+\lambda-\Sigma_b(\omega))\,(-\omega+\lambda-\Sigma_b(-\omega))^*-4\Delta^2}\right) \\ &= \frac{|\omega+\lambda-\Sigma_b(-\omega)|^2\,\Sigma_b''(\omega)-\Delta^2\Sigma_b''(-\omega)}{\left|(\omega+\lambda-\Sigma_b(\omega))\,(-\omega+\lambda-\Sigma_b(-\omega))^*-4\Delta^2\right|^2} \\ &\propto -A(\omega)\mathrm{Sgn}(\omega)+B(\omega)\mathrm{Sgn}(-\omega) \end{aligned} \tag{7.16}$$

where $A(\omega)$ and $B(\omega)$ are positive for any given frequency, and we assumed that $\Sigma_b(\omega)$ is causal, so that ultimately $G_b''(\omega) \propto -\mathrm{Sgn}(\omega)$, as expected for a causal bosonic propagator.

□ $\Delta \to 0$ **limit**

Taking the limit of vanishing Δ in eqns (7.11)-(7.14) leads to the same equations as the one derived in the case of a single impurity.

The constraint on Δ (the second equation in (7.15)), corresponding to the saddle-point in this variable, can also be rewritten as:

$$\Delta = -J_H\langle B_{12}\rangle = -J_H\langle\sum_{m,\sigma}\sigma b_{1,m,\sigma}b_{2,m,-\sigma}\rangle \tag{7.17}$$

In the limit of $\Delta \to 0$, this equation imposes that $\langle B_{12}\rangle = 0$, preventing the formation of pairs of bosons. In this limit, the system behaves as two perfectly screened impurities which are decoupled from each other, on average. Since the impurities are identical, the physical properties averaged over them look like the ones of a single impurity with the same spin.

□ $\Delta \to \infty$ **limit**

In the limit of large Δ, the Heisenberg interaction dominates and as a first approximation, one can neglect the Kondo interaction: this amounts to neglecting the

self-energy inside the bosonic propagator. The bosonic spectral function then reads:

$$\rho_b(\omega) = \frac{\lambda + \lambda^*}{2\lambda^*}\delta\left(\omega + \lambda^*\right) + \frac{\lambda^* - \lambda}{2\lambda^*}\delta\left(\omega - \lambda^*\right) \tag{7.18}$$

where $\lambda^* = -\sqrt{\lambda^2 - \Delta^2}$. This spectral function is made out of two $\delta-$functions, peaked at symmetric positions in frequency, so that one can identify a symmetric gap $\Delta_{\rm gap} = -2\lambda^*$. By construction, $\lambda^* > \lambda$, but they are both negative so that the bosonic propagator is still causal.

The constraints impose that, in the zero temperature limit:

$$\left\{ \begin{array}{rcl} p_0 & = & \displaystyle\int_{-\infty}^{0} d\omega\ \rho_b(\omega) = \frac{\lambda - \lambda^*}{2\lambda^*} \\ \displaystyle\frac{1}{J_H} & = & \displaystyle 2\int_{-\infty}^{0} d\omega\ {\rm Im}\left(\frac{G_b(\omega)}{\lambda - \omega - i\delta}\right) \end{array} \right. \Longrightarrow \left\{ \begin{array}{rcl} \lambda & = & -J_H(1+2p_0) \\ \Delta^2 & = & 4p_0(1+p_0)J_H^2 \end{array} \right. \tag{7.19}$$

It follows that in the large Δ limit, which corresponds to the large J_H limit, the gap in the bosonic spectral function increases with J_H. The typical temperature over which a Fermi liquid develops becomes larger (increasing linearly with J_H) but since the Kondo interaction becomes weaker, this Fermi liquid looks more and more like a trivial one, with a vanishing specific heat coefficient as $J_H \to \infty$. This is consistent with the picture of two impurities locked in a spin singlet: they only weakly renormalize the surrounding Fermi liquid which then looks as if it is non-interacting.

7.2 Phase diagram and quantum critical point

In this section, we solve numerically the set of self-consistent equations for various values of the temperature and the Heisenberg coupling. We can isolate three regions of the $(T_K/J_H, T/J_H)$ phase diagram: a Kondo dominated Fermi liquid, a Heisenberg dominated Fermi liquid and an intermediate region in between. This crossover region between the two Fermi liquids is governed by a quantum critical point, whose existence is underlined by the behavior of the phase shift and the entropy.

7.2.1 Tools for exploring the phase diagram

□ Free energy and entropy

One can generalize the expression of the free energy functional to encompass the case of a two-impurity Kondo-Heisenberg model. The derivation is quite similar to the one presented in Appendix A, and the reader is referred to the Publication 3 for a detailed calculation in the more general case of a Kondo lattice, so that we only

mention here the final result for the model Hamiltonian as defined in (7.1). The averaged impurity free energy is given by:

$$\begin{aligned} F_{\rm imp} &= NT\sum_n \left[\frac{1}{2}\log\left((-i\nu_n+\lambda-\Sigma_b(-i\nu_n))G_b^{-1}(i\nu_n)\right)+\Sigma_b(i\nu_n)G_b(i\nu_n)\right] \\ &\quad -KT\sum_n\left[\log(-G_\chi^{-1}(i\omega_n))+\Sigma_\chi(i\omega_n)G_\chi(i\omega_n)\right]+\Phi_{LW}[G_b,G_\chi,G_c] \\ &\quad +Np_0\lambda \end{aligned} \tag{7.20}$$

Proceeding similarly to Appendix A, one can carry out the temperature derivative of the impurity free energy, which leads to the following expression for the averaged impurity entropy:

$$\begin{aligned} \frac{S_{\rm imp}}{N} &= -\int\frac{d\omega}{\pi}\left[\frac{\partial n(\omega)}{\partial T}\left(\frac{1}{2}{\rm Im}\log\left((\tilde{G}_b(-\omega))^*G_b^{-1}(\omega)\right)+G_b'(\omega)\Sigma_b''(\omega)\right)\right. \\ &\quad \left.+\gamma\frac{\partial f(\omega)}{\partial T}\left({\rm Im}\log\left(-G_\chi^{-1}(\omega)\right)+G_\chi'(\omega)\Sigma_\chi''(\omega)-G_{c0}''(\omega)\tilde{\Sigma}_c'(\omega)\right)\right] \end{aligned} \tag{7.21}$$

where $\tilde{G_b}^{-1}(\omega)=\omega+i\delta+\lambda-\Sigma_b(\omega)$ and $\tilde{\Sigma}_c=N\Sigma_c$.

□ Sum rules and phase shift

It is possible, using our expression of the impurity free energy to derive sum rules associated to the conserved quantities of the system. A detailed proof for a generic Hamiltonian is provided in the Publication 3 and we only sketch here the main aspects of the method and the final result in the case of our two-impurity model.

Each conserved quantity Q which commutes with the Hamiltonian leads to a gauge invariance of the underlying quantum fields, such that the action and all physical properties are invariant under the transformation:

$$c_{\mathbf{k}\mu\alpha}\rightarrow e^{iq_c\theta(\tau)}c_{\mathbf{k}\mu\alpha},\qquad \chi_\mu\rightarrow e^{iq_\chi\theta(\tau)}\chi_\mu,\qquad b_{m,\sigma}\rightarrow e^{iq_b\theta(\tau)}b_{m,\sigma} \tag{7.22}$$

where q_ζ is the gauge charge associated to each field.

Provided this gauge invariance is unbroken, one can show that this leads to a Ward identity at zero temperature, which then allows to write some kind of generalized Friedel sum rule for the conserved quantity:

$$Q=\frac{1}{\pi}{\rm Im}\left[q_bN\log(-G_b^{-1}(0))-q_\chi K\log(-G_\chi^{-1}(0))-q_cNK\log(-G_c^{-1}(0))\right] \tag{7.23}$$

where all Green's functions are retarded ones.

Applying (7.23) to the conservation of the total electric charge in the case of our two-impurity model, one can write the change in the total charge related to the impurities as:

$$\Delta Q_e=NK\frac{\delta_c}{\pi}-K\frac{\delta_\chi}{\pi}=0\qquad\Longrightarrow\qquad\delta_c=\frac{\delta_\chi}{N} \tag{7.24}$$

where we used that in the large bandwidth limit this change in the total charge is ruled by the Anderson-Clogston compensation theorem [117] and goes like $O(T_K/D)$, so that it can be neglected. The respective phase shifts[2] are defined as:

$$\begin{cases} \delta_c &= -\mathrm{Im}\log\left(1 - G_{c0}(0)\Sigma_c(0)\right) \underset{N\to\infty}{=} \pi\rho_0 \dfrac{\tilde{\Sigma}_c'(0)}{N} \\ \delta_\chi &= \mathrm{Im}\log\left(J_K - \Sigma_\chi(0)\right) \end{cases} \tag{7.25}$$

The result of (7.24) ensures that, even though the conduction electron phase shift vanishes in the large-N limit, it is possible to keep track of its evolution at the order $O(1/N)$, thanks to the $\chi-$fermion phase shift, which stays finite in the large-N limit.

□ Phase diagram

Solving the set of self-consistent equations, and using the above-defined entropy as a guide, we could map out the $\left(\dfrac{T_K}{J_H}, \dfrac{T}{J_H}\right)$ phase diagram as presented in fig. 7.2. We now proceed to the detailed study of the three regions we could identify in the phase diagram.

7.2.2 Renormalized Fermi liquid region (I)

We saw that in the limit of vanishing Δ, the physics at low temperature is Fermi-liquid like and the physical properties averaged over the two impurities are the ones of a single impurity with identical spin. In the large-N limit, the expected cross-over between the $\Delta = 0$ and the $\Delta \neq 0$ region (where pair condensation of bosons appears) looks like a sharp phase transition and one can identify a line of departure from the unpaired regime (represented as a dotted line in fig. 7.2). We believe this is a consequence of our mean-field treatment of the Heisenberg interaction, and expect the cross-over to be recovered once fluctuations are included.

We refer to this Fermi liquid region of the phase diagram, as "Kondo dominated", since the value of the Heisenberg coupling is still small enough for the Kondo physics to dominate and the system basically behaves as two impurities screened by the conduction electrons only weakly coupled to each other.

□ Entropy

As bosonic pairs condense, the linear temperature dependence of the entropy is preserved at low temperatures, indicating that the Fermi-liquid behavior survives. As the Heisenberg coupling J_H is increased, one can observe two effects:

[2]Note that this definition of the conduction electron phase shift coincides with the argument of the T-matrix $T(\omega) = \frac{G_c(\omega)\Sigma_c(\omega)}{G_{c0}(\omega)}$, up to an additional π.

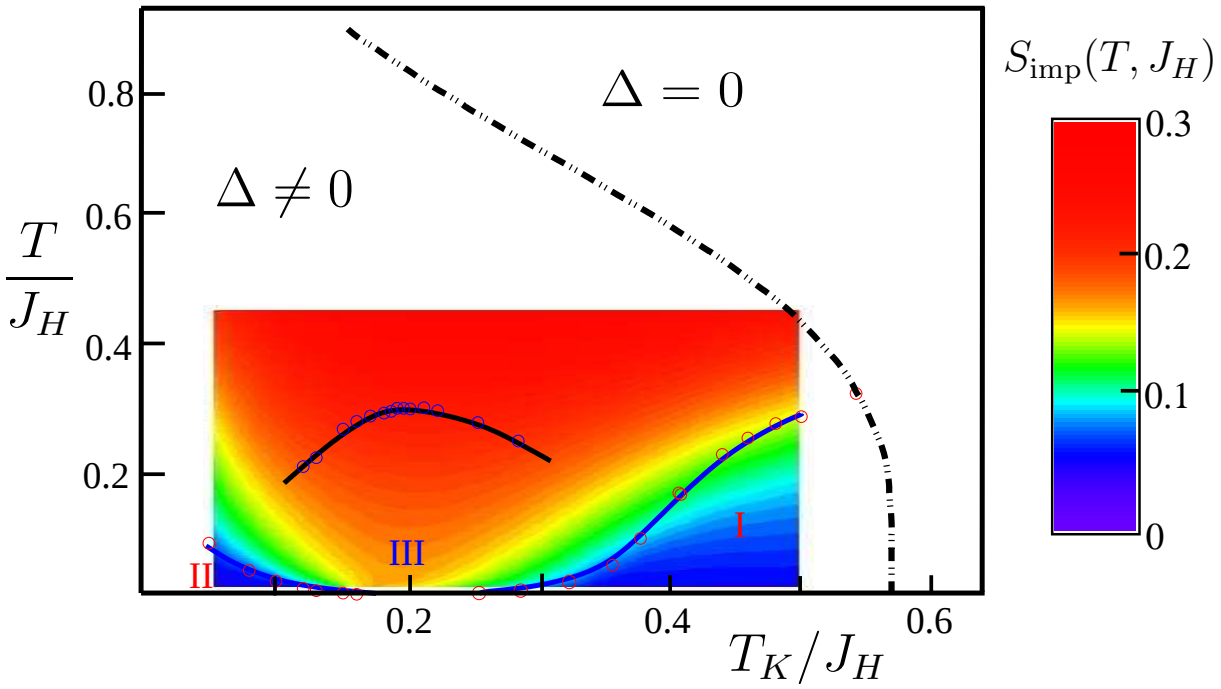

Figure 7.2: Phase diagram of the two-impurity Kondo-Heisenberg model. The circles mark the position of a local maximum in the specific heat. The color coded plot corresponds to the averaged impurity entropy $S_{\rm imp}(T, J_H)$.

- The typical temperature scale below which the Fermi liquid behavior develops drops rapidly as one departs from the $\Delta = 0$ solution. This scale is estimated from the local maximum of the specific heat linear coefficient (i.e. the inflexion point of the entropy curve).

- The specific heat linear coefficient saturates at a low-temperature value that increases with the Heisenberg coupling.

This suggests that the range in temperature of the Fermi liquid collapses in parallel with an enhancement of the Fermi liquid renormalized parameters.

□ Spectral functions

As we argued before, the exactly screened single impurity solution leads to a Fermi liquid with a well-developed gap in the spectral functions confining the Schwinger bosons and the $\chi-$fermions below a temperature of the order of the gap. This picture seems to stay valid in the case of the two-impurity system: the spectral functions look like the ones of a perfectly screened single impurity, with a gap at low-energy, and a saturation of both inverse propagators at zero energy.

However, as the Heisenberg coupling is increased, the confining gap shrinks,

which is consistent with the drop of the Fermi liquid scale observed from the entropy data.

In this region, the zero-temperature phase shift of the $\chi-$fermion is equal to π. This result can be understood by relating δ_χ to the sign of the renormalized Kondo coupling constant. Bearing in mind that $\delta_\chi = \mathrm{Im}\log\left(J_K - \Sigma_\chi(0)\right) = -\mathrm{Im}\log J_K^*$, one sees that $\delta_\chi = \pi$ corresponds to a residual ferromagnetic coupling $J_K^* < 0$. This can be understood from a strong coupling point of view, where adding a Schwinger boson to the Fermi liquid ground state increases the impurity spin $S \to S + \frac{1}{2}$ and leads to a tiny residual underscreened spin and thus to an effective ferromagnetic coupling.

7.2.3 Magnetically correlated region (II)

In the opposite limit of a large Heisenberg coupling, one expects the two impurities to screen each other, at which stage the Kondo effect barely plays any role (hence the denomination "Heisenberg dominated" for the corresponding region of the phase diagram). In the phase diagram, fig. 7.2, this limit corresponds to the lower part of the T/J_H axis. We saw from a brief analysis of the saddle-point equations that for $J_H \to \infty$, a symmetric gap develops in the bosonic spectral function, and the Fermi liquid ground state is given by the original non-interacting conduction band. This behavior is confirmed by our numerical simulation where one sees a symmetric gap, of the order of J_H and a vanishing specific heat coefficient indicating that the impurities do not affect the surrounding conduction bath.

As one slightly departs from this solution (i.e. upon reducing the Heisenberg coupling), a gap survives in the bosonic spectral function and is still symmetric. Further away, one observes the same kind of features as in the Kondo dominated region, namely a drop in the typical temperature scale T^* below which a Fermi liquid solution develop (associated to a collapse of the confining gap) as well as an increase in the specific heat coefficient (see fig. 7.3).

The low-temperature phase shift of the $\chi-$fermion extracted from the data seems to vanish, which again can be understood from the point of view of a residual Kondo coupling: $\delta_\chi = 0$ suggests an antiferromagnetic $J_K^* > 0$. In this region, the local moments mutually screen each other so that adding a Schwinger boson at any site leads to a tiny residual spin that can undergo a Kondo effect with the conduction electrons, hence the antiferromagnetic residual coupling.

7.2.4 Quantum critical region (III)

Our numerical results indicate that both Fermi liquid regions I and II collapse at the same point in the phase diagram, suggesting the presence of a quantum critical point for a value J_H^C of the Heisenberg coupling.

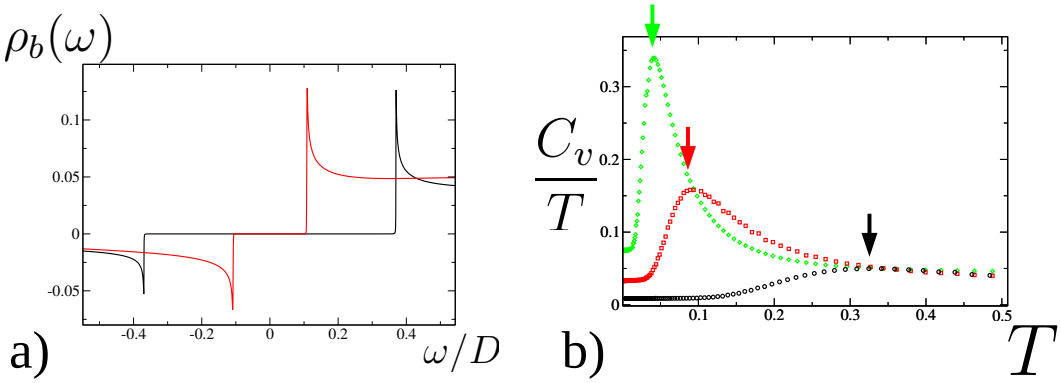

Figure 7.3: Magnetically correlated region (II): a) Symmetric gap in the bosonic spectral function for $J_H = 0.7D$ (red curve) and D (black curve), b) Specific heat coefficient for $J_H = D$ (black circles), $J_H = 0.7D$ (red squares) and $J_H = 0.5D$ (green diamonds). The arrows mark the position of the Fermi temperature T^*.

□ Signatures of a quantum critical point

The existence of a quantum critical point is confirmed by the following observations:

▷ Closing gap

As one gets closer to J_H^C at low temperature, coming from either region of the phase diagram, the gap in the spectral functions shrinks. It turns out that the collapse of the gap towards zero occurs at the same point as a function of the Heisenberg coupling.

▷ Jump in the phase shift

Upon increasing the Heisenberg coupling, the phase shift of the $\chi-$fermion goes from π in the Kondo dominated region, to 0 in the Heisenberg dominated one. Moreover, because of the confining gap, this phase shift can only be 0 or π. It follows that the phase shift jumps at the point where the gap closes.

▷ Residual entropy

Coming from either side of the quantum critical point, and as approaching J_H^C, the impurity entropy seems to develop a knee at a finite value before dropping suddenly towards zero once the temperature is of the order of the gap. As the point where the gap closes, i.e. right on top of the critical point, the entropy reaches a finite value and saturates, even at the lowest temperatures, suggesting a finite residual entropy.

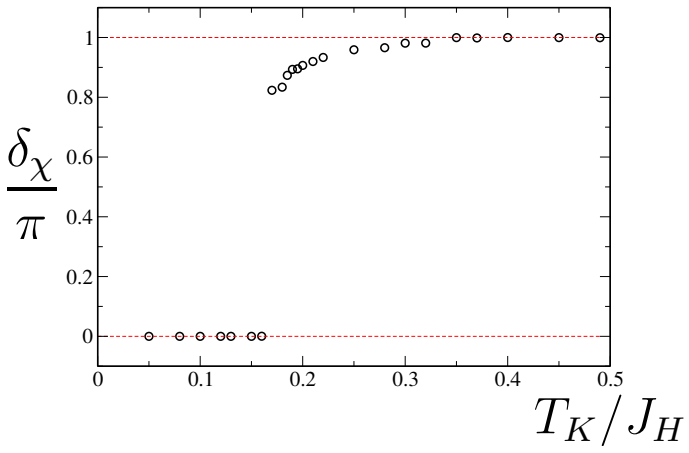

Figure 7.4: χ-fermion phase shift δ_χ/π has a function of the Heisenberg coupling at $T = 0.02T_K$. The intermediate values in the quantum critical regime are attributed to the finiteness of the temperature.

□ Low-energy analysis

The numerical solution suggests that, as one approaches the quantum critical point, not only the gap in the spectral functions closes, but also the real part of the inverse Green's functions taken at zero energy vanishes. This allows us to carry out a low-energy analysis at zero temperature, in the spirit of what has been done in the case of the overscreened single impurity.

The technical details of the derivation are provided in Appendix D, and we only mention the results here. Starting from a power-law ansatz for the propagators, one has from the self-consistency conditions:

$$G_b(\omega) \sim \frac{A e^{i\theta \mathrm{Sign}(\omega)}}{|\omega|^{\frac{2\gamma}{1+2\gamma}}} \tag{7.26}$$

$$G_\chi(\omega) \sim -\frac{1}{A\rho_0 J_K^2(1+2\gamma)} \frac{e^{-i\theta \mathrm{Sign}(\omega)}\mathrm{Sign}(\omega)}{|\omega|^{\frac{1}{1+2\gamma}}} \tag{7.27}$$

where A and θ are parameters fixed by the constraints.

This power-law behavior of the propagators at low-energy is very reminiscent of what has been obtained in the case of the overscreened single impurity. However, the exponents we obtain are the ones that one would expect from a single impurity model with a spin of size $\frac{2S}{N} = \gamma$ and a number of channels $\frac{K}{N} = 2\gamma$.

Close to the critical point, the exactly screened two-impurity model behaves as an overscreened single impurity with an effective doubling of the screening channels. This last result is quite strong since a lot of properties have been derived concerning

the overscreened single impurity solution and extends to the critical region of our two-impurity model, like e.g. ω/T-scaling, the existence of a residual entropy, ...

7.3 Discussion

In this section, we highlight the main results of previous studies of two spin-1/2 impurities coupled to a bath of conduction electrons via the Kondo interaction and compare them to our results for the two-impurity multichannel Kondo-Heisenberg model. We do recover similar results for the low-temperature behavior (generalized to a multichannel model) but not for the stability of the critical point.

7.3.1 Jones-Varma critical point

The problem of two spin-1/2 magnetic impurities embedded in a metallic host was first studied by Jones and Varma [115, 118, 119] in the late eighties. They found that for a small antiferromagnetic effective coupling between the impurities, the low-temperature behavior is that of a correlated Kondo effect, i.e. the fixed-point Hamiltonian is that for two independent Kondo impurities but the spin-spin cross correlator $\langle \mathbf{S}_1 \mathbf{S}_2 \rangle$ is non-zero. For a strong coupling between the impurities, no Kondo effect occurs, and the asymptotic phase shift is zero.

In between these two regimes, they found the existence of an unstable non-Fermi liquid fixed point: the so-called "Jones-Varma critical point". This fixed point was then studied in glory details by means of numerical renormalization group [115, 118, 119], conformal field theory [120, 121], and Abelian bosonization [122, 123].

This critical point displays physical properties reminiscent of a two-channel single impurity Kondo problem which we analyze in detail in the next paragraph. However, it turns out that this fixed point is unstable with respect to particle-hole asymmetry. Indeed, it was proved by Affleck et al. [121] that the critical point only exists if the Hamiltonian is invariant under a general particle-hole transformation of the form:

$$\begin{cases} \epsilon_{\mathbf{k}'} & = & -\epsilon_{\mathbf{k}} \\ (\mathbf{k}+\mathbf{k}')\cdot\mathbf{R} & = & 2n\pi, \quad n \in \mathbb{N} \end{cases} \tag{7.28}$$

where $\mathbf{k}'$ is a function of $\mathbf{k}$.

7.3.2 Low-temperature physics close to the QCP

We now review some of the results concerning the Jones-Varma critical point (which we also identify as the $N = 2$ case in what follows) and compare them to the results we obtained for our quantum critical point. Since we studied a slightly different model (generalization to $SU(N)$ and large number of screening channels), and study it in the large-N limit, only a qualitative comparison is relevant here.

□ Two-channel like physics

Our low-energy analysis of the Green's functions at criticality suggests that at the quantum critical point, the system looks like a single impurity coupled to twice as much channels of conduction electron. The antiferromagnetic coupling generates a second set of screening channels

The Jones-Varma critical point was studied using Abelian bosonization, where it could be mapped onto a two-channel single impurity model [122]. The author also argued that the physics responsible for the non-Fermi liquid behavior of this fixed point was the same as the one of an overscreened single impurity coupled to two channels of conduction electrons, so that an effective doubling of the original number of channels is also observed in this model.

□ Entropy

In the case of the Jones-Varma critical point, it was found that the impurity entropy saturates at a finite value of $\log 2/2$ as $T \to 0$ (i.e. half the high temperature value).

In our model, we also find a residual entropy at the QCP at low temperature. According to our low-energy analysis at the QCP, we can argue that this residual entropy is given by the formula derived for the overscreened single impurity, with an effective number of channels $\gamma_{\text{eff}} = 2p_0$:

$$\lim_{T\to 0} s_{\text{imp}} = \frac{1+2p_0}{2\pi}\text{Im}\left[\text{Li}_2\left(e^{2i\frac{\pi p_0}{1+2p_0}}\right) + \text{Li}_2\left(e^{2i\frac{\pi}{1+2p_0}}\right) - \text{Li}_2\left(e^{2i\frac{\pi(1+p_0)}{1+2p_0}}\right)\right] \quad (7.29)$$

□ Specific heat coefficient

As one would expect from a two-channel single impurity, the specific heat at the Jones-Varma fixed point diverges as a function of temperature like $\log T$.

Using the results of the overscreened single impurity, combined with our low-energy analysis of the two-impurity quantum critical point, we can deduce that the specific heat diverges at low temperatures for values of the impurity spin such that $p_0 \geq 1/2$. In particular, a logarithmic divergence is recovered for $p_0 = \gamma = 1/2$, which would correspond to the Jones-Varma case, if one were to naively take the $N \to 2$ limit of our result. Moreover, there are two local maxima in the specific heat coefficient as a function of temperature close to the quantum critical point (hence the two sets of dots in the region III of the phase diagram). This double bump feature suggests a two stage quenching process related to the generation of a second set of channels. The same behavior is observed as one approaches the Jones-Varma critical point from the temperature axis (see Fig. 7.5).

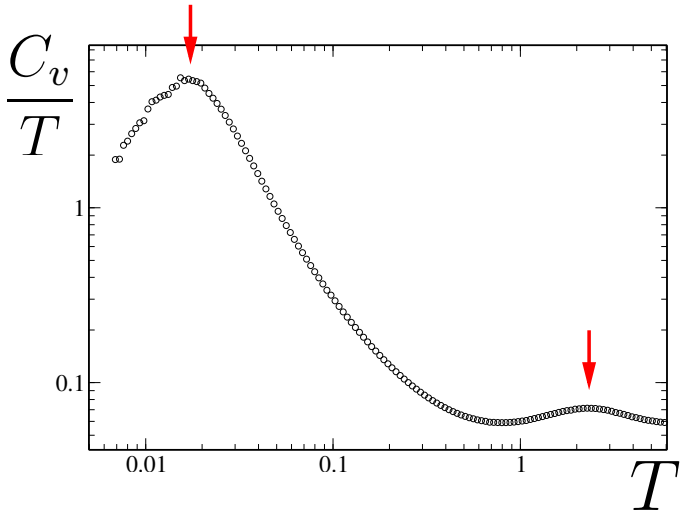

Figure 7.5: Specific heat as a function of temperature, close to the QCP. The double-log scale is used to show the presence of two local maxima in the specific heat.

□ Phase shift

For $N = 2$, it is convenient to rewrite the total phase shift as the sum of an "even" and "odd" component, δ_e and δ_o. This denomination is related to the construction of even and odd parity fields, obtained after an exact reduction of the original Hamiltonian to a one-dimensional one. It can be proved [121] that the particle-hole symmetry defined in (7.28) ensures that both δ_e and δ_o can only take values 0 and $\pi/2$: $\delta_e = \delta_o = \pi/2$ in the Kondo-screening phase, and $\delta_e = \delta_o = 0$ when the impurities form a singlet. The particle-hole symmetry enforces that the transition between the two regimes can only occur through one or more critical points, hence justifying the existence of the Jones-Varma critical point in this case.

This is precisely the behavior we observed for the $\chi-$fermion phase shift in our model: at zero temperature, it jumps from π in the renormalized Fermi liquid region, to 0 in the magnetically correlated region. The conduction electron phase shift is then given by the extension of the sum rule to our two-impurity Hamiltonian. It follows that the impurity averaged phase shift for the conduction electrons jumps from $\delta_c = \pi/N$ to 0 as one increases the inter-impurity coupling.

□ Uniform susceptibility

We do not notice any remarkable feature in the uniform susceptibility in the low temperature limit: it is non-monotonic as a function of the Heisenberg coupling and grows on both side of the critical region, to finally reach a finite value at the QCP.

This behavior is comparable to the $N = 2$ case where the uniform susceptibility saturates at low temperature for any value of the coupling between impurities.

7.3.3 Stability of the critical point

This is where our results differ most drastically from the ones of the $N = 2$ case.

We saw that for $N = 2$, the particle-hole symmetry as defined in (7.28) plays an important role as if it is not respected, the Jones-Varma fixed point no longer exists. This can be argued from the analysis of the phase shifts. In the particle-hole symmetric case, both δ_e and δ_o can only take values 0 and $\pi/2$, and one goes from a region where $\delta_e = \delta_o = \pi/2$ to a region where $\delta_e = \delta_o = 0$ through the Jones-Varma critical point.

When the particle-hole symmetry is broken (or if it does not respect (7.28)), it becomes possible to cross smoothly from unitary scattering in both even and odd channels ($\delta_e = \pi/2, \delta_o = \pi/2$) to no scattering at all ($\delta_e = 0, \delta_o = 0$).

In the large-N limit, the numerical solution always displays a quantum critical point for a given value of the Heisenberg coupling, independently of the particle-hole symmetry of the conduction band. This survival of the Jones-Varma critical point at large N in the absence of particle-hole symmetry is a consequence of the gap in the spectral functions. In the Kondo screening regime, the two-impurity sum rule imposes that:

$$\delta_e + \delta_o = \frac{2\pi}{N} \tag{7.30}$$

whereas, in the magnetically correlated region of the phase diagram, the total phase shift is 0 since the impurities form a singlet and the surrounding conduction electrons are nearly free.

One could imagine crossing smoothly from one regime to the other but this is prevented by the gap in the spectral functions. If a gap exists, the associated phase shift for the $\chi-$fermion is forced to be either 0 or π, and one has to go from one to the other through one or more critical points. As we argued when dealing with the perfectly screened single impurity, the gap is expected to arise independently on the shape of the conduction band, and in particular it is not sensitive to particle-hole asymmetry. On the other hand, our analysis of the limiting case $\Delta \to \infty$ suggests the existence of a gap even for a vanishing Kondo effect, i.e. for any conduction band. As a conclusion, we are quite confident that a gapped solution arises in both the Kondo and the Heisenberg dominated regions, leading to a necessary jump in the conduction electron phase shift and to the existence of a critical point separating these two regimes.

7.4 Conclusion

In this chapter, we studied a system of two impurity coupled via an exchange interaction, as well as a Kondo coupling to the bath of conduction electrons. We proved that our method can capture the manetic correlations appearing in such a

system. The comparison of our results to the previous approaches applied to the same system reveals a good qualitative agreement.

A few points deserve some complimentary study.

▷ Spin-spin cross-correlator and staggered susceptibility

In the Jones-Varma study the cross-correlator between impurities and the staggered susceptibility show a remarkable behavior as one approaches the critical point. The staggered susceptibility seems to diverge logarithmically with temperature as one approaches the critical point from above, while the spin-spin crosse correlator stays finite over the whole phase diagram (including the Kondo dominated region) and saturates at a constant value at the critical point.

The observation of such features has not been carried out in our model and deserves to be addressed.

▷ Pure Kondo

Another question one might ask concerns the RKKY coupling. We considered here a Kondo-Heisenberg model, but one could argue that a pure Kondo two-impurity model could also be studied.

Indeed, it can be readily seen from scaling arguments that the RKKY coupling has the same scaling as the Heisenberg term, and does not vanish in the large-N limit:

$$J_{RKKY} \quad \propto \quad \underbrace{\left(\frac{1}{\sqrt{N}}\right)^4}_{\text{4vertices}} \times \underbrace{K}_{\sum_\mu} \quad \propto \quad N \tag{7.31}$$

For an antiferromagnetic coupling, this would require to use adjoint representations for the spins. Our first analysis of this model led to the derivation of saddle-point equations that look the same as the one derived in this chapter under the condition that the conduction electron band respect particle-hole symmetry.

Considering the dramatic importance of particle-hole symmetry in the original Jones-Varma fixed point, it is legitimate to wonder whether it affects the existence of the QCP in this case. Moreover, for the RKKY coupling, it could also appear that the retardation effects slightly change the low-energy analysis carried out for the Kondo-Heisenberg model. we are currently investigating these issues.

CHAPTER 8

Conserving approximation for the single impurity model

Contents

In this chapter, we go back to the case of a perfectly screened single impurity, and investigate a new approach based on a conserving approximation, that cures some of the failures of the original large-N method. We show that this method reproduces the important results of the infinite N limit, and leads to a finite phase shift as well as a finite T-matrix for the Fermi liquid ground-state at low temperature. The main results of this chapter have been published in the Publication 5, the rest is presented here for the first time.

8.1 Model and set of equations

We showed in section 6 that the exactly screened multichannel Kondo model, taken in the large-N limit, leads to a solution that displays the low-temperature thermodynamics of an interacting Fermi-liquid. Nevertheless, the transport properties are the ones of a trivial Fermi liquid, with a vanishing T-matrix and phase shift at the impurity site.

Our main goal in this section is to try to construct a method leading to a Fermi liquid ground-state with both non-trivial thermodynamics and transport properties. Our motivation lies in the extension of such a method to describe the physics of quantum dots out of equilibrium.

8.1.1 Infinite U Anderson model

As pointed out in [112], it is possible to generalize the large-N limit for the Kondo model to the infinite U Anderson model. The latter is a slightly different model, known to display a greater variety of behavior than the Kondo model, as it allows, among others, charge fluctuations on the impurity site.

The model we consider here is a generalized multichannel Anderson model given by the Hamiltonian:

$$\begin{aligned} H &= H_K + H_{\rm int} \\ & H_K = \sum_{\mathbf{k}} \sum_{\sigma=1}^{N} \sum_{\mu=1}^{K} \epsilon_{\mathbf{k}} c^\dagger_{\mathbf{k}\sigma\mu} c_{\mathbf{k}\sigma\mu} + \epsilon_0 \sum_{\sigma} b^\dagger_\sigma b_\sigma \\ & H_{\rm int} = \frac{V}{\sqrt{N}} \sum_{\mathbf{k}} \sum_{\sigma,\mu} \left(c^\dagger_{\mathbf{k}\sigma\mu} F^\dagger_\mu b_\sigma + b^\dagger_\sigma F_\mu c_{\mathbf{k}\sigma\mu} \right) \end{aligned} \tag{8.1}$$

where we extended the spin symmetry group to $SU(N)$. Here $c^\dagger_{\mathbf{k}\sigma\mu}$ creates a conduction electron with momentum $\mathbf{k}$, channel index μ and spin index σ. The bilinear product $b^\dagger_\sigma F_\mu$ between a Schwinger boson $b^\dagger_\sigma$ and a slave fermion[1] F_μ creates a local-

[1]Note that for obscure notational reasons, this fermionic field behaves as the particle-hole symmetric of the χ-fermion used in the context of the Kondo model in previous chapters.

ized electron, which hybridizes with the conduction electron according to $H_{\rm int}$. The energy ϵ_0 of the singly occupied impurity is taken to be negative.

The constraint preventing the double-occupancy of the impurity site in the $N = 2$ case is replaced here by a constraint on the total number of Schwinger bosons and slave fermions:

$$\sum_\sigma b_\sigma^\dagger b_\sigma + \sum_\mu F_\mu^\dagger F_\mu = p_0 \tag{8.2}$$

and we enforce that $p_0 = \gamma$ since we restrict ourselves to the case of perfect screening.

Following the method of Parcollet and Georges for the Kondo model [103], it is possible to derive a set of saddle-point equations for the infinite U Anderson model in the limit $N \to \infty$, starting from the action and applying the method of steepest descent, after a few transformations (see Section 6.1.3). This set of saddle-point equations reads:

$$\begin{aligned}
\Sigma_b(\tau) &= -\gamma V^2 G_c(\tau) G_F(\tau) && \text{(8.3a)}\\
\Sigma_F(\tau) &= -V^2 G_c(\beta-\tau) G_b(\tau) && \text{(8.3b)}\\
G_b^{-1}(i\nu_n) &= i\nu_n + \lambda_0 - \epsilon_0 - \Sigma_b(i\nu_n) && \text{(8.3c)}\\
G_F^{-1}(i\omega_n) &= i\omega_n + \lambda_0 - \Sigma_F(i\nu_n) && \text{(8.3d)}\\
p_0 &= -G_b(\tau = 0^-) + \gamma G_F(\tau = 0^-) && \text{(8.3e)}
\end{aligned}$$

where we use the conventional definition of the imaginary time Green's function, $G_\phi(\tau) = -\langle T\phi(\tau)\phi^\dagger(0)\rangle$.

A few differences appear compared to the equations governing the Kondo case: the bare propagator of the slave fermion now has a frequency dependence, and the slave fermion F participates in the constraint.

It is possible to recover the Kondo model in the limit:

$$\left\{ \begin{array}{lcl} V & \to & \infty \\ \epsilon_0 & \to & -\infty \end{array} \right. \qquad \text{with} \quad J_K = \frac{V^2}{-\epsilon_0} \quad \text{fixed} \tag{8.4}$$

In this case, the kinetic bosonic term of the Hamiltonian saturates the constraint which becomes independent on the slave fermion F. Defining $G_\chi(\tau) = G_F(\beta-\tau)\frac{\epsilon_0^2}{V^2}$ and the corresponding self-energy, one recovers in the limit stated in Eq. (8.4) the saddle-point equations (6.27) of the multichannel Kondo model, with a chemical potential $\lambda = \lambda_0 - \epsilon_0$.

8.1.2 Conserving approximation

We showed in section 6 that the saddle-point equations can be derived using the Luttinger-Ward functional. The latter is given by the sum of two-particle irreducible diagrams and reduces to a single two-loop diagram in the large-N limit, the other contributions being small in powers of N. Taking the derivative of the

Luttinger-Ward functional $\Phi_{LW}[G_b, G_F, G_c]$ with respect to G_b and G_F, one obtains the equations for the self-energy of the Scwhinger boson and the salve fermion. The fermionic self-energy can also be derived from the same procedure: it turns out to be unimportant for the low-energy spectral functions as it scales like $1/N$, but it plays a significant role in the thermodynamics since it enters in the entropy formula as an overall $O(N)$ contribution. Note however that, in this case, the conduction electron self-energy Σ_c is computed at a given temperature using the Green's functions G_b and G_F obtained from solving the saddle-point equations which are themselves independent on Σ_c. In other words, the conduction electron self-energy does not enter the self-consistency loop that only relates G_b and G_F, through the corresponding self-energies.

In this paragraph, we proceed in a slightly different manner, even though the starting point is the same. In the case of the infinite U Anderson model, the Luttinger-Ward functional (Fig. 8.1) looks just the same as in the Kondo model, the only difference coming from a factor $V/\sqrt{N}$ instead of $J_K/\sqrt{N}$ at the vertex.

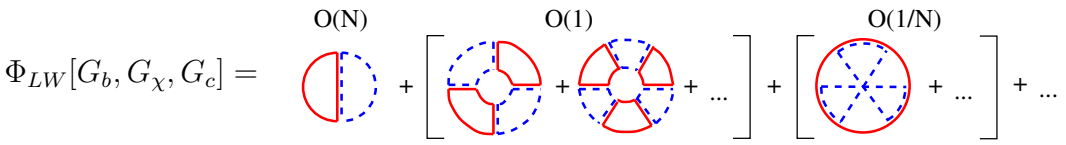

Figure 8.1: Luttinger-Ward functional grouped in powers of $1/N$. Schwinger bosons are represented by solid lines, slave fermions by dashed lines and conduction electrons by double lines.

Instead of taking the limit of infinite N, we consider the conserving approximation which amounts to neglecting all the diagrams in the Luttinger-Ward functional, but the leading order $O(N)$ term. We emphasize that contrary to the large-N limit where the reduction of the Luttinger-Ward functional was exact, here this is an approximation, as for finite N, we do neglect the higher-order terms.

One may wonder at this stage to what extent this differs from the large-N limit, since we ultimately consider the contribution of the same, unique diagram. The essential difference is that in the case of the conserving approximation stated above, the conduction electron self-energy no longer vanishes, and enters the full self-consistency which now encloses the following set of equations, obtained from taking the derivative of Φ_{LW} with respect to the Green's functions:

$$\Sigma_b(\tau) = -\gamma V^2 G_F(\tau) G_c(\tau) \tag{8.5a}$$
$$\Sigma_F(\tau) = -V^2 G_b(\tau) G_c(\beta - \tau) \tag{8.5b}$$
$$\Sigma_c(\tau) = -\tilde{\gamma} V^2 G_b(\tau) G_F(\beta - \tau) \tag{8.5c}$$

where G_b, G_F and G_c are the fully dressed imaginary-time Green's functions, and we introduced the new parameter $\tilde{\gamma} = \frac{1}{N}$.

The Dyson's equations for all three propagators now read:

$$G_b^{-1}(i\nu_n) = i\nu_n + \lambda_0 - \epsilon_0 - \Sigma_b(i\nu_n) \quad (8.6a)$$
$$G_F^{-1}(i\omega_n) = i\omega_n + \lambda_0 - \Sigma_F(i\nu_n) \quad (8.6b)$$
$$G_c^{-1}(i\omega_n) = G_{c0}^{-1}(i\omega_n) - \Sigma_c(i\omega_n) \quad (8.6c)$$

and we choose the bare conduction electron propagator, so that the associated density of states is a flat band, $\rho_{c0}(\omega) = -\frac{1}{\pi}\mathrm{Im}G_{c0}(\omega + i\delta) = \rho_0\Theta(D^2 - \omega^2)$.

As always, one has to enforce the constraint on the total number of bosons and slave fermions by adjusting the chemical potential λ_0:

$$p_0 = -G_b(\tau = 0^-) + \gamma G_F(\tau = 0^-) \quad (8.7)$$

with $p_0 = \gamma$ in our case, since we focus on the perfectly screened case only.

8.2 Thermodynamics and transport properties

We now solve self-consistently the set of equations (8.5)-(8.6), and study some of the properties of the low-temperature solution. We focus on the thermodynamics, to check whether the new self-consistency preserves the Fermi-liquid like features, and on the transport properties, to see whether this new method leads to interesting non-trivial results.

8.2.1 Existence of a gap

The first important element to stress out is that the full self-consistency does not affect the existence of the gap. The low-temperature Green's functions of both the boson and the slave fermion are gapped at low-energy. Note that the gap also appears in the conduction electron self-energy, but not in the associated full propagator since the bare conduction electron Green's function contains a finite imaginary part:

$$\mathrm{Im}G_c(\omega + i\delta) = \frac{\mathrm{Im}G_{c0}(\omega) + |G_{c0}(\omega)|^2\mathrm{Im}\Sigma_c(\omega)}{|1 - G_{c0}(\omega)\Sigma_c(\omega)|^2} \quad (8.8)$$

This allows to extend the consequences of the gap studied in section 6 to the case of the infinite U Anderson model:

- Rigid shift

  Starting from a given solution of the set of equations (8.5), and applying a small change of the chemical potential, one obtains a new solution of the equations where the Green's functions have been shifted in frequency by the change in λ_0. This can be proved analytically from the self-energy equations

in a similar way to the Kondo model. Note however that only G_b and G_F, and their associated self-energies can be rigidly shifted, Σ_c, although gapped, is not sensitive to a shift in the chemical potential λ_0:

$$\begin{aligned}\Sigma_c(\omega,\lambda_0+\delta\lambda_0) &= -\frac{\tilde{\gamma}V^2}{\pi}\int_{-\infty}^{0} d\Omega\ [G_b''(\Omega,\lambda_0+\delta\lambda_0)\ G_F(\Omega-\omega,\lambda_0+\delta\lambda_0)^* \\ &\qquad -G_F''(\Omega,\lambda_0+\delta\lambda_0)G_b(\Omega+\omega,\lambda_0+\delta\lambda_0)] \\ &= -\frac{\tilde{\gamma}V^2}{\pi}\int_{-\infty}^{0} d\Omega\ [G_b''(\Omega+\delta\lambda_0,\lambda_0)\ G_F(\Omega-\omega+\delta\lambda_0,\lambda_0)^* \\ &\qquad -G_F''(\Omega+\delta\lambda_0,\lambda_0)G_b(\Omega+\omega+\delta\lambda_0,\lambda_0)] \\ &= \Sigma_c(\omega,\lambda_0)+\int_{0}^{\delta\lambda_0} d\Omega\ [G_b''(\Omega,\lambda_0)\ G_F(\Omega-\omega,\lambda_0)^* \\ &\qquad -G_F''(\Omega,\lambda_0)G_b(\Omega+\omega,\lambda_0)] \qquad (8.9)\end{aligned}$$

where the last integral vanishes due to the gap in both $G_b''(\omega)$ and $G_F''(\omega)$.

- Low-temperature behavior

  Although the entropy formula changes a little compared to the large-N approach (see next paragraph), one can still argue that the gap in both the bosonic and the fermionic self-energy leads to a low-temperature entropy dominated by the contribution from the conduction electrons. We analyze in the next paragraphs whether this contribution is still Fermi-liquid like.

Finally, the numerical solution of the set of equations suggests that the gap depends in a non-trivial way on the value of N.

8.2.2 Thermodynamics and identities

□ Entropy

Following Luttinger and Ward [105, 106, 107], we build the free energy of the system from the various Green's functions and the Luttinger-Ward functional. After subtracting the free energy of the conduction electron gas in the absence of the impurity, we define the impurity free energy as:

$$\begin{aligned}F_{\rm imp}=F-F_{\rm bulk} &= N\int\frac{d\omega}{\pi}\ n(\omega){\rm Im}\left(\log(-G_b^{-1}(\omega))+G_b(\omega)\Sigma_b(\omega)\right) \\ &\quad +K\int\frac{d\omega}{\pi}\ f(\omega){\rm Im}\left(\log(-G_F^{-1}(\omega))+G_F(\omega)\Sigma_F(\omega)\right) \\ &\quad +NK\int\frac{d\omega}{\pi}\ f(\omega){\rm Im}\left(\log\left(\frac{G_c^{-1}(\omega)}{G_{c0}^{-1}(\omega)}\right)+G_c(\omega)\Sigma_c(\omega)\right) \\ &\quad +p_0N\lambda+\Phi_{LW}[G_b,G_\chi,G_{c0}] \qquad (8.10)\end{aligned}$$

Applying the same procedure as the one explained in Appendix A for the case of the large-N Kondo model, we can extract from (8.10) a closed-form expression for the impurity entropy which reads:

$$\begin{aligned} S_{\text{imp}} &= -N\int\frac{d\omega}{\pi}\left[\frac{\partial n(\omega)}{\partial T}\left(\text{Im}\log\left(-G_b^{-1}(\omega)\right)+G_b'(\omega)\Sigma_b''(\omega)\right)\right. \\ &\quad +K\frac{\partial f(\omega)}{\partial T}\left(\text{Im}\log\left(-G_\chi^{-1}(\omega)\right)+G_\chi'(\omega)\Sigma_\chi''(\omega)\right) \\ &\quad \left.+NK\frac{\partial f(\omega)}{\partial T}\left(\text{Im}\log\left(\frac{G_c^{-1}(\omega)}{G_{c0}^{-1}(\omega)}\right)+G_c'(\omega)\Sigma_c''(\omega)\right)\right] \end{aligned} \tag{8.11}$$

Numerically, the impurity entropy shows a linear behavior at low temperatures suggesting that a Fermi-liquid state develops below a given temperature T^*, of the order of the gap in the spectral functions. It is possible from the entropy formula (8.11) to extract an analytic expression of the specific heat coefficient at low temperature. Taking the derivative with respect to temperature, this leads after a few rearrangements:

$$\lim_{T\to 0}\frac{C_v}{T}=-\frac{\pi^2}{3}NK\rho_c(0)\left.\frac{d\Sigma_c'}{d\omega}\right|_{\omega=0} \tag{8.12}$$

The conserving approximation applied to the infinite U Anderson model leads to very similar results to the large-N approach: the low-temperature impurity entropy is Fermi-liquid like in both cases and the saturation of the low temperature specific heat coefficient is given by the same expression provided that one replaces the bare conduction electron spectral function by the full one.

□ Friedel sum rule

The expression (8.10) of the impurity free energy allows us to derive sum rules for the conserved quantities. In particular, it is possible to write a sum rule associated with the conservation of the total electric charge. Following the method mentioned in section 7.2.1 and detailed in Publication 3, we can write the change in the total charge Q_e due to the presence of the impurity, as a function of the various Green's functions:

$$\Delta Q_e=-\frac{1}{\pi}\left[NK\text{Im}\log\left(1-G_{c0}(0)\Sigma_c(0)\right)-K\text{Im}\log\left(-G_F^{-1}(0)\right)\right] \tag{8.13}$$

The change in the total charge can also be written explicitly as $\Delta Q_e = n_c - n_F - n_c^0$, where n_c and n_c^0 corresponds to the number of conduction electron with and without the impurity, and n_F is the number of clave fermions. Note that n_F comes with a minus sign because the slave fermions have an opposite charge compared to the conduction electrons (hence the name "holons" often used to designate them).

In a similar spirit, one can write another sum rule, for the total number Q_{bF} of Schwinger bosons and slave fermions, since this quantity is conserved due to the explicit constraint. Following the same method, we have:

$$\begin{aligned} Q_{bF} &= \sum_{\alpha} \langle b_{\alpha}^{\dagger} b_{\alpha} \rangle + \sum_{\mu} \langle F_{\mu}^{\dagger} F_{\mu} \rangle \\ &= \frac{1}{\pi} \left[N \mathrm{Im} \log \left(-G_b^{-1}(0) \right) - K \mathrm{Im} \log \left(-G_F^{-1}(0) \right) \right] \end{aligned} \tag{8.14}$$

This can be simplified further using that the renormalized chemical potential $\lambda^* = G_b^{-1}(0)$ is real (because of the gap) and negative so that the first term actually vanishes at low temperature. Since we focus on the exactly screened case, we impose that $Q_{bf} = K$, so that ultimately, the second sum rule, Eq. (8.14), reduces to $\mathrm{Im} \log \left(-G_F^{-1}(0) \right) = -\pi$.

Substituting it into (8.13), and recalling that the conduction electron phase shift is given by $\delta_c = -\mathrm{Im} \log \left(1 - G_{c0}(0) \Sigma_c(0) \right)$, we have the following Friedel sum rule:

$$\begin{aligned} \delta_c &= \frac{\pi}{N} \frac{K - n_F}{K} + \frac{\pi \Delta n_c}{NK} \\ &= \frac{\pi}{N} \frac{K - n_F}{K} + O\left(\frac{T_K}{ND} \right) \end{aligned} \tag{8.15}$$

where $\Delta n_c = n_c - n_c^0 = -\frac{NK}{\pi} \int_{-\infty}^{0} d\omega \ \mathrm{Im} \left(G_c(\omega) - G_{c0}(\omega) \right)$. According to the Clogston-Anderson compensation theorem [117], the change in the electronic charge due to a Kondo or Anderson impurity vanishes in the large bandwidth limit like the ratio of the Kondo temperature to the bandwidth, allowing us to replace $\Delta n_c = O(N \frac{T_K}{D})$.

We determined the conduction electron phase shift from the numerical solution of the full self-consistent equations, and compared it to the phase shift obtained from plugging the large-N solution into the $O(1/N)$ expression into Σ_c. The results are presented in Fig. 8.2, and show that our conserving approximation preserves the sum rule (8.15) for each value of N.

□ Yamada-Yosida-Yoshimori identity

Along with the Friedel sum rule, our conserving approximation preserves some important interrelationships of the Fermi liquid among which the so-called "Yamada-Yosida-Yoshimori" identity, which relates the specific heat coefficient to the spin, charge and channel susceptibilities.

This identity can be derived from Nozières local Fermi liquid theory [124] which relates the quasiparticle spectrum in the Fermi-liquid ground-state to the conduction electron phase shift, and its response to an applied field, or a change in chemical

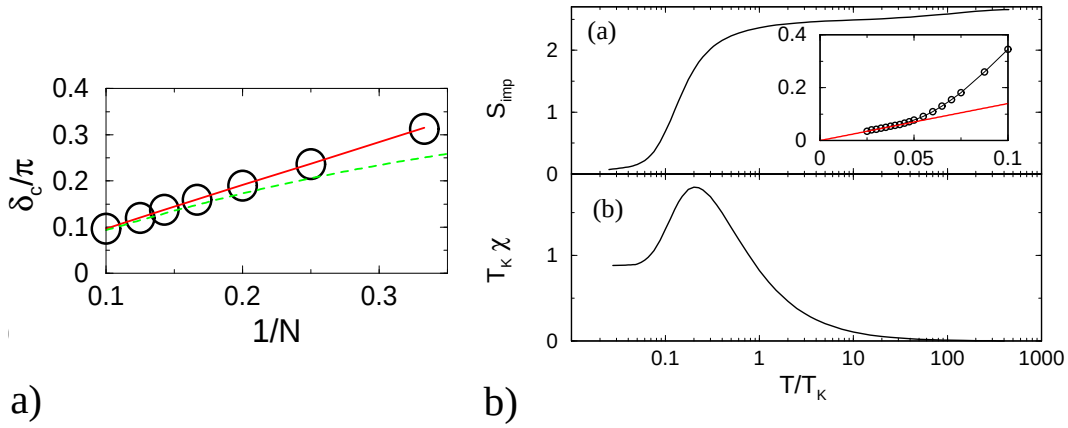

Figure 8.2: a) Phase shifts extracted from the calculated T-matrices, for $K = 1$ and $n_F \simeq 0.04$. The solid line stands for $(K - n_F)/NK$ and the dashed line shows the phase shift obtained without imposing the self-consistency on the conduction electron. b) Entropy and impurity spin susceptibility as a function of temperature, obtained for $K = 1$ and $N = 4$. In the inset: the low-temperature entropy shows a linear behavior.

potential. In the context of our generalized multichannel Kondo or Anderson model, this derivation is presented in Appendix C, and the main result reads:

$$NK(N+K)\frac{\delta C_v}{C_v^{(0)}} = K(N^2-1)\frac{\delta\chi_s}{\chi_s^{(0)}} + N(K^2-1)\frac{\delta\chi_f}{\chi_f^{(0)}} + (N+K)\frac{\delta\chi_c}{\chi_c^{(0)}} \tag{8.16}$$

where δC_v and $\delta\chi$ are, respectively, the change in the specific heat and the susceptibility due to the impurity, and $\chi^{(0)}_{s,f,c}$ denote the spin, flavor, and charge susceptibility in the absence of the impurity.

Note that in the special case of the Kondo model, the interaction does not affect the charge or the channel index so that both χ_f and χ_c are zero, and the previous result (8.16) reduces to the Wilson ratio:

$$W = \frac{\delta\chi_s/\chi_s^{(0)}}{\delta C_v/C_v^{(0)}} = \frac{N(N+K)}{N^2-1} \tag{8.17}$$

where we recover the Bethe ansatz result [114].

□ Susceptibility

Computing numerically the solution to the full set of self-consistent equations in the presence of an external magnetic field coupled to both the conduction electrons and the Schwinger bosons, we extract the impurity susceptibility as a function of temperature. The general shape is similar to the one of the local susceptibility

studied in the large-N limit of the perfectly screened impurity: the $1/T$ behavior at high temperature crosses over after reaching a maximum, and saturates at a finite value as $T \to 0$. This saturation at low temperature is another hint that the conserving approximation does describe some of the physical properties of the Fermi-liquid ground-state.

The major difference compared to the large-N limit is that now, despite the gap in the spectral functions, the frequency-dependent susceptibility is not gapped. This is because the dynamic spin susceptibility no longer writes as a simple convolution of two bosonic propagators like in the large-N limit, and is now made of a whole series of diagrams. This same gap in the spectral functions allows one to extend the derivation carried out by Shiba on the finite U Anderson model [125]: the presence of a finite scale in the excitation spectrum allows one to replace the Matsubara summations by integrals at low temperatures, so that one can generalize Shiba's results to the infinite U Anderson model. In our multichannel version of the Anderson model, the Shiba relationship writes:

$$\left.\frac{\chi_s''(\omega)}{\omega}\right|_{\omega=0} = \frac{\pi N}{2K}\left(\frac{\chi_s}{N}\right)^2 \tag{8.18}$$

where χ_s is the impurity spin susceptibility, and the $''$ notation stands for the imaginary part.

This relationship guarantees that the imaginary part of the frequency-dependent spin susceptibility is linear at low frequencies, ensuring that the spin response function decays as $1/t^2$ in time, as expected from a Fermi liquid.

8.2.3 Transport properties

We now turn to a discussion of the electron scattering off the impurity.

□ T-matrix

The electron scattering is determined by the conduction electron T-matrix, defined as:

$$T(\omega + i\delta) = \frac{G_c(\omega + i\delta)\Sigma_c(\omega + i\delta)}{G_{c0}(\omega + i\delta)} \tag{8.19}$$

As the temperature is lowered, a sharp peak develops in the imaginary part of the T-matrix, close to the Fermi energy. Unlike the peaks appearing in the spectral functions, this feature does not diverge at low temperature, and finally saturates a decade below the Kondo temperature. Note however that the associated structure in the conduction electron self-energy does diverge as $T \to 0$, and the saturation in the T-matrix arises from a compensation between the numerator and the denominator, both dominated by Σ_c at low temperature.

Due to the low-energy gap in the conduction electron self-energy, the T-matrix at the Fermi energy is given by:

$$\begin{aligned} T_c''(0) &= \frac{-\pi\rho_0 Sigma_c'(0)^2}{|1+i\pi\rho_0\Sigma_c'(0)|^2} = \frac{-\frac{\tan^2\delta_c}{\pi\rho_0}}{|1-i\tan\delta_c|^2} \\ &= -\frac{\sin^2\delta_c}{\pi\rho_0} \end{aligned} \tag{8.20}$$

where we considered the large bandwidth limit, and thus neglected the real part of the bare conduction electron Green's function.

It follows from (8.20) that the fully developed resonance is pinned at the Fermi energy, to the Langreth sum-rule value [126] of $-(\sin^2\delta_c)/(\pi\rho_0)$. This could be verified numerically, as one can see in Fig. 8.3.

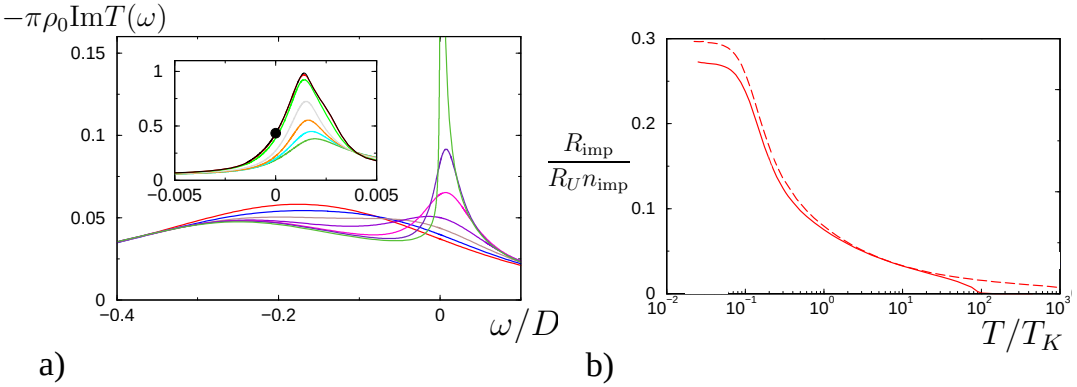

Figure 8.3: a) T-matrix as a function of frequency for decreasing temperature: a resonance develops close to the Fermi energy. Inset: Magnification of the resonance, the dot marks the value $\sin^2\delta_c$. b) Impurity contribution to the resistivity for two different values of the hybridization.

□ Resistivity

Various important physical properties, such as the impurity resistivity in the dilute limit, can be related to the conduction electron T-matrix.

The impurity contribution R_i to the resistivity of the system is connected to the thermal average of the T-matrix:

$$R_i = n_i R_U \left[\int d\omega \, \left(-\frac{\partial f}{\partial \omega}\right) \frac{1}{\pi\rho_0 |T''(\omega)|} \right]^{-1} \tag{8.21}$$

where R_U is the unitary resistivity, and n_i is the density of impurities in the dilute limit.

We plot the resistivity for a given set of parameters in Fig. 8.3. This impurity resistivity increases as one lowers the temperature and saturates at a constant value given by:

$$\lim_{T\to 0} \frac{R_i}{R_U} = n_i \pi \rho_0 |T''(0)| = n_i \sin^2 \delta_c \tag{8.22}$$

8.3 The $N \to 2$ limit

Our conserving approximation does not only recover the thermodynamic aspects of the Fermi liquid already studied in the large-N limit, but also correctly describes the transport properties of the system via a finite T-matrix.

It is natural to try to extend this scheme down to the physical case of $N \to 2$, and study whether, in the Kondo limit, this recovers the expected properties of the local Fermi liquid, in particular the $\pi/2$ conduction electron phase shift and the quadratic frequency dependence of the conduction electron self-energy.

8.3.1 Spectral functions

□ Low-energy gap

The first important feature to notice as one reduces N, is that the gap in the spectral functions shrinks and ultimately seems to close in the limit $N \to 2$.

This leads to two opposite expectations. The closing of the gap looks promising for the recovery of the expected conduction self-energy of the local Fermi liquid, as no gap in Σ_c is known to appear in this case. A collapsing gap is a necessary condition to get the quadratic dependence of the imaginary part Σ_c'', characteristic of a Fermi liquid. On the other side, a vanishing gap suggests that both the Schwinger bosons and the slave fermions contribute to the thermodynamics, which is problematic unless they recombine to generate a Fermi-liquid like behavior.

The absence of a gap also prevents the extension of most of the results concerning the conserving approximation, as they were derived assuming the presence of a scale in the excitation spectrum.

□ Conduction electron self-energy

We saw for a given value of N that the low-temperature T-matrix saturates, and that this saturation was associated to a compensation between numerator and denominator of the diverging conduction electron self-energy.

The collapse of the gap does not affect the divergence, and one does not recover the quadratic term in frequency, expected for the local Fermi liquid.

This divergence manifests itself at the boundary of the gap, and leads to a dip in the full conduction electron spectral function which ultimately touches zero at low temperature. As one lowers N towards 2, the gap closes and the dip in the spectral

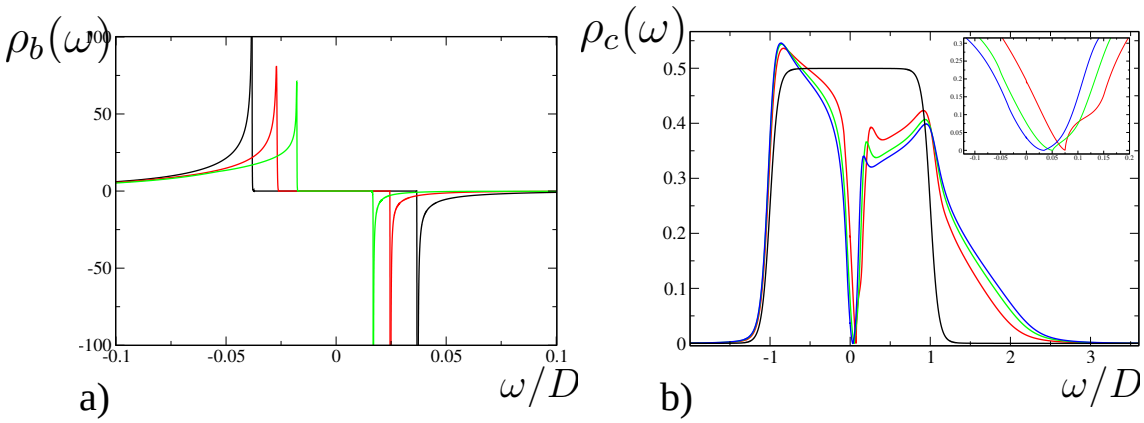

Figure 8.4: a) Closing of the gap in the bosonic spectral function as one reduces N: $1/N = 0.3$ in black, $1/N = 0.4$ in red and $1/N = 0.45$ in green. b) Conduction electron spectral function: for bare fermions (black), for $1/N = 0.3$ (red), 0.4 (green), and 0.45 (blue). The dip gets deeper and closer to the Fermi energy as $N \to 2$. Inset: tip of the dip for the three previous values of N.

function ρ_c gets closer to the Fermi energy. This suggests that at low temperature, the solution of the self-consistent equations in the limit of $N \to 2$ might be better described by a Kondo pseudogap model, where the conduction electron spectral function is depleted close to the Fermi energy.

8.3.2 Low-energy analysis

It is known from other studies on the Kondo pseudogap [127, 128, 129] that the actual behavior of the system at low temperature strongly depends on the power-law decay of the spectral function close to the Fermi energy. In our case, this decay relates to the divergence of the conduction electron self-energy at low temperature, and could be obtained from a low-energy analysis of the set of self-consistent coupled equations (similar to the one carried out for the overscreened single impurity and the quantum critical regime of the two-impurity model) which becomes possible for $N \to 2$ because of the closing gap.

This low-energy analysis is a bit more difficult than the one carried out in the case of the two-impurity system, and now involves all three Green's functions.

Note however that such a low-energy analysis only works well below the Kondo temperature, which itself might vanish in the limit $N \to 2$, as it has been observed in the Kondo pseudogap problem.

We are currently investigating the evolution of the Kondo temperature as a function of N. If this reveals that T_K remains finite as $N \to 2$ (eventually for a given range of the other parameters), such a low-energy analysis would be clearly called on.

8.4 What is still missing?

Although the conserving approximation cures some of the drawbacks of the large-N limit, we just argued that it still has some failures. In particular, the low-temperature transport properties are recovered, but not at the level of the conduction electron Green's function. In this section, we briefly explore the possible ways of fixing these remaining issues.

8.4.1 Uncontrolled ways of fixing the method

It seems that the main missing ingredient of both the large-N and the conserving approaches is the absence of vertex corrections. However, a full account of these vertex corrections would not be tractable in any simple way.

A first treatment that might lead to interesting results amounts to neglecting all vertex corrections but the simplest one, for which the external frequencies are taken to be zero (see Fig. 8.5). This would lead to a temperature-dependent renormalization of the Kondo coupling J_K.

Although completely uncontrolled, such an approach could lead to some insight concerning the role of the vertex corrections.

8.4.2 Box representation and matrix models

An idea developed in [130], and earlier in [112], amounts to including on top of the spin index running from 1 to N and the channel index running from 1 to K, a color index running from 1 to Q (where both K and Q scale with N). In terms of Young tableaux, this corresponds to a box representation of the impurity spin, represented in the perfectly screened case by a rectangle of size $K \times Q$ (see Fig. 8.5).

This suggests an analogous treatment to the ones carried out so far. Note however that in this case, the conduction electron no longer plays a special role, since there are $O(N^2)$ flavors of all three fields. As a consequence, all three self-energies are of the same order in N, in particular Σ_c does not vanish in the large-N limit.

Nevertheless, there is a major drawback to this extension. Generalizing the Luttinger-Ward approach derived earlier to this multichannel-multicolor model, one readily sees that the sum of skeleton diagrams does not reduce to a single contribution, even in the large-N limit. There is a profusion of diagrams of order $O(N^2)$, given by the sum of all two-particle irreducible planar diagrams. An attempt to derive the saddle-point equations starting from the action, leads to the introduction of three $K \times K$ matrices: Q, $\bar{Q}$ and λ, analogous to the ones defined in Chapter 6. It follows that in the large-N limit, this model is also very hard to solve from a path-integral perspective.

Unfortunately, there is no simple way of resuming this series of diagrams apart from introducing two-particle irreducible self-energies, in which case the set of

saddle-point equations is hardly tractable in practice.

Cutting the sum to its first two-loop diagram leads precisely to the approach we studied in this chapter, up to a modification of the prefactors to take into account the existence of a new flavor.

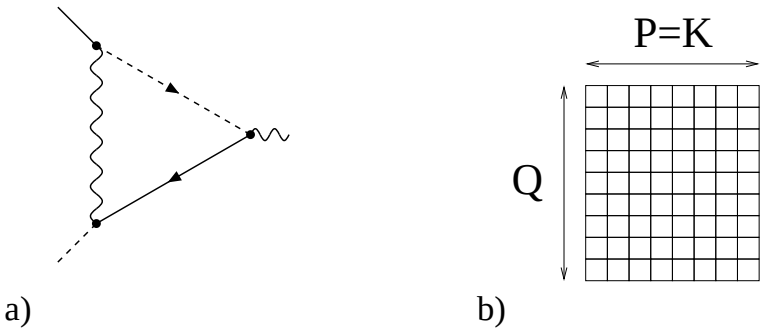

Figure 8.5: a) Simple vertex correction entering the renormalization of the Kondo coupling, b) Young tableaux for the box representation of the impurity spin in the exactly screened case.

8.5 Conclusion

In this chapter, we developed a new conserving approach to the exactly screened infinite U Anderson model. Unlike the large-N limit studied in Chapter 6, this method captures not only the thermodynamic aspects of the local Fermi liquid at low-temperature, but also the transport properties and some important interrelationships typical of the Fermi liquid ground-state.

However, we also proved that although this method cures the main failures of the large-N limit, it does not correctly describe the behavior of the conduction electron self-energy, especially in the limit of $N \to 2$.

One of the possible approaches to solve this issue involves an additional color index, but turns out to be much more difficult to carry out. This raises the question of the description of the Kondo physics with this type of formalism. Maybe the Kondo problem is too complex to be described by a large-N limit and a simple set of saddle-point equations, one can then only access some of the physics of the fully quenched Fermi liquid. This might also be an artifact of the current methods, in which case, a more clever approach, involving a different representation of the impurity spin, or the extension to another symmetry group (e.g. $Sp(N)$), remains to be found.

An interesting development of our conserving approximation lies in the study of non-equilibrium quantum dots. An extension of our approach can be made using a Keldysh generalization [131] of the self-consistency equations. Many features of our

method (conserving properties, recovery of the interacting Fermi liquid, incorporation of the spin relaxation effects, ...) suggest that it will be a robust scheme to examine how spin and conduction electron dephasing effects evolve with voltage in quantum dots.

CHAPTER 9

Kondo lattice models: preliminary results

Contents

In this chapter, we consider a generalization of the Kondo and Kondo-Heisenberg model studied in Chapter 6 and 7 to a lattice. After deriving the large-N equations for these models, we explore some possible treatments leading if not to a full solution, at least to some insight concerning the properties displayed by such a system. Most of this work is very preliminary, and as such, has not been published at the moment.

9.1 Kondo lattice model

The Kondo Hamiltonian studied in Chapter 6 in the case of a single impurity can easily be extended to a large number $\mathcal{N}$ of impurities. In this situation, we consider a regularly spaced lattice of "impurities"[1] in three dimensions, invariant under translation.

9.1.1 Model and saddle-point equations

□ The model

The Hamiltonian of the Kondo lattice is a natural generalization of the single impurity one, which amounts to considering that the Kondo interaction occurs not only at the site of the isolated impurity, but at every site of a regular cubic lattice[2], leading to:

$$\begin{aligned} H &= H_{\text{band}} + H_{\text{Kondo}} \quad \text{where} \\ & H_{\text{band}} = \sum_{\mathbf{k}} \sum_{\alpha=1}^{N} \sum_{\mu=1}^{K} \epsilon_{\mathbf{k}} c^{\dagger}_{\mathbf{k}\alpha\mu} c_{\mathbf{k}\alpha\mu} \\ & H_{\text{Kondo}} = \frac{J_K}{N} \sum_{i} \sum_{\alpha,\beta} \sum_{\mu} S^{i}_{\alpha\beta} \psi^{\dagger}_{i\beta\mu} \psi_{i\alpha\mu} \end{aligned} \tag{9.1}$$

where ψ_i is the real-space counterpart of the conduction electron field $c_{\mathbf{k}}$, and we use a bosonic representation of the lattice spins, with the associated constraint:

$$S^{i}_{\alpha\beta} = b^{\dagger}_{i\alpha} b_{i\beta} - \frac{P}{N}\delta_{\alpha\beta} \tag{9.2}$$

$$\sum_{\alpha} b^{\dagger}_{i\alpha} b_{i\alpha} = P \tag{9.3}$$

The electronic dispersion for the cubic lattice is described by a simple constant hopping term between nearest neighbour of the metallic host lattice:

$$H_{\text{band}} = t \sum_{\langle i,j \rangle} \sum_{\alpha=1}^{N} \sum_{\mu=1}^{K} c^{\dagger}_{i\alpha\mu} c_{j\alpha\mu} \quad \Longrightarrow \quad \epsilon_{\mathbf{k}} = 2t \left(\cos(k_x a) + \cos(k_y a) + \cos(k_z a) \right) \tag{9.4}$$

where a is the impurity lattice spacing.

[1] The term "impurities" is a bit misleading here as it suggests some kind of randomness, while we are interested in a regular lattice. We still refer to it though, since this model is a natural extension of the single-impurity one.

[2] The structure of the lattice does not matter much at this stage, we restrict ourselves to the cubic case for simplicity.

Moreover, we focus only on the exactly screened regime, for which the size P of the impurity line representation equals the number K of channels.

We saw that the typical energy scale over which the Kondo singlet develops is not given by the Kondo coupling but rather by the Kondo temperature T_K. We also argued that the Kondo interaction leads, when many impurities are present, to an effective interaction between the localized spins, mediated by the conduction electron: the so-called RKKY interaction [88, 89, 90]. We presented in Chapter 5 Doniach's picture of the Kondo lattice [92], which predicts from comparing the typical energy scale of the Kondo and RKKY interactions that the system can go from magnetically ordered state (when $T_{RKKY} \gg T_K$) to a Fermi liquid ground-state (when $T_K \gg T_{RKKY}$) upon increasing the Kondo coupling J_K. At zero temperature, this requires the existence of a quantum critical point between the two phases.

□ Large-N equations

Proceeding exactly as we did in Chapter 6 (say from a path-integral formalism), it is possible to derive the saddle-point equations for this model in the large-N limit. This requires the introduction of new fields which are now dependent on the position in real space, namely $Q_{ij}(\tau, \tau')$ and $\bar{Q}_{ij}(\tau, \tau')$. These fields are determined from applying the method of steepest descent, and can be related to the bosonic and fermionic self-energies.

In practice, the generalization of the method to a large number of impurities is not more difficult than the original single impurity derivation, and leads to the following set of equations:

$$\text{Dyson's equations:} \quad G_b^{-1}(\mathbf{k}, i\nu_n) = i\nu_n + \lambda - \Sigma_b(\mathbf{k}, i\nu_n) \tag{9.5a}$$

$$G_\chi^{-1}(\mathbf{k}, i\omega_n) = J_K - \Sigma_\chi(\mathbf{k}, i\omega_n) \tag{9.5b}$$

$$\text{Schwinger boson:} \quad \Sigma_b(\mathbf{r}, \tau) = \gamma J_K^2 G_c(\mathbf{r}, \tau) G_\chi(-\mathbf{r}, -\tau) \tag{9.5c}$$

$$\chi\text{−fermion:} \quad \Sigma_\chi(\mathbf{r}, \tau) = -J_K^2 G_c(\mathbf{r}, \tau) G_b(-\mathbf{r}, -\tau) \tag{9.5d}$$

$$\text{Conduction electron:} \quad G_{c0}(\mathbf{k}, i\omega_n) = \sum_{\mathbf{k}} \frac{1}{i\omega_n - \epsilon_{\mathbf{k}}} \tag{9.5e}$$

$$\text{Constraint:} \quad -G_b(\mathbf{r}, \tau = 0^-) = p_0 \delta(\mathbf{r}) \tag{9.5f}$$

Because of the momentum dependence, this set of equations is much more difficult to solve both analytically and numerically: one now has to deal with a convolution over a four-dimensional space. The full-fledge lattice is a hard problem to tackle and one has to think of approximate ways of treating the interesting physics related to this model.

This set of self-consistent equations is only suitable for the description of the Fermi-liquid region of the phase diagram. Indeed, the development of magnetic ordering leads, in this kind of bosonic representation, to a condensation of the

Schwinger bosons and an hybridization of the χ-fermions with the conduction electron fields. In the magnetic state, one has to take into account the bosonic condensation explicitly, and treat the hybridization through the definition of a single fermionic field, whose associated Green's function contains anomalous propagators.

9.1.2 Luttinger sum rule

The Luttinger theorem is among the very few results one can extract from the large-N equations without any further approximation. This can be derived from a Luttinger-Ward perspective in a very similar way to the two-impurity Friedel sum-rule studied in Chapter 7. The full derivation of the Luttinger sum rule for the Kondo lattice model is presented in Publication 3, and we now only highlight the main steps.

The conservation of the total charge leads to a Ward identity, provided that the Schwinger boson is uncondensed, i.e. that we are in the non-magnetic region of the phase diagram. In the paramagnet, this Ward identity allows to write the total electric charge as:

$$Q_e = -\frac{1}{\pi}\sum_{\mathbf{k}} \mathrm{Im}\left[NK\log(-G_c^{-1}(\mathbf{k},0+i\delta)) + K\log(G_\chi^{-1}(\mathbf{k},0+i\delta))\right] \tag{9.6}$$

which now involves a trace over momentum.

The first term in this expression is the electron Fermi surface volume:

$$-\sum_{\mathbf{k}}\frac{1}{\pi}\mathrm{Im}\log\left[\epsilon_{\mathbf{k}}+\Sigma_c(\mathbf{k},0+i\delta)-\mu-i\delta\right] = \sum_{\mathbf{k}}\Theta(\mu-E_{\mathbf{k}}) = \frac{\mathrm{v}_{FS}}{(2\pi)^3}, \tag{9.7}$$

where μ is the chemical potential and the region where $E_k-\mu=\epsilon_k-\mu+\mathrm{Re}\Sigma_c(k,E_k)$ is negative defines the interior of the Fermi surface.

The second term can be interpreted in a similar way - the momentum trace over the logarithm of G_χ^{-1}

$$\sum_{\mathbf{k}}\frac{1}{\pi}\mathrm{Im}\log\left[J_K-\Sigma_\chi(\mathbf{k},0+i\delta)\right] = \sum_k \theta[-J_K^*(\mathbf{k})] = \frac{\mathrm{v}_\chi}{(2\pi)^3} \tag{9.8}$$

can be seen as the volume of the region in momentum space where the effective interaction $J_K^*(\mathbf{k}) = J_K^2 G_\chi(\mathbf{k},0+i\delta)^{-1}$ is negative, or ferromagnetic.

Following our earlier discussion, the ferromagnetic sign of the residual interaction is a consequence of the fact that additional spins added to the paramagnetic state completely decouple from the Fermi sea. In the simplest scenario, $J_K^*(\mathbf{k}) < 0$ for all $\mathbf{k}$, in which case $\frac{\mathrm{v}_\chi}{(2\pi)^3}=1$, and the sum rule leads to the following result for the Fermi surface volume:

$$N\frac{\mathrm{v}_{FS}}{(2\pi)^3} = n_e + 1 \tag{9.9}$$

where n_e is the electron density per unit cell, per conduction electron channel: $n_e = Q_e/K$.

It follows that the total Fermi surface volume expands by one unit per unit cell, due to the Kondo interaction with the lattice of localized spins. To preserve the overall charge density, the electron Fermi surface volume is forced to enlarge to "screen" the finite background density of charged χ-fermions.

In the magnetically ordered state, the boson field condenses, causing the conduction and χ fields to hybridize to produce a single species. In this case, the sum rule becomes:

$$Q_e = -\frac{1}{\pi}\sum_{\mathbf{k}} \mathrm{Im}\log\left[-G_f^{-1}(\mathbf{k}, 0+i\delta)\right] \tag{9.10}$$

where G_f is the admixed propagator for the combined conduction and χ fields.

The right-hand side cannot be separated into χ and conduction parts, and as such, defines an admixed set of Fermi surfaces, with an average Fermi surface volume which counts the total charge per unit cell:

$$n_e = N\frac{\langle \mathrm{v}_{AFM}\rangle}{(2\pi)^3}. \tag{9.11}$$

If the transition from the paramagnet to the magnetic state occurs via a single quantum critical point, then our results indicate that the transition in the Fermi surface volume at the second order quantum critical point is abrupt: the total Fermi surface volume jumps as one crosses the QCP.

9.2 Kondo-Heisenberg lattice model

The other important model we defined in previous chapters is the Kondo-Heisenberg model, where one considers, on top of the Kondo interaction between the localized spins and the bath of conduction electrons, a direct exchange between the impurities, described by an Heisenberg interaction. In this section, we extend the two-impurity model studied in Chapter 7 to the case of a lattice.

9.2.1 Model and saddle-point equations

□ The model

Like the model studied in Chapter 7, we choose to restrict ourselves to the antiferromagnetic Heisenberg coupling, and describe this interaction in terms of the short-range bosonic pair operator.

The Hamiltonian of the Kondo-Heisenberg lattice, with a bosonic representation

of the localized spins, is given by:

$$\begin{aligned} H &= H_{\rm band} + H_{\rm Kondo} + H_{\rm Heisenberg} \quad \text{where} \\ H_{\rm band} &= \sum_{\mathbf{k}} \sum_{\alpha=1}^{N} \sum_{\mu=1}^{K} \epsilon_{\mathbf{k}} c^{\dagger}_{\mathbf{k}\alpha\mu} c_{\mathbf{k}\alpha\mu} \\ H_{\rm Kondo} &= \frac{J_K}{N} \sum_{i} \sum_{\alpha,\beta} \sum_{\mu} b^{\dagger}_{i\alpha} b_{i\beta} \psi^{\dagger}_{i\beta\mu} \psi_{i\alpha\mu} \\ H_{\rm Heisenberg} &= \frac{J_H}{N} \sum_{\langle i,j \rangle} \left(\sum_{m\sigma} \sigma b^{\dagger}_{i,m,\sigma} b^{\dagger}_{j,m,-\sigma} \right) \left(\sum_{m'\sigma'} \sigma' b_{i,m',\sigma'} b_{j,m',-\sigma'} \right) \end{aligned} \tag{9.12}$$

where $\langle i.j \rangle$ denotes the sum over nearest neighbors, and we recast the N spin indices under the form $\left(m = 1 \ldots \frac{N}{2}, \sigma = \pm\right)$.

Like the Kondo lattice model presented in the previous section, this model is expected to display (at least) two ground-states in the exactly screened regime: a magnetic state governed by the Heisenberg interaction and for which the Schwinger bosons condense, and a Fermi liquid state where the Kondo interaction dominates and leads to nearly independent fully quenched impurities.

□ Large-N equations

After decoupling both the Kondo and the Heisenberg interaction terms, introducing in the process two sets of fields ($\chi_{i,\mu}$ and $\Delta_{i,j}$) and integrating the conduction electrons out of the partition function, we end up with an effective action that looks like Eq. (7.3) obtained for the two-impurity system, namely:

$$\begin{aligned} S &= \int_0^{\beta} d\tau \sum_{i,m,\sigma} b^{\dagger}_{i,m,\sigma}(\tau) \left(\partial_\tau - \lambda_i(\tau)\right) b_{i,m,\sigma}(\tau) - \frac{1}{J_K} \int_0^{\beta} d\tau \sum_{i,\mu} \chi^{\dagger}_{i,\mu}(\tau) \chi_{i,\mu}(\tau) \\ &- \frac{1}{N} \sum_{i,j} \int_0^{\beta} d\tau d\tau' \sum_{\mu} \chi_{j,\mu}(\tau') \chi^{\dagger}_{i,\mu}(\tau) \; G_{c0}(i-j;\tau-\tau') \sum_{m,\sigma} b_{j,m,\sigma}(\tau') b^{\dagger}_{i,m,\sigma}(\tau) \\ &+ \sum_{\langle i,j \rangle} \int_0^{\beta} d\tau \left(\Delta^{\dagger}_{i,j}(\tau) \sum_{m,\sigma} \sigma b_{i,m,\sigma}(\tau) b_{j,m,-\sigma}(\tau) + \text{h.c.} \right) \\ &+ \frac{N}{J_H} \sum_{\langle i,j \rangle} \int_0^{\beta} d\tau \; \Delta^{\dagger}_{i,j}(\tau) \Delta_{i,j}(\tau) + p_0 N \sum_i \int_0^{\beta} d\tau \; \lambda_i(\tau) \end{aligned} \tag{9.13}$$

Since $\Delta_{i,j}$ represents a pair of bosons with opposite "spins" (σ is different for the two bosons involved in the pair), it is symmetric under the exchange $\sigma \to -\sigma$, so that it has to be antisymmetric in space: $\Delta_{i,j} = -\Delta_{j,i}$. We now assume a static local solution for the chemical potential $\lambda_i = \lambda$ and the bosonic pair field $\Delta_{i,j} = \text{Sgn}(i-j)\Delta$.

We proceed exactly as we did for the two-impurity model studied in Chapter 7: after introducing two new fields $Q(i,j,\tau,\tau')$ and $\bar{Q}(i,j,\tau,\tau')$, we can build an effective action $S(Q,\bar{Q},\lambda,\Delta)$ where every term scales like N. Relating the bosonic and fermionic self-energies to the fields Q and $\bar{Q}$, the saddle-point equations read:

$$\Sigma_b(\mathbf{r},\tau) = \begin{bmatrix} \gamma J_K^2 G_\chi(-\mathbf{r},-\tau)G_{c0}(\mathbf{r},\tau) & 0 \\ 0 & \gamma J_K^2 G_\chi(\mathbf{r},\tau)G_{c0}(-\mathbf{r},-\tau) \end{bmatrix} \quad (9.14a)$$

$$\Sigma_\chi(\mathbf{r},\tau) = -\frac{J_K^2}{2} G_{c0}(\mathbf{r},\tau)\left(G_b^{(++)}(-\mathbf{r},-\tau) + G_b^{(--)}(\mathbf{r},\tau)\right) \quad (9.14b)$$

$$p_0 = -\frac{1}{2}\sum_{\mathbf{k}}\left[G_b^{(++)}(\mathbf{k},\tau=0^-) + G_b^{(--)}(\mathbf{k},\tau=0^+)\right] \quad (9.14c)$$

$$\frac{|\Delta|^2}{J_H} = \frac{1}{12}\sum_{\mathbf{k}} G_b^{-+}(\mathbf{k},\tau=0^-)\Delta_{\mathbf{k}} \quad (9.14d)$$

where the matrix form is expressed in the space of $\sigma = \pm$ (the χ-fermion propagator being diagonal in this basis), and we considered a cubic structure of spacing a for the lattice of localized spins.

The Dyson's equations have the following expression:

$$G_b^{-1}(\mathbf{k},i\nu_n) = \begin{bmatrix} i\nu_n+\lambda & -\Delta_{\mathbf{k}} \\ -\Delta_{\mathbf{k}}^* & -i\nu_n+\lambda \end{bmatrix} - \Sigma_b(\mathbf{k},i\nu_n) \quad (9.15a)$$

$$G_\chi^{-1}(\mathbf{k},i\omega_n) = J_K - \Sigma_\chi(\mathbf{k},i\omega_n) \quad (9.15b)$$

where $\Delta_{\mathbf{k}} = -4i\Delta\left[\sin(k_x a)+\sin(k_y a)+\sin(k_z a)\right]$

9.2.2 Uncontrolled local approximation

As the main additional difficulty of this new set of equations lies in the momentum dependence of the propagators, a first simple approximation one can make amounts to neglecting this very momentum dependence in the self-energies. Such an approximation is based on the assumption that the relevant physics leading to the self-energies is local, i.e. that there is very little interplay between the Kondo and Heisenberg mechanisms. This is an *uncontrolled* approximation as no small parameter allows us to neglect the non-local terms. However it might be sufficient to capture the competition between the Kondo screening and the development of magnetism.

Within this local approximation, our set of equations (9.14) and (9.15) dramat-

ically simplifies:

$$\begin{aligned}
\Sigma_b(\tau) &= -\gamma J_K^2 G_{c0}(\tau) G_\chi(\beta-\tau) && \text{(9.16a)}\\
\Sigma_\chi(\tau) &= -J_K^2 G_{c0}(\tau) G_b(\beta-\tau) && \text{(9.16b)}\\
G_b(i\nu_n) &= \sum_{\mathbf{k}} \frac{1}{i\nu_n + \lambda - \Sigma_b(i\nu_n) - \frac{|\Delta_{\mathbf{k}}|^2}{-i\nu_n+\lambda-\Sigma_b(-i\nu_n)}} && \text{(9.16c)}\\
G_\chi(i\omega_n) &= \frac{1}{J_K - \Sigma_\chi(i\omega_n)} && \text{(9.16d)}\\
p_0 &= -G_b(\tau=0^-) && \text{(9.16e)}\\
\frac{|\Delta|^2}{J_H} &= \frac{1}{12}\sum_{\mathbf{k}} T\sum_n e^{i\nu_n 0^+} \\
&\quad \times \frac{|\Delta_{\mathbf{k}}|^2}{(i\nu_n+\lambda-\Sigma_b(i\nu_n))\,(-i\nu_n+\lambda-\Sigma_b(-i\nu_n)) - |\Delta_{\mathbf{k}}|^2} && \text{(9.16f)}
\end{aligned}$$

The sum over momentum is evaluated by introducing $\eta_{\mathbf{k}}$ such as $\Delta_{\mathbf{k}} = 4i\Delta\eta_{\mathbf{k}}$. We then define a "density function" for $\eta_{\mathbf{k}}$:

$$\begin{aligned}
\rho(\eta) &= \sum_{\mathbf{k}} \delta(\eta - \eta_{\mathbf{k}}) \\
&= \frac{1}{2\pi}\int_{-\infty}^{+\infty} dx\; e^{i\eta x}\,[J_0(x)]^3 && \text{(9.17)}
\end{aligned}$$

which allows to replace summations over momentum by integrals over η with the function $\rho(\eta)$, which turns out to be the Fourier transform of the Bessel function of the first kind, elevated to the power 3.

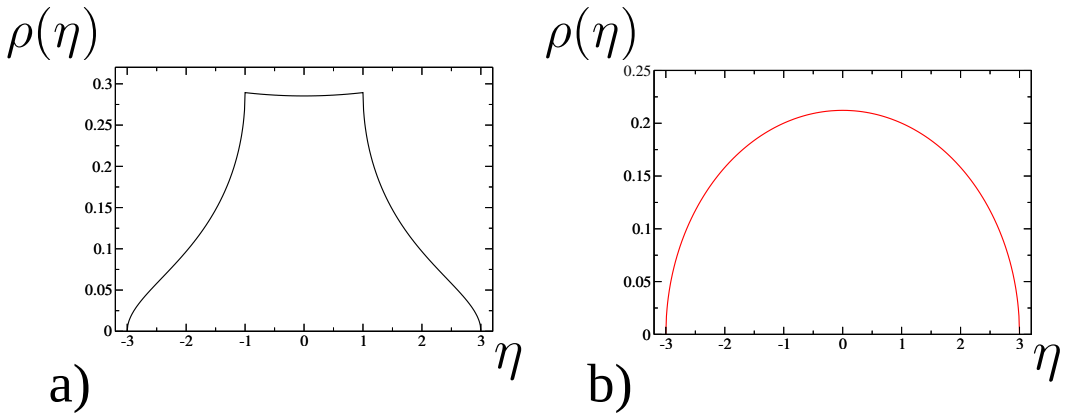

Figure 9.1: a) Plot of the function $\rho(\eta)$ obtained by numerical integration, b) Approximate form of the same function, used to compute analytically the summation over momentum. The edges are the same in both cases and go like $\sqrt{\epsilon}$ for $\eta = \pm(3-\epsilon)$.

We solved numerically the set of equations (9.16) as a function of temperature, for various values of the Heisenberg coupling. To do so, we replaced the function $\rho(\eta)$ by a slightly modified one (see Fig. 9.1) which allows to perform analytically the momentum summations.

We could map out the phase diagram presented in Fig. 9.2. Along with the line separating the $\Delta = 0$ region, from the region where pairs start condensing, we could also isolate a region of the phase diagram where a magnetic order develops. This transition line is determined by obtaining a solution of the set of self-consistent equations for increasingly larger values of Δ. At fixed temperature, we obtain a critical Δ_c above which the solution for the bosonic spectral function seems to develop some finite weight at zero energy, violating the causality rules. As these rules are built into the equations, this violation signals that the set of equations is no longer valid, which suggests that the Schwinger bosons undergo a condensation.

At low enough fixed temperature, we find a paramagnetic solution in a small region of the phase diagram below the transition line. This result suggests that there exists a region where both a magnetic and a non-magnetic states are present. As a consequence, we expect the transition towards the magnetic state to be of the first order at low temperature.

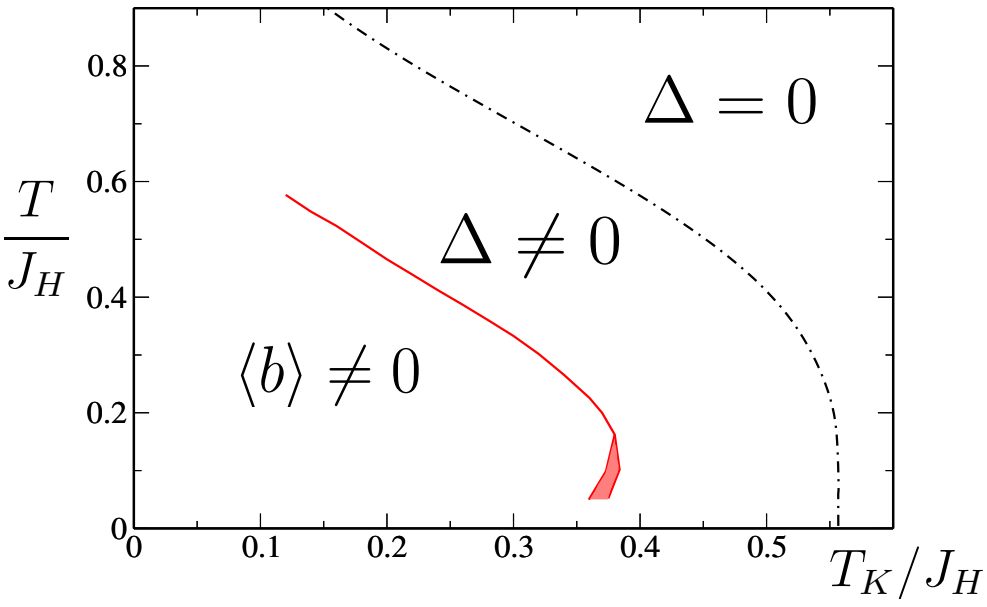

Figure 9.2: Phase diagram of the 3-dimensional lattice with the local approximation. The dashed line separating the region where pair correlations develop is unchanged compared to the two-impurity model studied earlier. The red line corresponds to a transition towards the magnetic region where Schwinger bosons condense. The splitting of this line at low temperature signals the presence of a first order transition into the magnetic state.

9.3 Conclusion

Very few results can be derived concerning these models without making new assumptions. The challenge at this stage is to find clever approximations that would capture the important physics of the problem, while partially allowing a numerical or an analytical treatment of the Kondo lattice model.

9.3.1 Looking for a gap

We saw in our study of the one and two impurity systems that the gap, and more importantly the closing of the gap, plays a significant role in the physics of the system. In the case of the Kondo lattice, we expect the gap to display a momentum dependence. The study of the gap in momentum space could be very insightful as for the relevant physics close to the quantum critical point. However, the study of the gap involves solving the full set of saddle-point equations.

A first step towards this route is to analyze the necessary conditions for a gap to be stabilized by the large-N equations. This might already be sufficient to reduce the relevant region of momentum space.

9.3.2 Kondo hedgehog

Another possible way of getting around the many difficulties related to the lattice is to consider a slightly different model. It can be argued that the competition between the Kondo effect and the magnetic ordering can be successfully mimicked by considering a cruder version of the Kondo lattice model, where we treat the electrons only to the extent that they provide spins which tend to be aligned antiparallel to the localized moments.

This was the reasoning behind Doniach's Kondo necklace model [92]. The large-N treatment developped here could be extended to a two or three dimensional version of Doniach's idea: a Kondo hedgehog model.

9.3.3 Dynamical mean-field theory

As a final example of the possible extensions of our approach to encompass the physics of the lattice, we mention the Dynamical Mean-Field Theory[3] (DMFT).

The use of our approach as an impurity solver or as a two-impurity solver might lead to interesting results when plugged back into a DMFT scheme. Such a treatment of the Kondo lattice model could provide enough of the non-local character of the system and lead to a better understanding of the important elements of the quantum critical regime.

[3] A detailed introduction to this technique goes way beyond the scope of this section. For a detailed review on DFMT, the reader is referred to [132]

PUBLICATION 3

Sum rules and Ward identities in the Kondo lattice

Phys. Rev. B, **72**, 094430 (2005)

PUBLICATION 4

Schwinger-boson approach to the fully screened Kondo model

Phys. Rev. Lett., **96**, 016601 (2006)

PUBLICATION 5

Conserving many-body approach to the infinite U Anderson model

cond-mat/0601015

Appendices

APPENDIX A

Generalized Luttinger-Ward scheme: free energy and entropy

Contents

In this appendix, we derive the free energy functional and the entropy for a single impurity using a Luttinger-Ward picture. The same kind of derivation extends to the Kondo lattice model and is presented in details in the Publication 3.

A.1 Free energy

The idea of the demonstration is to define a functional of the Green's functions and to prove that this definition matches the one of the free energy.

The full propagators of the theory are given by the following Dyson's equations:

$$G_b^{-1}(i\nu_n) = i\nu_n + \lambda - \Sigma_b(i\nu_n) \quad \text{(A.1)}$$

$$G_\chi^{-1}(i\omega_n) = J_K - \Sigma_\chi(i\omega_n) \quad \text{(A.2)}$$

$$G_c^{-1}(i\omega_n) = G_{c0}^{-1}(i\omega_n) - \Sigma_c(i\omega_n) \quad \text{(A.3)}$$

Following Luttinger and Ward, we will regard $G_{b,c,\chi}$ as a variational function, and $\Sigma_{b,c,\chi}$ as a derived quantity.

We now consider the effect of tuning up the strength of the Kondo interaction from zero to J_K, by replacing $J_K \to \alpha J_K$ where $\alpha \in [0,1]$, keeping the chemical potential of the conduction electrons and bosons fixed. Now the partition function is given by

$$Z = Tr[e^{-\beta H}] = \int \mathcal{D}[c,b,\chi] e^{-\int_0^\beta \mathcal{L} d\tau} \tag{A.4}$$

where $\mathcal{D}[c,b,\chi]$ is the measure of the path integral. If we vary α inside this expression, we obtain

$$\begin{aligned} \frac{dZ}{d\alpha} &= \int \mathcal{D}[c,b,\chi] \sum_{j\nu} \int_0^\beta d\tau \left(-J_K \chi^\dagger_{j\nu} \chi_{j\nu} \right) e^{-\int_0^\beta \mathcal{L} d\tau} \\ &= \beta Z \times (-J_K) \sum_{j\nu} \langle \chi^\dagger_{j\nu} \chi_{j\nu} \rangle \end{aligned} \tag{A.5}$$

so that if $F = -T \ln Z$ is the free energy, then

$$\frac{dF}{d\alpha} = J_K \sum_{j\nu} \langle \chi^\dagger_{j\nu} \chi_{j\nu} \rangle = K J_K T \sum_n G_\chi(i\omega_n), \tag{A.6}$$

We next consider the expression

$$\begin{aligned} \tilde{F} &= NT \sum_n \log(-G_b^{-1}(i\nu_n)) - KT \sum_n \log(-G_\chi^{-1}(i\omega_n)) \\ &\quad -NKT \sum_n \log(-G_c^{-1}(i\omega_n)) + NT \sum_n \Sigma_b(i\nu_n) G_b(i\nu_n) \\ &\quad -KT \sum_n \Sigma_\chi(i\omega_n) G_\chi(i\omega_n) - NKT \sum_n \Sigma_c(i\omega_n) G_c(i\omega_n) \\ &\quad +Np_0\lambda + \Phi_{LW}[G_b, G_\chi, G_c] \end{aligned} \tag{A.7}$$

where $\Phi_{LW}[G_b, G_\chi, G_c]$ is given by the sum of all closed, two-particle irreducible skeleton Feynman graphs for the Free energy.

As mentioned earlier, the Luttinger Ward functional $\Phi_{LW}[G_b, G_\chi, G_c]$ has the property that its variation with respect to $G_{b,c,\chi}$ generates the self energies,

$$\begin{aligned} \delta\Phi_{LW}[G_b, G_\chi, G_c] &= -N \int d\tau \Sigma_b(\tau) \delta G_b(\beta - \tau) - K \int d\tau \Sigma_\chi(\tau) \delta G_\chi(\beta - \tau) \\ &\quad -NK \int d\tau \Sigma_c(\tau) \delta G_c(\beta - \tau) \end{aligned} \tag{A.8}$$

The variation of the log term in $\tilde{F}$ with respect to $G_{b,c,\chi}$ is given by

$$\delta \left(T \sum_n \log(-G^{-1}(i\omega_n)) \right) = -T \sum_n G^{-1}(i\omega_n) \delta G(i\omega_n) \tag{A.9}$$

By using the relation $\Sigma[G] = G_0^{-1} - G^{-1}$, the variation in the remaining terms in $\tilde{F}$ are given by

$$\delta\left(T\sum_n \Sigma(i\omega_n)G(i\omega_n)\right) = T\sum_n G_0^{-1}(i\omega_n)\delta G(i\omega_n) \tag{A.10}$$

Combining these variations with the one of the Luttinger-Ward functional, one sees that $\tilde{F}$ identically vanishes

$$\frac{\delta\tilde{F}}{\delta G_b} = \frac{\delta\tilde{F}}{\delta G_c} = \frac{\delta\tilde{F}}{\delta G_\chi} = 0. \tag{A.11}$$

Now the Hubbard Stratonovich transformation that we have carried out on the original Hamiltonian to decouple the Kondo interaction assures that the only place that the coupling constant αJ_K enters, is in $[G_\chi^0]^{-1} = \alpha J_K$. This means that in the r.h.s of Eq. (A.7) α enters explicitly only through $\Sigma_\chi = \alpha J_K - G_\chi^{-1}$. Then,

$$\begin{aligned}\frac{d\tilde{F}}{d\alpha} &= \underbrace{\frac{\delta\tilde{F}}{\delta G_{b,c,\chi}}}_{=0}\frac{\partial G_{b,c,\chi}}{\partial\alpha} + \frac{\partial\tilde{F}}{\partial\alpha} \\ &= TJ_K\sum_n G_\chi(i\omega_n)\end{aligned} \tag{A.12}$$

But by comparison with (A.6), we see that $\frac{d\tilde{F}}{d\alpha} = \frac{dF}{d\alpha}$ and since, $F(\alpha=0) = \tilde{F}(\alpha=0)$ in the non-interacting case, the two quantities must be equal for all α, i.e

$$\begin{aligned}F &= NT\sum_n \log(-G_b^{-1}(i\nu_n)) - KT\sum_n \log(-G_\chi^{-1}(i\omega_n)) \\ &\quad -NKT\sum_n \log(-G_c^{-1}(i\omega_n)) + NT\sum_n \Sigma_b(i\nu_n)G_b(i\nu_n) \\ &\quad -KT\sum_n \Sigma_\chi(i\omega_n)G_\chi(i\omega_n) - NKT\sum_n \Sigma_c(i\omega_n)G_c(i\omega_n) \\ &\quad +Np_0\lambda + \Phi_{LW}[G_b, G_\chi, G_c]\end{aligned} \tag{A.13}$$

There are various points to make about this derivation:

- The derivation is very general. Its correctness only depends on the stationarity of $\tilde{F}[G]$ with respect to variations in G and the equivalence between $dF/d\alpha$ and $d\tilde{F}/d\alpha$.

- The above Free energy functional can be used as a basis for developing conserving approximations that generalize the Kadanoff Baym approach to a constrained system[108].

A.2 Entropy

We know from the derivation of the self-energy equations from the Luttinger-Ward functional that $\Sigma_c \sim O\left(\frac{1}{N}\right)$. It then becomes possible to expand the electronic Dyson's equation in powers of $1/N$, which in turn leads to the following simplification in the free energy functional:

$$\begin{aligned} -NKT\sum_n \log(-G_c^{-1}(i\omega_n)) &= -NKT\sum_n \log(-G_{c0}^{-1}(i\omega_n)) \\ &\quad +NKT\sum_n \Sigma_c(i\omega_n)G_{c0}(i\omega_n) \\ -NKT\sum_n \Sigma_c(i\omega_n)G_c(i\omega_n) &= -NKT\sum_n \Sigma_c(i\omega_n)G_{c0}(i\omega_n) \end{aligned}$$

Combining these two terms, we are left with a term of order N^2 that corresponds to the free energy of the free electronic gas. Subtracting this bulk free energy from the one we are considering, we are left with the impurity contribution to the free energy, which one can write in terms of retarded Green's functions as:

$$\begin{aligned} \frac{F_{\text{imp}}}{N} &= \int \frac{d\omega}{\pi}\, n(\omega)\text{Im}\left(\log(-G_b^{-1}(\omega)) + G_b(\omega)\Sigma_b(\omega)\right) \\ &\quad +\gamma\int \frac{d\omega}{\pi}\, f(\omega)\text{Im}\left(\log(-G_\chi^{-1}(\omega)) + G_\chi(\omega)\Sigma_\chi(\omega)\right) \\ &\quad +p_0\lambda + \frac{1}{N}\Phi_{LW}[G_b, G_\chi, G_{c0}] \end{aligned} \tag{A.14}$$

Using the stationarity of the free energy with respect to the Green's functions and the chemical potential, one can directly read from (A.14) the expression for the impurity contribution to the entropy:

$$\begin{aligned} \frac{S_{\text{imp}}}{N} &= -\int \frac{d\omega}{\pi}\, \frac{\partial n(\omega)}{\partial T}\text{Im}\left(\log(-G_b^{-1}(\omega)) + G_b(\omega)\Sigma_b(\omega)\right) \\ &\quad -\gamma\int \frac{d\omega}{\pi}\, \frac{\partial f(\omega)}{\partial T}\text{Im}\left(\log(-G_\chi^{-1}(\omega)) + G_\chi(\omega)\Sigma_\chi(\omega)\right) \\ &\quad -\frac{1}{N}\frac{\partial \Phi_{LW}}{\partial T} \end{aligned} \tag{A.15}$$

One now has to work a little on the expression of the Luttinger-Ward functional in order to extract a closed form expression for its temperature derivative. First of all, we saw in chapter 6 that only the leading order diagram of Φ_{LW} survives once we take the large-N limit, so that the Luttinger-Ward functional writes:

$$\Phi_{LW}[G_b, G_\chi, G_c] = KJ^2\int d\tau G_c(\tau)G_b(\beta-\tau)G_\chi(\beta-\tau) \tag{A.16}$$

As a starting point, it is useful to convert the imaginary time original expression of the Luttinger-Ward functional into real frequency. In order to do so, we make the following substitution:

$$\begin{aligned} G_{\text{bosonic}}(\tau) &= \int d\omega\ e^{-\omega\tau} n(-\omega)\rho_{\text{bosonic}}(\omega) \\ G_{\text{fermionic}}(\tau) &= -\int d\omega\ e^{-\omega\tau} f(-\omega)\rho_{\text{fermionic}}(\omega) \end{aligned} \tag{A.17}$$

where $0 \leq \tau \leq \beta$.

It follows, after performing the remaining integral over imaginary time:

$$\begin{aligned} \frac{\Phi_{LW}[G_b, G_\chi, G_c]}{N} &= -\gamma J^2 \fint d\omega_c d\omega_\chi d\omega_b \frac{\rho_b(\omega_b)\rho_c(\omega_c)\rho_\chi(\omega_\chi)}{\omega_\chi + \omega_b - \omega_c} \\ &\quad \times (f(\omega_c)n(-\omega_b)f(-\omega_\chi) + f(-\omega_c)n(\omega_b)f(\omega_\chi)) \\ &= -\gamma J^2 \fint d\omega_c d\omega_\chi d\omega_b \frac{\rho_b(\omega_b)\rho_c(\omega_c)\rho_\chi(\omega_\chi)}{\omega_\chi + \omega_b - \omega_c} \\ &\quad \times (f(\omega_\chi)n(\omega_b) - f(\omega_c)n(\omega_b) - f(\omega_c)(1 - f(\omega_\chi))) \end{aligned} \tag{A.18}$$

Taking the derivative with respect to temperature, and using the argument of stationarity of the total free energy with respect to the Green's functions, one can write:

$$\begin{aligned} \frac{1}{N}\frac{\partial \Phi_{LW}}{\partial T} &= \gamma J^2 \fint d\omega_c d\omega_\chi d\omega_b \frac{\rho_b(\omega_b)\rho_c(\omega_c)\rho_\chi(\omega_\chi)}{\omega_\chi + \omega_b - \omega_c} \\ &\quad \times \left[\left(f(\omega_\chi)\frac{\partial n(\omega_b)}{\partial T} - f(\omega_c)\frac{\partial n(\omega_b)}{\partial T} \right) \right. \\ &\quad + \left(n(\omega_b)\frac{\partial f(\omega_\chi)}{\partial T} + f(\omega_c)\frac{\partial f(\omega_\chi)}{\partial T} \right) \\ &\quad \left. + \left(-n(\omega_b)\frac{\partial f(\omega_c)}{\partial T} - (1 - f(\omega_\chi))\frac{\partial f(\omega_c)}{\partial T} \right) \right] \end{aligned} \tag{A.19}$$

One can recognize in this last expression a combination of Fermi and Bose functions reminiscent of the saddle-point equations for the self-energies. It turns out that using these saddle-point equations, eq. (A.19) reduces to:

$$\begin{aligned} \frac{1}{N}\frac{\partial \Phi_{LW}}{\partial T} &= -\int \frac{d\omega}{\pi}\frac{\partial n(\omega)}{\partial T} G''_b(\omega)\Sigma'_b(\omega) - \gamma \int \frac{d\omega}{\pi}\frac{\partial f(\omega)}{\partial T} G''_\chi(\omega)\Sigma'_\chi(\omega) \\ &\quad -\gamma \int \frac{d\omega}{\pi}\frac{\partial f(\omega)}{\partial T} G''_{c0}(\omega)\tilde{\Sigma}'_c(\omega) \end{aligned} \tag{A.20}$$

where $\tilde{\Sigma}_c = N\Sigma_c \sim O(1)$.

Plugging back the expression for $\frac{\partial \Phi_{LW}}{\partial T}$ into the impurity entropy, one sees that it cancels some of terms from the first part of the expression. The final entropy formula in the large-N limit then reads:

$$\begin{aligned}\frac{S_{\rm imp}}{N} &= -\int \frac{d\omega}{\pi}\left[\frac{\partial n(\omega)}{\partial T}\left(\mathrm{Im}\log\left(-G_b^{-1}(\omega)\right)+G_b'(\omega)\Sigma_b''(\omega)\right)\right. \\ &\left.+\gamma\frac{\partial f(\omega)}{\partial T}\left(\mathrm{Im}\log\left(-G_\chi^{-1}(\omega)\right)+G_\chi'(\omega)\Sigma_\chi''(\omega)-G_{c0}''(\omega)\tilde{\Sigma}_c'(\omega)\right)\right] \quad \text{(A.21)}\end{aligned}$$

APPENDIX B

Local vs. impurity susceptibility

Contents

In this appendix, we compare the local to the impurity susceptibility. It is often much easier to compute the local susceptibility rather than the impurity susceptibility. However, most of the known analytical results (in particular for the exactly screened impurity) relates to the impurity susceptibility. We prove in this appendix that they are indeed related and can be considered roughly equal at zero-temperature, in the large bandwidth limit.

B.1 Local susceptibility

By definition, the local susceptibility is the response of the system to an applied external magnetic field that couples to the impurity spin *o*nly, hence the name

"local". In the case of a Schwinger boson representation of the impurity spin, this local susceptibility can be expressed as:

$$\begin{aligned}\chi_{\rm loc} &= \frac{1}{N^2}\int_0^\beta d\tau \sum_{\alpha\beta}\langle S_{\alpha\beta}(\tau)S_{\beta\alpha}(0)\rangle \\ &= \int_0^\beta d\tau G_b(\tau)G_b(\beta-\tau) \\ &= \int \frac{d\omega}{\pi}\, n(\omega){\rm Im}\left[G_b(\omega+i\delta)^2\right] \end{aligned} \tag{B.1}$$

In terms of Feynman diagrams, one can represent the local susceptibility as a particle-hole bubble of bosonic lines, as is illustrated on fig. B.1.

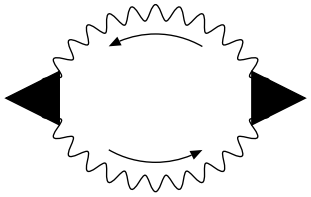

Figure B.1: Local spin susceptibility

B.2 Impurity susceptibility

The impurity susceptibility is defined as the response of the whole system to an external magnetic field, after one subtracts the contribution of the bulk conduction electrons. In this case, the magnetic field is coupled to both the impurity spin and the spin of the conduction electrons:

$$\chi_{\rm imp} = \chi_{\rm Total} - \chi_{\rm bulk} \tag{B.2}$$

In general, this impurity susceptibility is given by an infinite sum of Feynman diagrams. However, in the large-N limit, this sum becomes finite, and one only has to take account a few diagrams on top of the local susceptibility, as represented in fig. B.2. It is important to notice that all four[1] diagrams contributing to the impurity susceptibility have the same scaling in N, because every time a pair of vertices is included (factor of $(1/\sqrt{N})^2 = 1/N$) there is also an internal sum over the channel index (bringing a factor of γN).

[1]One shouldn't forget that $\chi_{\rm loc}$ is the first diagram contributing to the impurity susceptibility

B.2.1 χ_2

The contribution from this diagram writes[2]:

$$\begin{aligned}\chi_2 &= -2\gamma J_K^2 T^2 \sum_{n,m}\left(\sum_{\mathbf{k}} \frac{1}{(i\omega_n - \epsilon_{\mathbf{k}})^2}\right) G_\chi(i\omega_n - i\nu_m) G_b(i\nu_m)^2 \\ &= 2T\sum_m V_b(i\nu_m) G_b(i\nu_m)^2 \\ &= 2\int \frac{d\omega}{\pi}\, n(\omega) \mathrm{Im}\left[V_b(\omega+i\delta) G_b(\omega+i\delta)^2\right] \end{aligned} \tag{B.3}$$

where we defined the "renormalized vertex" V_b as:

$$\begin{aligned} V_b(i\nu_m) &= -\gamma J_K^2 T \sum_n G_{c2}(i\omega_n) G_\chi(i\omega_n - i\nu_m) \\ &= -\gamma J_K^2 \int d\omega_1 d\omega_2 \rho_{c2}(\omega_1)\rho_\chi(\omega_2) \frac{f(\omega_1)-f(\omega_2)}{\omega_1-\omega_2-i\nu_m} \end{aligned} \tag{B.4}$$

and $G_{c2}(i\omega_n) = \sum_{\mathbf{k}} \frac{1}{(i\omega_n - \epsilon_{\mathbf{k}})^2} = -\frac{\partial G_c}{\partial \omega}$.

Note that V_b has no dimension.

B.2.2 χ_3

Now that we have defined V_b, the contribution from χ_3 can trivially be rewritten as:

$$\begin{aligned}\chi_3 &= T\sum_m V_b(i\nu_m)^2 G_b(i\nu_m)^2 \\ &= \int \frac{d\omega}{\pi}\, n(\omega) \mathrm{Im}\left[V_b(\omega+i\delta)^2 G_b(\omega+i\delta)^2\right] \end{aligned} \tag{B.5}$$

[2]We have dropped here the overall factor of N^2, since we want the impurity susceptibility to be of order $O(1)$.

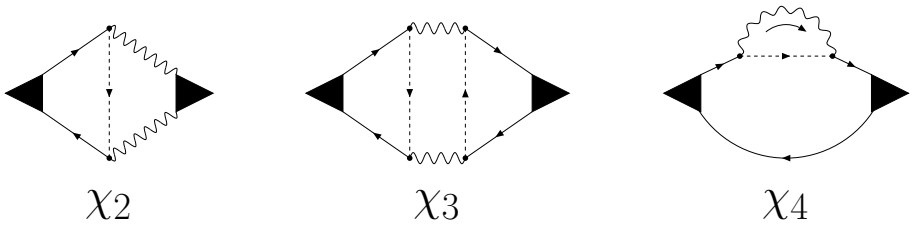

Figure B.2: Extra diagrams to add to the local susceptibility to compute the impurity susceptibility

B.2.3 χ_4

From the diagrammatic representation of χ_4, one recognizes the fermionic self-energy Σ_c defined in chapter 6. χ_4 then writes:

$$\begin{aligned}\chi_4 &= -2\gamma NT\sum_n G_{c3}(i\omega_n)\Sigma_c(i\omega_n) \\ &= -2\gamma N\int\frac{d\omega}{\pi}\, f(\omega)\mathrm{Im}\left[G_{c3}(\omega+i\delta)\Sigma_c(\omega+i\delta)\right] \end{aligned} \tag{B.6}$$

where $G_{c3}(i\omega_n) = \sum_{\mathbf{k}} \dfrac{1}{(i\omega_n-\epsilon_{\mathbf{k}})^3} = \frac{1}{2}\frac{\partial^2 G_c}{\partial\omega^2}$.

Keep in mind that the conduction electron self-energy is of order $O(1/N)$ so that the overall external factor of N makes this contribution to the impurity susceptibility of order $O(1)$.

B.2.4 χ_{imp}

Putting everything together, one notices that the first three diagrams can be grouped into a simple form, leading to the final result:

$$\begin{aligned}\chi_{\mathrm{imp}} &= \int\frac{d\omega}{\pi}n(\omega)\left[G_b(\omega+i\delta)^2\left(1+V_b(\omega+i\delta)\right)^2\right] \\ &\quad +2\gamma N\int\frac{d\omega}{\pi}\, f(\omega)\mathrm{Im}\left[G_{c3}(\omega+i\delta)\Sigma_c(\omega+i\delta)\right] \end{aligned} \tag{B.7}$$

B.3 Zero-temperature limit

In the case of a flat band of conduction electron, one can readily compute G_{c2} and G_{c3}:

$$\begin{aligned} G_{c0} &= -i\pi\rho_0\Theta(D^2-\omega^2) \\ G_{c2} &= i\pi\rho_0\left(\delta(\omega+D)-\delta(\omega-D)\right) \\ G_{c3} &= \frac{-i\pi}{2}\rho_0\left(\delta'(\omega+D)-\delta'(\omega-D)\right) \end{aligned} \tag{B.8}$$

where we considered the large bandwidth limit, for which one can dropped the real part of G_{c0} since it is $O(\omega/D)$ smaller than the imaginary part.

From these expressions, one can compute the "renormalized vertex" V_b in the zero-temperature limit:

$$V_b(\omega+i\delta) = \gamma\rho_0 J_K^2\left[G'_\chi(-D)-G'_\chi(D)\right] \tag{B.9}$$

In the large bandwidth limit, the zero-temperature self-energy of the $\chi-$fermion reads:

$$\begin{aligned} \Sigma_\chi(D) &= -i\pi\rho_0 J_K^2 p_0 \\ \Sigma_\chi(-D) &= -i\pi\rho_0 J_K^2 (1+p_0) \end{aligned} \tag{B.10}$$

Combining all these results, we can rewrite the zero-temperature impurity susceptibility as:

$$\chi_{\rm imp} = \left(1 + \frac{\pi^2\gamma(1+2p_0)(\rho_o J)^3}{[1+(\pi\rho_0 J p_0)^2]\,[1+(\pi\rho_0 J(1+p_0))^2]}\right)^2 \chi_{\rm loc} + \gamma N \rho_0 \left.\frac{d\Sigma_c'}{d\omega}\right|_{\omega=-D} \tag{B.11}$$

As a conclusion, one can see from this last expression that at zero temperature, in the large bandwidth limit, it is possible to identify the local and the impurity susceptibility:

$$D \gg T_K \Longrightarrow \chi_{\rm loc} \underset{T\to 0}{\sim} \chi_{\rm imp} \tag{B.12}$$

APPENDIX C

Fermi liquid identities

Contents

In this appendix, we derive some of the important interrelationships between physical variables of the Fermi liquid, namely the Yamada-Yosida-Yoshimori relationship between spin, charge, flavor susceptibilities and specific heat [133, 134, 135].

Historically, this relationship was obtained from the analysis of a full perturbation theory. We present here a derivation similar in spirit to the one of Nozières and Blandin [104].

C.1 Scattering phase shift

The two basic electron-electron vertices have the following structure:

$$\Gamma_1 = c^\dagger_{\alpha\mu} c^\dagger_{\beta\mu'} c_{\beta\mu'} c_{\alpha\mu} \tag{C.1}$$

$$\Gamma_2 = c^\dagger_{\beta\mu} c^\dagger_{\delta\mu'} c_{\gamma\mu'} c_{\alpha\mu} \boldsymbol{\sigma}_{\alpha\beta} \cdot \boldsymbol{\sigma}_{\gamma\delta} \tag{C.2}$$

where Γ_1 and Γ_2 are recast in terms of Feynman diagrams in fig. C.1, and $\sigma_{\alpha\beta}$ is a generator of $SU(N)$ verifying:

$$\boldsymbol{\sigma}_{\alpha\beta} \cdot \boldsymbol{\sigma}_{\gamma\delta} = 2\delta_{\alpha\delta}\delta_{\beta\gamma} - \frac{2}{N}\delta_{\alpha\beta}\delta_{\gamma\delta} \tag{C.3}$$

The most general combination invariant under both spin and channel rotation is then:

$$\sum_{\alpha\beta\mu\mu'} \left[A\ c^\dagger_{\alpha\mu} c^\dagger_{\beta\mu'} c_{\beta\mu'} c_{\alpha\mu} + B\ c^\dagger_{\beta\mu} c^\dagger_{\alpha\mu'} c_{\beta\mu'} c_{\alpha\mu} \right] \tag{C.4}$$

where we kept only the dominant terms in the large-N limit.

Considering a small departure from the Fermi liquid fixed point, these interaction terms are expected to be small, and can be treated within first order perturbation theory leading to the following effective Hamiltonian:

$$H_{\text{eff}} = 2 \sum_{\alpha\beta\mu\mu'} \left[A\left(1 - \delta_{\alpha\beta}\delta_{\mu\mu'}\right) + B\left(\delta_{\alpha\beta} - \delta_{\mu\mu'}\right) \right] \langle n_{\beta\mu'} \rangle n_{\alpha\mu} \tag{C.5}$$

where $n_{\alpha\mu} = c^\dagger_{\alpha\mu} c_{\alpha\mu}$ is the number operator, and $\langle n_{\alpha\mu} \rangle$ its expectation value.

One can then determine the scattering phase shift of an incoming conduction electron with quantum numbers α and μ as a function of the energy ϵ and the electron distribution $\delta\langle n_{\alpha\mu} \rangle$ measured from the ground-state. Using the above effective Hamiltonian, it is possible to reduce the general expression of the phase shift as:

$$\begin{aligned} \delta_{\alpha\mu} &= \delta_0 + \epsilon\delta' + \sum_{\beta\mu'} \phi_{\alpha\beta}\psi_{\mu\mu'}\delta\langle n_{\alpha\mu} \rangle \\ &= \delta_0 + \epsilon\delta' + \phi_1 \sum_{\beta\mu'} \left(\delta_{\mu\mu'} - \delta_{\alpha\beta}\right) \delta\langle n_{\beta\mu'} \rangle + \phi_2 \sum_{\beta\mu'} \left(1 - \delta_{\alpha\beta}\delta_{\mu\mu'}\right) \delta\langle n_{\beta\mu'} \rangle \end{aligned} \tag{C.6}$$

Following [124], the response of this phase shift to various field variations can be related to the specific heat and the susceptibilities.

C.2 Specific heat

Upon increasing the temperature, the electron energy changes like:

$$\tilde{\epsilon}_{\alpha\mu} = \epsilon - \frac{\delta_{\alpha\mu}(\tilde{\epsilon})}{\pi\rho_0} \tag{C.7}$$

where the phase shift is only given by the first two terms, the change of population $\delta\langle n \rangle$ due to an increase in temperature being zero.

This leads to the following change in the electronic density of states:

$$\delta\rho = \rho_0 \left[\frac{d\epsilon}{d\tilde{\epsilon}} - 1 \right] = \frac{\delta'}{\pi} \tag{C.8}$$

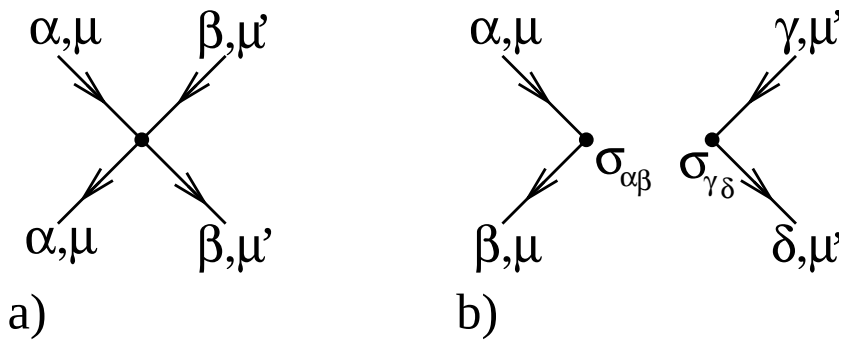

Figure C.1: Diagrammatic representation of the two basic electron-electron vertices: a) is the vertex already existing in the absence of the impurity (denoted as Γ_1), and b) is the vertex related to the scattering off the impurity (defined as Γ_2).

and hence a correction to the specific heat:

$$\frac{\delta C_v}{C_v} = \frac{\delta\rho}{\rho_0} = \frac{\delta'}{\pi\rho_0} \tag{C.9}$$

C.3 Susceptibilities

C.3.1 Charge susceptibility

Upon a small change in the chemical potential of the conduction electron Λ, one probes the change of the charge susceptibility, which can be expressed in terms of the scattering phase shift as:

$$\frac{\delta\chi_c}{\chi_c} = \frac{1}{\pi\rho_0}\frac{\Delta\delta_{\alpha\mu}}{\Delta\Lambda} \tag{C.10}$$

$$= \frac{1}{\pi\rho_0}\left[\delta' + \rho_0\phi_1(N-K) + \rho_0\phi_2(NK-1)\right] \tag{C.11}$$

where we have used that $\epsilon \sim \Delta\Lambda$ and $\delta\langle n\rangle \sim \rho_0\Delta\Lambda$.

C.3.2 Spin susceptibility

In order to extract the spin susceptibility, one has to apply an external magnetic field that couples to the system: the change in the spin susceptibility is then related to the response of the phase shift to this magnetic field in the same fashion as (C.10).

A variation of this magnetic field leads to a change in the electron population $\langle n_{\alpha\mu}\rangle \sim \rho_0\ \mathrm{Sgn}(\alpha - (N+1)/2)$, leading to the following result:

$$\frac{\delta\chi_s}{\chi_s} = \frac{1}{\pi\rho_0}\left[\delta' - \rho_0\phi_1 K - \rho_0\phi_2\right] \tag{C.12}$$

C.3.3 Channel susceptibility

Consider now an equivalent of the magnetic field that couples to the channel flavor. The same analysis as before leads to the channel susceptibility:

$$\frac{\delta\chi_f}{\chi_f} = \frac{1}{\pi\rho_0}\left[\delta' + \rho_0\phi_1 N - \rho_0\phi_2\right] \tag{C.13}$$

where we used that the change of electron population due to a variation of the channel field is $\langle n_{\alpha\mu}\rangle \sim \rho_0 \,\mathrm{Sgn}(\mu - (K+1)/2)$.

C.4 Results

Combining (C.9), (C.11), (C.12) and (C.13), one can get rid of the variables δ', ϕ_1 and ϕ_2 and obtain an expression relating the specific heat and the various susceptibilities:

$$NK(N+K)\frac{\delta C_v}{C_v} = K(N^2-1)\frac{\delta\chi_s}{\chi_s} + N(K^2-1)\frac{\delta\chi_f}{\chi_f} + (N+K)\frac{\delta\chi_c}{\chi_c} \tag{C.14}$$

This relationship extends the Yamada-Yosida-Yoshimori relationship to the generalized $SU(N) \times SU(K)$ Kondo model.

In the case of a Kondo impurity, since the interaction conserves the number of conduction electron and does not affect the channel index, one expects that $\delta\chi_c = 0$ and $\delta\chi_f = 0$, so that (C.14) directly gives the Wilson ratio:

$$W = \frac{\delta\chi_s/\chi_s}{\delta C_v/C_v} = \frac{N(N+K)}{N^2-1} \tag{C.15}$$

which recovers the result obtained from Bethe ansatz [114].

Finally, in the large-N limit, this expression of the Wilson ratio reduces to:

$$W = 1 + \gamma \tag{C.16}$$

APPENDIX D

QCP in the two-impurity model: low-energy analysis

Contents

In this appendix, we derive the low-energy behavior of the Schwinger boson's and $\chi-$fermion's propagators, at the quantum critical point, in the case of a two-impurity Kondo-Heisenberg model.

D.1 Ansatz

As one approaches the quantum critical point from either side, the numerical solution suggests that both inverse propagators vanish at zero energy. Such a behavior

suggests that the Green's functions diverge like power-laws at zero frequency. Our starting point is then given by the following ansatz for the propagators:

$$G_b(\omega) \sim \frac{A_+\Theta(\omega) + A_-\Theta(-\omega)}{|\omega|^\alpha} \tag{D.1}$$

$$G_\chi(\omega) \sim \frac{B_+\Theta(\omega) + B_-\Theta(-\omega)}{|\omega|^\beta} \tag{D.2}$$

where $A_\pm$ and $B_\pm$ are complex numbers and we separate the positive from the negative energy sectors in case of a spectral asymmetry.

Since we are interested in what happens at the quantum critical point, we consider the zero-temperature limit of the saddle-point equations defining the self-energies:

$$\begin{cases} \Sigma_b(\omega) = -\gamma J^2\rho_0 \left(\displaystyle\int_{-\omega}^{-D} d\Omega\ G'_\chi(\Omega) + i \int_0^{-\omega} d\Omega\ G''_\chi(\Omega) \right) \\ \Sigma_\chi(\omega) = J^2\rho_0 \left(\displaystyle\int_{-\omega}^{-D} d\Omega\ G'_b(\Omega) + i \int_0^{-\omega} d\Omega\ G''_b(\Omega) \right) \end{cases} \tag{D.3}$$

where $\rho_0 = \frac{1}{2D}$.

Inserting the ansatz into this set of equations and using Dyson's equations, we are able to extract a new set of self-consistent equations for the parameters of our ansatz, which can then be solved analytically.

D.2 Derivation

D.2.1 Bosonic parameters

Plugging (D.2) into (D.3a), one has:

$$\begin{cases} \Sigma_b(\omega > 0) = \dfrac{\gamma J^2\rho_0 D^{1-\beta}}{1-\beta}\mathrm{Re}B_- - \dfrac{\gamma J^2\rho_0 B_-^*}{1-\beta}\omega^{1-\beta} \\ \Sigma_b(\omega < 0) = \dfrac{\gamma J^2\rho_0 D^{1-\beta}}{1-\beta}\mathrm{Re}B_- + \dfrac{\gamma J^2\rho_0 B_+^*}{1-\beta}|\omega|^{1-\beta} \end{cases} \tag{D.4}$$

In the two-impurity model, the Dyson's equation for the bosonic propagator reads:

$$G_b^{-1} = \omega + \lambda - \Sigma_b(\omega) - \frac{|\Delta|^2}{-\omega + \lambda - \Sigma_b(-\omega)^*} \tag{D.5}$$

Replacing Σ_b in this last expression by eq. (D.4), and expanding in the denomi-

nator for small frequency, one is left with:

$$G_b^{-1} = \frac{\left(\lambda - \frac{\gamma J^2 \rho_0 D^{1-\beta} \mathrm{Re} B_-}{1-\beta}\right)^2 - |\Delta|^2}{\lambda - \frac{\gamma J^2 \rho_0 D^{1-\beta} \mathrm{Re} B_-}{1-\beta}} - \frac{\gamma J^2 \rho_0 |\omega|^{1-\beta}}{1-\beta}\left(B_+^* \Theta(-\omega) - B_-^* \Theta(\omega)\right)$$
$$- \frac{|\Delta|^2}{\left(\lambda - \frac{\gamma J^2 \rho_0 D^{1-\beta} \mathrm{Re} B_-}{1-\beta}\right)^2} \frac{\gamma J^2 \rho_0 |\omega|^{1-\beta}}{1-\beta} \left(B_+ \Theta(\omega) - B_- \Theta(-\omega)\right) \tag{D.6}$$

Imposing self-consistency with our original ansatz, one can identify:

$$\begin{cases} \left(\lambda - \dfrac{\gamma J^2 \rho_0 D^{1-\beta} \mathrm{Re} B_-}{1-\beta}\right)^2 = |\Delta|^2 \\ \dfrac{1}{A_+} = \gamma J^2 \rho_0 \dfrac{B_-^* - B_+}{1-\beta} \\ \dfrac{1}{A_-} = \gamma J^2 \rho_0 \dfrac{B_- - B_+^*}{1-\beta} \\ \alpha = 1 - \beta \end{cases} \tag{D.7}$$

D.2.2 Fermionic parameters

One can now do the same procedure for the χ fermions, first inserting (D.1) into (D.3b):

$$\begin{cases} \Sigma_\chi(\omega > 0) = -\dfrac{J^2 \rho_0 D^{1-\alpha}}{1-\alpha} \mathrm{Re} A_- + \dfrac{J^2 \rho_0 A_-^*}{1-\alpha} \omega^{1-\alpha} \\ \Sigma_\chi(\omega < 0) = -\dfrac{J^2 \rho_0 D^{1-\alpha}}{1-\alpha} \mathrm{Re} A_- - \dfrac{J^2 \rho_0 A_+^*}{1-\alpha} |\omega|^{1-\alpha} \end{cases} \tag{D.8}$$

Replacing this last expression of Σ_χ into $G_\chi^{-1} = J - \Sigma_\chi$, one has:

$$G_\chi^{-1}(\omega) = J + \frac{\rho_0 J^2 D^{1-\alpha} \mathrm{Re} A_-}{1-\alpha} - \frac{\rho_0 J^2 |\omega|^{1-\alpha}}{1-\alpha}\left(A_-^* \Theta(\omega) - A_+^* \Theta(-\omega)\right) \tag{D.9}$$

Again, the self-consistency with the original ansatz imposes:

$$\begin{cases} J + \dfrac{\rho_0 J^2 D^{1-\alpha} \mathrm{Re} A_-}{1-\alpha} = 0 \\ \dfrac{1}{B_+} = -\dfrac{J^2 \rho_0 A_-^*}{1-\alpha} \\ \dfrac{1}{B_-} = \dfrac{J^2 \rho_0 A_+^*}{1-\alpha} \\ \beta = 1 - \alpha \end{cases} \tag{D.10}$$

D.2.3 Analysis of the self-consistent equations

From a first look at the set of equations (D.7) and (D.10), one can already see that $A_+ = A_-^*$ and $B_+ = -B_-^*$, so that we only focus on A_+ and B_+ in what follows. Our set of equations then reduces to:

$$\begin{cases} J + \dfrac{\rho_0 J^2 D^{1-\alpha} \mathrm{Re} A_+}{1-\alpha} = 0 \\ \left(\lambda + \dfrac{\gamma J^2 \rho_0 D^{1-\beta} \mathrm{Re} B_+}{1-\beta}\right)^2 = |\Delta|^2 \\ \dfrac{1}{A_+} = -\dfrac{2\gamma J^2 \rho_0 B_+}{1-\beta} \\ \dfrac{1}{B_+} = -\dfrac{J^2 \rho_0 A_+}{1-\alpha} \\ \alpha + \beta = 1 \end{cases} \tag{D.11}$$

From the last three equations, one can extract that:

$$\alpha = \frac{2\gamma}{1+2\gamma} \tag{D.12}$$

$$\beta = \frac{1}{1+2\gamma} \tag{D.13}$$

It is useful at this stage to rewrite $A_+ = Ae^{i\theta}$ and $B_+ = Be^{i\phi}$. Since the product A_+B_+ is a real negative number, one has $\theta + \phi = \pi$ (2π) and $AB\rho_0 J^2(1+2\gamma) = 1$. Everything can then be re-expressed as a function of A and θ as:

$$G_b(\omega) \sim \frac{Ae^{i\theta \mathrm{Sign}(\omega)}}{|\omega|^{\frac{2\gamma}{1+2\gamma}}} \tag{D.14}$$

$$G_\chi(\omega) \sim -\frac{1}{A\rho_0 J^2(1+2\gamma)} \frac{e^{-i\theta \mathrm{Sign}(\omega)} \mathrm{Sign}(\omega)}{|\omega|^{\frac{1}{1+2\gamma}}} \tag{D.15}$$

D.3 General remarks

D.3.1 Causality

As a first check, one has to make sure that the final expressions we just obtained satisfy the causality of the retarded Green's functions. Looking at the imaginary part of the bosonic propagator, one can immediately see that $\mathrm{Im}G_b(\omega) \sim \mathrm{Sign}(\omega)\sin\theta$, which has the right properties provided that $\sin\theta$ is negative.

The same inspection on G_χ leads to $\mathrm{Im}G_\chi(\omega) \sim \sin\theta$, so that again the causality rules are respected provided that $\sin\theta$ is negative.

D.3.2 Spectral asymmetry

It is interesting to notice that in this case there is no spectral asymmetry like the one observed for the overscreened single impurity. Indeed, in the case of the two-impurity critical region, the prefactor is either equal or opposite depending whether one is considering the real or the imaginary part of the Green's functions. This feature seems to be a consequence of the particular Dyson's equation for the bosonic field which mixes in this case the positive and negative frequency regions (both $\Sigma_b(\omega)$ and $\Sigma_b(-\omega)$ enter the Dyson's equation giving $G_b(\omega)$)

Bibliography

[1] T. Andrews *Phil. trans. Roy. Soc.*, vol. 159, p. 575, 1869.

[2] L. Landau and E. Lifshitz, *Statistical Physics Part 1.* Pergamon, 3rd Ed., 1994.

[3] J. Hertz *Phys. Rev. B*, vol. 14, p. 1165, 1976.

[4] P. Coleman and A. Schofield *Nature*, vol. 433, p. 226, 2005.

[5] H. v. Lhneysen, T. Pietrus, G. Portisch, H. G. Schlager, A. Schrder, M. Sieck, and T. Trappmann *Phys. Rev. Lett.*, vol. 72, p. 3262, 1994.

[6] J. Custers, P. Gegenwart, H. Wilhelm, K. Neumaier, Y. Tokiwa, O. Trovarelli, C. Geibel, F. Steglich, C. Ppin, and P. Coleman *Nature*, vol. 424, p. 524, 2003.

[7] J. Hubbard *Proc. Roy. Soc. A*, vol. 276, p. 238, 1963.

[8] E. Stoner *Rep. Prog. Phys.*, vol. 11, p. 43, 1946.

[9] M. Béal-Monod *Sol. St. Comm.*, vol. 14, p. 677, 1974.

[10] J. Hertz and M. Klenin *Phys. Rev. B*, vol. 10, p. 1084, 1974.

[11] L. Landau *JETP*, vol. 16, p. 203, 1946.

[12] T. Moriya and A. Kawabata *J. Phys. Soc. Jpn*, vol. 34, p. 639, 1973.

[13] T. Moriya, *Spin fluctuations in itinerant electron magnetism.* eds. Springer-Verlag, 1985.

[14] A. Millis *Phys. Rev. B*, vol. 48, p. 7183, 1993.

[15] A. Murani, A. Tari, and B. Coles *J. Phys. F*, vol. 4, p. 1769, 1974.

[16] M. Nicklas, M. Brando, G. Knebel, F. Mayr, W. Trinkl, and A. Loidl *Phys. Rev. Lett.*, vol. 82, p. 4268, 1999.

[17] D. Sokolov, M. Aronson, W. Gannon, and Z. Fisk *Phys. Rev. Lett.*, vol. 96, p. 116404, 2006.

[18] C. Pfleiderer, M. Uhlarz, S. Hayden, R. Vollmer, H. von Löhneysen, N. Bernhoeft, and G. Lonzarich *Nature*, vol. 412, p. 58, 2001.

[19] S. S. Saxena, P. Agarwal, K. Ahilan, F.M.Grosche, R. Haselwimmer, M. Steiner, E. Pugh, I. Walker, S. Julian, P. Monthoux, G. Lonzarich, A. Huxley, I. Sheikin, D. Braithwaite, and J. Flouquet *Nature*, vol. 406, p. 587, 2000.

[20] D. Aoki, A. Huxley, E. Ressouche, D. Braithwaite, J. Flouquet, J.-P. Brison, E. Lhotel, and C. Paulsen *Nature*, vol. 413, p. 613, 2001.

[21] M. Uhlarz, C. Pfleiderer, and S. Hayden *Phys. Rev. Lett.*, vol. 93, p. 256404, 2004.

[22] C. Pfleiderer and A. Huxley *Phys. Rev. Lett.*, vol. 89, p. 147005, 2002.

[23] C. Pfleiderer, G. McMullan, S. Julian, and G. Lonzarich *Phys. Rev. B*, vol. 55, p. 55, 1997.

[24] N. Doiron-Leyraud, I. R. Walker, L. Taillefer, M. J. Steiner, S. R. Julian, and G. G. Lonzarich *Nature*, vol. 425, p. 595, 2003.

[25] C. Pfleiderer, D. Reznik, L. Pintschovius, H. von Löneysen, M. Garst, and A. Rosch *Nature*, vol. 427, p. 227, 2004.

[26] D. Belitz, T. Kirkpatrick, and T. Vojta *Phys. Rev. B*, vol. 55, p. 9452, 1997.

[27] C. Pethick and G. Carneiro *Phys. Rev. A*, vol. 7, p. 304, 1973.

[28] A. Chubukov and D. Maslov *Phys. Rev. B*, vol. 69, p. 121102(R), 2004.

[29] A. Chubukov and D. Maslov *Phys. Rev. B*, vol. 68, p. 155113, 2003.

[30] B. Altshuler, L. Ioffe, and A. Millis *Phys. Rev. B*, vol. 50, p. 14048, 1994.

[31] J. Gan and E. Wong *Phys. Rev. Lett.*, vol. 71, p. 4226, 1993.

[32] A. Abanov, A. V. Chubukov, and J. Schmalian, *The physics of Superconductors*. K.H. Bennemann and J.B. Ketterson eds, Springer, 2003, 2003.

[33] A. Chubukov, D. Maslov, S. Gangadharaiah, and L. Glazman *Phys. Rev. B*, vol. 71, p. 205112, 2005.

[34] L. B. Ioffe and A. I. Larkin *Phys. Rev. B*, vol. 39, p. 8988, 1989.

[35] P. A. Lee *Phys. Rev. Lett.*, vol. 63, p. 680, 1989.

[36] M. Lawler, D. Barci, V. Fernández, E. Fradkin, and L. Oxman *Phys. Rev. B*, vol. 73, p. 085101, 2006.

[37] A. Chubukov and D. Khveshchenko cond-mat/0604376.

[38] G. Eliashberg *Sov. Phys. JETP*, vol. 16, p. 780, 1963.

[39] A. Abanov and A. V. Chubukov *Phys. Rev. Lett.*, vol. 93, p. 255702, 2004.

[40] A. Chubukov, A. Finkelstein, R. Haslinger, and D. Morr *Phys. Rev. Lett.*, vol. 90, p. 077002, 2003.

[41] D. L. Maslov and A. V. Chubukov unpublished.

[42] G. Y. Chitov and A. J. Millis *Phys. Rev. Lett.*, vol. 86, p. 5337, 2001.

[43] G. Y. Chitov and A. J. Millis *Phys. Rev. B*, vol. 64, p. 0544414, 2001.

[44] A. Chubukov, D. Maslov, and A. J. Millis *Phys. Rev. B*, vol. 73, p. 045128, 2006.

[45] V. M. Galitski, A. V. Chubukov, and S. D. Sarma *Phys. Rev. B*, vol. 71, p. 201302, 2005.

[46] J. Betouras, D. Efremov, and A. Chubukov *Phys. Rev. B*, vol. 72, p. 115112, 2005.

[47] V. Oganesyan, S. A. Kivelson, and E. Fradkin *Phys. Rev. B*, vol. 64, p. 195109, 2001.

[48] W. Metzner, D. Rohe, and S. Andergassen *Phys. Rev. Lett.*, vol. 91, p. 066402, 2003.

[49] L. Dell'Anna and W. Metzner *Phys. Rev. B*, vol. 73, p. 045127, 2006.

[50] H. Y. Kee and Y. B. Kim *J. Phys. Cond. Matt.*, vol. 16, p. 3139, 2004.

[51] A. J. Millis, A. J. Schofield, G. G. Lonzarich, and S. A. Grigera *Phys. Rev. Lett.*, vol. 88, p. 217204, 2002.

[52] D. Belitz, T. R. Kirkpatrick, and T. Vojta *Rev. Mod. Phys.*, vol. 77, p. 579, 2005.

[53] S. Brazovskii *Sov. Phys. JETP*, vol. 41, p. 85, 1975.

[54] D. Belitz, T. R. Kirkpatrick, and A. Rosch *Phys. rev. B*, vol. 73, p. 054431, 2006.

[55] D. Belitz, T. R. Kirkpatrick, and A. Rosch cond-mat/0604427.

[56] A. Chubukov and A. Tsvelik cond-mat/0511708.

[57] D. Maslov private communication.

[58] W. de Haas, J. de Boer, and G. den Berg *Physica*, vol. 1, p. 1115, 1934.

[59] J. Kondo *Prog, Theor. Phys.*, vol. 32, p. 37, 1964.

[60] M. Sarachik, E. Corenzwit, and L. Longinotti *Phys. Rev. A*, vol. 135, p. 1041, 1964.

[61] C. Zener *Phys. Rev.*, vol. 81, p. 440, 1951.

[62] P. Anderson *J. Phys. C*, vol. 3, p. 2439, 1970.

[63] K. Wilson *Rev. Mod. Phys.*, vol. 47, p. 773, 1975.

[64] P. Anderson *Phys. rev.*, vol. 124, p. 41, 1961.

[65] J. Schrieffer and P. Wolf *Phys. Rev.*, vol. 149, p. 491, 1966.

[66] L. Glazman and L. Kouwenhoven *Physics World*, vol. 14, p. 33, 2001.

[67] H. Manoharan, C. Lutz, and D. Eigler *Nature*, vol. 403, p. 512, 2000.

[68] V. Madhavan, W. Chen, T. Jamneala, M. Crommie, and N. Wingreen *Science*, vol. 280, p. 567, 1998.

[69] J. Li and W.-D. Schneider *Phys. Rev. Lett.*, vol. 80, p. 2893, 1998.

[70] G. Fiete and E. Heller *Rev. Mod. Phys.*, vol. 75, p. 933, 2003.

[71] L. Kouwenhoven, C. Marcus, P. McEuen, S. Tarucha, R. Westervelt, and N. Wingreen, *Mesoscopic electron transport*. eds L.L. Sohn, L.P. Kouwenhoven and G.Schön (Kluwer), 1997.

[72] L. Kouwenhoven and C. Marcus *Physics World*, vol. 11, p. 35, 1998.

[73] I. Aleiner, P. Brouwer, and L. Glazman *Phys. Rep.*, vol. 358, p. 309, 2002.

[74] D. Goldhaber-Gordon, H. Shtrikman, D. Mahalu, D. Abusch-Magder, U. Meirav, and M. Kastner *Nature*, vol. 391, p. 156, 1998.

[75] S. Tarucha, D. Austing, S. Sasaki, Y. Tokura, W. van der Wiel, and L. Kouwenhoven *Appl. Phys. A*, vol. 71, p. 367, 2000.

[76] M. Kastner *Ann. Phys. (Leipzig)*, vol. 9, p. 885, 2000.

[77] S. Tarucha, D. Austing, T. Honda, R. van der Hage, and L. P. Kouwenhoven *Phys. Rev. Lett.*, vol. 77, p. 3613, 1996.

[78] L. Glazman and M. Raikh *JETP Lett.*, vol. 47, p. 452, 1990.

[79] T. Ng and P. Lee *Phys. Rev. Lett.*, vol. 61, p. 1768, 1988.

[80] W. vander Wiel, S. D. Franceschi, T. Fujisawa, J. Elzerman, S. Tarucha, and L. Kouwenhoven *Science*, vol. 289, p. 2105, 2000.

[81] T. Costi, *Concepts in Electron Correlations.* eds A.C.Hewson and V.Zlatic (Kluwer), 2003.

[82] M. Pustilnik, L. Glazman, D. Cobden, and L. Kouwenhoven *Lecture Notes in Physics*, vol. 579, p. 3, 2001.

[83] H. Jeong, a.M. chang, and M. Melloch *Science*, vol. 293, p. 2221, 2001.

[84] N. J. Craig, J. M. Taylor, E. A. Lester, C. M. Marcus, M. P. Hanson, and A. C. Gossard *Science*, vol. 304, p. 565, 2004.

[85] Y. Oreg and D. Goldhaber-Gordon *Phys. Rev. Lett.*, vol. 90, p. 136602, 2003.

[86] P. Mehta and N. Andrei cond-mat/0508026.

[87] H. Frölich and F. Nabarro *Proc. Roy. Soc. A*, vol. 175, p. 382, 1940.

[88] M. Ruderman and C. Kittel *Phys. Rev.*, vol. 96, p. 99, 1954.

[89] T. Kasuya *Prog. Theor. Phys.*, vol. 16, p. 45, 1956.

[90] K. Yosida *Phys. Rev.*, vol. 106, p. 893, 1957.

[91] J. Friedel *Phil. Mag.*, vol. 43, p. 153, 1952.

[92] S. Doniach *Physica B*, vol. 91, p. 231, 1977.

[93] K. Andres, J. Graebner, and H. Ott *Phys. Rev. Lett.*, vol. 35, p. 1779, 1975.

[94] G. Stewart *Rev. Mod. Phys.*, vol. 73, p. 797, 2001.

[95] J. Custers, *Quantum-critical behavior in the heavy-fermion compounds* $YbRh_2Si_2$ *and* $CeIn_{3-x}Sn_x$. PhD thesis, Technische Universität Dresden, 2004.

[96] P. Gegenwart, Y. Tokiwa, K. Neumaier, C. Geibel, and F. Steglich cond-mat/0406260.

[97] A. Schroeder *Nature*, vol. 407, p. 351, 2000.

[98] B. Coqblin and J. Schrieffer *Phys. Rev.*, vol. 185, p. 847, 1969.

[99] J. Schwinger, *Quantum theory of angular momentum.* Academic, New York, 1965.

[100] A. Abrikosov *Physics*, vol. 2, p. 5, 1965.

[101] N. Read and R. Newns *J. Phys. C*, vol. 16, p. 3273, 1983.

[102] A. Auerbach and K. Levin *Phys. Rev. Lett.*, vol. 57, p. 877, 1986.

[103] O. Parcollet and A. Georges *Phys. Rev. Lett.*, vol. 79, p. 4665, 1997.

[104] P. Nozières and A. Blandin *Journal de Physique*, vol. 41, p. 193, 1980.

[105] J. Luttinger *Phys. Rev.*, vol. 119, p. 1153, 1960.

[106] J. Luttinger and J. Ward *Phys. Rev.*, vol. 118, p. 1417, 1960.

[107] J. Luttinger *Phys. Rev.*, vol. 121, p. 1251, 1961.

[108] G. Baym *Phys. Rev.*, vol. 127, p. 1391, 1962.

[109] G. Baym and L. Kadanoff *Phys. Rev.*, vol. 124, p. 287, 1961.

[110] O. Parcollet, A. Georges, G. Kotliar, and A. Sengupta *Phys. Rev. B*, vol. 58, p. 3794, 1998.

[111] E. Müller-Hartmann *Z. Phys. B*, vol. 57, p. 281, 1984.

[112] O. Parcollet, *Effet Kondo et modèles quantiques désordonnés: limites de grand-N*. PhD thesis, Université Paris VI, 1998.

[113] J. Friedel *Phil. Mag.*, vol. 43, p. 153, 1952.

[114] A. Jerez, N. Andrei, and G. Zaránd *Phys. Rev. B*, vol. 58, p. 3814, 1998.

[115] B. Jones and C. Varma *Phys. Rev. Lett.*, vol. 58, p. 843, 1987.

[116] N. Read and S. Sachdev *Phys. Rev. Lett.*, vol. 66, p. 1773, 1991.

[117] A. Clogston and P. Anderson *Bull. Am. Phys. Soc.*, vol. 6, p. 124, 1961.

[118] B. Jones, C. Varma, and J. Wilkins *Phys. Rev. Lett.*, vol. 61, p. 125, 1988.

[119] B. Jones and C. Varma *Phys. Rev. B*, vol. 40, p. 324, 1989.

[120] I. Affleck and A. Ludwig *Phys. Rev. Lett.*, vol. 68, p. 1046, 1992.

[121] I. Affleck, A. Ludwig, and B. Jones *Phys. Rev. B*, vol. 52, p. 9528, 1995.

[122] J. Gan *Phys. Rev. Lett.*, vol. 74, p. 2583, 1995.

[123] J. Gan *Phys. Rev. B*, vol. 51, p. 8287, 1995.

[124] P. Nozières *J. Low Temp. Phys.*, vol. 17, p. 31, 1974.

[125] H. Shiba *Prog. Theor. Phys.*, vol. 54, p. 967, 1975.

[126] D. Langreth *Phys. Rev.*, vol. 150, p. 516, 1966.

[127] D. Withoff and E. Fradkin *Phys. Rev. Lett.*, vol. 64, p. 1835, 1990.

[128] K. Ingersent and Q. Si *Phys. Rev. Lett.*, vol. 89, p. 076403, 2002.

[129] M. Vojta *Phys. Rev. Lett.*, vol. 87, p. 097202, 2001.

[130] P. Coleman and I. Paul *Phys. Rev. B*, vol. 70, p. 1, 2004.

[131] L. Keldysh *JETP*, vol. 20, p. 1018, 1965.

[132] A. Georges, G. Kotliar, W. Krauth, and M. Rozenberg *Rev. Mod. Phys.*, vol. 68, p. 13, 1996.

[133] K. Yamada *Prog. Theor. Phys.*, vol. 53, p. 970, 1975.

[134] K. Yosida and K. Yamada *Prog. Theor. Phys.*, vol. 53, p. 1286, 1975.

[135] A. Yoshimori *Prog. Theor. Phys.*, vol. 55, p. 67, 1976.